University of Alberta

Development of Rapid Techniques for Healthcare and Environment Monitoring

by
Naga Siva Kumar Gunda

A thesis submitted to the Faculty of Graduate Studies and Research in partial fulfillment of the requirements for the degree of

Doctor of Philosophy

Department of Mechanical Engineering

Spring 2014
Edmonton, Alberta

To My Family and Friends

Abstract

The development of rapid detection techniques to be applied at the point of use, has been gaining significant attention in the recent years. Rapid techniques are important and preferable methods in healthcare and environment sector due to the advantages they offer such as low-cost and reduced requirement of resources, both in terms of material and personnel. They are of utmost importance particularly in rural settings, where the facilities are inadequate. The main focus of the present thesis is to develop and assess the applicability, efficacy and advantages of such rapid techniques for healthcare and environment monitoring. Two problems have been considered to address the requirement for rapid techniques, one from healthcare monitoring sector (cardiac marker detection) and another one from environmental sector (water-borne pathogen detection). The first problem involves the development of rapid microfluidic based methods for the detection of cardiac markers (myoglobin and troponin), in order to predict the on-set of myocardial infarction. The second problem involves the development of a field test kit for the rapid detection of total coliform and *Escherichia coli* (*E.coli*) in potable water in order to address the needs of environmental monitoring. The rapid detection techniques presented in this thesis are simple, efficient, easy to use, inexpensive, reliable and have a great potential to be applied at the point of use.

Acknowledgements

I would like to take this opportunity to thank everyone who has helped me throughout my graduate studies. First and foremost, I would like to express my deepest gratitude to my thesis supervisor, Dr. Sushanta Mitra, for his continuous guidance, enthusiasm, support, and timely encouragement throughout my graduate studies.

I would like to thank the members of my supervisory committee, Dr. Thomas Thundat and Dr. Aloke Kumar, for their valuable suggestions. I would also like to thank my previous supervisory committee members Dr. Subir Bhattacharjee and Dr. Mavanur Suresh, for their valuable inputs in my research work.

I gratefully acknowledge Dr. Selvaraj Naicker, for his constant support and assistance in various aspects. Technical interactions with him allowed me to develop practical knowledge and to learn the industry trends.

I would like to acknowledge CMC Microsystems for the loan of test instrumentation and the CMC Microfluidic Carrier Platform, that contributed to this research. CMC is a non-profit corporation funded by the Natural Sciences and Engineering Research Council of Canada (NSERC), with matching contributions from industry. I am grateful to all the Mechanical Engineering department office staff, machine shop staff, and IT personnel for their generous help at different stages. I am also thankful to all the support staff at National Institute for Nanotechnology (NINT) and Nanofab.

I would like to acknowledge the financial support from Alberta Ingenuity, now part of Alberta Innovates-Technology Futures, provided through the Graduate Student Scholarship in Nanotechnology. I am grateful to the Natural Sciences and Engineering Research Council (NSERC) of Canada and Enterprise and Advanced Education for the financial support through research grant.

I would like to thank Stream Technologies, Inc. (Edmonton, AB, Canada) and

Biological and Medicinal Chemistry Laboratory (BMCL), University of Alberta, Edmonton, Canada for providing different strains of *E.coli*. I would also like to thank Tata Consultancy Services (Mumbai Innovation Lab, India), Bhavan's Research Center, Mumbai, India and King Edward Memorial (KEM) Hospital, Mumbai, India, for their help in collecting water samples in India, constructive feedback on the developed methods and conducting the laboratory testing of collected water samples for verification.

I am thankful to all past and present members of Micro Nano Transport Laboratory (MNTL) for their co-operation and useful discussions. I would like to thank Dr. Prashant Waghmare, presently a postdoctoral fellow in MNTL, for his overwhelming support at various occasions. I would like to thank Ravi Chavali and Aleksey Baldygin for their help and support at various occasions. I express my special thanks to my friends Naresh Miriyala, Ranjit Alampally and Mayank Pandey for their constant support and encouragement.

Finally, I would like to express my sincere thanks to my parents and my sister for their patience, encouragement and understanding.

Contents

List of Tables

List of Figures

Chapter 1

Introduction

1.1 Background and Motivation

Traditional laboratory based testing for detecting target biomolecules, e.g., myoglobin, troponin, dengue, *Escherichia coli* (*E.coli*), *Listeria*, etc., be it present in human serum or in water and food products, is an expensive process [1–6]. This becomes even more challenging for limited resource communities, where specialized laboratories are sparsely available coupled with almost non-existence of technical manpower. In addition, often the connectivity of such communities to the urban centers is virtually absent, which makes even more difficult to transport samples for conventional laboratory testing. This begs the question that whether in the twenty first century, with the advancement of different disciplines of science and engineering, coupled with rise of social media and internet proliferation [7–10], is it possible to bring together some convergent technologies to create rapid detection platforms for different biomolecules? This thesis delves on this broader scientific challenge of bringing affordable low-cost technology right to the end-users.

Currently, in the healthcare sector, one of the key challenges that are causing a big concern is the rapid increase in the cases of heart attacks (approximately 7.2 million deaths per year over the entire world) [11]. Based on Framingham heart study, 5% heart attacks occur in people <40 years old, 45% in people < 65 years old [12, 13]. A study indicates that there is a 23% increase in the risk of heart attacks due to work related stress in the recent years [14]. This has multiplied due to the sedentary life styles in growing middle class population, for example, in China approximately 1.04 million deaths occur per year [15–17], in India approximately 1.25 million deaths occur per year [18]. It should be emphasized that certain food

habits among South Asian population are also a contributing factor for deaths related to the heart diseases.

Acute myocardial infarction (AMI), commonly known as a heart attack, results from the interruption of blood supply to a part of the heart, causing heart cells to die [16, 22]. Typical symptoms of AMI include sudden chest pain, shortness of breath, nausea, vomiting, palpitations, sweating, and anxiety [21]. A sizable proportion of myocardial infarctions (22-64 %) are "silent", that is without chest pain or other symptoms [22]. Current diagnostic tests available to detect heart muscle damage are an electrocardiogram (ECG), echocardiography, cardiac MRI and various blood tests [5–7, 16, 17]. Blood tests are used to measure the concentrations of certain cardiac markers (myoglobin, troponin I, troponin T, and CK-MB) in the blood sample using standard enzyme-linked immunosorbent assay (ELISA) [5–7, 16, 17]. However, these tests are expensive, time consuming, unreliable and requires a qualified professional to perform the test. Most people panic when experiencing chest pain often assuming that it is a heart attack. Patients frequently present to the emergency room (ER) with non-specifc symptoms, which have a broad differential diagnosis. In most cases of chest pain, cardiac etiology is generally ruled out, however, ruling it out still requires a large number of lengthy and costly tests, resulting in extended stays in overcrowded ERs. In US alone, 6 million individuals present at hospitals complaining about chest pain, but only 8% of these individuals are diagnosed as having a heart attack. The rest of the 92% individuals are diagnosed as having non-cardiac pain [12, 27]. Each year approximately 70,000 heart attacks occur in Canada. That is one heart attack every 7 minutes and costs the Canadian economy $ 20.9 billion each year [28–30]. In this regard, there is a strong need for an early diagnosis of heart attack as well as a device that can be used as a primary check to eliminate false alarms and panic in cases of non-cardiac chest pains. The key challenge is timely intervention of 911 dispatchers/medical doctors in the first 5 min of the event. Can a rapid diagnostic system be a solution to this global challenge in public health?

Several lateral flow and Lab-on-a-Chip (LOC) based rapid tests are developed to measure the concentration of cardiac markers either qualitatively or quantitatively [31]. RAMP 3.2® (Response Biomedical Corporation, Canada) produces fluorescent intensity based benchtop diagnostic system, where it detects troponin

I, CK-MB and myoglobin from whole blood samples within 15 min or less. This system consists of compact fluorescent analyzer and a disposable test cassette. Disposable test cartridge is based on immuno-chromatography lateral flow technology. The test cassette comprises of fluorescently labelled antibodies on polymer particles specific to target cardiac marker of interest. These labelled antibodies bind with cardiac markers (if any) in the blood samples and forming an antigen-antibody polymer complex at the detection zone. The fluorescence emitted by the polymer complex at the detection zone is measured using compact fluorescent analyzer. Similar type of fluorescence based detection technology has been used in other commercial devices such as Triage cardiac panel® (Biosite Diagnostics, Inc., San Diego, CA, USA), Cobas h232® (Roche Diagnostics), cardiac reader systems (Roche diagnostics Ltd.), Alpha Dx® (First Medical Inc., Mountain View, CA, USA). All of these devices measures standard cardiac markers (myoglobin, CK-Mb and troponin I) within 8 to 15 min. Some other commercial devices such as cardiac STATus® (Nanogen) and evidence investigator biochip array (Randox laboratories Ltd.) work based on chemiluminometric detection instead of fluorescent detection. Companies such as Artron Laboratories (Burnaby, BC, Canada), Spectral Diagnostics, Inc., (Toronto, ON, Canada), Blue Cross Bio-Medical Corp., (Beijing, China), MagnaBioSciences, LLC., (San Diego, CA, USA), LumiQuick Diagnostics, Inc., (Santa clara, USA), Rapid Diagnostics (Burlingame, CA, USA), Cortez Diagnostics, Inc., (Calabasas, CA, USA), and Diagnostics Automation (USA) have lateral flow rapid tests. Most of them provide qualitative measurements by change in color at the detection zone. In addition some of the companies provide color intensity readers to quantify the concentration of cardiac markers. Abott® point of care released i-STAT® for detecting cardiac markers that can detect the markers within couple of minutes. It uses the amperometric electrochemical detection principle to quantify the concentration of markers from blood sample. Most of these devices are still not available for rapid emergency use at home, emergency room, or ambulances, due to several drawbacks such as lack of reproducibility, sensitivity, etc. Moreover, these test kits and instruments are expensive and need professional expertise to analyze the results. In addition, the levels of cardiac markers vary with time after AMI and hence a continuous monitoring of cardiac marker levels is needed and it can be achieved by using low-cost

disposable test kits.

Another area where such rapid detection techniques can be applied is the environmental sector. Water is an extremely valuable resource that has direct impact on the quality of human life. To maintain the high quality standards, water monitoring has become very essential to detect pathogens such as *E.coli*. Presence of *E.coli* is a good indicator of possibility of other viruses, protozoans, etc. in water. The traditional method for the detection of *E.coli* involves the membrane filtration followed by the plating method on agar gel, incubation and counting the number of cells. Alternatively, fermentation methods were used to observe the production of gas due to target water-borne pathogens. However these methods are laboratory based, labor intensive, requires qualified individuals to perform the test, and takes more than 24 hours to get the results. In the last ten years, United States Environmental Protection Agency (USEPA) has approved ten methods and none of them provide results in less than an hour. These methods are time consuming and the turnaround time is more than 18 hours. None of them are suitable for field-testing and need the service of skilled personnel.

As mentioned earlier, water monitoring is critical to ensure safe drinking water for communities. Access to clean water has huge implications in terms of public health. As per World Health Organization (WHO), loss in number of working days due to water borne diseases is 73 million each year. In United States, according to Center for Disease Control and Prevention (CDC), 73,000 cases of *E.coli* infection are estimated each year with a mortality rate of approximately 8.9% [32]. In Canada, Walkerton, ON, experienced an outbreak of *E.coli* in 2000, due to improper monitoring of water distribution system [33]. It was estimated that 2300 cases of infection and 7 deaths [33]. As per study conducted by Schuster et al. [34], there were 288 recorded outbreaks in Canada from 1974 to 2001. Typical water borne diseases and infections are viral (e.g., hepatitis A, SARS (severe acute respiratory syndrome), poliomyelitis, polyomavirus); bacterial (e.g., botulism, cholera, dysentery, leptospirosis, typhoid, E.coli and coliform infection); protozoal (e.g., amoebiasis, cyclosporiasis cryptosporidiosum, giardia, microsporidiosis); parasitic (e.g., schistosomia, guinea worm disease (dracunculiasis), taeniasis, fasciolopsiasis); and toxins (e.g., fluoride, arsenic, cadmium, numerous organic chemicals), which use water as a common means of propagation [35–37]. Diarrhea is a com-

mon symptom of infection caused by water borne diseases due to contaminated potable water [35]. In developing countries, approximately 2.2 million deaths per year occur due to water borne diseases and among them 1.08 million deaths occur in India alone [38, 39]. Ninety percent of these deaths are children under age five [39]. Hence, availability of rapid tools to monitor water quality not only empowers the communities with access to clean water but also delivers much needed intervention for public health.

It is evident that healthcare and environmental sectors are some of the areas where science and engineering can provide game-changing technology for the masses. In keeping this spirit, the main objectives of this thesis are outlined in the next section.

1.2 Objectives

The main objectives of this thesis work are:

- Exploring different options to develop a rapid test kits for early prediction of potential heart attacks;
- Development of rapid techniques for water borne pathogen detection in contaminated potable water samples;

The drawbacks mentioned for the early diagnosis of heart attacks can be eliminated to a certain extent with the help of microfluidic based Lab-on-a-Chip (LOC) biosensor platforms. These microfluidic based biosensor platforms offer numerous advantages over the conventional protocols in terms of swift analysis time, cost effectiveness, and portability [40–42]. A typical LOC device contains sample preparation chamber (separation), reaction chambers (mixers) and sensing area (detection). The present study aims to develop and optimize the design parameters and experimental conditions to demonstrate a highly sensitive method for rapid detection of cardiac markers.

Similarly for water monitoring, the drawbacks mentioned for regular screening of water samples for pathogen detection can be eliminated to a certain extent by developing rapid techniques. The ability to identify biological molecules or pathogens associated with certain enzymatic activity is considered as a possibility

to develop a rapid method to detect total coliform and *E.coli* in water samples. *E.coli* is known to secrete β-galactosidase and β-glucuronidase enzymes and therefore these enzymes can be used as the markers/indicators for total coliform and *E.coli* pathogens, respectively [53–55]. The detection of enzymes using defined substrate technology is well-known, robust and cost effective. The present work explores new methods and chemicals to accelerate the enzymatic reaction to detect the *E.coli* within less time.

1.3 Thesis organization

This thesis has been organized based on published papers. The guidelines from the Faculty of Graduate Studies and Research (FGSR) at the University of Alberta have been followed to prepare this paper based thesis. This thesis consists of eleven chapters.

Chapter 1 (the present chapter) serves as the introduction to the thesis and provides the central motivation and objectives of the thesis.

Chapter 2 emphasizes the development of mathematical model for simulating dielectrophoretic (DEP) behavior of a myoglobin molecule in a microchannel to provide a theoretical basis for the separation and detection of cardiac markers. In this chapter, DEP theory is explained briefly and dielectric myoglobin model is introduced. This chapter provides the solution methodologies and analyzes the behavior of myoglobin under DEP.

Chapter 3 presents the use of dielectrophoresis (DEP) and electrothermal (ET) forces to develop on-chip micromixers and microconcentrators.

Chapter 4 focuses on experimental investigation of behavior of myoglobin molecules on a microelectrode surface under the influence of dielectrophoresis. In this chapter, materials and methods required to conduct the DEP experiments are described with the emphasis on microelectrode fabrication, equipment, electrical connections, myoglobin preparation and manipulation.

Chapters 5, 6 and 7 focuses on the immobilization of antibodies on silicon and gold surfaces. In particular for biomolecules related to cardiac marker detection.

Chapters 8, 9 and 10 focuses on the development of rapid detection techniques for water-borne pathogens. Chapter 8 presents the development of a simple, easy

to use, rapid and field deployable method for detecting total coliform and *E.coli* in contaminated water using microcentrifuge tubes. Chapter 9 illustrates the development of Mobile Water Kit (MWK): a smartphone compatible low-cost water monitoring system for rapid detection of total coliform and *E.coli*. Chapter 10 emphasizes on development of sensitive and rapid method for detecting total coliform and *E.coli* in contaminated water using Micro-spot integrated with wells (MSIW).

Finally, Chapter 11 draws conclusions with important observations and introduces possible directions for future work based on the outcomes of the research.

Bibliography

[1] D. Powell and S. A. Seabury. Medical care spending and labor market outcomes. *RAND Corporation*, 2014.

[2] O. Y. Bang, B. Ovbiagele, and J. S. Kim. Evaluation of cryptogenic stroke with advanced diagnostic techniques. *Stroke*, STROKEAHA–113, 2014.

[3] I. Satyamurthy, J. J. Dalal, J. Sawhney, J. Mohan, S. A. Chogle, N. Desai, S. P. Sathe, and A. S. Maisel. The indian consensus document on cardiac biomarker. *Indian Heart Journal*, 66(1):73–82, 2014.

[4] D. W. Carroll. Medical issues and medical professionals. *American Psychological Association*, 2013.

[5] B. Zhang, A. W. Morales, R. Peterson, L. Tang, and J. Y. Ye. Label-free detection of cardiac troponin i with a photonic crystal biosensor. *Biosensors and Bioelectronics*, 58:107–113, 2014.

[6] J. A. Macoviak, S. Poulis, and A. Vlachos. Remotely-executed medical diagnosis and therapy including emergency automation, February 27 2014. US Patent 20,140,058,755.

[7] C. Gnanasambandam, A. Madgavkar, N. Kaka, J. Manyika, M. Chui, J. Bughin, and M. Gomes. Online and upcoming: The internet impact on india. *Technology, Media and Telecom Practice, Mc Kinsey and Company*, 2012.

[8] A. M. Kaplan and M. Haenlein. Users of the world, unite! the challenges and opportunities of social media. *Business horizons*, 53(1):59–68, 2010.

[9] S. Kalathil and T. C. Boas. The internet and state control in authoritarian regimes: China, cuba and the counterrevolution. *First Monday*, 6(8), 2001.

[10] J.-Y. Kim. The impact of internet use patterns on political engagement: A focus on online deliberation and virtual social capital. *Information Polity*, 11(1):35–49, 2006.

[11] S. Shurin. Morbidity and mortality: 2012 chart book on cardiovascular, lung, and blood diseases. *National heart, lung and blood institutes website*, 2012.

[12] V. L. Roger, A. S. Go, D. M. Lloyd-Jones, E. J. Benjamin, J. D. Berry, W. B. Borden, D. M. Bravata, S. Dai, E. S. Ford, C. S. Fox, et al. Heart disease and stroke statistics 2012 update a report from the american heart association. *Circulation*, 125(1):e2–e220, 2012.

[13] R. Vigen, T. M. Maddox, and L. A. Allen. Aging of the united states population: impact on heart failure. *Current heart failure reports*, 9(4):369–374, 2012.

[14] M. Kivimäki, S. T. Nyberg, G. D. Batty, E. I. Fransson, K. Heikkilä, L. Alfredsson, J. B. Bjorner, M. Borritz, H. Burr, A. Casini, et al. Job strain as a risk factor for coronary heart disease: a collaborative meta-analysis of individual participant data. *The Lancet*, 380(9852):1491–1497, 2012.

[15] P. Chau, M. Wong, and J. Woo. Trends in ischaemic heart disease hospitalisation and case fatality in the hong kong chinese population 2000–2009: a secondary analysis. *BMJ open*, 3(8), 2013.

[16] A. Moran, D. Gu, D. Zhao, P. Coxson, Y. C. Wang, C.-S. Chen, J. Liu, J. Cheng, K. Bibbins-Domingo, Y.-M. Shen, et al. Future cardiovascular disease in china markov model and risk factor scenario projections from the coronary heart disease policy model–china. *Circulation: Cardiovascular Quality and Outcomes*, 3(3):243–252, 2010.

[17] X. Zhang, Z. Lu, and L. Liu. Coronary heart disease in china. *Heart*, 94(9):1126–1131, 2008.

[18] A. Indrayan. Forecasting vascular disease cases and associated mortality in india. *Burden of disease in India*, page 197, 2005.

[19] B. M. Mayr, O. Kohlbacher, K. Reinert, M. Sturm, C. Gropl, E. Lange, C. Klein, and C. G. Huber. Absolute myoglobin quantification in serum by combining two-dimensional liquid chromatography - electrospray ionization mass spectrometry and novel data analysis algorithms. *J Proteome Res*, 5:414–421, 2006.

[20] J. Wang, Q. Wang, L. Ren, X. Wang, Z. Wan, W. Liu, L. Li, H. Zhao, Manlin, D. Tong, and J. Xu. Carboxylated magnetic microbead-assisted fluoroimmunoassay for early biomarkers of acute myocardial infarction. *Colloids Surf, B*, 72:112–120, 2009.

[21] D. Bosch and L. McKay. Trauma & critical incident care for humanitarian workers. 2013.

[22] A. Sabzghabaei, S. Asgharzade, R. Miri, M. Shojaee, H. Alimohammadi, and K. Heidari. Short-term outcome of discharged low-risk chest pain without provoke ischemia study. *Emergency*, 1(2), 2014.

[23] G. T. Perkoff, R. L. Hill, D. M. Brown, and F. H. Tyler. The characterization of adult myoglobin. *The Journal of Biological Chemistry*, 237(9):2820–2827, 1962.

[24] A. M. Potts. Methods for separation of proteins. *Investigative Ophthalmology*, 4(4):531–538, 1965.

[25] W. H. Boesken, S. Boesken, and A. Mamier. Human myoglobin: Preparation, quantification and standardization. *Research in Experimental Medicine*, 171:71-78, 1977.

[26] J. Evan. Novel data analysis technique aids heart attack diagnosis. See also URL Lab Informatics, separationsNOW.com, February 2006.

[27] S. M. Haffner, S. Lehto, T. Rönnemaa, K. Pyörälä, and M. Laakso. Mortality from coronary heart disease in subjects with type 2 diabetes and in nondiabetic subjects with and without prior myocardial infarction. *New England journal of medicine*, 339(4):229–234, 1998.

[28] D. M. Cutler, M. B. McClellan, J. P. Newhouse, and D. K. Remler. Pricing heart attack treatments. In *Medical care output and productivity*, 305–362. University of Chicago Press, 2001.

[29] B. L. Hicken, D. Smith, M. Luptak, and R. D. Hill. Health and aging in rural America. *Rural Public Health: Best Practices and Preventive Models*, 241, 2014.

[30] M. Joffres, E. Falaschetti, C. Gillespie, C. Robitaille, F. Loustalot, N. Poulter, F. A. McAlister, H. Johansen, O. Baclic, and N. Campbell. Hypertension prevalence, awareness, treatment and control in national surveys from england, the usa and canada, and correlation with stroke and ischaemic heart disease mortality: a cross-sectional study. *BMJ open*, 3(8):e003423, 2013.

[31] H.-H. Chen, Y.-H. Chen, T.-C. Chen, and L.-G. Chen. Mobile energy expenditure tracking system based on heart rate and motion providing extra extensions for personalized care. In *Engineering in Medicine and Biology Society, EMBC, 2011 Annual International Conference of the IEEE*, pages 5256–5259. IEEE, 2011.

[32] P. S. Mead, L. Slutsker, V. Dietz, L. F. McCaig, J. S. Bresee, C. Shapiro, P. M. Griffin, and R. V. Tauxe. Food-related illness and death in the united states. *Emerging infectious diseases*, 5(5):607, 1999.

[33] K. J. Vicente and K. Christoffersen. The Walkerton E.coli outbreak: a test of rasmussen's framework for risk management in a dynamic society. *Theoretical Issues in Ergonomics Science*, 7(02):93–112, 2006.

[34] C. J. Schuster, J. J. Aramini, A. G. Ellis, B. J. Marshall, W. J. Robertson, D. T. Medeiros, and D. F. Charron. Infectious disease outbreaks related to drinking water in canada, 1974-2001. *Canadian Journal of Public Health*, 96(4), 2005.

[35] P. H. Gleick. *The world's water 2004-2005: the biennial report on freshwater resources*. Island Press, 2004.

[36] I. Borts. Water-borne diseases*. *American Journal of Public Health and the Nations Health*, 39(8):974–978, 1949.

[37] M. Demena, A. Workie, E. Tadesse, S. Mohammed, and T. Gebru. Water borne disease. 2003.

[38] S. L. Murphy, J. Xu, and K. D. Kochanek. Deaths: final data for 2010. *National vital statistics reports*, 61(4), 2013.

[39] I. Khurana and R. Sen. Drinking water quality in rural india: Issues and approaches. *WaterAid India*, 2008.

[40] H. Jiang, X. Weng, and D. Li. Microfluidic whole-blood immunoassays. *Microfluidics and Nanofluidics*, pages 1–24, 2010.

[41] C. C. Lin, J. H. Wang, H. W. Wu, and G. B. Lee. Microfluidic immunoassays. *JALA - Journal of the Association for Laboratory Automation*, 15(3):253–274, 2010.

[42] D. Erickson and D. Li. Integrated microfluidic devices. *Analytica Chimica Acta*, 507(1):11–26, 2004.

[43] B. H. Weigl, R. L. Bardell, and C. R. Cabrera. Lab-on-a-chip for drug development. *Advanced Drug Delivery Reviews*, 55(3):349–377, 2003.

[44] N. Lion, T. C. Rohner, L. Dayon, I. L. Arnaud, E. Damoc, N. Youhnovski, Z. Y. Wu, C. Roussel, J. Josserand, H. Jensen, J. S. Rossier, M. Przybylski, and H. H. Girault. Microfluidic systems in proteomics. *Electrophoresis*, 24(21):3533–3562, 2003.

[45] B. H. Lapizco-Encinas and M. Rito-Palomares. Dielectrophoresis for the manipulation of nanobioparticles. *Electrophoresis*, 28:4521–4538, 2007.

[46] M. P. Hughes. *Nanoelectromechanics in Engineering and Biology*. CRC Press, Boca Raton, 2003.

[47] X. B. Wang, Y. Huang, J. P. H. Burt, G. H. Markx, and R. Pethig. Selective dielectrophoretic confinement of bioparticles in potential energy wells. *J Phys D: Appl Phys*, 26:1278–1285, 1993.

[48] S. Edberg, E. Rice, R. Karlin, and M. Allen. Escherichia coli: the best biological drinking water indicator for public health protection. *Journal of Applied Microbiology*, 88(S1):106S–116S, 2000.

[49] M. Manafi. New developments in chromogenic and fluorogenic culture media. *International Journal of Food Microbiology*, 60(2):205–218, 2000.

[50] A. Rompré, P. Servais, J. Baudart, M.-R. de Roubin, and P. Laurent. Detection and enumeration of coliforms in drinking water: current methods and emerging approaches. *Journal of Microbiological Methods*, 49(1):31–54, 2002.

Chapter 2

Modeling of Dielectrophoretic Transport of Myoglobin [1]

2.1 Overview

Myoglobin is one of the premature identifying cardiac markers, whose concentration increases from 90 pg/ml or less to over 250 ng/ml in the blood serum of human beings after minor heart attack. Separation, detection and quantification of myoglobin play a vital role in revealing the cardiac arrest in advance, which is the challenging part of ongoing research. In the present work, one of the electrokinetic approaches i.e., dielectrophoresis (DEP) is chosen to separate the myoglobin. A mathematical model is developed for simulating dielectrophoretic behavior of a myoglobin molecule in a microchannel to provide a theoretical basis for cardiac marker detection. This chapter emphasizes the theoretical investigation of DEP transport of myoglobn.

2.2 Introduction

Heart attack, also known as myocardial infarction (MI) or acute myocardial infarction (AMI), is the death of heart muscles, which occurs when blood supply to any part of the heart is blocked [16, 22]. Early assessment of heart condition would avoid heart attacks in near future and researchers have been struggling for years to develop a viable solution. It has been found that the concentration of certain proteins and/or enzymes increases in the blood serum after infarction. Hence, these proteins or enzymes are considered as cardiac markers. The cardiac proteins

[1] A version of this chapter has been published. N. S. K. Gunda and S. K. Mitra. *Biomicrofluidics*, 4(1):14105, 2010.

like myoglobin, troponin I, troponin T, CK-MB, fatty acid-binding protein (also known as H-FABP) and isoenzymes appear in the blood serum of human beings immediately after MI [22, 23]. Myoglobin is one of the cardiac protein markers that can be used for early intervention after a heart attack. Myoglobin concentration level increases from approximately 90 pg/ml to over 250 ng/ml in the blood serum within the first 2-8 hours after heart muscles start dying [16, 17]. Therefore in this study, myoglobin is considered as the target molecule for early diagnosis of major heart attacks.

Several separation methods like SDS-polyacrylamide gel electrophoresis (SDS-PAGE), one dimensional gel (1-D) electrophoresis, isoelectric focusing, two dimensional (2-D) gel electrophoresis, anion-exchange chromatography, gel filtration chromatography, affinity chromatography and multi dimensional chromatography are well-known methods for myoglobin separation [5–7, 16, 17]. Most of these methods separate the myoglobin from tissue or blood based on molecular weight or size or ionic charge on the myoglobin molecules [5–7]. The separated myoglobin can be identified or detected by one of the following methods such as Western blotting [6], Edman degradation and mass spectrometry [16, 17]. Mass spectrometry is also used to determine the concentration of myoglobin [16, 17].

Huang et al. [8] proposed a bedside assay by sandwich dot-immunogold filtration for the diagnosis of AMI. This assay gives the qualitative measurements for increased human serum myoglobin. Radioimmunoassay [16] and enzyme linked immunosorbent assay (ELISA) [9, 10, 23] techniques are also used for qualitative determination of myoglobin concentration in blood serum or plasma. O'Regan et al. [11] developed a disposable immunosensor for the rapid detection of myoglobin in whole blood. The sensor is based on one step indirect sandwich assay. This indirect approach offers a wider working ranges for detection of concentration levels of myoglobin. Wang et al. [22] demonstrated the carboxylated magnetic microbead-assisted fluoroimmunoassay for the analysis of the early AMI protein markers, myoglobin and H-FABP. They detected myoglobin and H-FABP in the range of $25 - 250$ and $1 - 25$ ng/ml, respectively.

Commercial immunoassay instruments are also available for qualitative or quantitaive measurement of myoglobin concentration in blood serum or plasma. They are Access (Beckman Coulter, Brea, CA, USA), Triage cardiac panel(Biosite Diag-

nostics, San Diego, CA, USA), Dade Behring BN II Nephelometer, Dade Behring OPUS Immunoassay, Dimension RxL and Stratus CS (Dade Behring, Deerfield, IL, USA), AxSYM (Abbott Laboratories, Abbott Park, IL, USA), immunometric VIDAS MYO(BioMerieux, Marcy l'Etoile, France), Hitachi 917, Hitachi 911, Elecsys 2010 and Integra 400 (Roche Diagnostics, Penzberg, Germany), Olympus AU640 multi parameter analyzer (Olympus Optical Co. Ltd, Tokyo, Japan), Immulite turbo Myoglobin LSKMY (DPC France, La Garenne Colombes France), and AQT90 FLEX (Innotrac Diagnostics, Turku, Finland) [12–15].

Recently, a portable rapid myoglobin test cassette from Boston Biotechnology Co., Ltd, Fujian, China, was released in the market for qualitative assessment of human myoglobin in human serum, plasma and whole blood. The test cassette is an immunochromatography based, one step, in vitro test. It detects the myoglobin in blood serum or plasma, if the levels are 100 ng/ml or higher. But these instruments/methods provide different values of myoglobin levels [17]. In addition, this equipment is expensive and take hours for detection [16, 17]. Therefore, developing a cost-effective, accurate, reliable and standard technique for separating, detecting, and quantifying the myoglobin from a whole blood sample will be a major development in the early assessment of cardiac arrest. However, there is a limited understanding of micro-scale behavior and transport of such biomolecule in a microfluidic device. The current methods of separating myoglobin in a microchannel are very limited which cannot offer strong support for myoglobin separation and detection based on electrical properties such as permittivity and conductivity. Therefore, this chapter focuses on the theoretical investigation of manipulation of myoglobin molecules in a microfluidic device with the help of dielectrophoresis.

Dielectrophoresis (DEP) is the manipulation of dielectric or neutral particles because of polarization effects under nonuniform electric fields [2]. The net force created with DEP generates momentum in the particles. Particle movement towards regions of high electric field intensities is called positive DEP and occurs when the interior of the particle is more permissive to the field. The opposite effect is the movement towards lower electric field intensities called negative DEP, when the exterior is more permissive [2–4]. The frequency at which the DEP effect changes from positive DEP to negative DEP or negative DEP to positive DEP is called crossover frequency [2, 3]. The DEP force depends on both the gradient

of the electric field and electrical properties such as permittivity and conductivity of the particle and medium. It is important to note that the force due to DEP is based on the gradient of electric field and not the absolute value at any point. Analysis of movement of the particles in a nonuniform electric field needs accurate knowledge of the electric field distribution in the system.

DEP has significant advantages in the areas of biomedical, pharmaceutical, drug delivery, and point-of-care systems [2–5]. It helps in separating, trapping, concentrating, mixing, and sorting of particles with sizes varying from a few micron to nanometers such as cells, bacteria, viruses, DNA, and proteins [2–6, 21–32]. In the last few decades, application of DEP principle for manipulating biomolecules has increased because of improvements in micro/nano fabrication facilities [1]. Since DEP is based on the differences in dielectric properties of particles and suspended medium, there is no need of special sample preparation or chemical/biological modifications of the sample [34], when there are no competing molecules of same properties. The sample preparation is essential only when the sample contains similar characteristics molecules/particles with similar structure, mass and polarization. Availability of predefined properties of most of the important proteins has increased the use of DEP technique [4].

The initial experimentation on protein manipulation under DEP effects was conducted by Washizu et al.[7]. An array of 1 μm width corrugated microelectrodes with a minimum gap of 4, 15, and 55 μm between the electrodes was used for creating nonuniform electric fields. The trapping of avidin (68 kDa), concanavalin (52 kDa), chymotrypsinogen (25 kDa), and ribonuclease A (13.7 kDa) proteins at the edges of the electrodes under positive DEP was demonstrated. They measured protein concentration using a fluorescence detection unit and plotted a graph showing fluorescence intensity vs time, indicating a relation between the molecular weight and fluorescent intensity of proteins. Their work showed only the positive DEP of proteins. Later, Bakewell et al.[8] and Hughes et al.[9] showed the positive and negative DEP effect on proteins. They used polynomial electrodes with center gap of 2 μm for manipulating the avidin protein molecules. Zheng et al.[10, 11] reported manipulating bovine serum albumin (BSA) protein under positive DEP effects. They used the quadrupole gold microelectrodes with center gap of 5, 10, 20, and 50 μm for trapping the BSA proteins. They presented the mathematical

calculation of the Clausius-Mossotti (CM) factor for BSA protein. They modeled BSA protein as sphere of 5 nm diameters and predicted the crossover frequency of 100 MHz for the protein solution of conductivity 1 mS/m. Clarke et al.[12] demonstrated the dielectrophoretic concentration of proteins with nanopipette technique. Existing literature suggests that theoretical investigations on DEP manipulation of proteins such as myoglobin molecules are limited and are needed to support the experimental study. Therefore, the dielectrophoretic behavior of myoglobin is theoretically investigated in this work.

2.3 Brief introduction of DEP theory

When a neutral particle is placed in a nonuniform electric field, it experiences a net force due to induced dipole moment. This net force is known as the DEP force, which depends on the volume of particle, electrical properties of the medium and the particle, and magnitude and frequency of the applied AC electric field [2]. An AC electric field is used to avoid any membrane charging or hydrolysis effect on biomolecules [5]. Advantage of using microelectrodes is that large field gradient can be produced with lower volatges [1, 5].

The time averaged dielectrophoretic force $\mathbf{F}_{DEP}$ acts on any arbitrary shaped particle due to stationary wave nonuniform AC electric field. It is derived with slight modification of $\mathbf{F}_{DEP}$ acting on spherical particles provided by Pohl[2]

$$\mathbf{F}_{DEP} = \frac{3}{2}(vol)\varepsilon_m Re[K(\omega)]\nabla(\mathbf{E}\cdot\mathbf{E}) \tag{2.1}$$

where (vol) is the volume of particle, ε_m is the permittivity of medium, $Re[K(\omega)]$ is real part of CM factor and $\mathbf{E}$ is the applied electric field vector. CM factor for any arbitrary shaped particle is given as [41]

$$K(\omega) = \frac{1}{3}\frac{(\varepsilon_p^{'} - \varepsilon_m^{'})}{\varepsilon_m^{'} + A_\alpha(\varepsilon_p^{'} - \varepsilon_m^{'})} \tag{2.2}$$

where A_α is the depolarization factor, subscript α relates to axis of the particle x or y or z and $\varepsilon_p^{'}$ and $\varepsilon_m^{'}$ are complex permittivities of particle (here myoglobin) and medium respectively. They are given as

$$\varepsilon_p^{'} = \varepsilon_p - j\frac{\sigma_p}{\omega} \tag{2.3}$$

$$\varepsilon_m^{'} = \varepsilon_m - j\frac{\sigma_m}{\omega} \tag{2.4}$$

where ε_p and ε_m are permittivity of particle and medium respectively, σ_p and σ_m are conductivity of particle and medium respectively, ω is angular frequency of the applied field and $j = \sqrt{-1}$. Theoretically, $Re[K(\omega)]$ varies from -0.5 to +1 [2, 3]. It is observed that CM factor varies with respect to axis of the particle. But in the microchannel, the direction of DEP force acting on the particle is arbitrary. Hence, average CM factor is considered for the particle to calculate DEP force.

From Eq.2.1, it is observed that DEP force becomes less effective for small particles, mainly with molecular sizes and submicron particles where thermal effects are dominant. Most of the conventional DEP experiments demonstrated the response of particles with the change in frequency of the applied electric field to decide the crossover frequencies [42]. This crossover frequencies can be calculated from complex Clausius-Mossotti factor $K(\omega)$. If $Re[K(\omega)] \geq 0$, positive DEP occurs, otherwise it is negative DEP. The crossover frequency for any arbitrary shaped particle is given as

$$f_c = \frac{1}{2\pi}\sqrt{\frac{(\sigma_m - \sigma_p)[\sigma_m + A_\alpha(\sigma_p - \sigma_m)]}{(\varepsilon_p - \varepsilon_m)[\varepsilon_m + A_\alpha(\varepsilon_p - \varepsilon_m)]}} \tag{2.5}$$

It is observed that f_c can be calculated only when $\frac{(\sigma_m - \sigma_p)}{(\varepsilon_p - \varepsilon_m)} > 0$. If $\varepsilon_p = \varepsilon_m$, f_c will tend to ∞, and practically, it is not possible to apply such frequency for observing two types of DEP effects.

2.4 Dielectric myoglobin model

In this section, the modeling of myoglobin molecule for DEP and the calculation of depolarization factors for the different shapes of molecule are discussed. Myoglobin is a single chain globular protein of 153 amino acids containing heme (iron containing porphyrin) prosthetic group in the center around which remaining apoprotein folds [18–21, 43, 47, 49]. It has molecular weight of 16.7 kDa [18–21]. It is the primary oxygen carrying pigment of muscle tissues. Myoglobin has isoelectric point at pH 8.5, [17] where it acts as a neutral particle. It is observed that external electric fields and shear flow may change the conformation of myoglobin molecules and changes the charges on myoglobin surface. However, in the present work, it is assumed that the myoglobin remains electrically neutral at pH=8.5 under external electric fields and shear flow. Neurath [50] proposed the myoglobin molecule as

prolate spheroid of axial ratio 2.9 : 1 based on Svedberg theory. Later, based on X-ray studies, myoglobin molecule was represented as an oblate spheroid of axial ratio 2 : 1 [18]. Further, Grant et al. [21] have modeled the myoglobin molecule as a spheroidal shape of radius 1.53 nm surrounded by a uniform shell of bound water of thickness 0.35 nm. To the best of authors' knowledge, there is no universally accepted exact shape of the myoglobin molecule due to its globular structure. Therefore, the shape of the myoglobin molecule is approximated as sphere, oblate and prolate spheroids, as shown in Fig.2.1. Depolarization factor for the CM factor varies according to the shape of the particle which leads to change in DEP force. Yang et al. [41] reported the calculation of depolarization factor for ellipsoidal, oblate and prolate spheroid shapes. The sum of different axis depolarization factors for a particle should be unity. Considering a, b, and c as dimensions of the particles in the x, y, and z-axis directions respectively, the depolarization factors are given as

For Sphere ($a = b = c$):

$$A_x = A_y = A_z = \frac{1}{3} \tag{2.6}$$

For Oblate spheroid ($a = b > c$):

$$A_x = A_y = \frac{a^2 c}{2(a^2 - c^2)} \left[\frac{\pi/2}{\sqrt{(a^2 - c^2)}} - \frac{c}{a^2} \right] \tag{2.7}$$

$$A_z = 1 - 2A_x = 1 - 2A_y \tag{2.8}$$

For Prolate spheroid ($a > b = c$):

$$A_x = \frac{b^2}{2a^2 e^3} \left[\ln(\frac{1+e}{1-e}) - 2e \right] \tag{2.9}$$

$$A_y = A_z = \frac{(1 - A_x)}{2} \tag{2.10}$$

where eccentricity (e) is given as $\sqrt{(1 - \frac{b^2}{a^2})}$.

In the present study, the dimensions of different shapes of myoglobin molecule are derived based on the constant volume approach. According to Grant et al. [21], the volume of myoglobin is 15 nm^3. Based on this volume, the geometry of the different shapes of myoglobin is modeled as, (i) $a = b = c = r = 1.53$ nm (for sphere); (ii) $a = b = 1.93$ nm, $c = 0.96$ nm (for oblate spheroid); and (iii) $a = 2.43$ nm, $b = c = 1.21$ nm (for prolate spheroid). Three different cases are considered

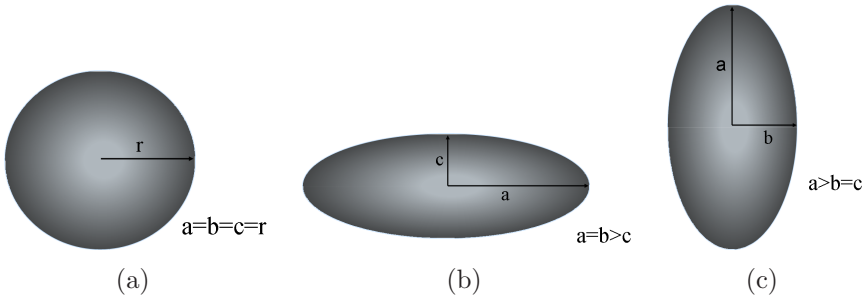

Figure 2.1: Approximated shapes of myoglobin molecule; (a) Sphere; (b) Oblate spheroid; (c) Prolate spheroid

for each shape of the molecule based on the surface characteristics of myoglobin: (i) isolated myoglobin molecule; (ii) myoglobin with effect of charge double layer using surface conductance method; and (iii) myoglobin with hydration layer. Isolated myoglobin molecule can be achieved by controlling the pH of the solution to 8.5 (isoelectric point of myoglobin). For pH other than 8.5, the myoglobin surface becomes charged and attracts the surrounding counter ions to form a charged double layer. Hughes et al. [51] replaced this type of effect with a numerical value for surface conductance K_s (typically of the order of $0.1 - 3\ nS$). This value is used to calculate the particle conductivity given by $\sigma_p = \sigma_{pbulk} + 2K_s/l_c$, where l_c is the characteristic length of the particle (assumed to be cube root of volume of the particle), and σ_{pbulk} is the conductivity of bulk myoglobin solution. This characteristic length is required since the orientation of myoglobin molecules in the microchannel is unknown. When myoglobin is suspended in water, it attracts one or two layers of bound water. Therefore, the third case considered here is the myoglobin with hydration layer. The permittivity and conductivity of the myoglobin molecule are different from the hydration layer. In this case, the DEP force shown in Eq.2.1 is still valid, if $\varepsilon_p^{'}$ is replaced with effective complex permittivity $\varepsilon_{peff}^{'}$ as given by [3, 41]

$$\varepsilon_{peff}^{'} = \varepsilon_h^{'}\left[\frac{\varepsilon_p^{'} + t_\alpha(\varepsilon_p^{'} + \varepsilon_h^{'})/q_\alpha}{\varepsilon_h^{'} + t_\alpha(\varepsilon_p^{'} + \varepsilon_h^{'})/q_\alpha}\right] \tag{2.11}$$

where t_α is the thickness of hydration layer along x, y, and z-axis, $q_\alpha = a$, b, and c for $\alpha = x$, y, and z, respectively and $\varepsilon_h^{'}$ is the complex permittivity of hydration layer which can be written as

$$\varepsilon_h^{'} = \varepsilon_h - j\frac{\sigma_h}{\omega} \tag{2.12}$$

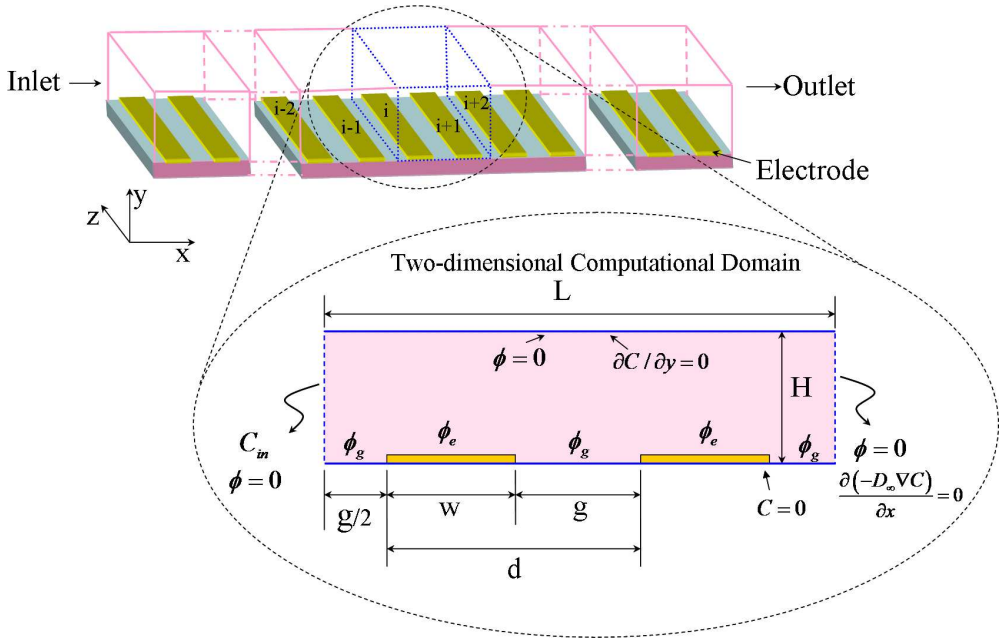

Figure 2.2: Schematic view of DEP microfluidic device considered for manipulating the myoglobin molecules. Enlarged view shows the two-dimensional computational domain considered for simulating the behavior of myoglobin molecules under DEP effects. Sinusoidal voltage of phase difference $2\pi/n$ and angular frequency ω are applied on the electrodes for producing nonuniform electric field. For myoglobin under stationary wave DEP, value of n will be 2 [37, 52, 53].

where ε_h and σ_h are permittivity and conductivity of hydration layer, respectively.

2.5 Mathematical modeling

This section describes the mathematical modeling for dielectrophoretic manipulation of myoglobin molecules in aqueous solution. Figure 2.2 depicts the schematic view of the DEP microfluidics system considered for the manipulation of myoglobin under DEP effects. The device has infinite number of electrodes ($-\infty$,..., -3, -2, -1, 0, 1, 2, 3,..., ∞) on the bottom surface of the microchannel. The enlarged view in Fig.2.2 shows the two-dimensional computational domain considered for simulating the dielectrophoretic behavior of the myoglobin. Here L is the length of channel considered for computational purpose and H is the height. The bottom surface is embedded with array of parallel rectangular microelectrodes of width w and gap g in between the electrodes. The parameter d represents the sum of electrode width w and gap g and ϕ represents the applied electric potential. The notation i and $(i+1)$ represents the i^{th} and $(i+1)^{th}$ electrodes, respectively.

2.5.1 Governing equations

The governing equations for transporting myoglobin molecule under DEP are proposed in this section. The governing equations are Laplace and convection-diffusion-migration equations. The Laplace equation is used for calculating electric field distributions whereas convection-diffusion-migration equation is used for calculating the spatial myoglobin molecule concentration distribution in a system.

The study is based on the following assumptions: (i) the aqueous myoglobin solution flowing through the microchannel is at steady state, incompressible and behaves as a Newtonian fluid; (ii) the myoglobin molecules in aqueous solution are assumed as point particles and hence their presence will not effect the electric field; (iii) no chemical reactions take place between the myoglobin molecules or between the molecules and walls of the channel; (iv) parabolic velocity profile across the channel is considered; (v)The ratio of myoglobin and medium densities are approximately equal to unity, which allows neglecting the gravitational sedimentation effect of myoglobin molecules [55–57]; (vi) For the range of fluid properties and applied voltages considered in this analysis, the heat dissipation and temperature rise in the fluid are negligible [47, 57]. Hence, AC electrothermal flow due to temperature gradients is neglected; (vii) For considered parameters or operating conditions, the movement of the particle due to AC electroosmosis is small as compared to the magnitude of DEP mobility [47, 57]. Also, we assume that our suspension is neutral (myoglobin particles are maintained at isoelectric point [17]) so the formation of electric double layer (EDL) along the electrode is small and hence, AC electroosmosis is neglected; and (viii) As per Docoslis et al. [59] and Yang et al. [60], it is observed that there are no detrimental effects to cell growth and metabolism for cells under high frequency (eg. 10MHz to 40MHz) electric fields strengths. In addition, Lin et al. [5] reported that there is no electrolysis and the corrosion at the electrodes under high frequency voltage waveforms. Therefore, the effects of high frequencies of applied voltage i.e exothermal effects are neglected.

Laplace equation

The electric field distribution in the system created by AC signal is described by the Laplace equation [45]

$$\nabla^2\phi = 0 \tag{2.13}$$

where ϕ is the applied electric potential. Solving Eq.2.13 with appropriate boundary conditions will provide the potential distribution in the computational domain. This potential distribution is used to calculate the DEP force acting on the different shapes of myoglobin molecules.

Convection-Diffusion-Migration Equation

The steady state concentration distribution of molecules in an aqueous solution with no chemical reactions can be given by convection-diffusion-migration equation as

$$\nabla\cdot(\mathbf{u}C) = \nabla\cdot(\mathbf{D}\cdot\nabla C) - \nabla\cdot(\frac{\mathbf{D}\cdot\mathbf{F}_{mig}}{k_BT}C) \tag{2.14}$$

where vector $\mathbf{u}$ is the velocity of the medium, C is the concentration of myoglobin molecules, $\mathbf{D}$ is diffusion coefficient tensor, $\mathbf{F}_{mig}$ is the migrational force vector on particles due to DEP, k_B is Boltzmann constant ($1.3806503 \times 10^{-23} m^2 kg s^{-2} K^{-1}$) and T is the ambient temperature. The first term of Eq.2.14 represents the transport due to convection, the second term is the transport due to diffusion, and the third term indicates the transport due to migration. Since the interactions between myoglobin molecules are neglected in the assumptions, diffusion tensor $\mathbf{D}$ can be simplified as the Stokes-Einstein diffusion coefficient D_∞,

$$D_\infty = \frac{k_BT}{f} \tag{2.15}$$

where $f = 12A_p\mu/l_c$. Here f is the friction factor, A_p is the projected area of the particle, μ is the dynamic viscosity of medium, and l_c is the characteristic length of particle. Both A_p and l_c depend on the shape of the particle and the direction of flow over it. The diffusion coefficient D_∞ for myoglobin is given as 1.5×10^{-11} m^2/s at 20^oC and 2.7×10^{-11} m^2/s at 37^oC [62]. Particles in a microchannel can be migrated due to attractive or repulsive dielectrophoretic forces ($\mathbf{F}_{mig} = \mathbf{F}_{DEP}$). The particle migration velocity for steady state problem can be given as

$$\mathbf{u}_{mig} = \frac{\mathbf{D}\cdot(\mathbf{F}_{mig})}{k_BT} = \frac{\mathbf{F}_{mig}}{f} \tag{2.16}$$

Combining and rearranging Eqs.2.14 - 2.16 and using the incompressibility condition, gives the following modified steady state convection-diffusion-migration equation

$$\nabla\cdot(\mathbf{u}_{tot}C) = D_\infty\nabla^2 C \tag{2.17}$$

where $\mathbf{u}_{tot} = \mathbf{u} + \mathbf{u}_{mig}$. Solving Eq.2.17 with appropriate boundary conditions will provide the spatial concentration distribution of myoglobin molecules in the computational domain. This concentration distribution is used to check the effectiveness of applying DEP force for manipulating myoglobin.

2.5.2 Non-dimensional analysis

The manipulation of myoglobin molecules under DEP effects depends on the operating parameters like applied voltage, inlet velocity of solution, and concentration of molecules. It is observed that optimization among the operating parameters is also important to decide the effectiveness of DEP force for separating myoglobin. Therefore, a non-dimensional analysis is conducted to correlate the parameters easily. The governing equations given in Eqs.2.13 and 2.17 can be non-dimensionalized using following parameters: $\phi^* = \phi/V_o$, $\nabla^* = w\nabla$, $\mathbf{u}^*_{tot} = \mathbf{u}_{tot}/u_{in}$, and $C^* = C/C_{in}$. Here V_o is the peak electric potential applied on the electrodes, u_{in} is the average inlet velocity of solution and C_{in} is the inlet particle concentration. The governing equations after applying non-dimensional parameters can be written as

$$\nabla^{*2}\phi^* = 0 \tag{2.18}$$

$$\nabla^*\cdot(\mathbf{u}^*_{tot}C^*) = \frac{1}{Pe}\nabla^{*2}C^* \tag{2.19}$$

where Pe is the Peclet number defined as $u_{in}w/D_\infty$. Appropriate boundary conditions to solve the above governing equations for manipulating myoglobin is provided in the Fig.2.2. ϕ_e and ϕ_g in the figure represents the electric potential at the electrodes and gap between the electrodes, respectively. The expressions for these potentials are given in the following section.

2.5.3 Solution methodology

The procedure for solving the model proposed in sections (4.1) and (4.2) is divided into two steps: (i) evaluating the electric field distribution in the system

using Eq.2.18; (ii) evaluating the particle spatial concentration distribution using Eq.2.19. The solution obtained in step (i) is used to find the dielectrophoretic force and is incorporated into step (ii) to calculate the concentration distribution of particles in the system under DEP effects.

The potential distribution is solved analytically as well as numerically. The analytical expression for potential and electric field distributions as well as DEP force in a microchannel containing parallel array of electrodes at the bottom surface has been already reported in many research papers on the basis of charge density method [1], Green's theorem [36, 37, 52, 53], conformal mapping [64], and Fourier series [65]. Closed form solutions are also developed for electric field and DEP forces by Morgan et al. [65] and Chang et al. [66]. Wang et al. [52] compared the analytical solution from Green's Theorem based method with charge density method, whereas Green et al. [67] compared the analytical solution from Fourier series method with numerical solution by finite element method. Clague et al. [53], and Crew et al. [68] studied the effect of electrode dimensions, channel height and applied voltage on gradient of electric field square. Molla et al. [36, 37] compared the Green's theorem based analytical and finite element based numerical solutions as well as studied the effect of applied voltages and frequencies on DEP force. In the present study, simple and modified analytical expressions for electric field and gradient of electric field square are derived based on Green's theorem method. In addition, a mesh-independent numerical solution using finite element method is also obtained. These analytical and numerical solutions are compared with Fourier series method [65] and closed form solutions (CFS) by Morgan et al. [65] and Chang et al. [66].

Here, the analytical expressions for potential, electric field and gradient of square electric field using Green's theorem method is derived. The potential and electric field distributions along the length of the electrodes are uniform for array of parallel rectangular electrodes. Therefore, the in-plane dimension of the system is neglected here. The Laplace equation for two-dimensional system is solved, as shown in Fig.2.2. Sinusoidal voltage of phase difference $2\pi/n$ and angular frequency ω are applied on the electrodes for producing nonuniform electric field. For myoglobin under stationary wave DEP, value of n will be 2 [37, 52, 53]. The analytical solution for the Laplace equation using Green's theorem for upper half-

space, $y \geq 0$ is given as

$$\phi(x,y) = \frac{y}{2\pi}\int \frac{\phi dx_0}{[(x-x_0)^2+y^2]} \tag{2.20}$$

where x_0 represents the point in x direction on the electrode plane and ϕ represents the surface potential on the electrode plane. The potential distribution is solved by piecewise integration of Eq.2.20 with surface potential boundary conditions on electrode plane. Assuming the linear variation of surface potential at gap between the electrodes [36, 37, 52, 53, 65–68], the surface potential boundary conditions on electrodes and gap between electrodes are given as

$$\phi_e(x_0) = \phi cos\left(\omega t + \frac{2\pi i}{n}\right) \tag{2.21}$$

$$\phi_g(x_0) = \phi\left\{S\left[x_0 - (id + \frac{w}{2})\right] + cos\left(\omega t + \frac{2\pi i}{n}\right)\right\} \tag{2.22}$$

where $S = \{cos(\omega t + 2\pi(i+1)/n) - cos(\omega t + 2\pi i/n)\}/g$, the limits of x_0 for electrodes varies from $id - w/2$ to $id + w/2$ and the limits of x_0 for gap between the electrodes varies from $id + w/2$ to $(i+1)d - w/2$. Here i is the i^{th} electrode and varies from $-\infty$ to $+\infty$. Substituting the Eqs.2.21 and 2.22 into Eq.2.20 and integrating yields the potential distribution expression as

$$\begin{aligned}\phi(x, y \geq 0) =& \frac{1}{\pi}\sum_{i=-\infty}^{\infty}\left\{-\phi_e(x)\left(tan^{-1}\left[\frac{x-q_i}{y}\right] - tan^{-1}\left[\frac{x-p_i}{y}\right]\right)\right\} \\ &+ \frac{1}{\pi}\sum_{i=-\infty}^{\infty}\left\{+\phi_g(x)\left(tan^{-1}\left[\frac{x-q_i}{y}\right] - tan^{-1}\left[\frac{x-p_{i+1}}{y}\right]\right)\right. \\ &\left. -\frac{Sy}{2}\left(ln\left[(x-q_i)^2+y^2\right] - ln\left[(x-p_{i+1})^2+y^2\right]\right)\right\}\end{aligned} \tag{2.23}$$

where $p_i = id - w/2$, $q_i = id + w/2$, and $p_{i+1} = (i+1)d - w/2$. Electric field distribution in the system can be calculated from the above potential distribution expression using $\mathbf{E} = -\nabla\phi$. The term $\nabla(\mathbf{E}\cdot\mathbf{E})$ in Eq.2.1 can be expressed for a two-dimensional computational domain as follows:

$$\frac{\partial}{\partial x}(\mathbf{E}\cdot\mathbf{E}) = 2(E_x\frac{\partial E_x}{\partial x} + E_y\frac{\partial E_y}{\partial x}) \tag{2.24}$$

$$\frac{\partial}{\partial y}(\mathbf{E}\cdot\mathbf{E}) = 2(E_x\frac{\partial E_x}{\partial y} + E_y\frac{\partial E_y}{\partial y}) \tag{2.25}$$

where E_x is electric field in the x direction, E_y is electric field in the y direction. Reader can refer to the appendix A for the detailed expressions for E_x, E_y, $\partial E_x/\partial x$, $\partial E_y/\partial x$, $\partial E_x/\partial y$ and $\partial E_y/\partial y$.

Analytical methods give exact solution to the potential and electric field distributions in the system as well as DEP force on the myoglobin molecules. This analytical method is only applicable to simplified geometries (mainly two-dimensional) like infinite array of parallel electrodes. However, most of the applications, electrode geometries and layouts are different and not possible to simplify as two-dimensional models. Solving the two-dimensional convection-diffusion-migration equation by analytical methods is a tedious process due to elliptical nature of equation. Therefore, numerical method is implemented to obtain approximate solutions for electric field and myoglobin molecule concentration distributions in the system. The governing equations and the boundary conditions described earlier are implemented in a finite element based software COMSOL Multiphysics version 3.5a, to study the dielectrophoretic behavior of myoglobin. To obtain the numerical solution, only two electrodes are used for simulations instead of array of electrodes as it is periodic in nature (as shown in Fig.2.2). The two-dimensional computational domain is discretized with quadrilateral elements. The electrode edges are discretized with finer elements to capture the effect of high electric field strength. The model uses Lagrange-quadratic elements for calculating parameters inside the domain like electric potential, electric field, etc. The structured (mapped) mesh scheme is used to discretize the computational domain. The simultaneous linear equations produced by the finite element method are solved using direct elimination solver (PARDISO). A mesh independent finite element solution is achieved with around $12,000$ elements. The convection-diffusion-migration model is solved with small artificial isotropic diffusion ($= 0.05$) to improve the convergence and to reduce the oscillations in concentration profile [38].

2.6 Results and discussions

Results for the dielectrophoretic behavior of the myoglobin molecules in aqueous solution are presented in this section. For the simulations, the length and height of the channels are taken as $L = 400\ nm$ and $H = 300\ nm$, respectively. The length of the channel depends on the number of electrodes in that array. The electrode width and gap between the electrodes are given as $w = 100\ nm$ and $g = 100\ nm$, respectively. Thickness of the electrodes is assumed to be very small as compared

to the height of channel and hence neglected in the simulations. The dielectric properties of the myoglobin and aqueous solution considered for the analysis [21] are given as: $\varepsilon_p = 83.5\varepsilon_o$, $\varepsilon_m = 78.5\varepsilon_o$, $\sigma_p = 0.01\ S/m$ and $\sigma_m = 0.065\ S/m$. Here $\varepsilon_0 = 8.854 \times 10^{-12}\ C^2 N^{-1} m^{-2}$ is the permittivity of free space. The simulations are conducted at applied voltages of $1\ V$ to $100\ V$ peak to peak at different frequencies. With 100 V, electric field between electrodes is approximately $\sim 10^9$ V/m for the present configuration. In realistically, this electric field strength is more than the breakdown electric field strength ($\sim\ 5 \times 10^5$ V/m) of a glass and most of the polymers. In addition, such high applied voltages may peel of the electrode from the surface of the microchannels. Hence, it is necessary to take proper care while applying this type of high applied voltages for such small electrode configurations. The aqueous solution of myoglobin is maintained at 20^oC and is pumped into the microchannel with concentration $C_{in} = 1\ mol/m^3$ and inlet average velocity $u_{in} = 0.1\ mm/s$. At the outlet of the microchannel, the boundary condition for the concentration is kept as zero. Thus, the non-dimensional parameters used in the present study are given as $L^* = 4$, $H^* = 3$, $w^* = 1$ and $g^* = 1$.

The accurate calculation of the electric field is an important criteria since the DEP force acts on myoglobin molecules is directly proportional to electric field gradient. It is observed that proper attention is required while calculating electric field at the electrode edges. A significant amount of electric field variation is anticipated at the electrode edges since the boundary condition shifts from surface potential to surface charge condition. Therefore, a refined mesh is required around the electrode-gap interface to acquire the peaks in the DEP force profile.

Figure 2.3 shows the comparison of non-dimensional electric field along the length of channel near the electrodes for Green's theorem based analytical solution, Fourier series based analytical solution [65], finite element based numerical solution, CFS by Morgan et al. [65] and CFS by Chang et al. [66] The horizontal axis in this figure shows the non-dimensional length of the channel (x^*), whereas vertical axis shows the non-dimensional electric field ($\mathbf{E}^*$). The different symbols in the figure indicates the different solution methods. The electric field is maximum at the edges of the electrodes and minimum else where. But the magnitude of the electric field at the center of the electrode is very less than the electric field at the mid point of the gap between the electrodes. Excellent agreement

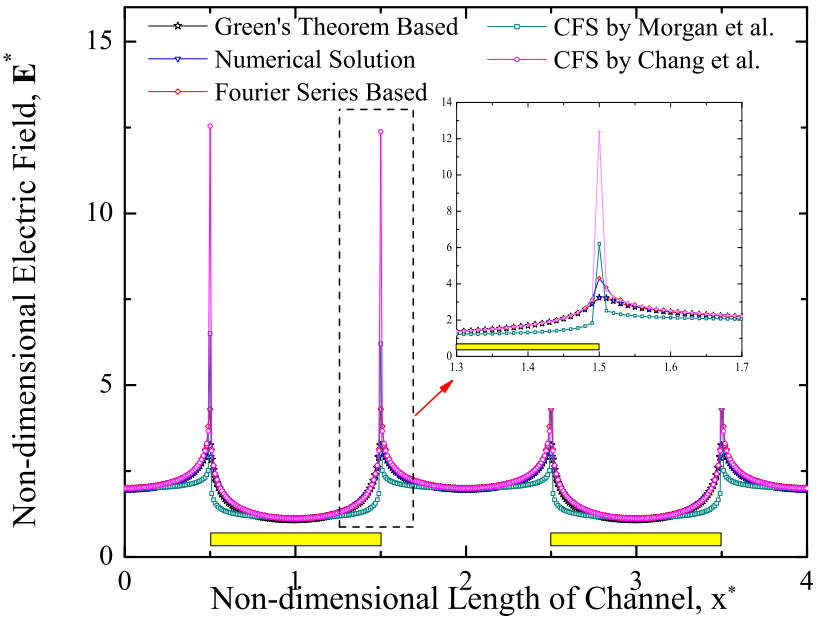

Figure 2.3: Comparison of non-dimensional electric field along the length of channel near the electrodes for different solution methods

is observed between Green's theorem based analytical solution and finite element based numerical solution. However, slight discrepancies are identified at the edge of the electrode for Green's theorem based/numerical solution with Fourier series based analytical solution and CFS by Chang et al. [66]. The peak magnitude for non-dimensional electric field for CFS by Chang et al. [66] compared with other solution methods. CFS by Morgan et al. [65] has slight flat profile along the electrodes/gap between electrodes compared to semi circular curved profile of non-dimensional electric field for other solution methods.

As discussed earlier, DEP force depends on the volume of myoglobin, real part of the CM factor and the gradient of square electric field. Since effect of presence of the myoglobin molecules on electric field is neglected, gradient of square electric field is independent of shape, size, and properties of myoglobin. Hence, the variation of square electric field gradient along the length of channel and height of the channel is studied. Figure 2.4 illustrates the comparison of non-dimensional square electric field gradient with respect to length of channel near the electrode plane for Green's theorem based analytical solution, numerical solution based on COMSOL

multiphysics, CFS by Morgan et al. [65] and CFS by Chang et al. [66]. The horizontal axis in this figure shows the non-dimensional length of the channel (x^*) and vertical axis shows the non-dimensional square electric field gradient ($\nabla^*(\mathbf{E}^*\cdot\mathbf{E})^*$). The different solution methods are indicated with different symbols in the figure. The results show that the square electric field gradient is maximum at the edges of the electrodes and tapers off to zero at a distance about w/4 from each edge. The magnitude of non-dimensional square electric field gradient is in the range of 10^{-1} to 10^{10} for an applied electric potential of $\phi^* = 1$. The attraction or repulsion of particles can be achieved significantly due to large gradient of electric field at the edges of the electrodes. The variation profile of non-dimensional square electric field is almost matched with Green's theorem based solution, numerical solution, and CFS by Morgan et al. [65] and Chang et al. [66]. The Fourier series based solution is not compared here due to some large discrepancies with other solution methods. The excellent agreement is identified with Green's theorem based solution and numerical solution, whereas some slight difference in non-dimensional square electric field gradient is observed along the length of the channel (except the edges of electrode) with other solution methods. CFS by Chang et al. [66] and Morgan et al. [65] are providing the maximum non-dimensional square electric field gradient at the edges of the electrode compared to Green's theorem method and finite element method.

Figure 2.5 depicts the comparison of non-dimensional square electric field gradient with respect to the height of channel at electrode edge, mid point of electrode and mid point of gap between the electrodes with different solution methods. The horizontal axis in this figure shows the non-dimensional height of the channel (y^*) whereas vertical axis shows the non-dimensional square electric field gradient ($\nabla^*(\mathbf{E}^*\cdot\mathbf{E})^*$). The non-dimensional square electric field gradient is exponentially decayed along the height of channel at the edges of the electrodes. At mid point of electrodes, the square electric field gradient is monotonically increased up to $y^* = 0.32$ and then linearly decreased along the height of channel. The linear decaying of square electric field is observed at the mid point of gap between the electrodes. At the height $y^* = 1.25$, the gradient of square electric field is constant throughout the channel length and magnitude is decreased along the height of channel. This decides the effectiveness of DEP force in the channel. The pro-

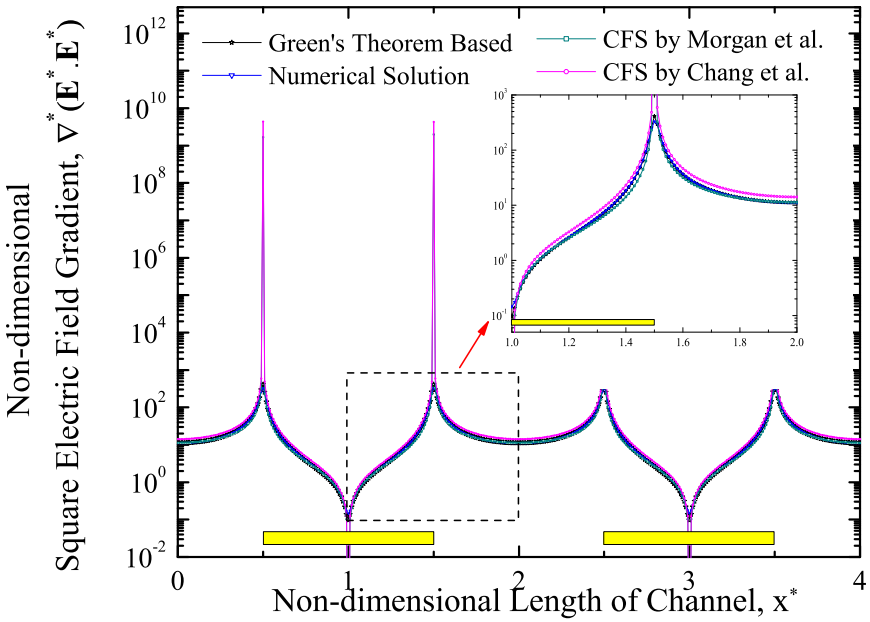

Figure 2.4: Comparison of non-dimensional square electric field gradient along the length of channel near the electrodes for different solution methods

files for variation of non-dimensional square electric field gradient with different solution methods are matched for all the cases. There is some discrepancy with profiles along the height of channel at mid point of electrodes for Green's theorem based solution or numerical solution with CFS by Morgan et al. [65] and Chang et al. [66].

Figure 2.6 shows the dependence of non-dimensional square electric field gradient on applied voltage along the length of channel near the electrodes. The horizontal axis in this figure shows the non-dimensional length of the channel (x^*), whereas vertical axis represents the non-dimensional gradient of the square electric field. Different symbols indicate the different voltages in the figure. It is observed that square electric field gradient is directly proportional to the applied voltage. The magnitude of peak non-dimensional square electric field gradient is increased from 3×10^2 to 3×10^6 for an increase in non-dimensional applied voltage (ϕ^*) from 1 to 100, respectively.

The type of DEP effect on the myoglobin molecule is determined by observing the real part of CM factor. As discussed earlier, this real part of CM factor depends

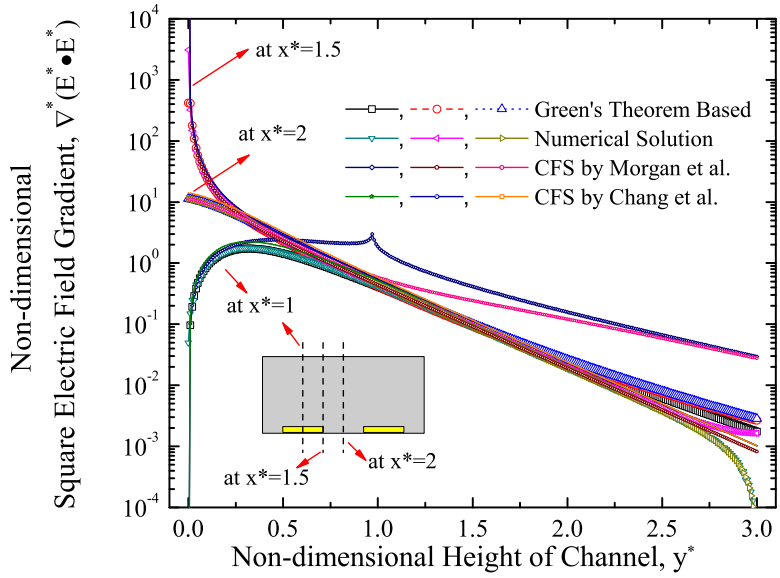

Figure 2.5: Comparison of non-dimensional square electric field gradient along the height of channel at edge of the electrode, mid point of the electrode and mid point of gap between the electrodes for different solution methods

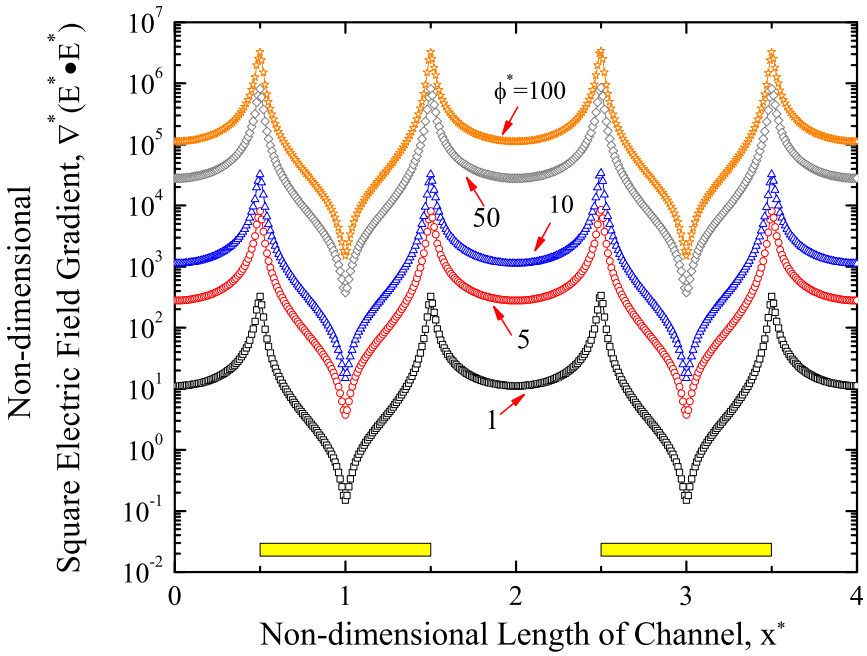

Figure 2.6: Comparison of non-dimensional square electric field gradient along the length of channel near the electrodes for different non-dimensional applied voltages

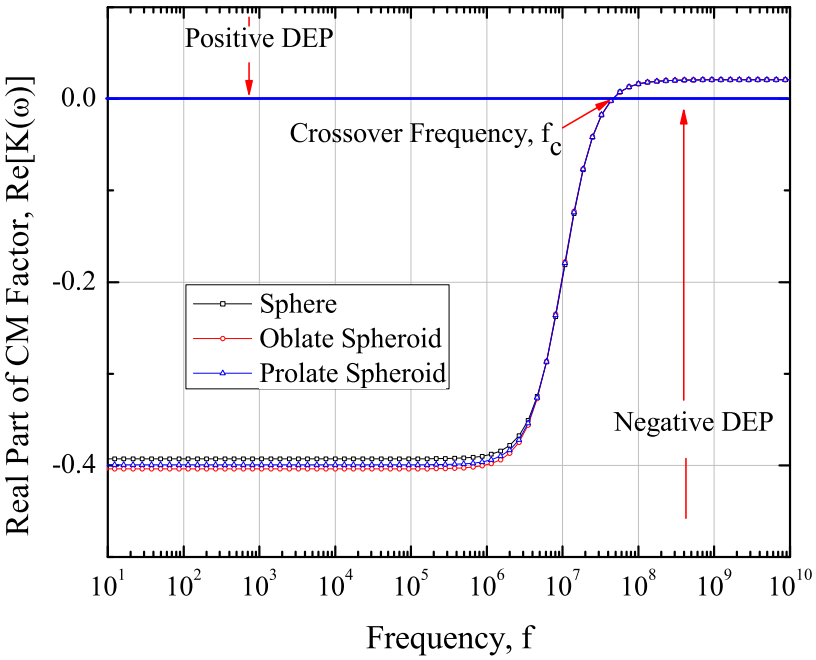

Figure 2.7: Comparison of real part of the CM Factor with respect to frequency of the applied electric field for different shapes of the myoglobin molecule

on the permittivity and conductivity of myoglobin molecule and aqueous solution, respectively, and frequency of the applied electric field. Figure 2.7 presents the comparison of real part of CM factor for different approximated shapes of myoglobin molecule in the applied electric field frequency range of 10 Hz to 10 GHz. Here horizontal axis represents the frequencies in the logarithmic scale whereas the vertical axis shows the real part of CM factor. The real part of CM factor depends on the axis of particle for arbitrary shapes like oblate and prolate spheroids. So, the average value for real part of CM factor is considered in the study. The real part of CM factor for all the approximated shapes is equal to zero at or around 40 MHz of applied electric field frequency. It has negative DEP for the frequency less than 40 MHz and positive DEP for the frequency more than 40 MHz. This indicates that 40 MHz is the crossover frequency (f_c) of the myoglobin for given material properties. It is also found that the real part of CM factor is more for sphere compared to the prolate and oblate spheroids in the frequency range of 10 Hz to 4.5 MHz. The real part of CM factor is same for all shapes at 4.5 MHz. The real part of CM factor increased in sigmoidal curve from 2 MHz to 100 MHz.

Beyond 100 MHz, the real part of CM factor for all shapes is same and constant through out the frequency range.

Figure 2.8 shows the comparison of crossover frequency for different shapes of myoglobin molecules with respect to conductivity of medium. Conductivity of medium indicated on the logarithmic scale of x-axis whereas the crossover frequency for all shapes of molecule shown on logarithmic scale of y-axis. Different symbols in the Fig.2.8 indicate the different particle conductivities. In Fig.2.8, it is found that the crossover frequency for any shape of the myoglobin is same at any particle conductivity and it is increased with increase in the medium conductivity. If the conductivity of particle is more than the conductivity of medium, the particles experienced positive DEP even though it is subjected to frequency lesser than the crossover frequency. The crossover frequency is determined for only two cases; (i) $\varepsilon_p > \varepsilon_m$ and $\sigma_p < \sigma_m$; (ii) $\varepsilon_p < \varepsilon_m$ and $\sigma_p > \sigma_m$. The other two cases do not have crossover frequency. They are (i) $\varepsilon_p > \varepsilon_m$ and $\sigma_p > \sigma_m$; (ii) $\varepsilon_p < \varepsilon_m$ and $\sigma_p < \sigma_m$. Figures 2.7 and 2.8 provide the operating frequency range to observe the response of myoglobin molecules under DEP effects. This crossover frequency analysis will be helpful in separating the myoglobin from other particles or from the whole blood sample.

The second case considered for myoglobin will increase its conductivity due to electric double layer formation. The effect of increase in myoglobin conductivity on crossover frequency is same as depicted in Fig.2.8. Figure 2.9 provides the effect of real part of CM factor with respect to frequency of applied electric field due to hydration layer on myoglobin. Here horizontal axis represents the frequencies in the logarithmic scale and the vertical axis shows the real part of CM factor. It is evident from the figure that the real part of CM factor for all approximated shapes is equal to zero at or around 28 MHz of applied electric field frequency. It has negative DEP for the frequency less than 28 MHz and positive DEP for the frequency more than 28 MHz. This indicates that 28 MHz is the crossover frequency of the myoglobin for given material properties at the time of hydration layer formation. Also, the real part of CM factor in the frequency range of 10 Hz to 28 MHz is larger for oblate spheroid compared to prolate spheroid and sphere. The real part of CM factor has same value for all shapes at 28 MHz and it is the crossover frequency for myoglobin with hydration layer. The real part of CM

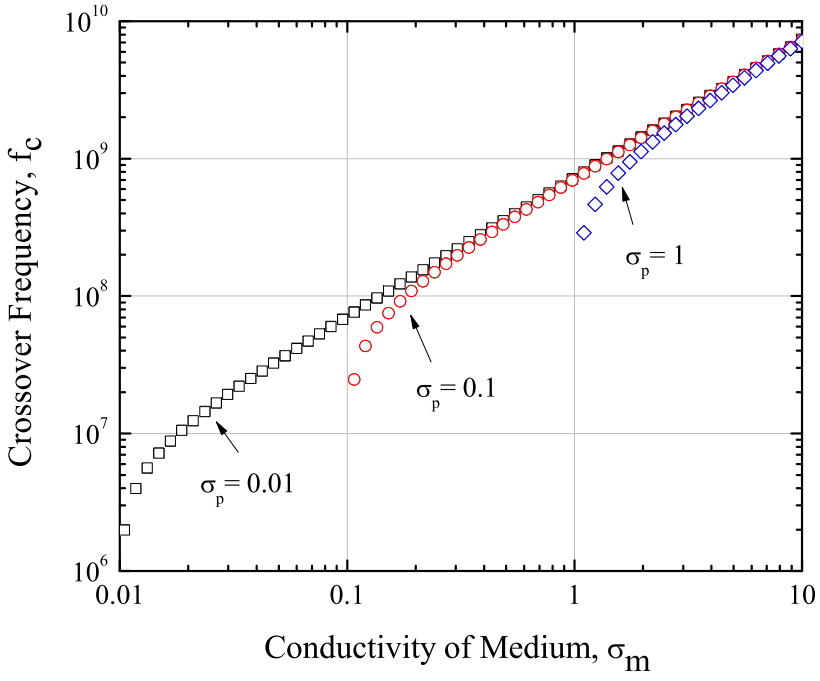

Figure 2.8: Comparison of crossover frequency with respect to change in conductivity of medium for different shapes of the myoglobin molecule

factor increased in sigmoidal curve from 10 MHz to 400 MHz. Beyond 28 MHz, the real part of CM factor for prolate spheroid is larger compared to sphere and oblate spheroids.

Figures 2.10 and 2.11 show the positive and negative DEP effects on the myoglobin molecules. Figure 2.10 illustrates the comparison of DEP force along the length of channel near the electrodes for different shapes of myoglobin at 50 MHz and 10 V applied electric potential. Figure 2.11 exhibit the comparison of DEP force along the length of channel near the electrodes for different shapes of the myoglobin at 1 KHz and 10 V applied electric potential. The variation profiles for DEP force and gradient of square electric field are similar along the length of the channel near the electrodes. Due to the variation of CM factor with frequency of applied electric field, the values of DEP forces has been changed for different shapes of myoglobin molecule. The peak value of DEP force in case of positive DEP effect is less than that observed in negative DEP effect. The magnitude of DEP force on different approximated shapes of the myoglobin molecules are same in the positive DEP effect. The peak magnitudes of DEP force on different shapes

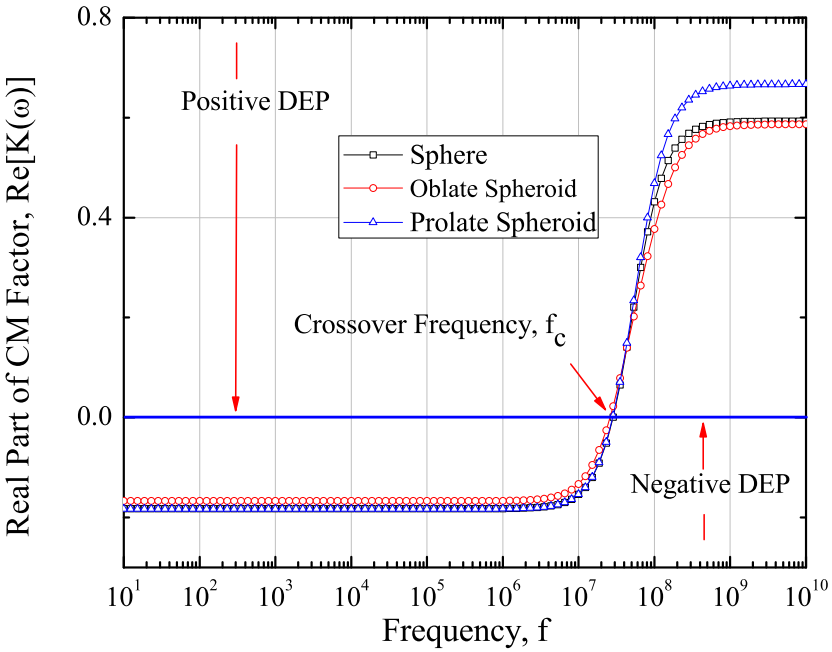

Figure 2.9: Comparison of real part of the CM Factor with respect to frequency of the applied electric field for different shapes of myoglobin with the hydration layer

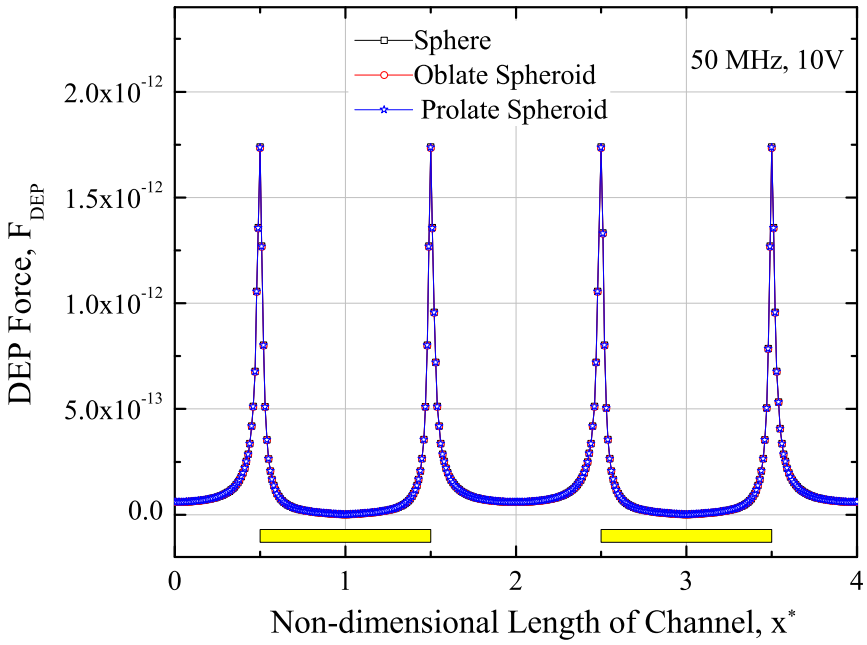

Figure 2.10: Comparison of DEP force on different shapes of the myoglobin molecule along the length of channel near the electrodes at $50MHz$ frequency and $10V$ applied voltage

of myoglobin are not matched in the negative DEP effect. The peak value of DEP force is more for oblate spheroid as compared to other shapes. This happens due to variation of the CM factor in negative DEP region. But the magnitudes are not significantly changed for these shapes. The magnitude of DEP forces are in the order of 10^{-12} to 10^{-10} at the edges of the electrode.

The effectiveness of this DEP force for manipulating nanosize myoglobin molecules can be evaluated by comparing the ratio of DEP force to Brownian force. If this ratio is greater than or equal to one, the DEP force is effective in manipulating the myoglobin otherwise it is not possible due to thermal randomization. According to Pohl [2] and Washizu et al. [7], the condition for checking the ratio of DEP force to Brownian motion is given by integrating Eq.2.1

$$\frac{\frac{3}{2}(vol)\varepsilon_m Re[K(\omega)](\mathbf{E}\cdot\mathbf{E})}{k_B T} \geq 1 \tag{2.26}$$

This condition is satisfied for the DEP forces plotted in the Figs.2.10 and 2.11.

The DEP results presented so far indicate that the myoglobin molecules either

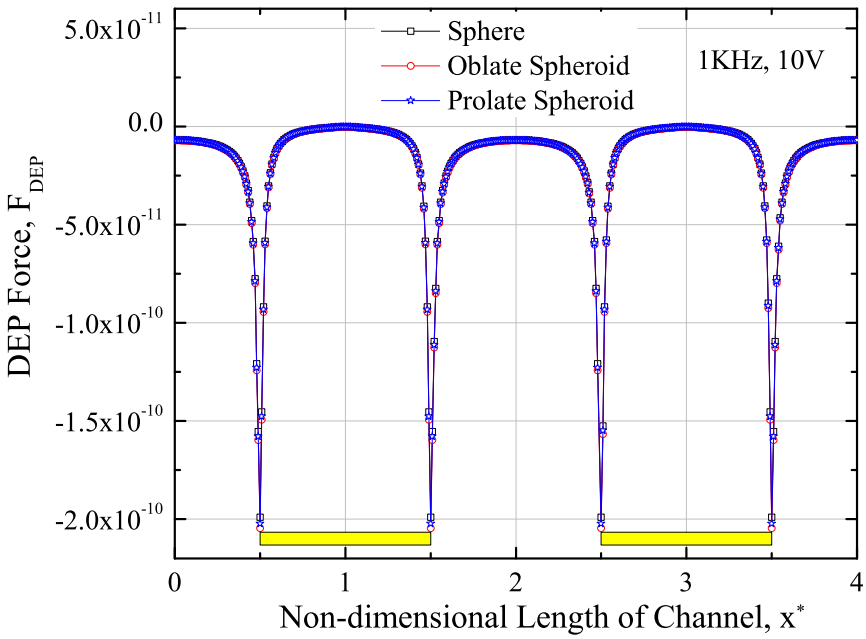

Figure 2.11: Comparison of DEP force on different shapes of the myoglobin molecule along the length of channel near the electrodes at $1KHz$ frequency and $10V$ applied voltage

trap or repel from the high electric field strengths i.e., at the edges of the electrodes under steady state conditions. However, under tangential flow conditions, when the interdigitated electrode array (3 pairs of electrodes) on the bottom surface of the channel is actuated by a 180^o phase shifted AC voltage (10V) at 1KHz frequency, it induces negative DEP forces on the myoglobin molecules that repels them away from the bottom surface of the channel (levitated above the bottom plane) and moves towards the outlet of the channel. Here, the aqueous solution of myoglobin is maintained at 20^oC and is pumped into the microchannel with concentration $C_{in} = 1\ mol/m^3$ and inlet average velocity $u_{in} = 0.1\ mm/s$.

Figure 2.12 shows the variation of non-dimensional concentration of the myoglobin molecules inside the microchannel. The molecules are levitated to certain height due to repulsive DEP forces. The concentration of different shapes of the myoglobin molecule does not have significant difference in the surface plot. Figure 2.13 shows the variation of concentration of the myoglobin molecules along the height of channel at different locations on the length of channel. Horizontal axis is non-dimensional distance (y^*) and vertical axis is non-dimensional concentration (C^*). The concentration of molecules is maximum at $y^* = 1.25$ height, beyond which there is no significant difference in the DEP force along the length of channel. These results show that DEP force is effective to manipulate as well as to control the Brownian motion of myoglobin. The shape of the myoglobin molecule does not have significant effect on magnitude of the DEP force. The validation of results like crossover frequencies and levitation heights of the myoglobin with experiments are in process. Figure 2.14 shows the variation of concentration of the myoglobin molecules along the length of channel at different locations on the height of channel. Horizontal axis is non-dimensional distance (x^*) and vertical axis is non-dimensional concentration (C^*). The concentration of molecules is maximum in between $y^* = 1$ and $y^* = 1.25$ height, beyond which there is no significant difference in the DEP force along the length of channel. At particular y^*, it is observed that C^* decreases down the channel after reaching maximum concentration at one point of the channel. These type of negative DEP experiments (levitating myoglobin molecules) can be conducted under the frequency range below 40 MHz and voltage range below 10 V.

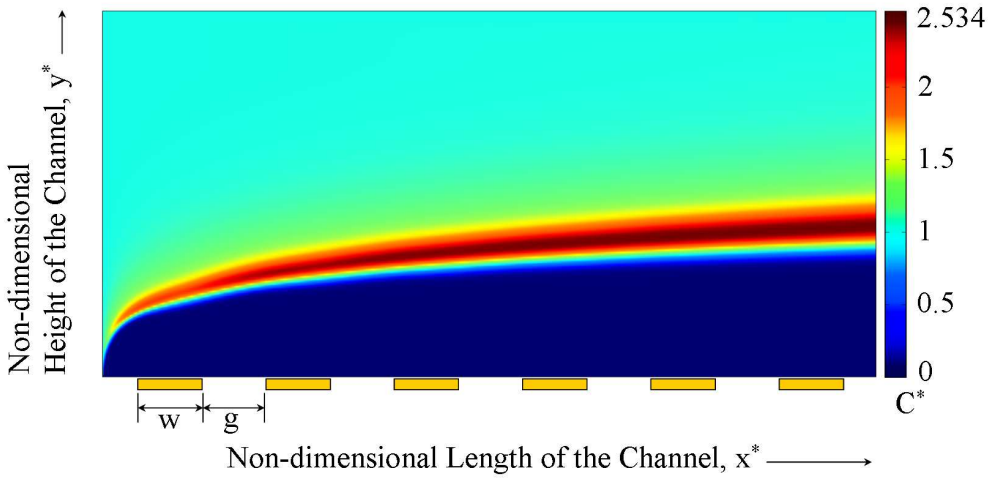

Figure 2.12: Variation of mass concentration of the myoglobin molecules inside the microchannel under DEP effects at $1KHz$ and $10V$ applied voltage

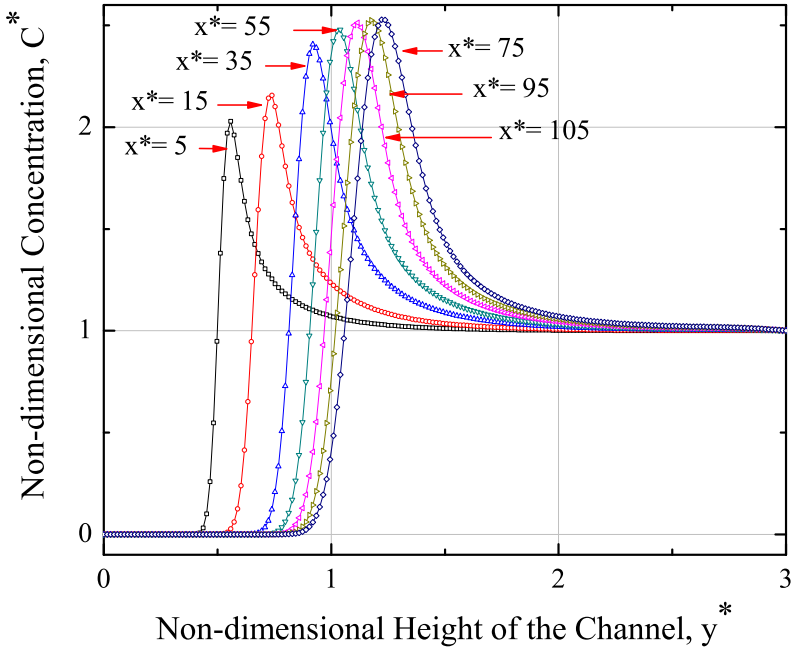

Figure 2.13: Variation of mass concentration of the myoglobin molecules along the height of channel under DEP effects at $1KHz$ and $10V$ applied voltage

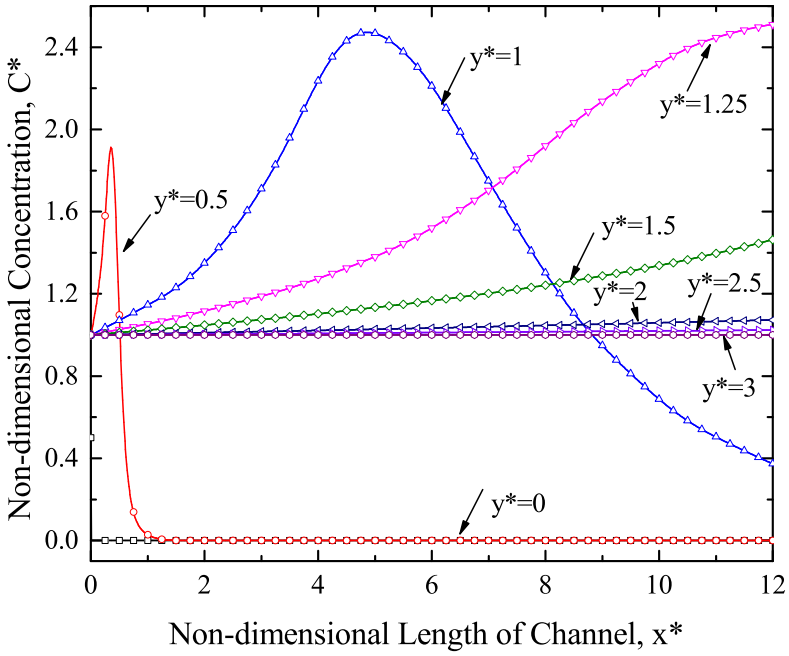

Figure 2.14: Variation of mass concentration of the myoglobin molecules along the length of channel under DEP effects at $1KHz$ and $10V$ applied voltage

2.7 Summary

Mathematical modeling and numerical simulation of dielectrophoretic behavior of a myoglobin molecule in a microchannel with parallel array of electrodes at the bottom wall of the microchannel are investigated. A dielectric myoglobin model is developed by approximating the shape of the myoglobin molecule as sphere, oblate, and prolate spheroids. A generalized dielectrophoretic force acting on respective shapes of the molecule is derived. Both the non-dimensional electric field and square electric field gradients are calculated with Green's theorem method and finite element method. The results are also compared with Fourier series method [65], closed form solutions by Morgan et al. [65] and Chang et al. [66]. The excellent agreement between Greens theorem based analytical solution and numerical solutions are observed. A crossover frequency of 40 MHz is obtained for given properties of the myoglobin molecules. This crossover frequency is increased with increase in conductivity of medium as well as myoglobin. The hydration layer reduced the crossover frequency of myoglobin molecules to 28 MHz. Both positive

and negative DEP effects on the myoglobin molecules are observed at 50 MHz and 1 kHz applied frequency, respectively. The effect of different shapes of myoglobin on the DEP force is studied and it is observed that there is no significant effect on DEP force. The concentration of molecules is maximum at $y^* = 1.25$ height at 1 KHz frequency and 10 V applied voltage. These findings give the potential of DEP force for manipulating nano-scale biomolecules.

Bibliography

[1] B. M. Mayr, O. Kohlbacher, K. Reinert, M. Sturm, C. Gropl, E. Lange, C. Klein, and C. G. Huber. Absolute myoglobin quantification in serum by combining two-dimensional liquid chromatography - electrospray ionization mass spectrometry and novel data analysis algorithms. *Journal of Proteome Research*, 5:414–421, 2006.

[2] J. Wang, Q. Wang, L. Ren, X. Wang, Z. Wan, W. Liu, L. Li, H. Zhao, M. Li, D. Tong, and J. Xu. Carboxylated magnetic microbead-assisted fluoroimmunoassay for early biomarkers of acute myocardial infarction. *Colloids and Surfaces B: Biointerfaces*, 72(1):112–120, 2009.

[3] F. Darain, P. Yager, K. L. Gan, and S. C. Tjin. On-chip detection of myoglobin based on fluorescence. *Biosensors and Bioelectronics*, 24:1744–1750, 2009.

[4] J. Evan. Novel data analysis technique aids heart attack diagnosis. See also URL Lab Informatics, separationsNOW.com, February 2006.

[5] G. T. Perkoff, R. L. Hill, D. M. Brown, and F. H. Tyler. The characterization of adult myoglobin. *The Journal of Biological Chemistry*, 237(9):2820–2827, 1962.

[6] A. M. Potts. Methods for separation of proteins. *Investigative Ophthalmology*, 4(4):531–538, 1965.

[7] W. Boesken, S. Boesken, and A. Mamier. Human myoglobin: Preparation, quantitation and standardization. *Research in Experimental Medicine*, 171(1):71–78, 1977.

[8] H. Qiaojia, T. Yuchai, L. Weiping, Y. Shuxuan, L. Xiaopeng, X. Bing, W. Yushui, L. Li, and Z. Zhongyong. Qualitative bedside assay of increased human serum myoglobin by sandwich dot-immunogold filtration for the diagnosis of acute myocardial infarction. *Clinica Chimica Acta*, 273:119–130, 1998.

[9] J. Dasso, J. Lee, H. Bach, and R. G. Mage. A comparison of elisa and flow

microsphere-based assays for quantification of immunoglobulins. *Journal of Immunological Methods*, 263:23–33, 2002.

[10] M. Zou, H. Gao, J. Li, F. Xu, L. Wang, and J. Jiang. Rapid determination of hazardous compounds in food based on a competitive fluorescence microsphere immunoassay. *Analytical Biochemistry*, 374(2):318–324, 2008.

[11] T. O'Regan, L. O'Riordan, M. Pravda, C. O'Sullivan, and G. Guilbault. Direct detection of myoglobin in whole blood using a disposable amperometric immunosensor. *Analytica Chimica Acta*, 460(2):141–150, 2002.

[12] R. Haas. Clinical instrumentation (general chemistry and immunoassay analyzers). *Analytical Chemistry*, 65(12):444R–449R, 1993.

[13] M. Panteghini. Recent approaches to the standardization of cardiac markers. *Scandinavian Journal of Clinical and Laboratory Investigation*, 61:95–102, 2001.

[14] F. Le Moigne, M.-C. Beauvieux, P. Derache, and Y.-M. Darmon. Determination of myoglobin: Comparative evaluation of the new automated VIDAS assay with two other immunoassays. *Clinical Biochemistry*, 35(4):255–262, 2002.

[15] M. Panteghini, T. Linsinger, A. Wu, F. Dati, F. Apple, R. Christenson, J. Mair, and H. Schimmel. Standardization of immunoassays for measurement of myoglobin in serum. Phase I: Evaluation of candidate secondary reference materials. *Clinica Chimica Acta*, 341(1-2):65–72, 2004.

[16] H. A. Pohl. *Dielectrophoresis*. Cambridge University Press, 1978.

[17] T. B. Jones. *Electromechanics of particles*. Cambridge University Press, 1995.

[18] M. P. Hughes. *Nanoelectromechanics in Engineering and Biology*. CRC Press, Boca Raton, 2003.

[19] J. Lin and J. Yeow. Enhancing dielectrophoresis effect through novel electrode geometry. *Biomedical Microdevices*, 9(6):823–831, 2007.

[20] N. T. Nguyen and S. T. Werely. *Fundamentals and Applications of Microfluidics*. Artech House, Boston, 2006.

[21] C. Church, J. Zhu, G. Wang, T.-R. J. Tzeng, and X. Xuan. Electrokinetic focusing and filtration of cells in a serpentine microchannel. *Biomicrofluidics*, 3(4):044109, 2009.

[22] Z. Gagnon, J. Mazur, and H.-C. Chang. Glutaraldehyde enhanced dielectrophoretic yeast cell separation. *Biomicrofluidics*, 3(4):044108, 2009.

[23] G. A. Ferrier, A. N. Hladio, D. J. Thomson, G. E. Bridges, M. Hedayatipoor, S. Olson, and M. R. Freeman. Microfluidic electromanipulation with capacitive detection for the mechanical analysis of cells. *Biomicrofluidics*, 2(4):044102, 2008.

[24] G. O. F. Parikesit, A. P. Markesteijn, O. M. Piciu, A. Bossche, J. Westerweel, I. T. Young, and Y. Garini. Size-dependent trajectories of dna macromolecules due to insulative dielectrophoresis in submicrometer-deep fluidic channels. *Biomicrofluidics*, 2(2):024103, 2008.

[25] F. Yang, X. Yang, H. Jiang, P. Bulkhaults, P. Wood, W. Hrushesky, and G. Wang. Dielectrophoretic separation of colorectal cancer cells. *Biomicrofluidics*, 4(1):013204, 2010.

[26] X. Zhu, H. Yi, and Z. Ni. Frequency-dependent behaviors of individual microscopic particles in an optically induced dielectrophoresis device. *Biomicrofluidics*, 4(1):013202, 2010.

[27] H. Hwang, D.-H. Lee, W. Choi, and J.-K. Park. Enhanced discrimination of normal oocytes using optically induced pulling-up dielectrophoretic force. *Biomicrofluidics*, 3(1):014103, 2009.

[28] M.-T. Wei, J. Junio, and H. D. Ou-Yang. Direct measurements of the frequency-dependent dielectrophoresis force. *Biomicrofluidics*, 3(1):012003, 2009.

[29] J.-R. Du, Y.-J. Juang, J.-T. Wu, and H.-H. Wei. Long-range and superfast

trapping of dna molecules in an ac electrokinetic funnel. *Biomicrofluidics*, 2(4):044103, 2008.

[30] N. Lewpiriyawong, C. Yang, and Y. C. Lam. Dielectrophoretic manipulation of particles in a modified microfluidic h filter with multi-insulating blocks. *Biomicrofluidics*, 2(3):034105, 2008.

[31] S. Basuray and H.-C. Chang. Designing a sensitive and quantifiable nanocolloid assay with dielectrophoretic crossover frequencies. *Biomicrofluidics*, 4(1):013205, 2010.

[32] S. Bunthawin, P. Wanichapichart, A. Tuantranont, and H. G. L. Coster. Dielectrophoretic spectra of translational velocity and critical frequency for a spheroid in traveling electric field. *Biomicrofluidics*, 4(1):014102, 2010.

[33] X. B. Wang, Y. Huang, J. P. H. Burt, G. H. Markx, and R. Pethig. Selective dielectrophoretic confinement of bioparticles in potential energy wells. *Journal of Physics D: Applied Physics*, 26:1278–1285, 1993.

[34] B. H. Lapizco-Encinas and M. Rito-Palomares. Dielectrophoresis for the manipulation of nanobioparticles. *Electrophoresis*, 28:4521–4538, 2007.

[35] M. Washizu, S. Suzuki, O. Kurosawa, T. Nishizaka, and T. Shinohara. Molecular dielectrophoresis of biopolymers. *IEEE Transactions on Industry Applications*, 30(4):835–843, 1994.

[36] D. Bakewell, M. Hughes, J. Milner, and H. Morgan. Dielectrophoretic manipulation of avidin and DNA. *Proceedings of the 20th Annual International Conference of the IEEE Engineering in Medicine and Biology Society*, 20(2):1079–1082, 1998.

[37] M. Hughes and H. Morgan. Dielectrophoretic characterization and separation of antibody-coated submicrometer latex spheres. *Analytical Chemistry*, 71(16):3441–3445, 1999.

[38] L. Zheng, J. Brody, and P. Burke. Electronic manipulation of DNA, proteins, and nanoparticles for potential circuit assembly. *Biosensors and Bioelectronics*, 20(3):606–619, 2004.

[39] L. Zheng, P. Burke, and J. Brody. Electronic manipulation of DNA and proteins for potential nano-bio circuit assembly. *Proceedings of SPIE - The International Society for Optical Engineering*, 5331:126–135, 2004.

[40] R. Clarke, S. White, D. Zhou, L. Ying, and D. Klenerman. Trapping of proteins under physiological conditions in a nanopipette. *Angewandte Chemie - International Edition*, 44(24):3747–3750, 2005.

[41] C. Yang and U. Lei. Quasistatic force and torque on ellipsoidal particles under generalized dielectrophoresis. *Journal of Applied Physics*, 102(9), 2007.

[42] M. Castellarnau, A. Errachid, C. Madrid, A. Jurez, and J. Samitier. Dielectrophoresis as a tool to characterize and differentiate isogenic mutants of *escherichia coli*. *Biophysical Journal*, 91(10):3937–3945, 2006.

[43] P. Schlecht, A. Mayer, G. Hettner, and H. Vogel. Dielectric properties of hemoglobin and myoglobin. i. influence of solvent and particle size on the dielectric dispersion. *Biopolymers - Peptide Science Section*, 7(6):963–974, 1969.

[44] E. Grant, G. South, and I. Walker. The dipole moment of myoglobin. *Biochemical Journal*, 122(5):765–767, 1971.

[45] G. South and E. Grant. Dielectric dispersion and dipole moment of myoglobin in water. *Proceedings of Royal Society London. Series A*, 328:371–387, 1972.

[46] E. H. Grant, B. G. R. Mitton, and G. P. South. An investigation by dielectric methods of hydration in myoglobin solutions. *Biochemical Journal*, 139:375–380, 1974.

[47] S. Gough. Models for dielectric relaxation of biopolymers: Myoglobin in aqueous solution, a five dispersion fit. *Journal of Solution Chemistry*, 12(10):729–739, 1983.

[48] E. H. Grant, V. E. R. M. ad N R V Nightingale, and R. J. Sheppard. Dielectric behavior of water in biological solutions: Studies on myoglobin, human low-density lipoprotein, and polyvinylpyrrolidone. *Bioelectromagnetics*, 7:151–162, 1986.

[49] G. Ruderman and J. de Xammar Oro. On the dielectric spectra of proteins in conducting media. *Journal of Biological Physics*, 18(3):167–174, 1991.

[50] H. Neurath. The apparent shape of protein molecules. *Journal of the American Chemical Society*, 61(7):1841–1844, 1939.

[51] M. Hughes, H. Morgan, and M. Flynn. The dielectrophoretic behaviour of submicron latex spheres: Influence of surface conductance. *Journal of Colloid and Interface Science*, 220(2):454–457, 1999.

[52] X. Wang, X. B. Wang, F. F. Becker, and R. C. P. Gascoyne. A theoretical method of electric field analysis for dielectrophoretic electrode arrays using green's theorem. *Journal of Physics D: Applied Physics*, 29:1649–1660, 1996.

[53] D. Clague and E. Wheeler. Dielectrophoretic manipulation of macromolecules: The electric field. *Physical Review E - Statistical, Nonlinear, and Soft Matter Physics*, 64(2 II):266051–266058, 2001.

[54] S. Molla, J. Masliyah, and S. Bhattacharjee. Simulations of a dielectrophoretic membrane filtration process for removal of water droplets from water-in-oil emulsions. *Journal of Colloid and Interface Science*, 287(1):338–350, 2005.

[55] K. Achterhold and F. Parak. Protein dynamics: Determination of anisotropic vibrations at the haem iron of myoglobin. *Journal of Physics Condensed Matter*, 15(18):S1683–S1692, 2003.

[56] N. Green, A. Ramos, and H. Morgan. Ac electrokinetics: A survey of sub-micrometre particle dynamics. *Journal of Physics D: Applied Physics*, 33(6):632–641, 2000.

[57] A. Castellanos, A. Ramos, A. Gonzalez, N. G. Green, and H. Morgan. Electrohydrodynamics and dielectrophoresis in microsystems: Scaling laws. *Journal of Physics D: Applied Physics*, 36(20):2584–2597, 2003.

[58] A. Ramos, H. Morgan, N. Green, and A. Castellanos. Ac electrokinetics: A review of forces in microelectrode structures. *Journal of Physics D: Applied Physics*, 31(18):2338–2353, 1998.

[59] A. Docoslis, N. Kalogerakis, and L. A. Behie. Dielectrophoretic forces can be safely used to retain viable cells in perfusion cultures of animal cells. *Cytotechnology*, 30:133142, 1999.

[60] L. Yang, P. P. Banada, A. K. Bhunia, and R. Bashir. Effects of dielectrophoresis on growth, viability and immuno-reactivity of listeria monocytogenes. *Journal of Biological Engineering*, 2(6):1–14, 2008.

[61] J. Masliyah and S. Bhattacharjee. *Electrokinetic and Colloid Transport Phenomena*. Willey Interscience, Hoboken, New Jersey, 2006.

[62] W. Moll. The diffusion coefficient of myoglobin in muscle homogenate. *Pflgers Archiv European J Physiology*, 299:247–251, 1968.

[63] S. Molla and S. Bhattacharjee. Prevention of colloidal membrane fouling employing dielectrophoretic forces on a parallel electrode array. *Journal of Membrane Science*, 255(1-2):187–199, 2005.

[64] M. Garcia and D. Clague. 2D electric field above a planar sequence of independent strip electrodes. *Journal of Physics D: Applied Physics*, 33(14):1747–1755, 2000.

[65] H. Morgan, G. I. Alberto, B. David, N. G. Green, and A. Ramos. The dielectrophoretic and traveling wave forces generated by interdigited electrode arrays: Analytical solution using fourier series. *Journal of Physics D: Applied Physics*, 34:1553–1561, 2001.

[66] D. Chang, S. Loire, and I. Mezic. Closed-form solutions in the electrical field analysis for dielectrophoretic and travelling wave inter-digitated electrode arrays. *Journal of Physics D: Applied Physics*, 36(23):3073–3078, 2003.

[67] N. Green, A. Ramos, and H. Morgan. Numerical solution of the dielectrophoretic and travelling wave forces for interdigitated electrode arrays using the finite element method. *Journal of Electrostatics*, 56(2):235–254, 2002.

[68] N. Crews, J. Darabi, P. Voglewede, F. Guo, and A. Bayoumi. An analysis of interdigitated electrode geometry for dielectrophoretic particle transport in

micro-fluidics. *Scandinavian Journal of Clinical and Laboratory Investigation*, 61.

[69] S. H. Molla and S. Bhattacharjee. Dielectrophoretic leviation in the presence of shear flow: Implications for colloidal fouling of filtration membranes. *Langmuir*, 23(21):10618–10627, 2007.

Chapter 3

On-Chip Dielectrophoresis and Electrothermal Based Micromixers and Microconcentrators [1]

3.1 Overview

A typical Lab-on-a-Chip (LOC) device contains sample preparation chamber (separation), reaction chambers (mixers) and sensing area (detection). The present study aims to develop simple and rapid LOC device for early prediction of heart attacks. The previous chapter discussed on manipulation and separation of myoglobin under DEP. In the present study, we use dielectrophoresis (DEP) and electrothermal (ET) forces to develop on-chip micromixers and microconcentrators. These type of micromixers and microconcentrators are very useful for performing antibody-antigen reactions and separation of target molecules in a LOC device. A microchannel with rectangular array of microelectrodes, patterned either on its bottom surface only or on both the top and the bottom surfaces, is considered for the analysis. A mathematical model to compute electrical field, temperature field, the fluid velocity, and the concentration distributions is developed. Both analytical and numerical solutions of standing wave DEP(SWDEP), traveling wave DEP (TWDEP), standing wave ET (SWET) and traveling wave ET (TWET) forces along the length and the height of the channel are compared. The effects of electrode size and their placement in the microsystem on micromixing and micro-

[1] A version of this chapter has been published. N. S. K. Gunda, S. Bhattacharjee, and S. K. Mitra, Biomicrofluidics, 6:034118, 2012.

concentrating performance are studied and compared to velocity and concentration profiles. SWET and TWET forces are used for mixing and producing concentration regions by circulating the fluid at a given location.

3.2 Introduction

AC electrokinetics is the study of particle manipulation arising due to the interaction of dielectric particles with nonuniform AC electric field [1]. This technique has been used in various biomedical applications for manipulating, separating, sorting and mixing of bioparticles such as cells, bacteria, viruses, DNA and proteins [2–9]. Dielectrophoresis (DEP) is a frequently used AC electrokinetic technique for manipulating suspended particles in a fluid medium. Usually, this technique is implemented by placing a suspension on a designed, planar microelectrode structure. In some cases, the high electric fields used for manipulating particles creates high power density in the vicinity of the electrodes due to conduction in the solution, causing localized Joule heating. The resulting temperature distribution surrounding the electrode changes the local conductivity and permittivity, causing electrothermal (ET) fluid flow [10–20]. ET fluid flow has been used previously for mixing particle suspensions [15].

Taking the advantage of manipulating the fluid by ET forces and the particles by DEP forces, the present study applies these techniques for developing micromixers and microconcentrators. Micromixer or microconcentrator is one of the important components in Lab-on-a-Chip (LOC) devices or micro-total analysis systems (μTAS). It is used for mixing the chemical reagents and biological analytes in chemical and biomedical analysis [6, 22]. In macroscale, mixing can be achieved by turbulence [6, 22, 23] whereas in microscale, mixing can be achieved by diffusion due to laminar flow in microfluidic systems [6, 22]. The application of DEP and ET enhances the mixing performance at microscale by enhancing diffusive transport. In the present study, the effects of DEP and ET on the performance of mixing and concentrating of particle suspensions are studied. Both standing wave (SW) and traveling wave (TW) types of DEP and ET effects are studied. Numerical and analytical solutions for SWDEP, SWET, TWDEP and TWET forces are calculated and the forces along the length and height of the channel are compared.

A microchannel with rectangular array of microelectrodes, patterned either on its bottom surface only or on both the top and the bottom surfaces of the channel, is considered for the analysis. The terms DEP and SWDEP are synonymous and same goes for ET and SWET. Henceforth, in this chapter, SWDEP and SWET will be used to describe dielectrophoresis and electrothermal effect, respectively.

A few studies are available in literature on micromixers based on DEP technique. Deval et al. [24] and Lee et al. [25] demonstrated chaotic dielectrophoretic micromixing in a simple microchannel geometry with integrated microelectrodes at the bottom surface. Frequency dependent DEP force was used for mixing the aqueous suspension of polystyrene particles. The combination of electrical actuation and channel geometry variation was used to create chaotic advection. Due to the interaction of electric field with velocity field both in time and space, saddle point regions were generated. At saddle point regions, the particles undergo a sequence of stretching and folding, leading to an exponential stretching rate. Chaotic trajectories, generated due to exponential stretching rate, induce the particles into fast and efficient mixing in the particle suspension. Recently, Gunda et al. [15] presented a numerical study on the dielectrophoretic micromixing with novel electrode geometry. They used a microchannel housing array of right angled triangular microelectrodes at the bottom surface. Mathematical model for mixing of two different types of colloidal suspensions was developed based on Laplace, Stokes and convection-diffusion-migration equations. The effects of electrode pairs and mixing length were studied on the microfluidic system and a mixing efficiency of $\sim 97\%$ was calculated for four pairs of electrodes.

Ramos et al. [10–12] described the various forces that are present in the particle suspension under nonuniform AC electric fields. They provided calculation of DEP and ET forces extensively. Later the same research group studied the ET fluid flow for pumping and mixing; DEP for manipulation, separation and sorting of micro- or nano-scale particles [27–32]. Sigurdson et al. [14] used the ET effects for binding of antigen in the fluid to antibody that is immobilized on the short length of the microchannel, to develop an immunosensor. Their numerical simulations showed the improvement of binding rate by a factor of 2 to 8. Later, Feldman et al. [18] developed a biotin-streptavidin heterogeneous assay using ET forces. They experimentally investigated the binding of a fluorescently-labelled streptavidin, which

was suspended in a high conductivity buffer, to biotin, which was immobilized on the channel surface. Their experiments and simulations demonstrated the binding rate of factor 9 at $10V_{rms}$ applied voltage. They also observed a difference of 1.5 orders of magnitude between the experimental and numerical velocity patterns.

Feng et al. [33, 34] presented the analytical and numerical solutions of ET flow in microfluidic systems. They applied this technique for mixing fluids and cleaning the contaminants trapped in microcavities. Their simulations showed that in the case of ET based mixing, the mixing time was reduced by three orders of magnitude compared to the diffusion based mixing. They also observed the chaotic behaviour of fluid flow under ET effects. They demonstrated the fast and efficient cleaning of trapped contaminants in microsystems using the combined effect of pressure driven and ET flows. Perch-Nielsen et al. [35] studied the TWET effects on fluid flow numerically. Their model suggested that the temperature distribution and velocity of the fluid flow depends on conductivity, applied voltage, geometry of the system and the type of substrate. They studied the effect of substrate materials (glass and silicon) on fluid flow and observed the opposite flow direction for the two materials in case of TWET flow. They also studied the effect of external applied temperature gradients in fluid flow and observed the reversal of the fluid flow under certain conditions. Molla and Bhattacharjee [36–38] have demonstrated the successful use of DEP forces to prevent fouling in membranes.

The present chapter focuses on the effect of electrode position, electrode size, number of electrode pairs, and applied voltage on the micromixing due to ET fluid flow and DEP.

3.3 Mathematical modeling

3.3.1 Forces acting on particles and fluid

This section describes the various forces acting on the particles and fluid when the particle suspension is under the influence of an AC electric field [10–12].

The interaction between particles and the medium influences the movement of suspended particles in the solution under AC nonuniform electric fields. The effect of gravity, Brownian motion, DEP, and particle-particle interactions influences the motion of the sub-micron particles. Gravity force is one of the main

external influencing forces that acts due to the difference in the mass density of the fluid and particles. Brownian motion is another important force acting on the sub-micron particles due to thermal randomization. The dielectrophoretic force is the interaction of a nonuniform electric field with the induced dipole moment of a particle. Electrostatic interactions and van der Waals interactions are important particle-particle interaction forces acting on sub-micron size particles. The electrical interaction force occurs between electrically charged particles, which can be described using Coulomb's law. van der Waals interaction, can be either attractive or repulsive in nature between particles depending on the interaction medium. If the solution has finite conductivity, the effects of electrical forces such as AC electroosmosis (ACEO) and ET forces on fluids can be dominant. ACEO occurs due to the interaction of the tangential components of the electric field with an electrical double layer, which forms on the electrode surface because of applied AC signal. ET forces act on the fluid due to the heat generated by AC electrical fields. In brief, the suspended particle suspension under AC electrical fields will undergo the effects of gravity, Brownian motion, DEP, and particle-particle interaction forces on particles and the effects of ACEO and ET forces on fluids.

Since the present study considers the neutrally buoyant, uncharged, non-interacting particles of $\sim 1 - 10$ micron size at low concentrations, the effects of gravity, Brownian motion, and particle-particle interaction forces are neglected. ACEO is applicable only when there is significantly large induced electric double layer. Castellanos et al. [6, 39] predicted that AC electroosmosis is not observable for frequencies greater than 100 kHz when medium electrical conductivity is 0.002 S/m. Similarly, Studer et al. [40] also estimated that ACEO is not important at any frequency for fluids with conductivity greater than 0.140 S/m. Castellanos et al. [6] presented fluid flow and particle flow maps to see which forces are dominant in microfluidic systems, and confirm the limitation of ACEO to relatively low conductivity solutions. Hence, it shows that ACEO is important for low conductivity solutions at low applied field frequencies. The medium conductivity used in this work is considerably high, 0.0575 S/m, the estimated frequency where ACEO is negligible for frequencies greater than $\sim$ 10 kHz. The study will be mostly at higher frequencies (15KHz and 30 MHz) where the EDL formation can be assumed to be small, hence the ACEO is neglected. The effects of the remaining two forces,

i.e., DEP and ET forces, are dominant in such cases, and studied in the present work. The remainder of this section discusses these two forces in detail.

Dielectrophoretic force

DEP is a phenomenon in which a force is exerted on uncharged particles because of the polarization effects that occur in nonuniform electric fields. Usually this force arises on all types of particles, charged or uncharged. However, the strength of the force depends mainly on electrical properties of the particles; medium, shape and size of the particles, magnitude, frequency and phase of the applied AC signal. The typical case is the induced dipole in a lossy dielectric homogeneous spherical particle. Under the influence of sinusoidal varying AC nonuniform electric field with an angular frequency ω, the time averaged DEP force (N) acting on the particle (where the particle is much smaller than the electric field nonuniformities) is given by: [2–4, 10–12, 44]

$$\mathbf{F}_{DEP} = \frac{1}{4}\upsilon\varepsilon_m \left[(\tilde{f}_{CM})_{\mathcal{R}} \nabla \left|\tilde{\mathbf{E}}\right|^2 - 2(\tilde{f}_{CM})_{\mathcal{I}} (\nabla \times (\mathbf{E}_R \times \mathbf{E}_R) \right] \tag{3.1}$$

where υ is the volume of particle ($= 4\pi a_p^3/3$) and a_p is the radius of particle. $\tilde{\mathbf{E}}$ is the applied electric field ($\tilde{\mathbf{E}} = -\nabla\tilde{\phi} = -(\nabla\phi_R + i\nabla\phi_I)$), ε_m is the permittivity of medium and $\tilde{f}_{CM}$ is Clausius-Mossotti (CM) factor, subscripts $\mathcal{R}$ and $\mathcal{I}$ indicates the real part and imaginary part of the component, respectively, which is given as:

$$\tilde{f}_{CM} = \frac{\tilde{\varepsilon}_p - \tilde{\varepsilon}_m}{\tilde{\varepsilon}_p + 2\tilde{\varepsilon}_m} \tag{3.2}$$

where $\tilde{\varepsilon}$ is complex permittivity and subscripts p and m represents the particle and medium, respectively. The complex permittivity is given as:

$$\tilde{\varepsilon} = \varepsilon - i\frac{\sigma}{\omega} \tag{3.3}$$

where σ is electrical conductivity, ω is angular frequency of the applied electric field, ε is the permittivity and $i = \sqrt{-1}$. For spatially varying field magnitude (180^o phase difference between adjacent electrodes), the first part of Eq.(3.1) will be non-zero, exhibiting SWDEP. For spatially varying phase (90^o phase difference between adjacent electrodes), the second part Eq.(3.1) will be non-zero, indicating TWDEP.

Electrothermal force

ET force is the body force exhibited on the fluid medium due to AC electric fields. The AC nonuniform electrical fields in the system generate heat (Joule heating) at the electrodes, which diffuses rapidly in the fluid medium, leading to the variations in the temperature of medium and concurrent variations in the conductivity and permittivity of medium. The variations in the permittivity and conductivity exert an electrical body force on the medium. The time averaged ET force on unit volume of fluid (N/m^3) is given as: [10–12, 35]

$$\begin{aligned}\mathbf{f}_{ET} =& \frac{1}{2}\left[\left\{\frac{\varepsilon_m(\alpha-\beta)}{1+(\omega\varepsilon_m/\sigma_m)^2}\left[(\nabla T\cdot\mathbf{E}_{\mathcal{R}})\mathbf{E}_{\mathcal{R}}+(\nabla T\cdot\mathbf{E}_{\mathcal{I}})\mathbf{E}_{\mathcal{I}}\right]\right\}\right.\\ &\left.+\left\{\frac{\omega\varepsilon_m^2(\alpha-\beta)}{\sigma_m\left(1+(\omega\varepsilon_m/\sigma_m)^2\right)}\left[(\nabla T\cdot\mathbf{E}_{\mathcal{R}})\mathbf{E}_{\mathcal{I}}-(\nabla T\cdot\mathbf{E}_{\mathcal{I}})\mathbf{E}_{\mathcal{R}}\right]\right\}\right]\\ &-\frac{1}{4}\varepsilon_m\alpha\nabla T\left[\left|\mathbf{E}_{\mathcal{R}}\right|^2+\left|\mathbf{E}_{\mathcal{I}}\right|^2\right]\end{aligned} \tag{3.4}$$

where T is the temperature, $\alpha = (\partial\varepsilon_m/\partial T)/\varepsilon_m$ and $\beta = (\partial\sigma_m/\partial T)/\sigma_m$. For spatially varying field magnitude (180^o phase difference between adjacent electrodes), the imaginary part of Eq.(3.1) will be zero, exhibiting SWET. For spatially varying phase (90^o phase difference between adjacent electrodes), the imaginary part will be non-zero, indicating TWET.

3.3.2 Governing equations

Governing equations required for solving the combined effects of DEP and ET are provided in this section.

Laplace equation

The phasor notation is used to describe the temporal electric field varying in a sinusoidal manner with angular frequency, ω. The potential distribution in the system created by the AC signal is given by the Laplace equation [45, 46]

$$\nabla^2\tilde{\phi} = 0 \tag{3.5}$$

where $\tilde{\phi} = \phi_{\mathcal{R}} + i\phi_{\mathcal{I}}$ is the potential phasor. Using Eq.(3.5), the electric field distribution can be calculated as

$$\tilde{\mathbf{E}} = -\nabla\tilde{\phi} \tag{3.6}$$

where $\tilde{\mathbf{E}} = \mathbf{E}_{\mathcal{R}} + i\mathbf{E}_{\mathcal{I}} = -\nabla\phi_{\mathcal{R}} - i\nabla\phi_{\mathcal{I}}$. This electric field phasor is used to calculate the time averaged dielectrophoretic force, $\mathbf{F}_{DEP}$ and electrothermal force, $\mathbf{F}_{ET}$ provided in Eq.(3.1) and Eq.(3.4), respectively.

Fourier's heat conduction equation

According to Ramos et al. [10], the typical diffusion time for temperature front in the present system can be estimated as ($t_{diff} = \rho_m c_p l^2/k$) 6ms. For the frequencies (10kHz and 20 MHz) used in the system, the temperature change ($\Delta T/T \approx 1/(2\omega t_{diff}$) is negligible. Hence, transient term is neglected for the heat equation. For the present system, $\rho_m c_p u_{av} l/k \approx 2 \times 10^{-2}$ [10], so convective term is neglected in the heat equation. The temperature distribution generated in the fluid medium due to AC electrical fields can be calculated from the steady state conduction equation as:

$$k\nabla^2 T + \sigma_m \left|\tilde{E}\right|^2 = 0 \tag{3.7}$$

where k is the thermal conductivity and T is the temperature of the suspension affected due to the electric field.

Stokes Equation

For steady state incompressible laminar flow, Stokes equation with electrothermal body force is given by

$$\nabla p = \mu\nabla^2\mathbf{u} + \mathbf{f}_{ET} \tag{3.8}$$

where p is the pressure and $\mathbf{u}$ is the velocity vector of the fluid medium.

Convection-diffusion-migration equation

The steady state concentration distribution of particles in the system with no chemical reactions can be given by the convection-diffusion-migration equation considering DEP force as the migration term [38, 47]

$$\nabla\cdot(\mathbf{u}c) = \nabla\cdot(\mathcal{D}_\infty\nabla c) - \nabla\cdot(\frac{\mathcal{D}_\infty\mathbf{F}_{DEP}}{k_B T_{amb}}c) \tag{3.9}$$

where c is the concentration of the particles, $\mathcal{D}_\infty$ is diffusion constant of the particle, T_{amb} is the ambient temperature and k_B is the Boltzmann constant ($= 1.381 \times 10^{-23}\ J/K$).

3.3.3 Computational geometry

Figure 3.1 depicts the two-dimensional (2D) schematic view of the microchannel considered for the study. Here W is the width of the electrode, G is the gap between electrodes, L is the length of the channel and H is the height of the channel. Appropriate boundary conditions required to solve the problem for SWDEP, SWET, TWDEP and TWET are shown in the figure, where, q is the heat flux entering/exiting through suspension into the channel (considered same at both the inlet and outlet of the channel), and u_{av} is the average velocity of the suspension entering the channel. Three types of electrode configurations are used in the study - electrodes at bottom, symmetric and asymmetric electrodes.

3.3.4 Solution methodology

A 2D computational domain is analyzed as shown in Fig. 3.1. The finite element method is used to solve the above governing equations inside the microchannel. The procedure for solving the concentration distribution under combined DEP and ET effects is divided into four steps: (i) evaluating the potential distribution in the system using Eq.(3.5) and electric field distribution in the system using Eq.(3.6); (ii) evaluating the temperature distribution in the system using Eq.(3.7); (iii) evaluating the flow field velocity distribution in the system using Eq.(3.8); and (iv) evaluating the particle spatial concentration distribution using Eq.(3.9). Steps (ii) and (iii) are coupled because the change in fluid velocity due to body force changes the temperature distribution in the system. The solution obtained in step (i) is used to find the DEP force and ET force at the initial condition. Thereafter, incorporating the ET force in Eq.(3.8) and solving both Eqs.(3.7) and (3.8) simultaneously, the temperature and velocity distribution can be calculated. Incorporating DEP force and velocity in Eq.(3.9), spatial concentration distribution of particles can be calculated next. Flow chart for solution methodology is given in Fig. 3.2.

The problem is implemented within a commercial based finite element analysis software, COMSOL MULTIPHYSICS (COMSOL Version 3.5a, COMSOL, Inc., Burlington, MA, USA). The computational model is discretized with Lagrange-quadratic quadrilateral elements (using mapped mesh scheme). The electrode edges are locally refined to capture the effect of high intensity electric field. A mesh

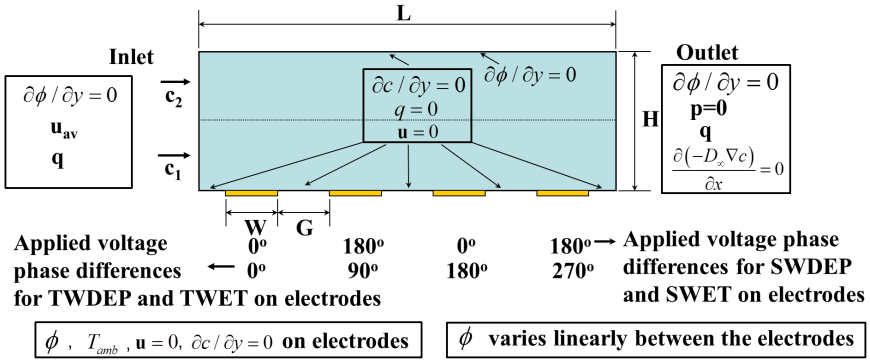

(a)

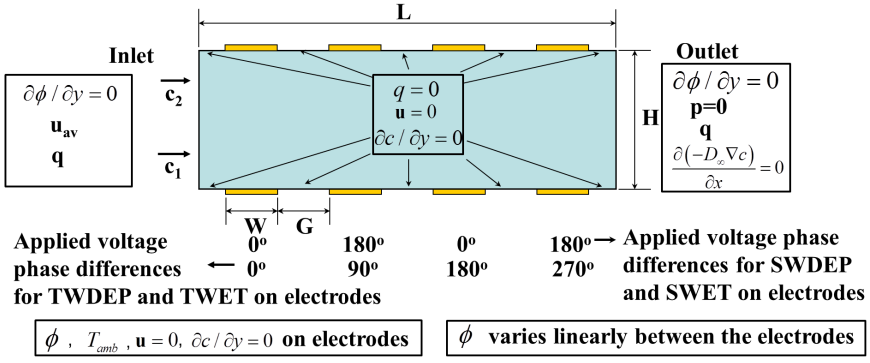

(b)

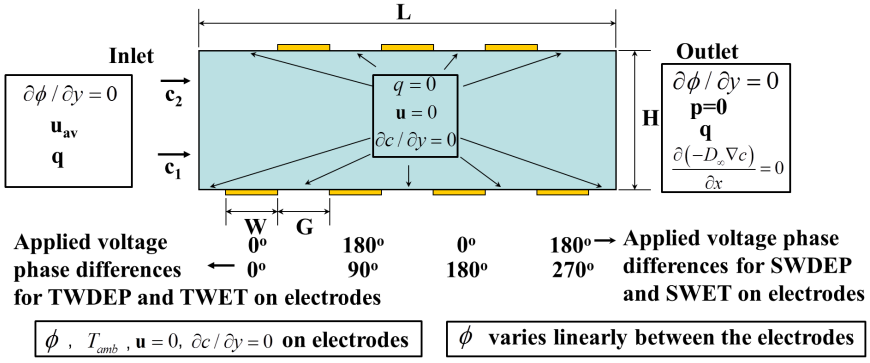

(c)

Figure 3.1: Two-dimensional schematic diagram considered for the analysis; (a) Electrodes at bottom surface only; (b) Symmetric electrodes on both top and bottom surfaces at 0^o phase; (c) Asymmetric electrodes on both top and bottom surfaces at 180^o phase difference.

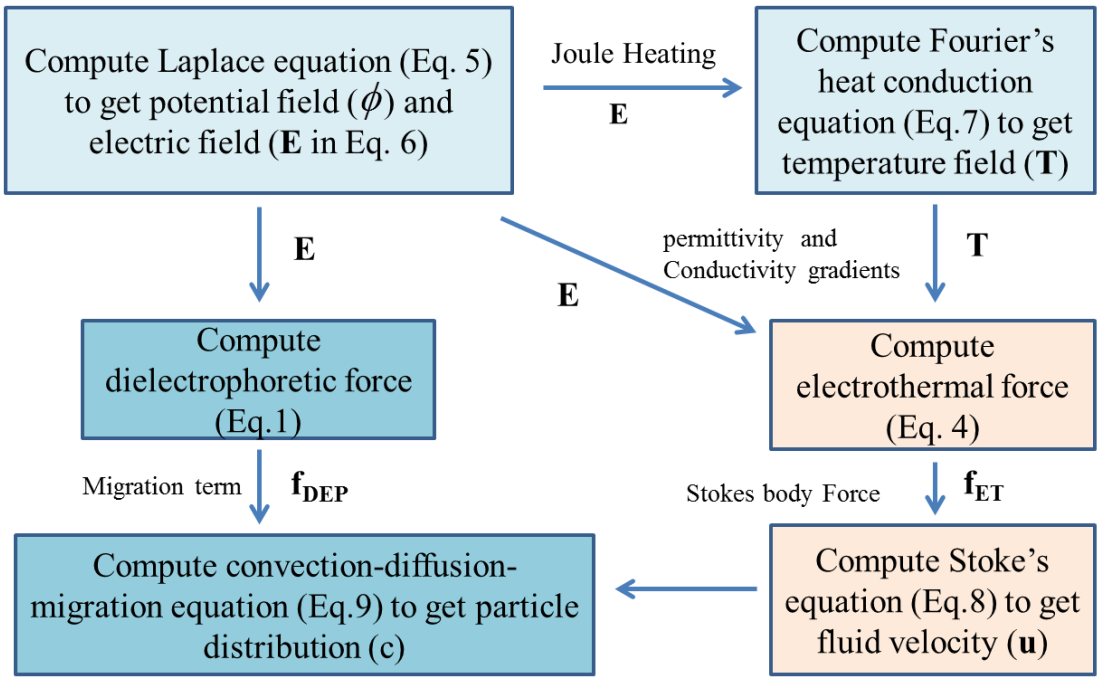

Figure 3.2: Flow chart for combined DEP and ET solution methodology

independent solution is achieved in this case with the domain finally consisting of 9600 elements. The simultaneous linear equations produced by the finite element method are solved using direct elimination solver (PARDISO). Analytical solution is also calculated for the computation domain shown in Fig. 3.1(a). SWDEP and TWDEP forces are calculated based on Fourier series method using the electrical field expressions given by Morgan et al. [44] in Eq.(3.1). SWET and TWET forces are calculated by incorporating the electric field expressions given by Morgan et al. [44] based on Fourier series method and temperature distribution expressions given by Ramos et al. [10] and Feng et al. [34] into Eq.(3.4).

3.4 Results and discussions

Results for the study of dielectrophoresis and electrothermal effects on micromixing and microconcentration are presented in this section. For the simulations, length and height of the channels are taken as $L = 240\mu m$ and $H = 40\mu m$, respectively. The channel length depends on the number of electrodes in that array. The width of electrode and gap between electrodes are taken as $W = 30\mu m$ and $G = 30\mu m$, respectively. The thickness of electrodes is assumed to be very small as compared

to the height of channel, and hence neglected in the simulations. The dielectric properties of the colloidal particle suspensions considered for the analysis are given as: $\varepsilon_p = 3\varepsilon_o$, $\varepsilon_m = 80.2\varepsilon_o$, $\sigma_p = 0.1\ S/m$ and $\sigma_m = 0.0575\ S/m$. Here $\varepsilon_0 = 8.854 \times 10^{-12}\ C^2N^{-1}m^{-2}$ is the permittivity of free space. The properties of the fluid taken for the analysis are given as: thermal conductivity $k = 0.598\ W/(mK)$; dynamic viscosity $\mu = 1.08 \times 10^{-3}\ Pas$; and density $\rho = 1000\ kg/m^3$. The particle radius a_p is taken as 1.5 μm. The particle suspensions are maintained at the ambient temperature $T_{amb} = 298\ K$. The simulations are conducted in the frequency of $15KHz$ for positive DEP and ET effects and $20MHz$ for negative DEP effects. All the figures shown for SWDEP and TWDEP are taken under $15V$ applied voltage on electrodes. SWET and TWET effects are simulated under $30V$ applied voltage on electrodes. The list of physical and chemical properties used in this study can be found in Table 3.1. All the results shown for the case when the width of the electrode is equal to gap between the electrodes ($W = G$). Similar results are observed for other electrode configurations ($W < G$ and $W > G$), which are not described here for the sake of brevity.

Property	Value
System	Latex particles in Water
Particle radius (a_p)	$1.5 \times 10^{-6}\ \mu m$
Density of particle (ρ_p)	$1000\ kg/m^3$
Density of water (ρ_m)	$1000\ kg/m^3$
Temperature (T_{amb})	$273\ K$
Boltzmann constant (k_B)	$1.38 \times 10^{-23}\ kg/m^3$
Dynamic viscosity of water (μ)	$1.0 \times 10^{-3}\ Ns/m^2$
Thermal conductivity (k)	$0.598\ W/mK$
Conductivity of Water (σ_m)	$0.0575\ S/m$
Permittivity of Water (ε_m)	$80.2\varepsilon_0\ C^2N^{-1}m^{-2}$
Conductivity of Particle (σ_p)	$0.1\ S/m$
Permittivity of particle (ε_p)	$3\varepsilon_0\ C^2N^{-1}m^{-2}$
Permittivity of free space (ε_0)	$8.854 \times 10^{-12}\ C^2N^{-1}m^{-2}$
Diffusion constant of the particle ($\mathcal{D}_\infty$)	$1 \times 10^{-11}\ m^2/s$
Inlet concentration (c)	$1\ \mu mol/m^3$
Electrode prperties	
Electrode width (W)	$30\ \mu m$
Gap between electrodes (G)	$30\ \mu m$
Voltage range (ϕ)	$15 - 30\ V$
Reference Voltage (ϕ_o)	$1\ V$
Frequency (F)	$10 - 10000\ KHz$
Channel dimensions	
Channel length (L)	$240 - 720\ \mu m$
Channel height (H)	$40\ \mu m$
Average velocity of fluid (u_{av})	$0.1 - 0.5\ mm/s$

Table 3.1: Physical and chemical properties of the system studied

3.4.1 Comparison of analytical and numerical solutions

Along channel length

Figure 3.3 illustrates the comparison of forces with respect to channel length near the electrode plane for both analytical and numerical solutions. This figure shows

four plots. The horizontal axis of each plot in this figure shows the non-dimensional length of the channel (x^*) and vertical axis shows the non-dimensional force term. In Fig. 3.3, the actual DEP force is non-dimensionalized as $\mathbf{F}_{DEP}/\varepsilon_o{\phi_o}^2$, whereas ET body force is non-dimensionalized as $\mathbf{f}_{ET}W/\varepsilon_o{\phi_o}^2$. Analytical solution is indicated using the circle symbol with red color whereas numerical solution is indicated using the square symbol with blue color. Figure 3.3(a) shows the non-dimensional SWDEP force variation along the length of the channel near electrodes. This plot shows that the DEP force is maximum at the edges of electrodes and minimum elsewhere. SWDEP force has a low value at the mid-point of the electrode compared to mid-point of the gap between electrodes. The attraction or repulsion of particles at the edges of electrodes can be achieved substantially due to a large electric field. Excellent agreement between Fourier series based analytical solution and finite element based numerical solution is observed. Figure 3.3(b) represents the non-dimensional SWET force profile along the length of the channel near electrodes. SWET force is also maximum at the edges of electrodes like the SWDEP force. But the SWET force is different than the SWDEP force at the mid-point of electrode and at the mid-point of the gap between electrodes. In this case, SWET force is minimum at the mid-point of the gap between electrodes compared to the mid-point of electrodes. A margin of deviation is observed between analytical and numerical solutions for SWET force at the mid-point of the electrode. Non-dimensional SWDEP force is the force acting on the particles and the value is in the orders of 0.02 to 900 whereas non-dimensional ET force is the force acting on the fluid medium and the value is in the orders of 0.01 to 1000. Figure 3.3(c) shows the variation of non-dimensional TWDEP force near the electrode plane along the length of the channel. Like SWDEP force, TWDEP force is maximum at the edges of the electrode, but its variation is different. The difference between the TWDEP force at the mid-point of the electrode and mid-point of the gap between the electrodes is very less as compared to DEP force. The TWDEP force values shown in the plot are three orders of magnitude less than the DEP force. Slight difference in the analytical and numerical solutions is observed for the force on the electrodes, but a significant difference of upto 79% is identified along the electrode gap and at the electrode edges. Analytical solution has captured the maximum TWDEP force at the electrode edges compared to numerical solution. Figure 3.3(d) illustrates

the change in non-dimensional TWET force along the length of the channel near the electrodes. Profiles for both SWET and TWET are similar, but the TWET force values are reduced by half compared to the ET force. Difference of upto 63% is observed between the analytical and numerical solution of TWET force along the electrode, but negligible difference exists along the gap.

Along the channel height

Figure 3.4 depicts the comparison of analytical and numerical solution of different force terms along the channel height at electrode edge, mid point of electrode and mid point of gap between the electrodes. The horizontal axis in this figure shows the non-dimensional height of the channel (y^*) whereas vertical axis shows the non-dimensional force term in logarithmic scale. In Fig. 3.4, the DEP force is non-dimensionalized as $\mathbf{F}_{DEP}/\varepsilon_o{\phi_o}^2$, whereas ET body force is non-dimensionalized as $\mathbf{f}_{ET}W/\varepsilon_o{\phi_o}^2$. At the edges of the electrodes, all force terms are exponentially decayed along the height of channel. In Fig. 3.4(a), non-dimensional SWDEP force is monotonically increased up to $y^* = 0.92$ and then linearly decreased along the height of channel at the mid-point of the electrode. The linear decaying of SWDEP force is observed at the mid point of gap between the electrodes. At the height $y^* = 2$ to $y^* = 3$, the SWDEP force is constant throughout the channel length and its magnitude is linearly decreased along the height of the channel. This decides the effectiveness of SWDEP force in the channel. Excellent agreement between the analytical and numerical solutions for SWDEP force is observed in all cases i.e., mid-point of electrode, edge of electrode and mid-point of gap. Some slight discrepancy in solutions for SWDEP force along the height of channel up to $y^* = 0.5$ at the mid-point of electrodes is observed. Figure 3.4(b) shows the variation profiles of the non-dimensional SWET force along the height of the channel at different locations. Similar trend between SWDEP force at the mid-point of the electrode and SWET force at the mid-point of the gap is observed. Analytical and numerical solutions of SWET force are in agreement up to $y^* = 1.8$, beyond this some discrepancies are observed. Figure 3.4(c) illustrates the non-dimensional TWDEP force variation along the height of the channel at different locations. A difference in the analytical and numerical solutions for the TWDEP force along the height of the channel is observed. Similar profile variations at the electrode

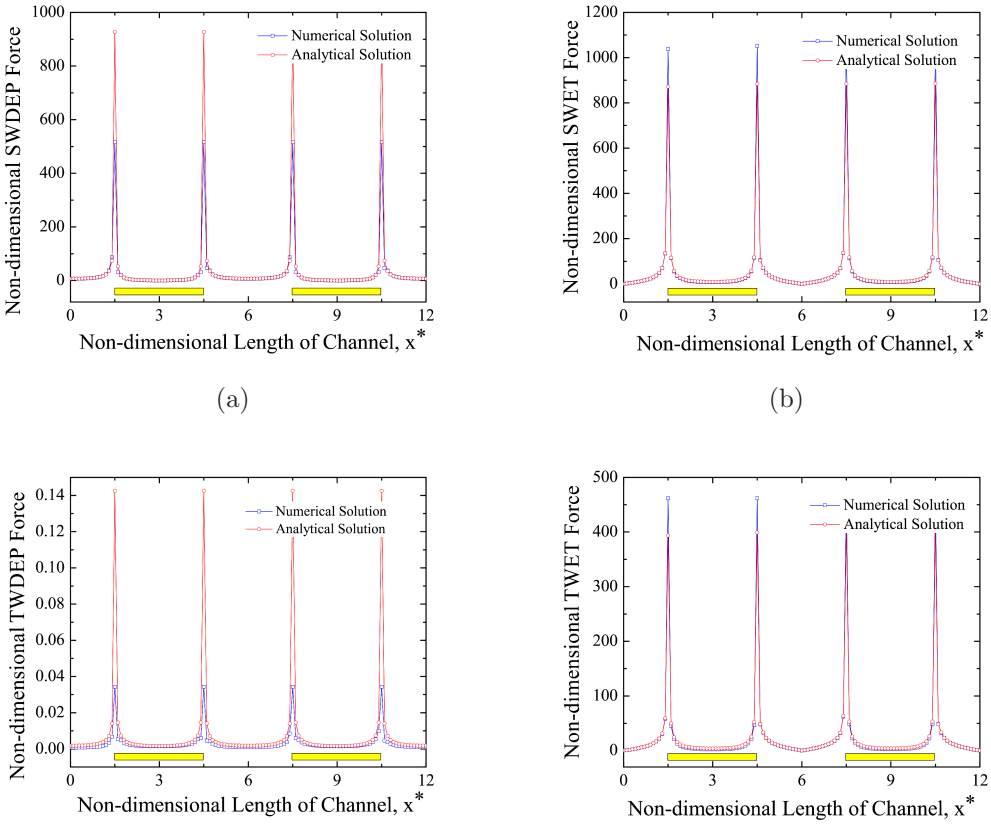

Figure 3.3: Comparison of analytical and numerical solution of force terms along the length of the channel near electrodes for the case where electrodes at bottom surface only; (a) Non-dimensional SWDEP Force; (b) Non-dimensional SWET force; (c) Non-dimensional TWDEP Force; (d) Non-dimensional TWET force. The horizontal axis in this plot is non-dimensionalized with respect to electrode width, which is $30\mu m$ in this case. Gap between electrodes is equal to electrode width. Applied voltage $\phi = 15V$ and frequency is $15KHz$. Here, DEP force is non-dimensionalized as $\mathbf{F}_{DEP}/\varepsilon_o {\phi_o}^2$, whereas ET body force is non-dimensionalized as $\mathbf{f}_{ET} W/\varepsilon_o {\phi_o}^2$;

edge and at the mid-point of the gap for both SWDEP and TWDEP forces are observed, but significant difference in the profile at the mid-point of the electrode is observed. The TWDEP force values are three orders of magnitude lower than the SWDEP force. The TWDEP force at the mid of the electrode decreases along the height of the channel up to or around $y^* = 1.35$ to $y^* = 1.4$, then increases up to $y^* = 2.5$ and then remains constant throughout the height of the channel. Figure 3.4(d) shows the non-dimensional TWET variation along the height of the channel at different locations. Some difference between the analytical and numerical solutions is observed for TWET force. Profiles for the SWET and TWET forces are similar at the mid of the electrode and the electrode edge, but significant difference in the profile variation at the mid of the gap is observed.

3.4.2 Effect of SWDEP force

Figure 3.5 shows the comparison of DEP velocity under positive DEP effect, in terms of contours and vectors for the following cases; (a) channel with electrodes at the bottom surface; (b) channel with electrodes at both top and bottom surfaces with the same position as in the previous case; (c) channel with electrodes at both top and bottom surfaces placed in alternate distances. Arrows in figure indicate the direction of particles movement due to DEP force. The length of the arrow does not indicate the magnitude of the DEP velocity. Contours in the figure indicate the constant DEP velocities along the curves. Converging of arrows at electrode edges indicate the collection of particles in that area, which can be used as concentration regions (or collectors). However, the distance traveled by the particle varies in the channel. Figure 3.6 shows the comparison of DEP velocity under negative DEP effect, in terms of contours and arrows for following cases; (a) channel with electrodes at the bottom surface; (b) channel with electrodes at both top and bottom surfaces with the same position as in the previous case; (c) channel with electrodes at both top and bottom surfaces placed in alternate distances. Arrows in the figure indicate the direction of particles movement due to DEP force. The length of the arrow does not indicate the magnitude of the DEP velocity. Contours in the figure indicate the constant DEP velocities. In this case, the direction of the particle movement has changed and the particles are being repelled from the electrode. As this is a closed channel, the particles are

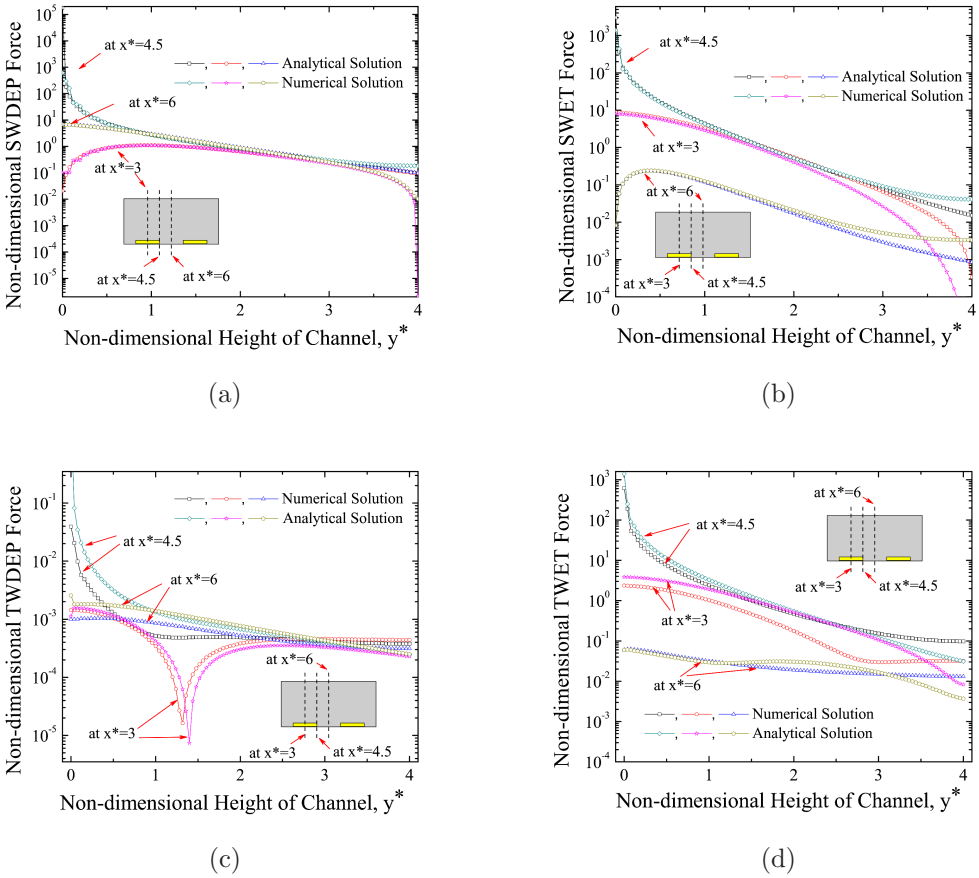

Figure 3.4: Comparison of analytical and numerical solution of force terms along the height of the channel at edge of the electrode, mid point of the electrode and mid point of gap between electrodes for the case where electrodes at bottom surface only; (a) Non-dimensional SWDEP Force; (b) Non-dimensional SWET force; (c) Non-dimensional TWDEP Force; (d) Non-dimensional TWET force. The horizontal axis in this plot is non-dimensionalized with respect to electrode width, which is $30\mu m$ in this case. Gap between electrodes is equal to electrode width. Applied voltage $\phi = 15V$ and frequency is $15KHz$. Here, DEP force is non-dimensionalized as $\mathbf{F}_{DEP}/\varepsilon_o {\phi_o}^2$, whereas ET body force is non-dimensionalized as $\mathbf{f}_{ET} W/\varepsilon_o {\phi_o}^2$;

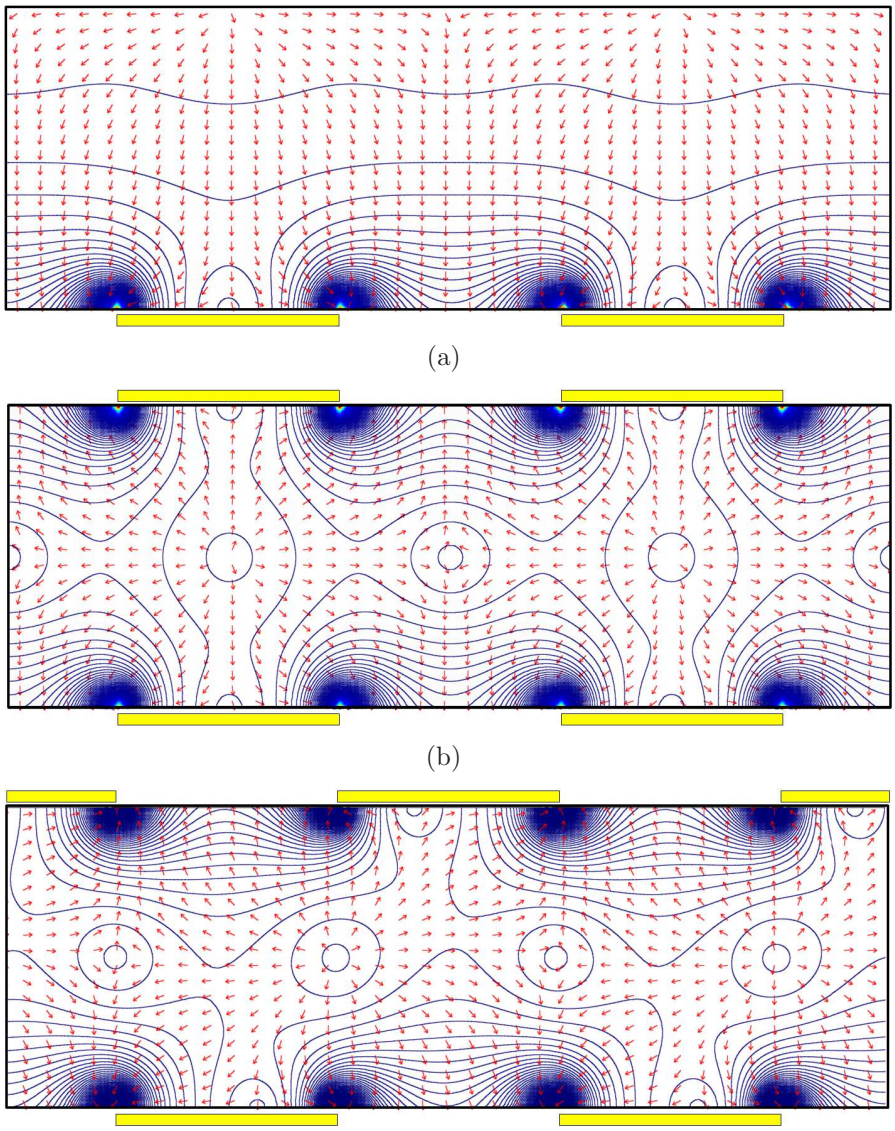

Figure 3.5: Comparison of DEP velocity contour and arrow plots under positive DEP effect for following cases; (a) channel with electrodes at the bottom surface; (b) channel with electrodes at both top and bottom surfaces with the same position as in the previous case; (c) channel with electrodes at both top and bottom surfaces placed in alternate distances

collecting at the top wall of the channel and at a position parallel to the mid-point of the electrode. The region where the particles are collecting is referred to as concentrating regions. Position of electrodes at both top and bottom changes the concentration regions. In Fig. 3.6(b), where the electrodes at both top and bottom of the channel are symmetrically located, the concentration region has shifted to the mid-point of the channel height and parallel to the mid-point of the electrodes. When the electrode position on the top of the channel is shifted by one electrode width, as shown in Fig. 3.6(c), the concentration regions are shifted from the mid-point of the electrode to the edge of the electrodes along the mid-plane of the microchannel.

3.4.3 Effect of SWET force

Figure 3.7 shows the comparison of fluid velocity under ET forces at applied voltage of $30V_{rms}$ and angular frequency of $15KHz$ in terms of scalar and contour plot for following cases; (a) channel with electrodes at the bottom surface; (b) channel with electrodes at both top and bottom surfaces with the same position as in the previous case; (c) channel with electrodes at both top and bottom surfaces placed in alternate distances. The figure shows the scalar plot of fluid velocity under ET force and contour shows the constant velocity in that curve. It is observed that near (around 0.01% of the height of the channel) the electrode edges, the fluid velocity is less which gradually increases up to a certain height and eventually starts decreasing along the channel height. The contours indicate that the fluid is circulating in the region above the electrode edges without getting transported along the channel. At these circulation regions, the particles also move from the bottom surface to the top surface of the channel and the particles and fluid in the lower half of channel can easily mix up with the colloidal suspension in the upper half of channel. Position of the electrodes can change the intensity and number of circulation regions across the channel. The colors in the contour plot indicate the velocity magnitudes. The legend in the right side of each graph indicates the colors used for velocity magnitudes in the contour and scalar plots. The shape of the circular regions also depends on the position of the electrode.

Figure 3.8 illustrates the comparison of scalar concentration and ET velocity in terms of stream lines and arrows for following cases; (a) channel with electrodes at

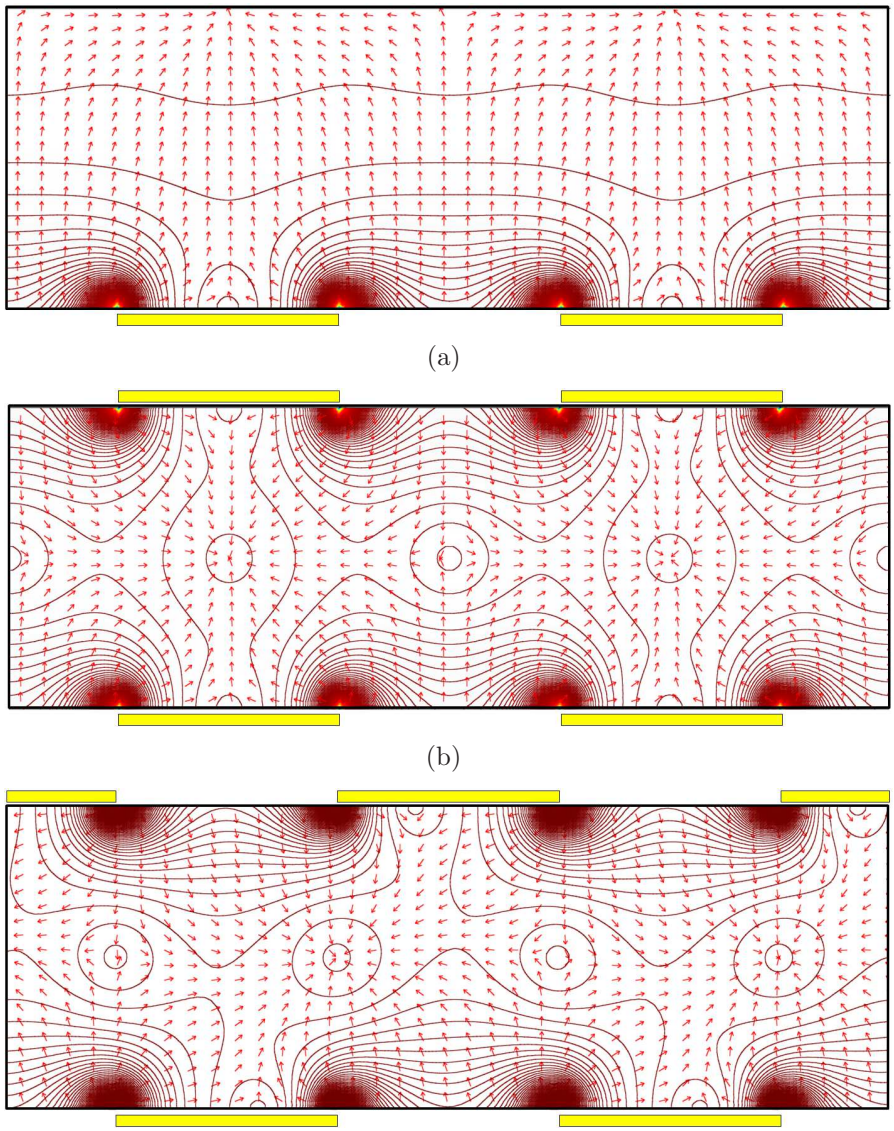

(a)

(b)

(c)

Figure 3.6: Comparison of DEP velocity contour and arrow plots under negative DEP effect for following cases; (a) channel with electrodes at the bottom surface; (b) channel with electrodes at both top and bottom surfaces with the same position as in the previous case; (c) channel with electrodes at both top and bottom surfaces placed in alternate distances

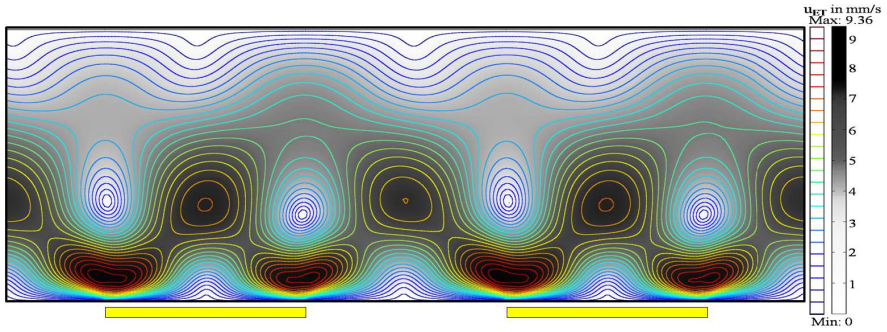

(a)

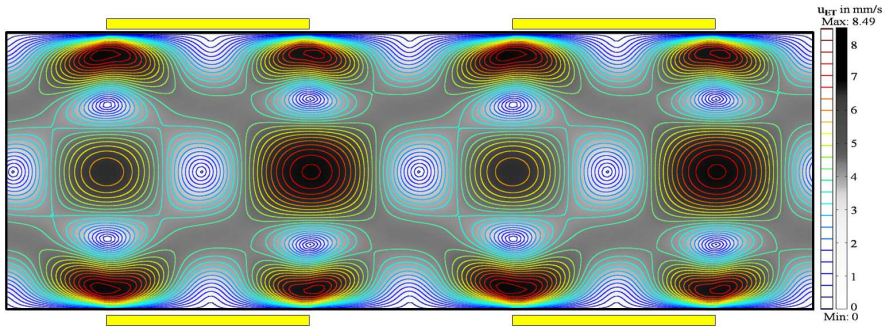

(b)

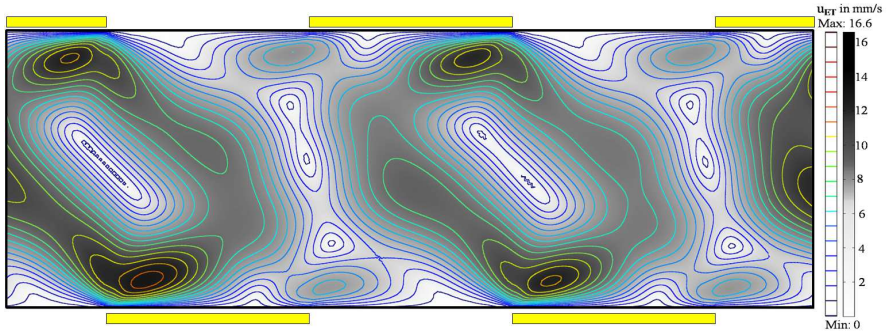

(c)

Figure 3.7: Comparison of fluid velocity scalar plot with contours under ET force at $30V_{rms}$ applied voltage for following cases; (a) channel with electrodes at the bottom surface; (b) channel with electrodes at both top and bottom surfaces with the same position as in the previous case; (c) channel with electrodes at both top and bottom surfaces placed in alternate distances

the bottom surface; (b) channel with electrodes at both top and bottom surfaces with the same position as in the previous case; (c) channel with electrodes at both top and bottom surfaces placed in alternate distances. Arrows in the figure indicates the direction of fluid medium under ET forces. The length of the arrow does not indicate the magnitude of the velocity. It is observed that, the particles in the fluid are moving along with the fluid. In Fig. 3.8(a), arrows and stream lines shows the movement of particles and the fluid movement in the channel where electrodes are placed at the bottom of the channel only. The size of circulation region depends on the applied voltage. The arrow directions at the beginning of the electrode and at the end of the electrode are opposite to each other which makes the fluid rotate at the same location instead of moving towards the other stream. If the applied voltage is less, the circulation region will be less and the fluid can easily move to opposite side making some small concentrated circulation region at the edges of electrodes. In Fig. 3.8(b), it is observed that, the size of the circulation regions is increased with the addition of electrodes at the top wall of the channel. In certain regions the suspension is well mixed at the upper half of the channel and in some other regions the suspension remains confined in the lower and upper halves of the channel, respectively. The effect of applied voltage on velocity of the suspension under ET forces is illustrated in Fig. 3.9. This figure compares the change in velocity and concentration distribution under ET force with respect to applied voltage of $15V_{rms}$ and $30V_{rms}$. The figure also clearly shows the difference in the number of circulation regions and their location in the form of contours and scalar plot of suspension velocity.

3.4.4 Effect of TWDEP force

Figure 3.10 shows the comparison of TWDEP velocity in terms of contours and arrows for following cases; (a) channel with electrodes at the bottom surface; (b) channel with electrodes at both top and bottom surfaces with the same position as in the previous case; (c) channel with electrodes at both top and bottom surfaces placed in alternate distances. Arrows in the figure indicate the direction of particles movement due to TWDEP force. The length of the arrow does not indicate the magnitude of the TWDEP velocity. Contours in the figure indicate the constant TWDEP velocities. This TWDEP can be used for moving the particles from the

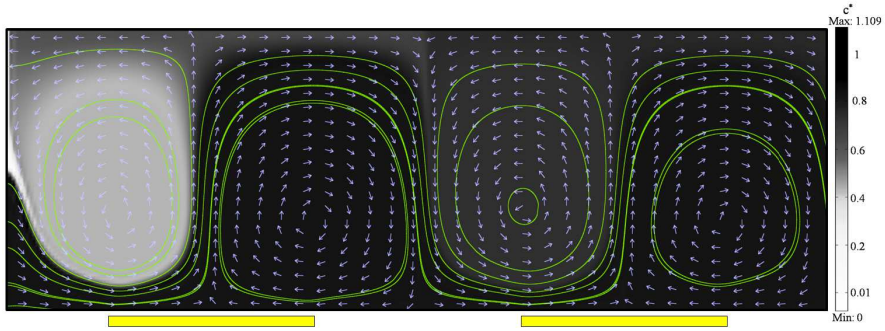

(a)

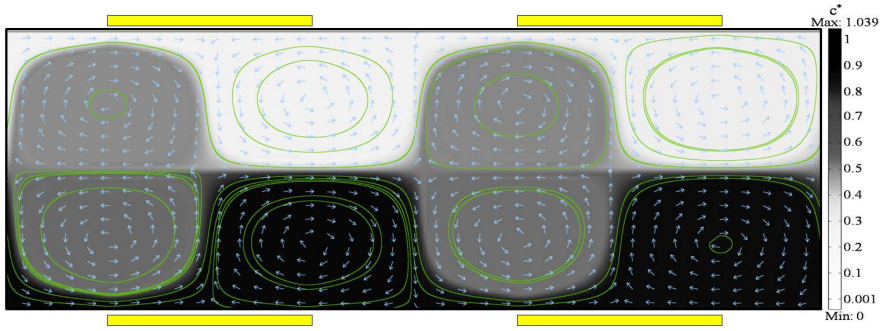

(b)

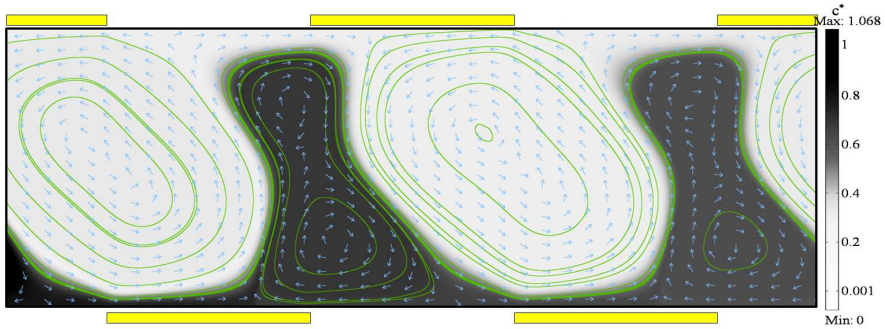

(c)

Figure 3.8: Comparison of scalar concentration and fluid velocity streamline and arrow plots under ET force at $30V_{rms}$ applied voltage for following cases; (a) channel with electrodes at the bottom surface; (b) channel with electrodes at both top and bottom surfaces with the same position as in the previous case; (c) channel with electrodes at both top and bottom surfaces placed in alternate distances

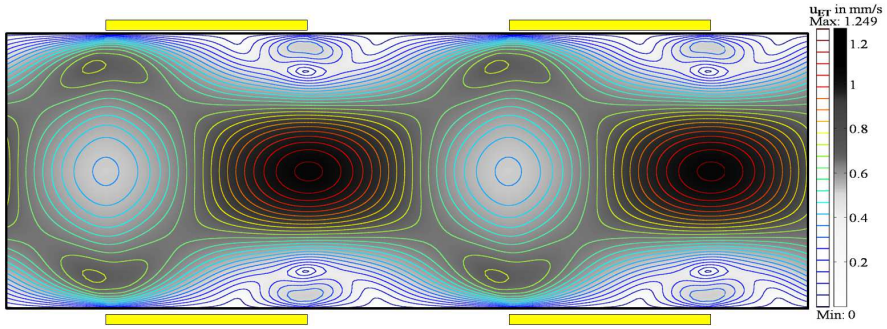

(a)

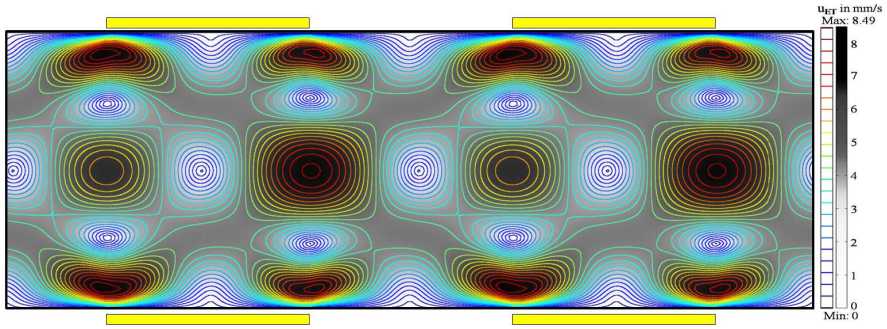

(b)

Figure 3.9: Comparison of change in velocity and concentration distribution under ET force with respect to applied voltage at electrodes for a case of channel having electrodes at both top and bottom surface; (a) Velocity scalar plot with contours at applied voltage of $15V_{rms}$; (b) Concentration scalar plot with velocity stream lines and arrows at applied voltage of $15V_{rms}$

inlet to the outlet of the channel. Later the movement of the particles has changed. This change in the direction of the particle near the electrode plane and away from the electrode plane can be used for mixing. Figure 3.10(b) shows the converging and diverging of arrows along the channel. There are no re-circulation regions in this case. Figure 3.10(c) shows the waviness in the direction of arrows from the top to the bottom and then bottom to top along the channel. This TWDEP force on the particles can be used for moving the particles from inlet to outlet as shown in the Fig. 3.10(a) and can be advantageously used in mixing of two different layers of the suspensions with electrode configurations shown in Figs. 3.10(b) and 3.10(c).

Figure 3.11 shows the effect of TWDEP with the different types of electrode shapes. The electrodes shown in the figures, are placed at the bottom of the channels. For this type of configurations, three-dimensional computational domain is necessary to solve the problem. The figure shows the direction of the particle movements in terms of arrows from the inlet to outlet. The waviness of arrows in the flow field shows the mixing of the two layers of suspensions which are introduced side by side in the channel. The effect of particle direction due to the edge effect of the right angled triangular electrodes is shown in the Figs. 3.11(a) and 3.11(b). The different types of triangular electrodes with blunt corners is shown in the Fig. 3.11(c). In all these cases, the direction of the particles has drastically changed at the slant edge of the electrodes.

3.4.5 Effect of TWET force

Figure 3.12 shows the comparison of TWET velocity in terms of scalar and contour plot for the following cases; (a) channel with electrodes at the bottom surface; (b) channel with electrodes at both top and bottom surfaces with the same position as in the previous case; (c) channel with electrodes at both top and bottom surfaces placed in alternate distances. Figure 3.13 illustrates the comparison of scalar concentration and TWET velocity in terms of stream lines and arrows for following cases; (a) channel with electrodes at the bottom surface; (b) channel with electrodes at both top and bottom surfaces with the same position as in the previous case; (c) channel with electrodes at both top and bottom surfaces placed in alternate distances. In both these figures, the circulation regions for all cases

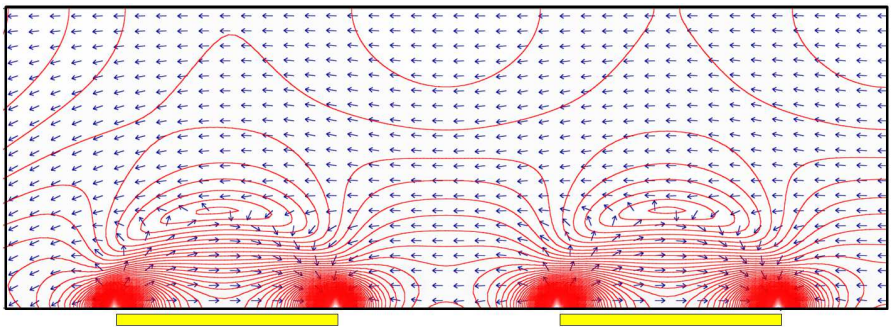

(a)

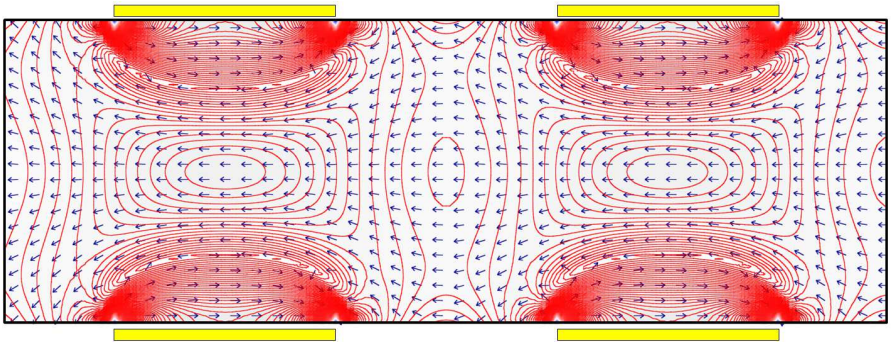

(b)

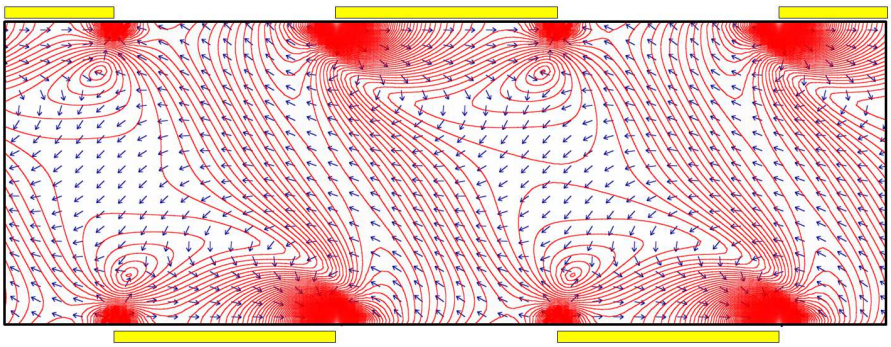

(c)

Figure 3.10: Comparison of TWDEP velocity contour and arrow plots for following cases; (a) channel with electrodes at the bottom surface; (b) channel with electrodes at both top and bottom surfaces with the same position as in the previous case; (c) channel with electrodes at both top and bottom surfaces placed in alternate distances

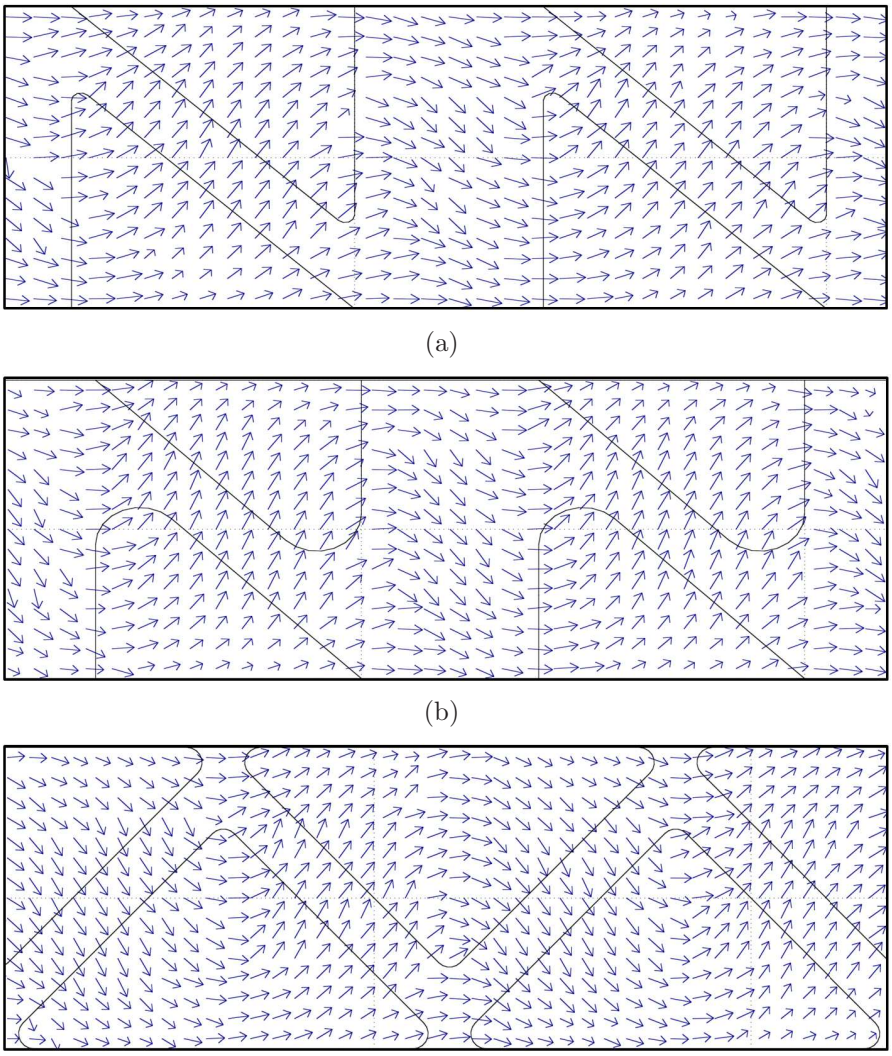

(a)

(b)

(c)

Figure 3.11: Plot showing the TWDEP velocity vector arrows at the mid of the channel, which has microelectrodes of (a) right angled triangular electrode with small curve at one corner,(b)right angled triangular electrode with large curve at one corner (c) triangular electrode with curves at all corners. The top view of the microchannel is shown here.

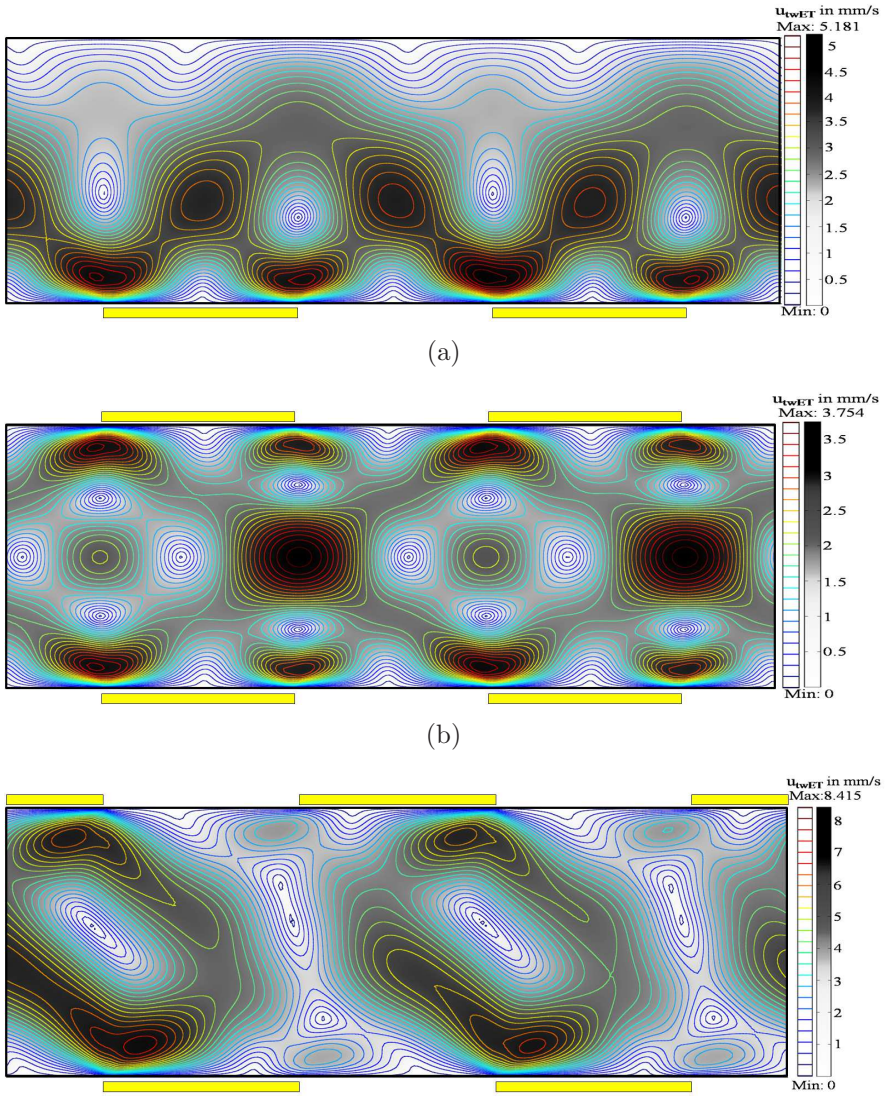

Figure 3.12: Comparison of fluid velocity scalar plot with contours under TWET force for following cases; (a) channel with electrodes at the bottom surface; (b) channel with electrodes at both top and bottom surfaces with the same position as in the previous case; (c) channel with electrodes at both top and bottom surfaces placed in alternate distances

is similar to the case of SWET force. Here in TWET, just the magnitude of the velocity has been reduced compared to the ET forces.

3.4.6 Comparison of particle velocity and particle vorticity

The variation of normalized total particle velocity due to combined effect of DEP and ET with respect to the change in channel height is shown in Fig. 3.14 for three different cases studied in this work. It is clearly seen in the Fig. 3.14 that DEP force is dominant at the electrode edges (at $x^* = 7.5$ and $x^* = 10.5$) whereas ET is dominant in other cases (at $x^* = 6$ and $x^* = 9$). A single peak in normalized particle velocity is observed in the case of channel with electrodes at the bottom surface whereas double peaks are found for channel with electrodes at both top and bottom surfaces. The particle velocity profiles are similar to those reported by He and Liu [48]. He and Liu observed that, the combined DEP and ET effect enhanced the particle-fluid flow. The change in velocity magnitudes along the channel height as well as along the length of channel, makes the particles move in vortex motion. Particles are trapped or concentrated at the points where velocity is zero, i.e. stagnation points. Variation of normalized total particle vorticity due to the combined effect of DEP and ET with respect to the change in channel height is shown in Fig. 3.15 for three different cases studied in this work. The peaks shown in the variation profiles of vorticity provide the information of closed streamlines which make the particles to concentrate at one location as well as to mix different types of particles in the same location.

Summarizing, the DEP forces can be used to collect the particles at different locations. Under Positive DEP effect, the particles are collected at electrode edges, irrespective of the position, size or number of electrodes. Under negative DEP effect, the particles are collected at the lower electric field strength regions. The location of the concentration regions can be shifted by changing the electrode position in the channel. Hence, DEP forces can be successfully used to create microconcentrators in a microfluidic chip. ET and TWET forces are used for mixing and producing concentration regions by circulating the fluid at a given location. The effect of forces can be changed with the applied voltage. The TWDEP method is the better method for mixing along the length of the channels among the four options explored in the present work. If two layers of particle

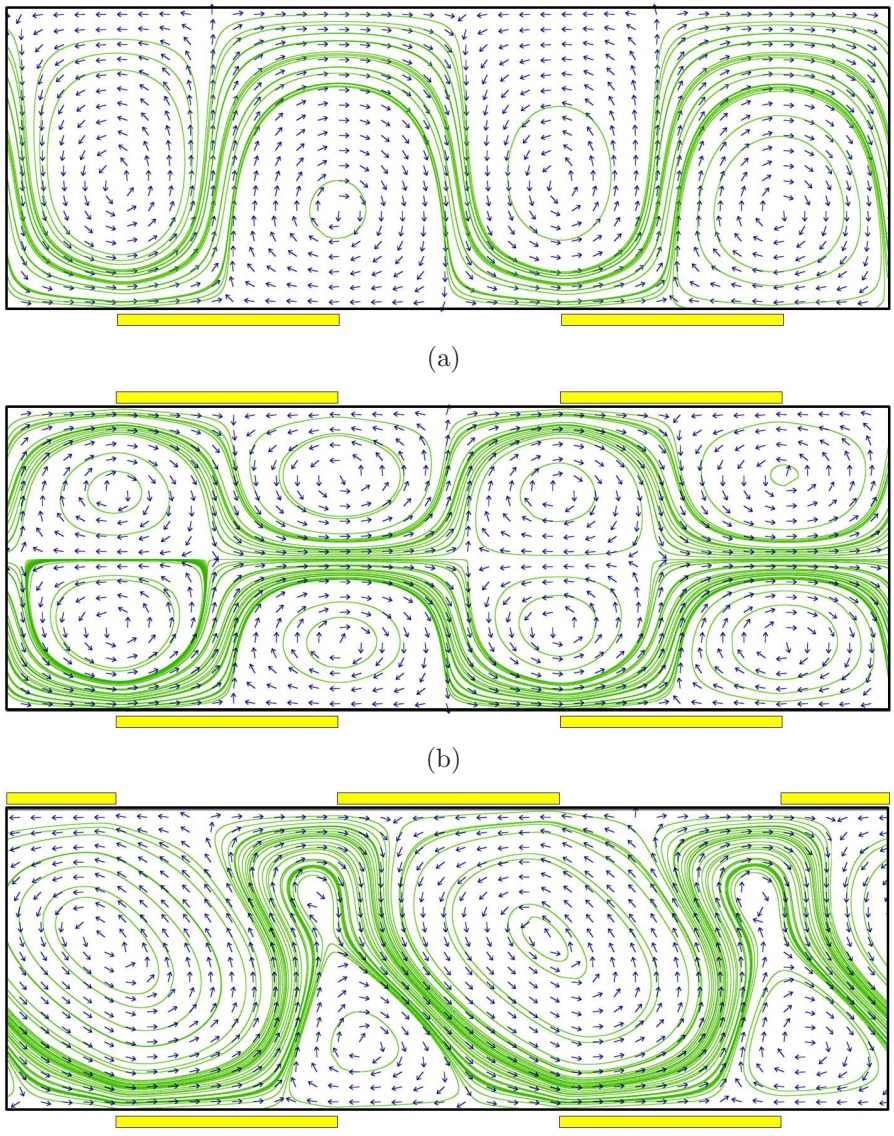

Figure 3.13: Comparison of fluid velocity streamline and arrow plots under TWET force for following cases; (a) channel with electrodes at the bottom surface; (b) channel with electrodes at both top and bottom surfaces with the same position as in the previous case; (c) channel with electrodes at both top and bottom surfaces placed in alternate distances

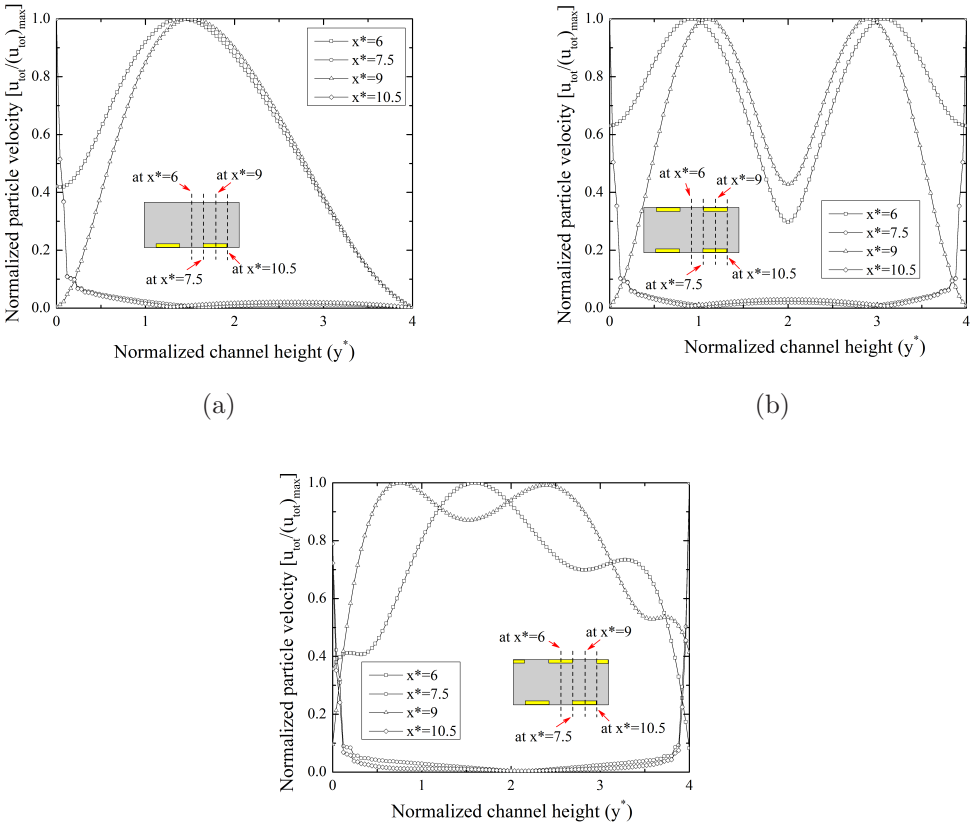

Figure 3.14: Comparison of normalized particle velocity $(u_{tot}/(u_{tot})_{max}$, Here u_{tot} is particle velocity due to combined effect of ET and DEP); (a) channel with electrodes at the bottom surface; (b) channel with electrodes at both top and bottom surfaces with the same position as in the previous case; (c) channel with electrodes at both top and bottom surfaces placed in alternate distances.

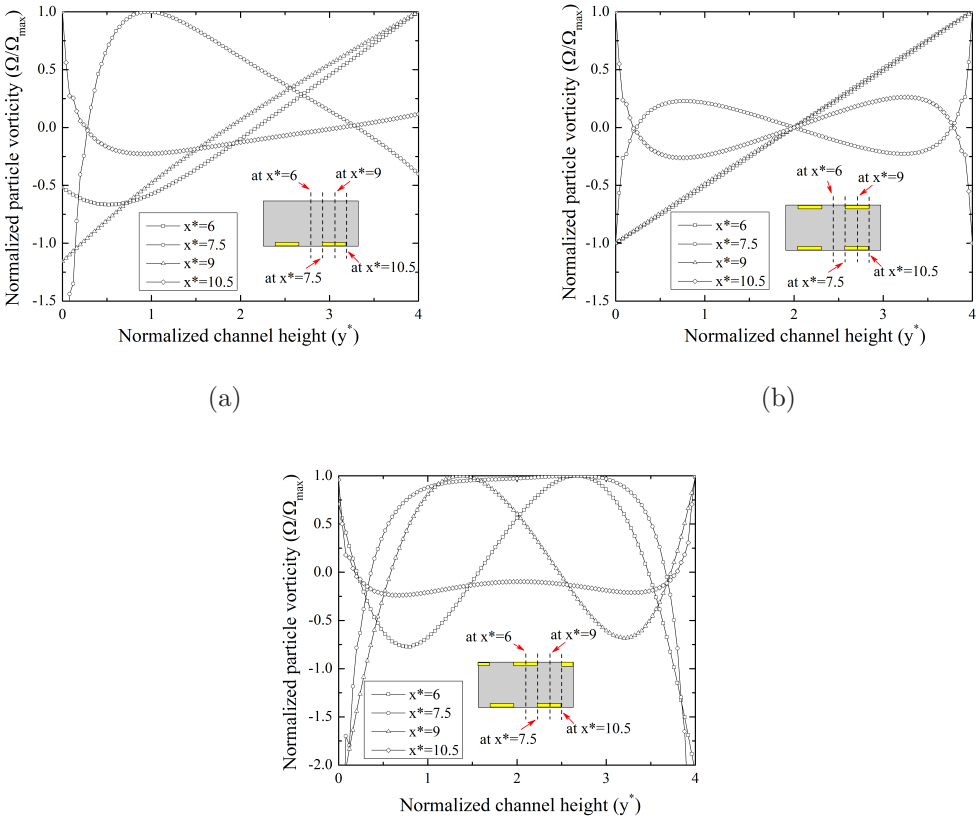

Figure 3.15: Comparison of normalized particle vorticity (Ω/Ω_{max}, Here Ω is particle vorticity due to combined effect of ET and DEP) (a) channel with electrodes at the bottom surface; (b) channel with electrodes at both top and bottom surfaces with the same position as in the previous case; (c) channel with electrodes at both top and bottom surfaces placed in alternate distances.

suspension are placed side by side in the channel, triangular electrode configuration can be used to mix the suspensions. If two layers are placed one on the top of the other, the rectangular electrode configuration with electrodes at the top and bottom will be efficient to mix the two layers of suspensions.

3.5 Summary

A mathematical model is developed based on Laplace, heat conduction, Stokes, and convection-diffusion-migration equations to calculate electric field, temperature, velocity, and concentration distributions, respectively. The effects of SWDEP, TWDEP, SWET and TWET on the performance of micromixers and microconcentrators are studied numerically. Analytical and numerical solutions of DEP and ET forces along the length of the channel and height of the channel are compared. The effects of electrode size and placement on micromixing and microconcentrating performance are studied and the velocity and concentration distributions have been compared. The results indicate that SWDEP forces can be used to collect the particles at different locations. SWET and TWET forces can be used to manipulate the fluid along with the particles. Based on position and size of the electrodes, the size and location of the concentration regions changes by both DEP and ET forces. The movement of particles from the lower half of the channel to the upper half of the channel is observed using TWDEP forces.

Bibliography

[1] H. C. Chang and L. Yeo. *Electrokinetically-driven microfluidics and nanofluidics*. Cambridge University Press, 2008.

[2] L. Yang. A review of multifunctions of dielectrophoresis in biosensors and biochips for bacteria detection. *Analytical Letters*, 45(2-3):187–201, 2012.

[3] U. Lei and Y. J. Lo. Review of the theory of generalised dielectrophoresis. *IET Nanobiotechnology*, 5(3):86–106, 2011.

[4] R. Pethig. Publisher's note: "review article-dielectrophoresis: Status of the theory, technology, and applications" [biomicrofluidics 4, 022811 2010]. *Biomicrofluidics*, 4(3):039901, 2010.

[5] M. Borgatti, N. Bianchi, I. Mancini, G. Feriotto, and R. Gambari. New trends in non-invasive prenatal diagnosis: Applications of dielectrophoresis-based lab-on-a-chip platforms to the identification and manipulation of rare cells (review). *International Journal of Molecular Medicine*, 21(1):3–12, 2008.

[6] A. Castellanos, A. Ramos, A. Gonzalez, N. Green, and H. Morgan. Electrohydrodynamics and dielectrophoresis in microsystems: scaling laws. *Journal of Physics D: Applied Physics*, 36:2584, 2003.

[7] I.-F. Cheng, C.-C. Lin, D.-Y. Lin, and H.-C. Chang. A dielectrophoretic chip with a roughened metal surface for on-chip surface-enhanced raman scattering analysis of bacteria. *Biomicrofluidics*, 4(3):034104, 2010.

[8] J.-R. Du and H.-H. Wei. Focusing and trapping of dna molecules by head-on AC electrokinetic streaming through join asymmetric polarization. *Biomicrofluidics*, 4(3):034108, 2010.

[9] E. Melvin, B. Moore, K. Gilchrist, S. Grego, and O. Velev. On-chip collection of particles and cells by AC electroosmotic pumping and dielectrophoresis using asymmetric microelectrodes. *Biomicrofluidics*, 5(3):034113, 2011.

[10] A. Ramos, H. Morgan, N. Green, and A. Castellanos. AC electrokinetics: A review of forces in microelectrode structures. *Journal of Physics D: Applied Physics*, 31(18):2338–2353, 1998.

[11] A. Ramos, H. Morgan, N. Green, and A. Castellanos. AC electric-field-induced fluid flow in microelectrodes. *Journal of Colloid and Interface Science*, 217(2):420–422, 1999.

[12] A. Castellanos, A. Gonzlez, A. Ramos, N. Green, and H. Morgan. Electrohydrodynamics in microelectrode structures. *Institute of Physics Conference Series*, 178:175–180, 2004.

[13] M. Sigurdson, C. D. Meinhart, D. Wang, X. Liu, J. J. Feng, S. Krishnamoorthy, and V. B. Makhijani. Transport enhancement in tunable laser cavity sensor. *American Society of Mechanical Engineers, Micro-Electromechanical Systems Division Publication (MEMS)*, pages 599–601, 2002.

[14] M. Sigurdson, C. Meinhart, D. Wang, X. Liu, J. Feng, S. Krishnamoorthy, and S. Sundaram. AC electrokinetics for microfluidic immunosensors. *American Society of Mechanical Engineers, Micro-Electromechanical Systems Division Publication (MEMS)*, 5:479–483, 2003.

[15] M. Sigurdson, C. D. Meinhart, and D. Wang. AC electrokinetics for biosensors. *American Society of Mechanical Engineers, Fluids Engineering Division (Publication) FED*, 260:101–105, 2004.

[16] M. Sigurdson, and D Wang, and C. D. Meinhart. Electrothermal stirring for heterogeneous immunoassays. *Lab on a Chip - Miniaturisation for Chemistry and Biology*, 5(12):1366–1373, 2005.

[17] D. Wang, M. Sigurdson, and C. D. Meinhart. Experimental analysis of particle and fluid motion in AC electrokinetics. *Experiments in Fluids*, 38(1):1–10, 2005.

[18] H. Feldman, M. Sigurdson, and C. D. Meinhart. AC electrothermal enhancement of heterogeneous assays in microfluidics. *Lab on a Chip - Miniaturisation for Chemistry and Biology*, 7(11):1553–1559, 2007.

[19] M. Sigurdson, H. Feldman, and C. Meinhart. AC electrokinetics for assay enhancement. *ASME International Mechanical Engineering Congress and Exposition, Proceedings*, 11 PART B:889–891, 2008.

[20] W. Yang Ng, A. Ramos, Y. Cheong Lam, and I. Rodriguez. Numerical study of dc-biased AC-electrokinetic flow over symmetrical electrodes. *Biomicrofluidics*, 6(1):012817, 2012.

[21] N. T. Nguyen and S. T. Werely. *Fundamentals and Applications of Microfluidics*. Artech House, Boston, 2006.

[22] N. T. Nguyen and Z. Wu. Micromixers - a review. *J Micromech Microeng*, 15:R1–R16, 2005.

[23] J. M. Ottino. *The Kinematics of Mixing: Stretching, Chaos, and Transport*. Cambridge University Press, Cambridge, New York, 1989.

[24] J. Deval, P. Tabeling, and C. M. Ho. A dielectrophoretic chaotic mixer. *Technical Digest of the 15th IEEE International Conference on MEMS (MEMS 2002)*, 1:36–39, 2002.

[25] Y. K. Lee, J. Deval, P. Tabeling, and C. M. Ho. Chaotic mixing in electrokinetically and pressure driven micro flows. *IEEE 14th International Conference on Micro Electro Mechanical System (MEMS 2001)*, 1:483–486, 2001.

[26] N. S. K. Gunda, S. K. Mitra, and S. Bhattacharjee. Dielectrophoretic mixing with novel electrode geometry. *Proceedings of the ASME 2009 Fluids Engineering Division Summer Meeting*, pages 463–468, 2009.

[27] N. Green, A. Ramos, A. Gonzlez, A. Castellanos, and H. Morgan. Electrothermally induced fluid flow on microelectrodes. *Journal of Electrostatics*, 53(2):71–87, 2001.

[28] A. Castellanos, A. Ramos, A. Gonzlez, H. Morgan, and N. Green. AC electric-field-induced fluid flow in microelectrode structures: Scaling laws. *IEEE International Conference on Conduction and Breakdown in Dielectric Liquids, ICDL*, pages 52–55, 2002.

[29] N. Green, A. Ramos, A. Gonzalez, H. Morgan, and A. Castellanos. Fluid flow induced by nonuniform AC electric fields in electrolytes on microelectrodes. III. observation of streamlines and numerical simulation. *Physical Review E*

- *Statistical, Nonlinear, and Soft Matter Physics*, 66(2):026305/1–026305/11, 2002.

[30] A. Ramos, A. Gonzalez, A. Castellanos, N. Green, and H. Morgan. Pumping of liquids with AC voltages applied to asymmetric pairs of microelectrodes. *Physical Review E - Statistical, Nonlinear, and Soft Matter Physics*, 67(5 2):056302/1–056302/11, 2003.

[31] A. Gonzlez, A. Ramos, A. Castellanos, H. Morgan, and N. Green. Electrothermal liquid motion in microsystems subjected to alternating and rotating electric fields. *American Society of Mechanical Engineers, Materials Division (Publication) MD*, 98:257–262, 2003.

[32] A. Ramos, A. Gonzlez, A. Castellanos, N. Green, and H. Morgan. Pumping of electrolytes using arrays of asymmetric pairs of microelectrodes subjected to AC voltages. *Institute of Physics Conference Series*, 178:187–192, 2004.

[33] J. J. Feng, S. Krishnamoorthy, and S. Sundaram. Numerical and analytical studies of electrothermally induced flow and its application for mixing and cleaning in microfluidic systems. *2004 NSTI Nanotechnology Conference and Trade Show - NSTI Nanotech 2004*, 2:450–453, 2004.

[34] J. Feng, S. Krishnamoorthy, and S. Sundaram. Numerical analysis of mixing by electrothermal induced flow in microfluidic systems. *Biomicrofluidics*, 1(2):024102, 2007.

[35] I. R. Perch-Nielsen, N. G. Green, and A. Wolff. Numerical simulation of travelling wave induced electrothermal fluid flow. *Journal of Physics D: Applied Physics*, 37(16):2323–2330, 2004.

[36] S. Molla and S. Bhattacharjee. Prevention of colloidal membrane fouling employing dielectrophoretic forces on a parallel electrode array. *Journal of Membrane Science*, 255(1-2):187–199, 2005.

[37] S. Molla, J. Masliyah, and S. Bhattacharjee. Simulations of a dielectrophoretic membrane filtration process for removal of water droplets from water-in-oil emulsions. *Journal of Colloid and Interface Science*, 287(1):338–350, 2005.

[38] S. H. Molla and S. Bhattacharjee. Dielectrophoretic leviation in the presence of shear flow: Implications for colloidal fouling of filtration membranes. *Langmuir*, 23(21):10618–10627, 2007.

[39] A. Castellanos, A. Ramos, A. A Gonzalez, N. G. Green, and H. Morgan. Manipulation of bio-particles in microelectrode structures by means of non-uniform AC electric fields. *American Society of Mechanical Engineers, Materials Division (Publication) MD*, 97:165–170, 2002.

[40] V. Studer, A. Ppin, Y. Chen, and A. Ajdari. An integrated AC electrokinetic pump in a microfluidic loop for fast and tunable flow control. *Analyst*, 129(10):944–949, 2004.

[41] H. A. Pohl. *Dielectrophoresis*. Cambridge University Press, 1978.

[42] T. B. Jones. *Electromechanics of particles*. Cambridge University Press, 1995.

[43] M. P. Hughes. *Nanoelectromechanics in Engineering and Biology*. CRC Press, Boca Raton, 2003.

[44] H. Morgan, A. Izquierdo, D. Bakewell, N. Green, and A. Ramos. The dielectrophoretic and travelling wave forces generated by interdigitated electrode arrays: Analytical solution using fourier series. *Journal of Physics D: Applied Physics*, 34(10):1553–1561, 2001.

[45] J. Masliyah and S. Bhattacharjee. *Electrokinetic and Colloid Transport Phenomena*. Willey Interscience, Hoboken, New Jersey, 2006.

[46] N. Green, A. Ramos, and H. Morgan. Numerical solution of the dielectrophoretic and travelling wave forces for interdigitated electrode arrays using the finite element method. *Journal of Electrostatics*, 56(2):235–254, 2002.

[47] A. Ramos, H. Morgan, N. Green, and A. Castellanos. AC electrokinetics: A review of forces in microelectrode structures. *Journal of Physics D: Applied Physics*, 31(18):2338–2353, 1998.

[48] G. He and D. Liu. Coupled electrohydrodynamic-dielectrophoretic pumping of colloidal suspensions in a microchannel. *ASME 2011 9th International Con-*

ference on Nanochannels, Microchannels, and Minichannels, ICNMM 2011, 1:219–227, 2011.

Chapter 4

Experimental Investigation of Dielectrophoretic Behavior of Myoglobin and Silica Particles [1]

4.1 Overview

The previous chapters focused on the theoretical understanding of the manipulation of myoglobin molecules under DEP and development of on-chip micromixers and microconcentrators. The present study investigates the behavior of myoglobin molecules on a microelectrode surface under the influence of dielectrophoresis. Microelectrodes are fabricated in transparent borofloat glass wafers with a sequence of microfabrication steps like piranha cleaning, metal deposition, optical lithography and etching. A detailed description of experimental setup to conduct DEP experiments on myoglobin is presented with a brief overview of myoglobin preparation. Silica particles are used to mimic the myoglobin molecules. It is observed that nanometer electrodes and 10 - 100V applied voltage are required to manipulate the myoglobin under DEP. Fabrication of nanoelectrodes can be achieved by electron beam lithography and function generators can be used to apply the required voltage. However, such high electric field strengths may peel of the electrode from the surface of the microchannel. In addition, the electric field strengths are higher than breakdown voltage of glass. Further, such high electric field strengths may denature the protein molecules. Hence, the present work uses large size electrodes

[1] A version of this chapter has been published. N. S. K. Gunda and S. K. Mitra, Paper # FEDSM-ICNMM2010-30306, Proceedings of ASME 2010 3rd Joint US-European Fluids Engineering Summer Meeting and 8th International Conference on Nanochannels, Microchannels, and Minichannels, FEDSM2010-ICNMM2010, Montreal, Canada, August 2-4, 2010.

to resolve this issue.

4.2 Introduction

The application of dielectrophoresis (DEP) in micro or nano-scale have increased in the last few decades due to improved nanofabrication facilities [1]. DEP is a phenomena in which the dielectric particles can be manipulated under nonuniform electric fields because of polarization effects. With the availability of dielectric properties of most biological molecules, the importance of DEP technique has increased in biomedical applications. DEP technique has been used to manipulate bioparticles such as cells, bacteria, viruses, DNA, and proteins [1–14]. The ability of DEP to manipulate such bioparticles is utilized for separating, trapping, concentrating, mixing, and sorting selective bioparticles [1–4, 15]. The effect of DEP on nano-sized particles is small because the DEP force is directly proportional to the cube root of a particle radius and also due to significant Brownian motion of nanoparticles. Due to these limitations, the use of DEP technique at nano-scale is limited. Very few researchers have worked on nanoparticle manipulation and the work on protein manipulation using this DEP technique is also not so much. In the present study, the dielectrophoretic behavior of nano-sized biomolecules such as myoglobin molecules, has been investigated experimentally. Myoglobin is a single chain globular protein of 153 amino acids containing heme (iron containing porphyrin) prosthetic group in the center, around which remaining apoprotein folds are present [16–21]. It has a molecular weight of 16.7 kDa and an approximated size of 1.53 nm radius [16–21]. Myoglobin is one of the important cardiac markers to identify the early detection of acute myocardial infarction [22, 23]. The findings of this work will be useful for separating the myoglobin from blood and detecting it, which will be helpful in predicting the heart attacks.

The initial experimentation on protein manipulation under DEP effects was conducted by Washizu et al.[7]. An array of 1 μm width corrugated microelectrodes with a minimum gap of 4, 15, and 55 μm between the electrodes was used for creating nonuniform electric fields. The trapping of avidin (68 kDa), concanavalin (52 kDa), chymotrypsinogen (25 kDa), and ribonuclease A (13.7 kDa) proteins at the edges of the electrodes under positive DEP was showed. They measured pro-

tein concentration using a fluorescence detection unit and plotted a graph showing fluorescence intensity vs time, indicating a relation between the molecular weight and fluorescent intensity of proteins. Their work showed only the positive DEP of proteins. Bakewell et al.[8] and Hughes et al.[9] demonstrated both positive and negative DEP effects on proteins. Manipulation of avidin protein molecules on 2 μm center gap polynomial electrode surface was observed. Later, Zheng et al.[10, 11] showed the manipulation of bovine serum albumin (BSA) protein under positive DEP effects. They trapped BSA proteins at the edges of the quadrupole gold microelectrodes which were fabricated with a center gap of 5, 10, 20, and 50 μm. Mathematical calculation of the Clausius-Mossotti factor for BSA protein was also presented. They modeled BSA protein as sphere of 5 nm diameters and the crossover frequency of 100 MHz was calculated for the protein solution of conductivity 1 mS/m. Clarke et al.[12] reported the dielectrophoretic concentration of proteins with nanopipette technique. Fluorescent labeled protein G and IgG concentration was observed with fluorescence detection. They used borosilicate pipettes of a 3.6^o half-cone angle and an inner diameter of 100-150 nm with an electrode both inside and outside of the pipette. They demonstrated both types of DEP effects with protein G at $1V$ and $0.1Hz$.

Recently, Gunda and Mitra [13, 14] presented the theoretical investigation of dielectrophoretic behavior of myoglobin in a microchannel housing rectangular microelectrodes at the bottom surface. They approximated the shape of the myoglobin as sphere, oblate and prolate spheroids. Their results shows that the effect of the shape of myoglobin on the DEP is not significant. They also calculated the efficient DEP force for manipulating myoglobin under given conditions. In addition, Gunda and Mitra [24] showed the different fabrication procedures for making a dielectrophoretic microfluidic device. They presented the different equipment required for conducting DEP experiments. They also provided results of positive DEP on polystyrene microparticles. Dalton et al.[25] provided the complete experimental setup with details of microfluidic chip platform required for DEP experiments. They eliminated the requirement of multiple layer fabrication for their platform. Their system also provided easy chip changes.

4.3 Materials and methods

The intended device is fabricated with two glass substrates with a network of microchannels, fluidic and electrical ports in top substrate and different set of microelctrodes in bottom substrates. Initially, the layout of microelectrode configuration (rectangular array of electrodes) and microchannel are designed with the L-Edit MEMS Design software (MemsPRO v6, Tanner Research, Inc., CA) and then exported to Laser Pattern Generator (Heidelberg DWL-200, Heidelberg Instruments, Germany) for fabricating the chrome mask.

4.3.1 Fabrication of microelectrodes

Fabrication of microelectrodes on glass substrate is described in this section. Piranha (H_2SO_4:H_2O_2 of 4:1 by volume)cleaned borofloat glass wafer (Paragon Optical Company, Inc., PA) of 4 in $\times$ 4 in and 1.1 mm thick is taken and a layer of 40 nm chromium and 200 nm gold sequentially deposited using planar magnetron sputtering system. The gold coated glass wafer is then spin-coated with a layer of $1-2$ μm positive photoresist(PPR)(HPR 504, Fujifilm Electronic Materials, Inc., Arizona) using Solitec resist spinner (Model 5110-CD, Solitec Wafer Processing, Inc., CA). Then, the PPR coated wafer is soft-baked at 110 ^oC for 90 s on a Solitec vacuum hot plate (Solitec Wafer Processing, Inc., CA). Using mask aligner, the spin-coated wafer is exposed to UV illumination (350-400 nm) through chrome mask for $2-3$ s to transfer the electrode structures on PPR. The wafer is then developed using PPR developer (HPRD 429, Fujifilm Electronic Materials, Inc., Arizona) for $20-30$ s. Later, gold and chromium are etched using gold etchant ($KI + I_2 + H_2O$) and chromium etchant ($K_3[Fe(CN)_6] + NaOH + H_2O$), respectively. Acetone is used to strip off the PPR. Finally, the wafer is cleaned in isopropyl alcohol and dried with nitrogen spray. The schematic of process flow for fabrication of microelectrodes is depicted in Fig. 4.1.

4.3.2 Fabrication of microchannels

In this section, fabrication of microchannels is described. The process of piranha cleaning and deposition of chromium and gold is similar to above mentioned procedure. Photolithography is carried out using mask containing microchannel struc-

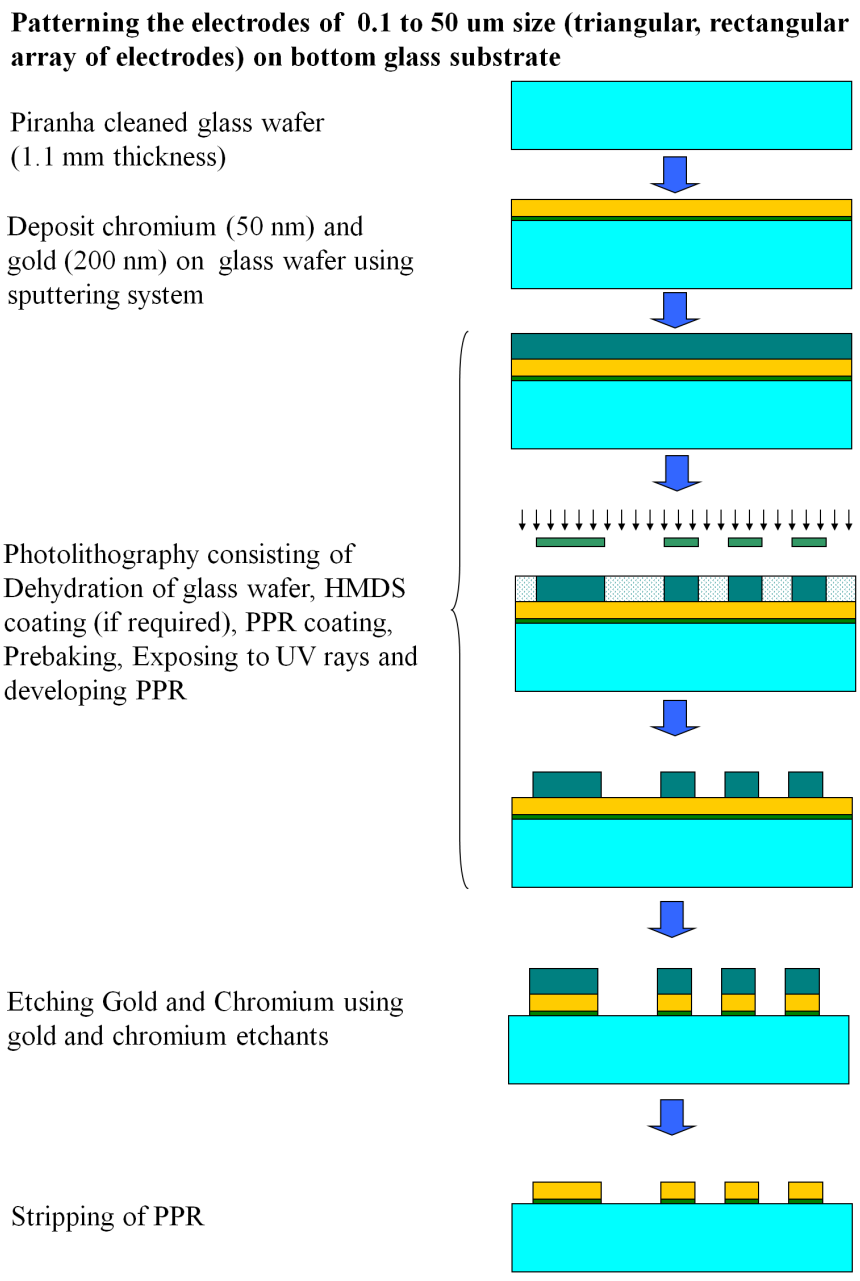

Figure 4.1: Process flow for fabrication of microelectrodes

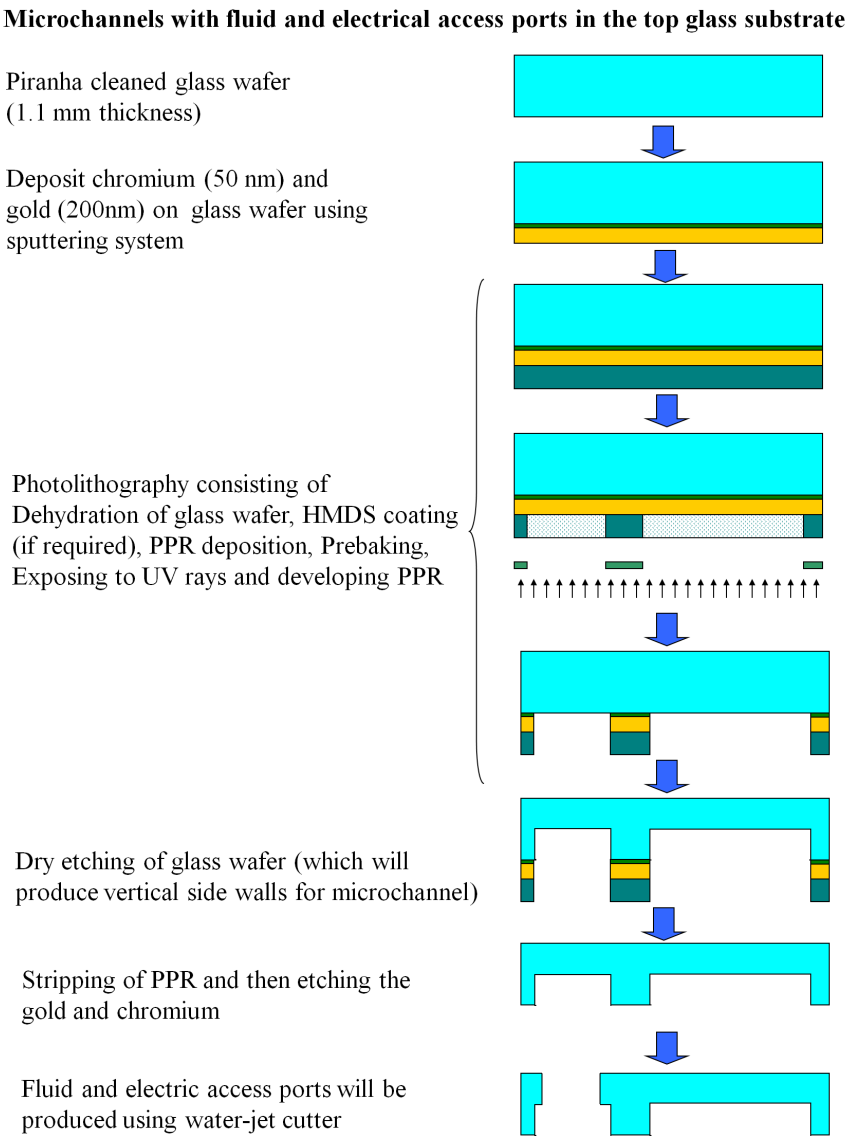

Figure 4.2: Process flow for fabrication of microchannels

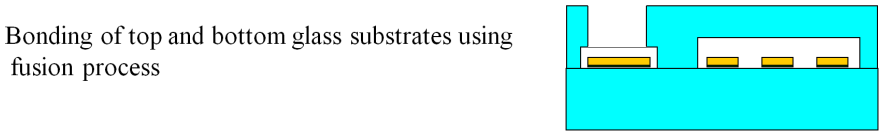

Figure 4.3: Schematic of bonded dielectrophoretic microfluidic chip

tures. The metal etching procedure is the one explained above. Channels are then etched in the borofloat substrate using wet or dry etching methods. Fluidic and electrical ports are drilled using water jet cutting machine (OMAX Corporation, Kent, WA, USA). The schematic of process flow for fabrication of microchannels is depicted in Fig. 4.2.

4.3.3 Bonding of two substrates

The above fabricated substrates are bonded using fusion process to form a closed channel. The schematic of bonded dielectrophoretic microfluidic chip is shown in Fig. 4.3. Several layouts of chips on glass wafer are diced using a diamond touch dicing saw.

4.3.4 Test equipment

Testing of the fabricated device under the influence of DEP phenomena requires AC voltage source generating four phases, high frequency and high voltage sinusoidal signal. Instruments like arbitrary waveform generator and voltage amplifier are used to generate the required AC signals and oscilloscope to check the generated signal for verification. A syringe pump is used to inject the sample into the device. A fully automated bright field and /or fluorescence inverted microscope with high speed monochrome camera is used to observe and capture the process of mixing and separation. The images captured at the detection site of the device are used to quantify the concentration of myoglobin from image processing analysis. The experimental testing set-up discussed above is presented in Fig. 4.4. The specification and other details of fluidic and electrical connections used in this work can be found in Gunda et al [C5].

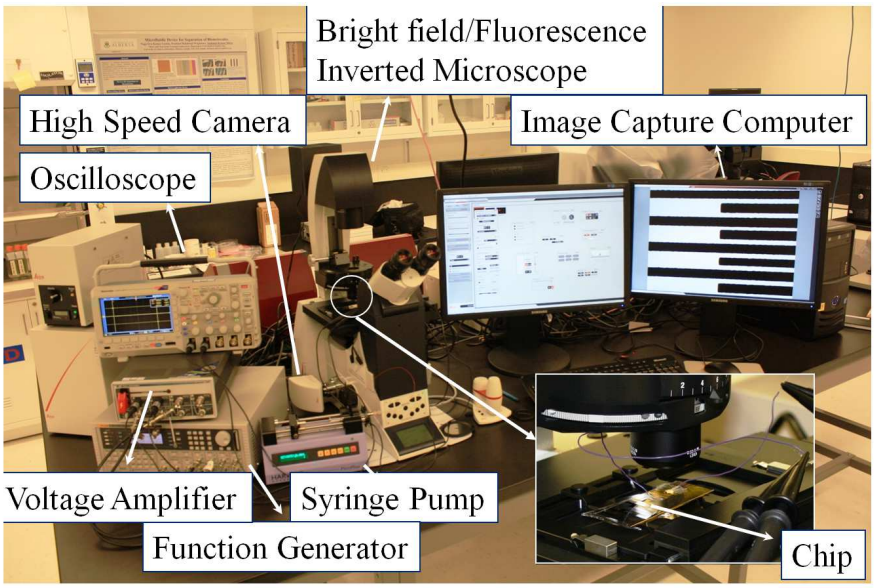

Figure 4.4: Testing set-up for DEP experiments

4.3.5 Sample preparation

The lyophilized form of myoglobin (Myoglobin 8M50, Hytest Ltd, Finland) sample is dialyzed against DI water (resistivity $> 1\ M\Omega cm$) to transform the globular structure of myoglobin molecules to monomeric structure. The sample is diluted by adding deionized water to get required concentration. Figure. 4.5 shows the comparison of myoglobin molecules before and after dialysis. Proper dialysis of myoglobin molecules is required to break the myoglobin into individual molecules. A drop of aqueous solution of myoglobin is poured on the microelectrode surface. The chip is cleaned using ethanol solution before placing the drop of myoglobin solution. Some of these experiments are also conducted on silica particles (Polysciences, Inc., Warrington, PA) and polystyrene particles (Bangs Laboratories, Inc., Fishers, In USA) to mimic the myoglobin molecules.

4.4 Results and discussions

In this section, the results of DEP effects on silica particles and myoglobin are presented. Silica particles of 5 μ diameter are used for the preliminary experiments. Both types of DEP effects are observed for the silica particles. Only positive DEP effect is observed for the myoglobin molecules. Figure 4.6 shows the positive DEP effect of silica particles under $5-10\ V$ applied voltage and for the frequency range

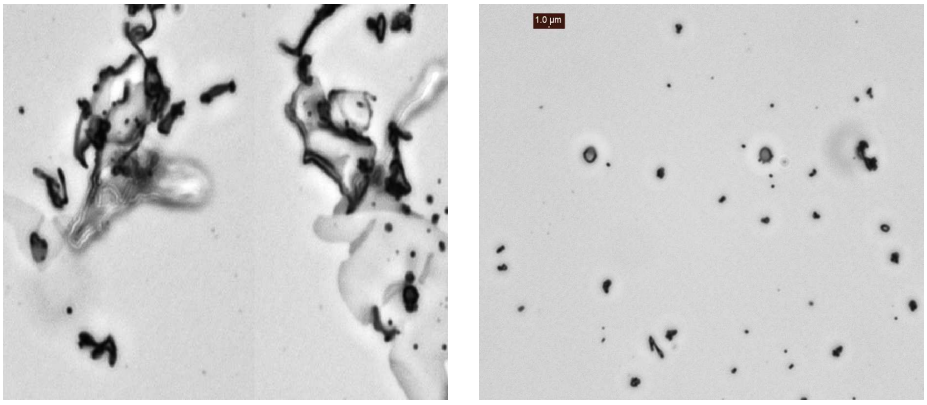

(a) (b)

Figure 4.5: Lyophilized form of myoglobin; (a) Before dialysis (b) After dialysis

of 0 to 1 KHz. It is clearly observed that the particles are trapped at the electrode edges. The image is acquired from the inverted microscope where the light source is placed at the top and a capturing camera is placed at the bottom of the chip. Figure 4.7 shows the negative DEP effect of silica particles under 10 V applied voltage for the frequency range of 10 KHz to 40 KHz. Under negative effects, the particles move from edges of the electrodes to the middle of the electrodes, to the mid-point of the gap between the electrodes. The spreading of the particles on the electrode surface is also observed when the frequency is shifted from 40 KHz to 60 KHz. Figure 4.8 shows the positive DEP effects on myoglobin. The polymeric structure of myoglobin molecules collecting at the electrode edges is observed under the conditions of 5 kHz frequency and 5 V. In Fig. 4.8, a few silica particles are also observed, which are not move to edge of the electrode. The movement of small monomeric structure of myoglobin is not observed under these conditions. Also the repulsion of myoglobin is not observed for the range of 0 to 10 MHz. The results indicate the requirement of higher frequencies to capture the negative DEP effects on myoglobin.

4.5 Summary

This study investigated the behavior of myoglobin molecules on a microelectrode surface under the influence of DEP. Silica particles are found to exhibit both positive and negative DEP effects. Positive DEP is observed at 0 to 1 KHz frequency range and $5-10$ V applied voltage, and negative DEP is observed at 10

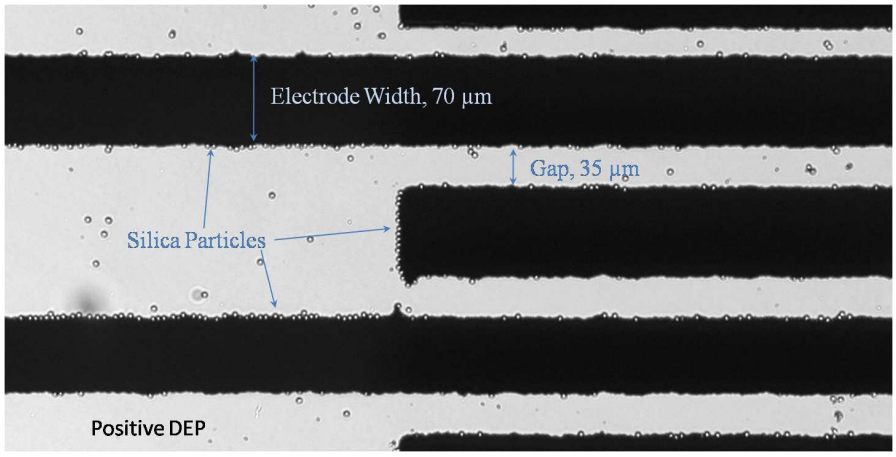

Figure 4.6: Positive DEP effect on silica particles

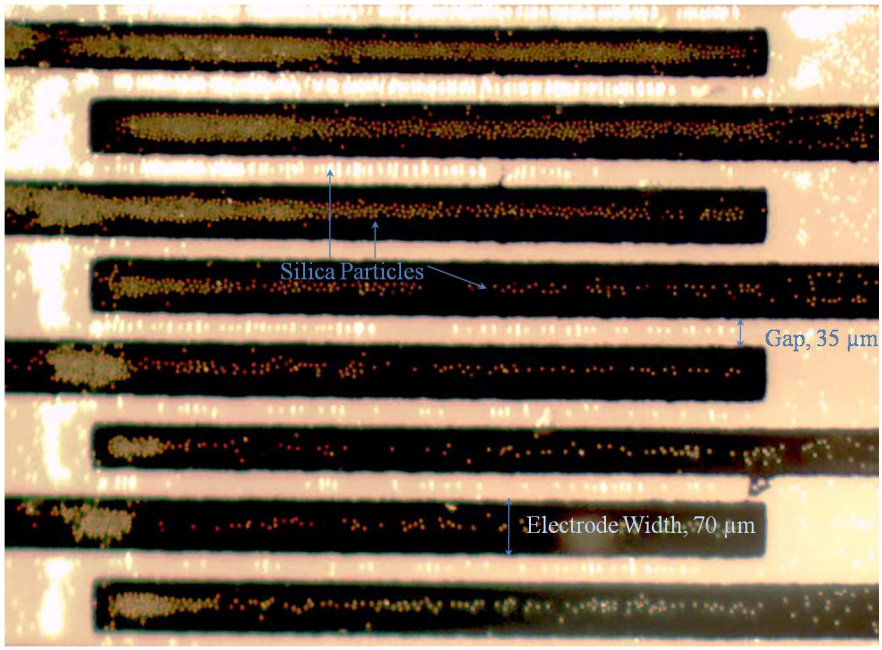

Figure 4.7: Negative DEP effect on silica particles

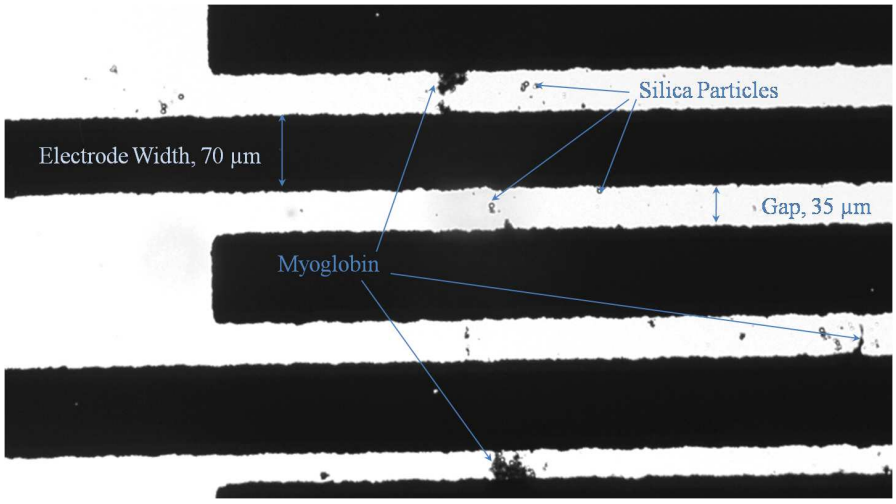

Figure 4.8: Positive DEP effect on myoglobin molecules

KHz to 40 KHz frequency range and 10 V applied voltage. Myoglobin responds to positive DEP effects at 5 kHz frequency and 5 V.

Polystyrene particles are also exhibited both types of positive DEP effects which are not shown in this report. In addition to positive and negative DEP effects on silica and polystyrene particles, motion of particles along the length of the channels due to traveling wave DEP is observed. Electrothermal fluid flow due to nonuniform electric fields along the edges of the electrodes is also observed. Separation of polystyrene particles from silica particles is carried out in one set of experiments. A new type of circular motion of silica particles in the plane of cross-section of channel is observed while polystyrene particles are moving along the length of the channels. Further work will be investigating the both types of DEP effects on monomeric structure of myoglobin.

Bibliography

[1] X. B. Wang, Y. Huang, J. P. H. Burt, G. H. Markx, and R. Pethig. Selective dielectrophoretic confinement of bioparticles in potential energy wells. *Journal of Physics D: Applied Physics*, 26:1278–1285, 1993.

[2] H. A. Pohl. *Dielectrophoresis*. Cambridge University Press, 1978.

[3] T. B. Jones. *Electromechanics of particles*. Cambridge University Press, 1995.

[4] M. P. Hughes. *Nanoelectromechanics in Engineering and Biology*. CRC Press, Boca Raton, 2003.

[5] J. Lin and J. Yeow. Enhancing dielectrophoresis effect through novel electrode geometry. *Biomedical Microdevices*, 9(6):823–831, 2007.

[6] N. T. Nguyen and S. T. Werely. *Fundamentals and Applications of Microfluidics*. Artech House, Boston, 2006.

[7] M. Washizu, S. Suzuki, O. Kurosawa, T. Nishizaka, and T. Shinohara. Molecular dielectrophoresis of biopolymers. *IEEE Transactions on Industry Applications*, 30(4):835–843, 1994.

[8] D. Bakewell, M. Hughes, J. Milner, and H. Morgan. Dielectrophoretic manipulation of avidin and DNA. *Proceedings of the 20th Annual International Conference of the IEEE Engineering in Medicine and Biology Society*, 20(2):1079–1082, 1998.

[9] M. Hughes and H. Morgan. Dielectrophoretic characterization and separation of antibody-coated submicrometer latex spheres. *Analytical Chemistry*, 71(16):3441–3445, 1999.

[10] L. Zheng, J. Brody, and P. Burke. Electronic manipulation of DNA, proteins, and nanoparticles for potential circuit assembly. *Biosensors and Bioelectronics*, 20(3):606–619, 2004.

[11] L. Zheng, P. Burke, and J. Brody. Electronic manipulation of DNA and proteins for potential nano-bio circuit assembly. *Proceedings of SPIE - The International Society for Optical Engineering*, 5331:126–135, 2004.

[12] R. Clarke, S. White, D. Zhou, L. Ying, and D. Klenerman. Trapping of proteins under physiological conditions in a nanopipette. *Angewandte Chemie - International Edition*, 44(24):3747–3750, 2005.

[13] N. S. K. Gunda and S. K. Mitra. Modeling of dielectrophoretic transport of myoglobin molecules in microchannels. *Biomicrofluidics*, 4(1):14105, 2010.

[14] N. S. K. Gunda and S. K. Mitra. Modeling of dielectrophoresis for myoglobin molecules in a microchannel with parallel electrodes. In *ASME International Mechanical Engineering Congress and Exposition, Proceedings*, volume 12, pages 605–611, 2010.

[15] N. S. K. Gunda, S. K. Mitra, and S. Bhattacharjee. Dielectrophoretic mixing with novel electrode geometry. *Proceedings of the ASME 2009 Fluids Engineering Division Summer Meeting*, pages 463–468, 2009.

[16] B. M. Mayr, O. Kohlbacher, K. Reinert, M. Sturm, C. Gropl, E. Lange, C. Klein, and C. G. Huber. Absolute myoglobin quantification in serum by combining two-dimensional liquid chromatography - electrospray ionization mass spectrometry and novel data analysis algorithms. *Journal of Proteome Research*, 5:414–421, 2006.

[17] J. Evan. Novel data analysis technique aids heart attack diagnosis. See also URL Lab Informatics, separationsNOW.com, February 2006.

[18] E. Grant, G. South, and I. Walker. The dipole moment of myoglobin. *Biochemical Journal*, 122(5):765–767, 1971.

[19] G. South and E. Grant. Dielectric dispersion and dipole moment of myoglobin in water. *Proceedings of Royal Society London. Series A*, 328:371–387, 1972.

[20] E. H. Grant, B. G. R. Mitton, and G. P. South. An investigation by dielectric methods of hydration in myoglobin solutions. *Biochemical Journal*, 139:375–380, 1974.

[21] E. H. Grant, V. E. R. M. ad N R V Nightingale, and R. J. Sheppard. Dielectric behavior of water in biological solutions: Studies on myoglobin, human low-

density lipoprotein, and polyvinylpyrrolidone. *Bioelectromagnetics*, 7:151–162, 1986.

[22] J. Wang, Q. Wang, L. Ren, X. Wang, Z. Wan, W. Liu, L. Li, H. Zhao, M. Li, D. Tong, and J. Xu. Carboxylated magnetic microbead-assisted fluoroimmunoassay for early biomarkers of acute myocardial infarction. *Colloids and Surfaces B: Biointerfaces*, 72(1):112–120, 2009.

[23] F. Darain, P. Yager, K. L. Gan, and S. C. Tjin. On-chip detection of myoglobin based on fluorescence. *Biosensors and Bioelectronics*, 24:1744–1750, 2009.

[24] N. S. K. Gunda, S. K. Mitra, and V. Ramgopal Rao. Fabrication of dielectrophoretic microfluidic device. *ASME Conference Proceedings*, pages 113–119, 2009.

[25] K. K. Dalton C. A cost effective, re-configurable electrokinetic microfluidic chip platform. *Sensors and Actuators, B: Chemical*, 123(1):628–635, 2007.

Chapter 5

Biofunctionalization of Silicon Surfaces [1]

5.1 Overview

As discussed earlier, typical Lab-on-a-Chip (LOC) device contains sample preparation chamber (separation), reaction chambers (mixers) and sensing area (detection). The main focus of the present study is to develop simple and rapid LOC device for early prediction of heart attacks. The previous chapters 2, 3, and 4 discussed on separation of myoglobin under DEP and development of on-chip micromixers. This chapter focuses on the sensing area where the separated molecules can be sensed with different detection systems. It is required that the sensing area should be reliable and need to sense low concentration of molecules in the sample. This chapter mainly contributes to the development of highly sensitive immunosensors for LOC device. In the present work, we developed and optimized a technique to produce a thin, stable silane layer on silicon substrate in a controlled environment using (3-aminopropyl) triethoxysilane (APTES) for proper immobilization of antibodies for sensing the target biomolecules such as myoglobin. The effect of APTES concentration and silanization time on the formation of silane layer are studied using spectroscopic ellipsometry and Fourier Transform Infrared Spectroscopy (FTIR). Biomolecules of interest are immobilized on optimized silane layer formed silicon substrates using glutaraldehyde linker. Surface analytical techniques such as ellipsometry, FTIR, contact angle measurement system, and atomic force microscopy are employed to characterize the bio-chemically modified silicon

[1] A version of this chapter has been submitted for publication. N. S. K. Gunda, M. Singh, L. Norman, K. Kaur and S. K. Mitra, Applied Surface Science, Under Review, 2014.

surfaces at each step of the biomolecule immobilization process. It is observed that a uniform, homogenous and highly dense layer of biomolecules are immobilized with optimized silane layer on the silicon substrate. The developed immobilization method is successfully implemented on different silicon substrates (flat and pillar). Also, different types of biomolecules such as anti-human IgG (rabbit monoclonal to human IgG), *Listeria monocytogenes*, myoglobin and dengue capture antibodies were successfully immobilized. Further, standard sandwich immunoassay (antibody-antigen-antibody) is employed on respective capture antibody coated silicon substrates. Fluorescence microscopy is used to detect the respective FITC tagged detection antibodies bound to the surface after immunoassay.

5.2 Introduction

Silicon has largely been used as a substrate material for fabricating a large number of microfluidic [15, 16] based biosensors. When silicon is exposed to air, it spontaneously gets oxidized and forms an amorphous silica layer, leading to the complexity in uniform, homogenous immobilization of biomolecules (proteins, antibodies, etc.) on silicon surfaces [15, 17]. Therefore, an appropriate technique for surface modification of silicon is required prior to which biomolecule immobilization can take place, one of the key steps towards producing better quality on-chip biosensors.

Strategies for attaching biomolecules on a substrate while maintaining its identity, structural conformation, and functionality are an evolving field of research. This can lead to the advances in the development of rapid and highly sensitive biosensors. Various surface modification strategies are available for silicon, among them covalent immobilization has a great potential. Covalent immobilization method using self-assembled layers of organosilane on a silicon surface [4] is a promising technique and it has many advantages compared to others such as physisorption (physical adsorption) and bioaffinity immobilization [5, 6, 15, 16]. Self assembled layers of organosilane are obtained by forming siloxane network after reacting with trace amount of water [7–9], which finds many applications towards biosensor development [4, 10].

Typically, the silanization process (formation of silane layer on silicon sub-

strate) consists of four steps. They are hydrolysis, condensation, hydrogen bond formation and curing [4, 11]. In the first step, hydrolysis of the silicon substrate leads to the formation of the reactive silanol group. In the second step, condensation of these silanol groups takes place leading to the formation of siloxane linkages over the surface. In the third step, hydrogen bonds are formed with -OH groups on the substrate. In the last step, a covalent bond (Si-O-Si) is formed between silicon in the organosilane and the silicon on the substrate with the subsequent loss of water molecules by curing. The silane layer polymerizes in the presence of water to form multilayers of silane [11]. It is better to produce silane layer in non-aqueous solution to avoid multilayers of silane formation. Multilayers of silane are not stable and washed away during commonly used cleaning steps of biomolecule immobilization leading to nonuniform (rough) and inhomogeneous surface. Therefore, it is important to perform curing after the hydrogen bond formation to stop the polymerization of the siloxane layer. Although silanization is a very well-known method of producing a silane layer on silicon surface, it suffers from the demerit that most of the silanization approaches produce a thick and non-uniform silane layer, which negatively impacts the sensitivity of any biosensor [7]. There are various other factors that affect the silanization process such as the concentration of the silane, silanization time, moisture (humidity), and temperature of the solution [12–15].

Growing silane layers on silicon substrate samples can be done with different methods. They are as follows: (a) by dipping the samples in silane solutions, (b) by drop casting the silane solution on samples, (c) by spin coating the silane solution on samples, and (d) by vaporizing the silane solution on samples under vacuum or heating [15, 16]. These methods can be applied at room temperature or at elevated temperatures based on the requirements [15, 16]. Every method has its own advantages and disadvantages. Among them, dipping the samples in silane solution is popular and easy to use. Silane solution can be prepared by dissolving the silane coupling reagents in aqueous solution, organic solution or mixture of organic solution and water [15, 16]. A thin and stable layer of silane can be formed with silane solutions prepared in organic solvents. Silane coupling reagents with different functional groups are available in the literature and among them (3-aminopropyl) triethoxysilane (APTES) is extensively employed for biomolecule

immobilization to develop biosensors [8, 14, 15, 15–17, 17–23].

Dixit et al. [24] developed an optimized protocol for rapid and high sensitivity enzyme-linked immunoassay by covalently immobilizing the antibodies on APTES modified polymeric surface. Their method was not demonstrated on the silicon surface. Wang and Jin [25] showed that the surface modified with APTES and glutaraldehyde has higher antibody binding capability compared to Di-chloro dimethylsilane (DDS). They also used mixed silane composition (i.e. APTES and methyl- triethoxysilane (MTES)) for covalent immobilization of antibody to reduce the number of APTES molecules on the surface [9]. Ahluwalia et al. [26] studied a number of antibody immobilization techniques using APTES silane for applications to optical immunosensors. They focused on the covalent binding and physical adsorption of proteins to improve the density and uniformity in orientation of antibodies on the substrate.

From the existing literature [8, 14, 15, 17–23], it has been observed that although silanization is a well-known process for immobilization of proteins, optimization of which has not yet been well developed with a well characterized protocol for producing a silane layer on a silicon surface. In the present study, optimized conditions required to produce a thin, stable silane layer for immobilization of biomolecules are investigated. APTES has been used to prepare silane layer on a silicon substrate for biomolecule immobilization with the help of glutaraldehyde linker. The silane layer obtained with APTES produces amine functionality on the surface. In order to produce aldehyde functionality, the silane formed surface is treated with glutaraldehyde. These aldehyde groups react with amine groups of the biomolecules such as antibodies to form amine linkage. Using this optimized silanization protocol, we have successfully demonstrated a highly sensitive standard sandwich immunoassay to detect different biomolecules of interest such as human IgG, *Listeria monocytogenes*, myoglobin and dengue. Also, this immobilization protocol is successfully implemented on different configurations of silicon substrates such as flat and pillared surfaces.

5.3 Material and Methods

5.3.1 Materials

The organosilane reagent (3-Aminopropyl)triethoxysilane (APTES) and the linker Glutaraldehyde (50% aqueous solution) were obtained from Sigma-Aldrich (St. Louis, MO, USA). APTES is silane coupling reagent with 3-aminopropyl group at one end, which terminates in a primary amine and silane reactive portion on another end with triethoxy group. The chemical formula of APTES is $C_9H_{23}NO_3Si$ with molecular weight of 221.37 g/mol. APTES is clear liquid with density of 0.946 g/ml at 25^oC. Glutaraldehyde is a homobifunctional aldehyde based crosslinker with chemical formula $C_5H_8O_2$. Glutaraldehyde contains 50% glutaral and 50% water. Glutaraldehyde is colorless water soluble solution with density of 1.16 g/ml at 25^oC. Both APTES and Glutaraldehyde containers should be tightly closed and stored in a dry and well-ventilated place. Human IgG full length protein, anti-human IgG antibody (rabbit monoclonal to human IgG) and FITC tagged anti-human IgG antibody (rabbit polyclonal to human IgG (FITC)) were procured from Abcam, Inc. (Toronto, ON, Canada). *Listeria monocytogenes* (ATCC strain 43251), unconjugated and FITC tagged rabbit anti-*Listeria monocytogenes* were acquired from Cedarlane (Burlington, ON, Canada). Human myoglobin antigen, myoglobin capture antibody and myoglobin detection antibody were purchased from Biospacific, Inc. (Emeryville, CA, USA). Dengue virus NS1 glycoprotein and capture and detection antibodies for dengue NS1 were acquired from Biospacific, Inc. (Emeryville, CA, USA). Fluorescein isothiocyanate (FITC) kit for coating detection antibodies was purchased from Innova Biosciences Ltd. (Babraham, Cambridge, United Kingdom). This FITC kit was also used for coating the myoglobin and dengue detection antibodies. All other consumable reagents such as toluene (anhydrous, 99.8%), phosphate buffer saline (PBS, pH 7.4), borate buffer and Tween 20 were obtained from Sigma Aldrich and were used as it is. PBS contains the following reagents (in concentrations): Sodium chloride (70.3%), Disodium hydrogenorthophosphate (12.3%), and Potassium chloride (17.4%). Borate buffer saline contains the following reagents (in concentration): Sodium chloride (85.7%), Borate monosodium salt (9.3%), and Boric acid (5%).

Majority of the data presented here are for flat silicon substrate of $1cm \times$

$1cm$. Silicon substrates of 100 mm diameter were obtained from Silicon Valley Microelectronics Inc. (Santa Clara, CA, USA) and cut into pieces of $1cm \times 1cm$. We have also explored the use of our optimized protocols (developed in this work) for complex microfabricated structures, like the silicon micropillars. This particular microfabricated structure has pillar dimension of 50 micron diameter with inter spacing of 75 microns, which was used earlier by our research group for detecting dengue virus NS1 [27, 28]. The detailed fabrication procedure for this type of complex micropillar patterns on silicon substrate can be found elsewhere [29–33].

5.3.2 Characterization Techniques

Several analytical techniques are used in the present work for characterizing each step of the biomolecule immobilization. Firstly, Fourier Transform Infrared Spectroscopy (FTIR) was used to identify the chemical composition of the modified surface. Secondly, spectroscopic ellipsometer was used to calculate the thickness of each layer formed on the surface after each modification. Thirdly, contact angle measurement was conducted to determine the wetting properties (hydrophobicity and hydrophilicity) of the surface. Fourthly, Atomic Force Microscopy (AFM) was used to observe the surface topography and to calculate the roughness. Lastly, Fluorescence Microscopy (FM) was used to detect the FITC tagged biomolecules on the silicon substrate after immunoassay.

Spectroscopic Ellipsometry

Spectroscopic Ellipsometry (Sopra GES 5, Semilab USA LLC., Billerica, MA, USA) was used to measure the surface thickness after each step of surface modification and biofunctionalization. All measurements were taken at an incidence angle of 74^o and with the wavelength range varying between 210 nm to 920 nm. The data was processed using Winelli Software [Semilab USA LLC., Billerica, MA, USA]. The ellipsometric parameters were fitted using dispersion law (Cauchy Law) [9, 18, 25]. The best fit for the experimental data and the theoretical model was obtained with refractive index of 1.42 and the extinction coefficient was set to zero and 0.01 for silane and glutaraldehyde, respectively [34]. For the antibody layer, the best fit was obtained for a refractive index of 1.45 and the extinction coefficient

equals to zero. Five measurements were taken for each sample to obtain the mean and the standard deviation values.

Fourier Transform Infrared Spectroscopy (FTIR)

Thermo Nicolet Nexus (670 FTIR, Thermo Scientific, USA) was used for conducting the chemical analysis of the samples after each step of surface modification. FTIR characterization was carried out at a grazing angle of 75^o. The resolution was 4 cm^{-1} with 1000 scans collected to improve the signal to noise ratio.

Contact Angle Measurement System

After each step of surface modification, the contact angle was measured using Kruss DSA 100 (Kruss GmbH, Hamburg, Germany) to observe the change in the surface energy of the silicon surface. The static water contact angle was measured at room temperature using sessile drop method followed by the image analysis of the drop profile. The volume of water used was 5 μl and the contact angle was measured $5s$ after the drop was deposited. For each sample, the reported value is average of the results obtained for five different locations on the substrate.

Atomic Force Microscopy (AFM)

Atomic Force Microscopy (AFM) experiments were carried out with Asylum Research Atomic Force Microscope MFP-3D (Santa Barbara, CA, USA). AFM was arranged on top of an Olympus IX 70/71 (Olympus Canada Inc., Richmond Hill, ON, Canada) inverted optical microscope. To minimize the force exerted from the scanning tip on the bio-chemically modified silicon surface, the AFM was operated in tapping mode at room temperature. All the measurements were performed in air for higher lateral resolution, using a silicon probe (Asylum Research, Santa Barbra, CA) with typical frequency of 300 kHz. The images, having a scan size of 1 $\mu m \times 1$ μm, were collected at a scan rate of 1 Hz with a line resolution of 512 $\times$ 512. All images were flattened using a first order line fit to correct for piezo-derived differences [35] between scan lines using the IGOR Pro software provided by WaveMetrics, Inc. (Lake Oswego, OR, USA). The roughness of the surface was determined by measuring the root-mean-square (RMS) parameter, which is defined as the root-mean-square average of the height (z) taken from the mean

data plane and can be expressed as $RMS = \sqrt{\frac{1}{N}\sum_{i=1}^{N} {z_i}^2}$, where z_i is the current value and N is the number of points within the analysis section.

Fluorescence Microscopy (FM)

A fully automated bright field and/or fluorescence inverted microscope (Leica DMI6000 B, Leica Microsystems Inc., ON) was used for capturing the images of fluorescent signal emitted by labelled biomolecules bound on the surface. This microscope contains C-mount couplers, accessory optics, motorized configurations, collimated light source, coaxial illumination fiber optics, infinity corrected objective lenses (5X, 10X, 20X and 50X to see a field of view up to 2 mm), high-resolution monochrome image acquisition digital camera (Leica DFC360X), computer, data acquisition system and Leica application suite software. It includes several filter cubes (L5, N3, etc.) for fluorescence imaging. We used filter system L5 for blue excitation (excitation filter: $BP480/40$, dichromatic mirror: 505, suppression filter: $BP527/30$) of FITC tagged biomolecules, which in turn emits the green fluorescence at 527 ± 30 nm wavelength.

5.4 Experimental Procedure

5.4.1 Cleaning of Silicon Substrates

An appropriate cleaning and surface activation of the silicon surface plays a crucial role in the silane growth. For cleaning the silicon substrate, the substrates were kept in a piranha solution ($3:1$; H_2SO_4 / H_2O_2) for 15 minutes. The substrates were then carefully rinsed with de-ionized (DI) water, and dried under a stream of nitrogen gas. The piranha solution (strong oxidizing agent) removes the organic contaminants and makes the surface more hydrophilic by hydroxylating the silicon surface.

After the cleaning step, oxygen plasma treatment for 10 min duration at 80 sccm, 150 mT, 225 W RF of the silicon substrate was done to control the activation of the -OH group on the surface, resulting in reducing the surface roughness (see AFM data) and improving the formation of homogeneous layer [36–41]. Oxygen plasma cleans the surface by removing the impurities and organic contaminants on the surface of silicon by chemical reaction with highly reactive oxygen radicals

and ablation by energetic oxygen ions [36–41]. Plasma treatment controls the hydrophilicity of the surface (makes it more -OH groups on the surface) to improve subsequent coating with functional groups. The silicon substrates were then carefully rinsed with DI water and dried under a stream of nitrogen gas. Finally, the substrates were dried in an oven at 110^o C for one hour to remove the moisture present on the surface. (Note: It is very critical to dehydrate the surface before the silanization step to avoid the silane bonding reaction with the entrained water molecules, which creates a bond that is actually on the top of the hydrated surface.)

5.4.2 Optimization of Silane layer

The effect of concentration of silane reagent (APTES) and silanization time for producing a stable silane layer for biomolecule immobilization are investigated here.

APTES Concentration

To study the effect of APTES concentration on growth and stability of silane layer on silicon substrate, different concentration of APTES solution was prepared in pre-heated anhydrous toluene (100 - 120^o C). The cleaned silicon substrates were then immersed in a solution of different concentrations of APTES for 12 hours of silanization (incubation) time (time at which the surface has reached saturation for growing silane layer) at room temperature in nitrogen ambient. The silicon substrates were then removed from the solution and rinsed with anhydrous toluene and dried in an oven at 100^o C for one hour. All the above steps were carried out in nitrogen glove box to reduce the effect of moisture on the silanization process.

Silanization Time

To study the effect of silanization time on growth and stability of silane layer on silicon substrate, the cleaned silicon substrates were immersed in a $2\%(v/v)$ APTES solution. Then the samples were incubated at different time intervals at room temperature in a nitrogen gas environment. The experimental set-up and the conditions remain the same as mentioned earlier.

5.4.3 Biomolecule immobilization on silicon substrate

Optimized conditions for growing stable layer of silane using APTES on silicon substrate are used for biomolecule immobilization.

Silanization of Cleaned Silicon using APTES

The cleaning steps were the same as outlined above. The cleaned silicon substrates were then immersed into a 2% solution of APTES in pre-heated (100 - 120^{o}C) anhydrous toluene for one hour. The silicon substrate was removed from the solution and rinsed with toluene and dried in an oven at 100^o C for one hour.

Generation of Aldehyde Group using Glutaraldehyde linker

The APTES modified silicon substrates were washed in PBS and allowed to react with 2.5% v/v glutaraldehyde in PBS for 30 min at room temperature. This was followed by thoroughly rinsing the substrate with DI water to avoid non-specific adsorption of the antibody.

Capture antibody Immobilization

The glutaraldehyde-activated surface was then reacted with 0.1 mg/ml of capture antibodies in PBS buffer; along with 1% Tween 20 at room temperature for 15 min to get a antibody layer. After this step, 2 mg/ml of BSA was added to block the remaining surface. Four different types of capture antibodies were used in this work: (a) Anti-Human IgG (Rabbit monoclonal to Human IgG), (b) unconjugated *Listeria monocytogenes* antibodies, (c) capture myoglobin antibodies, and (d) capture dengue antibodies; all of which were immobilized on glutaraldehyde-activated surface.

5.4.4 Immunoassay using capture antibody immobilized surfaces

In order to check the presence of covalently bound capture antibodies on the silicon substrates, the substrates were incubated with respective antigens of different biomolecules for 10 min and washed with PBS solution. The respective antigen-antibody complexes were then identified by incubating the substrates in respective

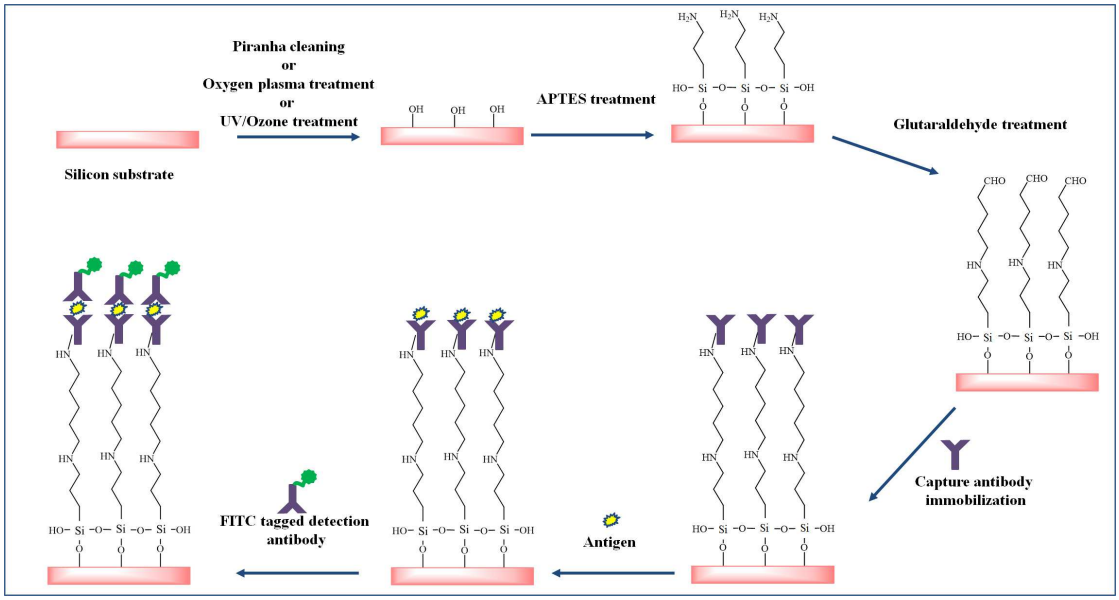

Figure 5.1: Schematic representation of detection of biomolecules on bio-chemically treated silicon substrates using APTES and glutaraldehyde linker. The method involves: (a) Silicon substrates cleaning (Piranha cleaning, Oxygen plasma treatment or UV/Ozone treatment); (b) Generation of silane layer using optimized APTES (2% v/v) solution; (c) treatment with glutaraldehyde solution; (d) Immobilization of capture antibodies (e) Addition of antigen biomolecules; and (f) Detection of antigens using FITC-tagged detection antibodies.

FITC tagged detection antibodies of different biomolecules for 10 min. The substrates were then rinsed in DI water and dried under a stream of nitrogen gas. Fluorescent images were acquired using the fluorescence microscope. Existence of fluorescence confirms the presence of respective antibody-antigen-antibody complex on the surface. The entire procedure of immunoassay on silicon substrates using APTES silane layer and glutaraldehyde linker is illustrated in Fig. 5.1. The method involves: (a) Silicon substrates cleaning (Piranha cleaning, Oxygen plasma treatment or UV/Ozone treatment); (b) Generation of silane layer using optimized APTES (2% v/v) solution; (c) treatment with glutaraldehyde solution; (d) Immobilization of capture antibodies (e) Addition of antigen biomolecules; and (f) Detection of antigens using FITC-tagged detection antibodies.

5.5 Results and Discussion

The main focus of the present work is to produce a thin, stable layer of silane on silicon substrate using APTES solution. Further, using the optimized thin, stable

silane layer for biomolecule immobilization, one can develop a reliable and highly sensitive immuno biosensors.

5.5.1 Optimization of silane layer thickness

Two experimental parameters were explored for silane growth: (1) APTES concentration and (2) silanization time. The thickness of the silane layer was measured for different APTES concentrations and silanization times using spectroscopic ellipsometer. The measured thickness values are plotted in Fig. 5.2(a) and 5.2(b) for different concentrations of APTES kept for 12 hours silanization time. Figure 5.2(a) shows a gradual increase in the thickness of the silane layer up to a certain concentration (6% APTES). Since the thickness of the APTES monolayer has been reported approximately to be around 2 nm, therefore Fig. 5.2(a) suggests the presence of multilayers for higher percentage of APTES solutions [34]. A thin silane layer can be obtained by using lower percentage of silane solution. It is also possible to grow a multilayer of silane for lower silane concentration if the silanization time is increased. The thickness of the silane layer at a particular concentration (2%) for different intervals of time is shown in Fig. 5.2(b). From the figures, it can be concluded that the thickness of silane layer increases with increase in silanization time at a fixed silane concentration. Therefore, it is important to optimize the silane concentration and silanization time to obtain a thin and stable layer (i.e., a monolayer of silane for substrate based bioassays). In addition to silane concentration and silanization time, the silanization processes are very sensitive to the presence of water. In the presence of water, the silane layer undergoes oligomerization to form multilayer of silane. The thicker layers of silane have a very fragile structure and gets washed away either in the presence of buffer or during various washing steps in an immunoassay process. Hence, it is important to get a uniform and homogeneous layer of silane formation on silicon. In the present study, a thickness comparable to monolayer of silane was achieved with a concentration of (2%) APTES and silanization time of one hour.

5.5.2 Silane layer characterization

As described in Fig. 5.1, the amine group present at the one end of the bifunctional APTES facilitates the conjugation of the biomolecules to silicon substrates. The

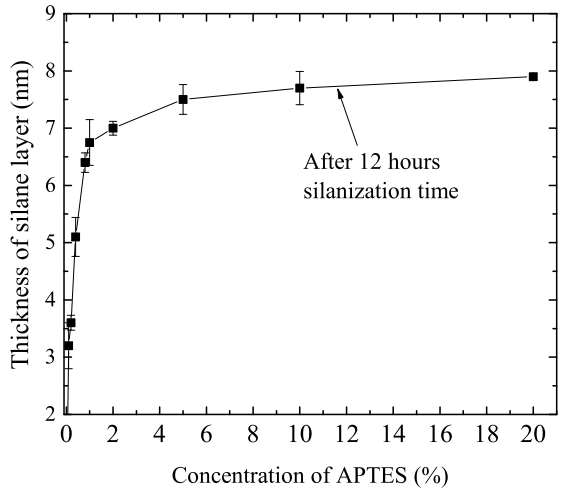

(a)

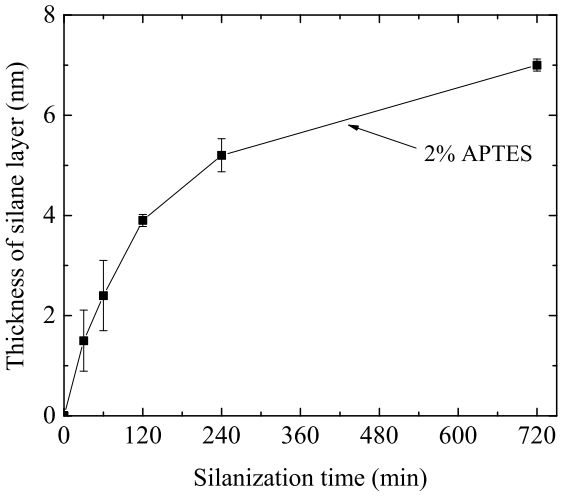

(b)

Figure 5.2: Characterization of silane layer: (a) Variation of thickness of the silane layer with change in APTES concentration; and (b) Variation of thickness of the silane layer with the increase in silanization time.

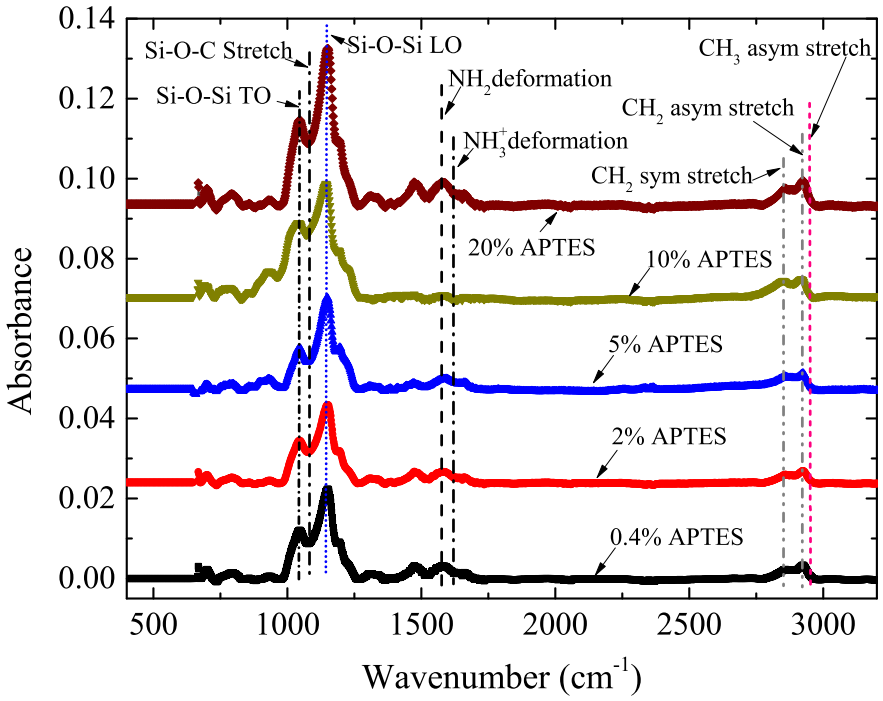

Figure 5.3: FTIR spectra of modified silicon surface after silanization with different concentrations of APTES.

NH_2 group of the APTES molecule forms amide covalent bond with carboxylic group of linker molecule and the Si-O group at the other end reacts with the silicon surface. Therefore, to achieve a uniform and homogeneous immobilization of the antibodies of different biomolecules, it is important that the amino group of the APTES molecule should be oriented away from the surface. The FTIR spectra of the APTES modified silicon surface in reference to the pretreated silicon surface is shown in Fig. 5.3. The band peaks at ~ 1140 cm^{-1} and ~ 1020 cm^{-1} correspond to Si-O-Si longitudinal optical (Si-O-Si LO) and transverse optical (Si-O-Si TO) stretching modes, respectively [8, 14]. The peak at ~ 1108 cm^{-1} relates to Si-O-C mode. The bands in the region of 2800 cm^{-1} to 2980 cm^{-1} and 1400 to 1700 cm^{-1} are assigned to CH_2 stretching and NH_2 bending, respectively [8, 14, 23, 42, 43]. As the concentration of the silane solution was decreased, the FTIR spectra became very weak because of the presence of a very thin silane layer ($\sim$ 3 nm) coupled with a very low reflectivity of silicon [15].

5.5.3 Biomolecule immobilization characterization

FTIR characterization was performed after every step of surface modification and anti-human IgG antibody (rabbit monoclonal to human IgG) immobilization. The FTIR spectra obtained for different layers were shown in Fig. 5.4. The first step of biomolecule immobilization is generating a thin, stable silane layer using APTES. The description of different peaks related to APTES on the surface is already discussed in the previous section of the manuscript. The second step of biomolecule immobilization is treating the silane layer surface with glutaraldehyde. Glutaraldehyde is homobifuncitional crosslinker with aldehyde groups on both ends with carbon chain spacer. Aldehyde group at one end of the glutaraldehyde reacts with amine of the silane layer and forms an amide bond. The aldehyde group at the other end of glutaraldehyde (or exposed surface) is used to react with amine groups of biomolecules such as antibodies. Here in the present work glutaraldehyde is used as crosslinker to bind APTES silane layer with antibodies. FTIR spectra of glutaraldehyde treated surface shows different peaks in the range of 1200 - 1500 cm^{-1}, which accounts for the stretching of C-N, C-O, and C-C groups. Peaks in the range from 1600 to 1900 cm^{-1} relates to the formation of amide bond between APTES to glutaraldehyde. The final step of biomolecule immobilization is binding the anti-human IgG (rabbit monoclonal to human IgG) capture antibody on the glutaraldehyde surface. The aldehyde groups on the surface reacts with amino groups of antibody for covalent immobilization by forming an amide bond. The peaks in the range from 1630 to 1697 cm^{-1} are because of amide I bands of the antibodies whereas peaks in the range from 1614 to 1630 cm^{-1} are due to amide II bands of the antibodies.

The thicknesses of the different layers formed in the process of surface modification and protein immobilization were measured using spectroscopic ellipsometry, which are shown in Fig. 5.5(a). The thickness of oxide layer was 1.5±0.32 nm. The silane layer thickness was found to be 2.4 ± 1.4 nm, which is close to the reported thickness of silane monolayer (2 nm) [34, 44]. The thickness of glutaraldehyde layer (glut layer) was calculated to be 0.9 ± 0.83 nm, while the thickness of anti-human IgG antibody (rabbit monoclonal to human IgG) layer was 5.04 ± 1.6 nm. The result suggests that there was a gradual increase in the thickness of each layer after every step.

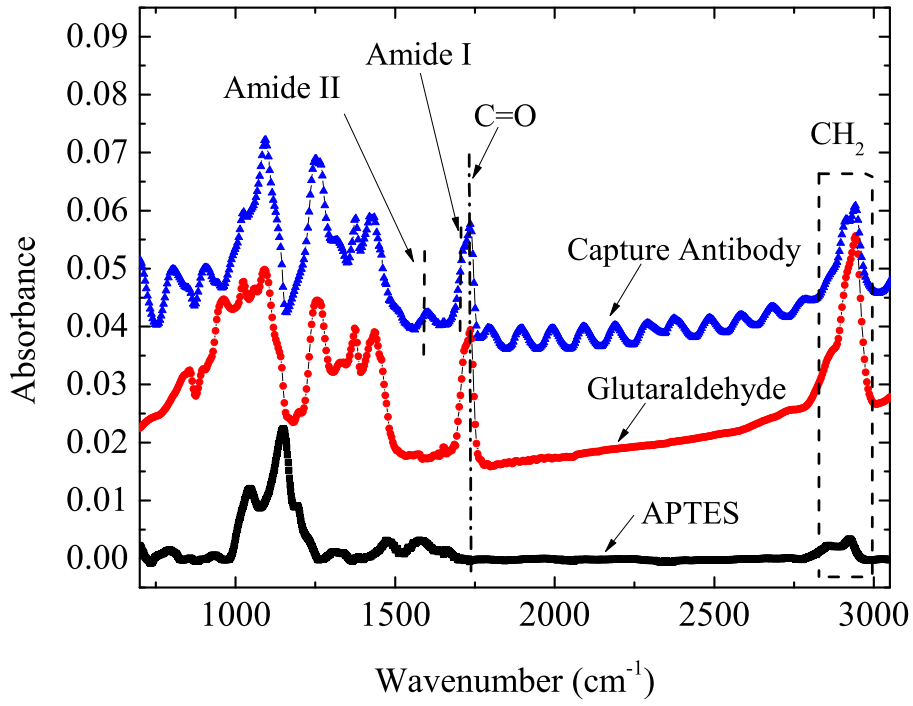

Figure 5.4: FTIR spectra of bio-chemically treated silicon surface after each step of surface modification and biomolecule immobilization.

The contact angle of deionized water (DI) water was measured on five different locations of the silicon substrate after each step of the surface modification and biofunctionalization, which is shown in Fig. 5.5(b). It is to be noted that the contact angle of water on silicon substrate varies based on different parameters like oxide layer thickness, cleaning methods, water pH, oxygen plasma treatment (particularly the RF power and exposure time), etc. Through a separate systematic study, we found that when the oxide layer thickness is around 1.5nm, the contact angle is 41 ± 4.2^o, which changes to 43 ± 5.1^o under oxygen plasma treatment with specific RF power (225W) and exposure time (10 min). However, these values changes quite significantly over one day period. Also, it is found that if one performs hydrofluoric (HF) acid treatment to remove the oxide layer, the value of the contact angle changes to 85.1 ± 2.3^o. Before any functionalization, the oxidized silicon surface is found to be more hydrophilic due to the presence of the -OH group. The hydrophobicity is found to be more for silanized silicon surface with water contact angle of 63 ± 4^o than for reference silicon substrate with contact angle of 41 ± 6.3^o. This may be because of the replacement of the

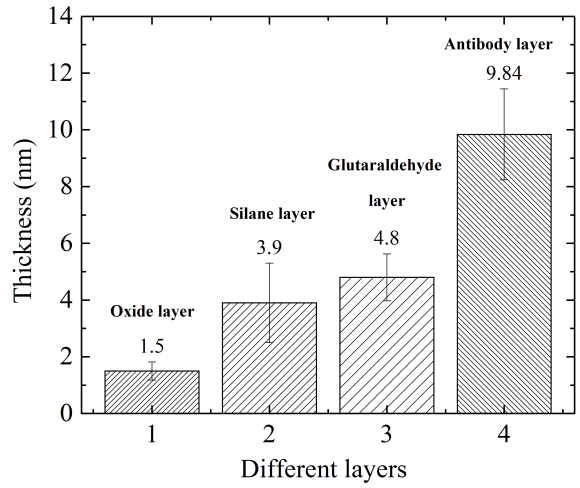

(a)

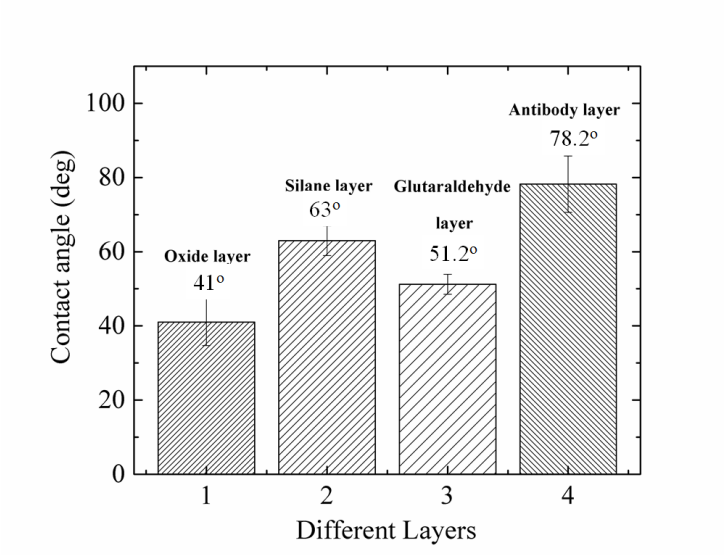

(b)

Figure 5.5: (a) Thickness of different layers after each step of surface modification and biomolecule immobilization. The values provided at the top of the bar graphs indicate the cumulative mean thickness of the given layer in reference to the silicon substrate. (b) Contact angle values of different layers after each step of surface modification and biomolecule immobilization. The values provided at the top of the bar graphs indicate the mean contact angle of a given layer.

-OH group by a more reactive and charged amine group on the surface. After glutaraldehyde treatment, the contact angle of the substrate was found to be 51.2 ± 2.7^o, which is close to the reported value of contact angle measurement for glutaraldehyde [5]. This shows that the treatment with glutaraldehyde makes the surface hydrophilic compared to the silanized surface. After the anti-human IgG antibody (rabbit monoclonal to human IgG) immobilization, the contact angle was found to be 78.2 ± 7.6^o, which can be attributed to the presence of the amine group of the protein structure. The change in contact angle after every step of surface modification and biofunctionalization can be considered as an indicator of the change in the surface properties of the functionalized silicon surface.

The surface topography of the chemically modified silicon substrate was studied using AFM. Tapping mode images were acquired following each step of the immobilization process. Figure 5.6 shows the AFM images obtained for the following substrates: (a) a bare silicon surface, (b) a substrate subjected to silanization with APTES, (c) a thin film terminated with glutaraldehyde, and (d) the immobilized anti-human IgG antibody (rabbit monoclonal to human IgG). The size of the scanning area is 1 $\mu m \times 1$ μm. A measured RMS roughness of 0.58 nm was observed for the bare silicon substrate (Fig. 5.6(a)). A slight decrease in the surface roughness, i.e., 0.51 nm, is observed after the oxygen plasma treatment (See Fig. B.1 in the appendix B) due to the removal of any unwanted impurities on the surface without any change in the bulk properties of silicon. The surface roughness increases considerably with the silanization process resulting in a measured RMS value of 0.69 nm (Fig. 5.6(b)). This increase in roughness can be attributed to the formation of multilayer of silane, but it is thin and stable compared with other concentrations of APTES. Figure 5.6(b) shows the packing of APTES on silicon surface (1m x 1m) after one hour incubation time. Here, we have also incorporated the AFM images of APTES layer on silicon surface for a larger surface area (5m x 5 m) in appendix B. This demonstrates that packing of silane layer is uniform and stable. In case of Fig. 5.6(c), the chemical ligation of the glutaraldehyde to the amine-terminated surface resulted in a RMS value of 0.51 nm. This observation indicates that the glutaraldehyde treatment results in a more homogeneous surface topography as compared to the APTES terminated one. However, an increase in the RMS surface roughness was observed after the antibody immobilization (Fig.

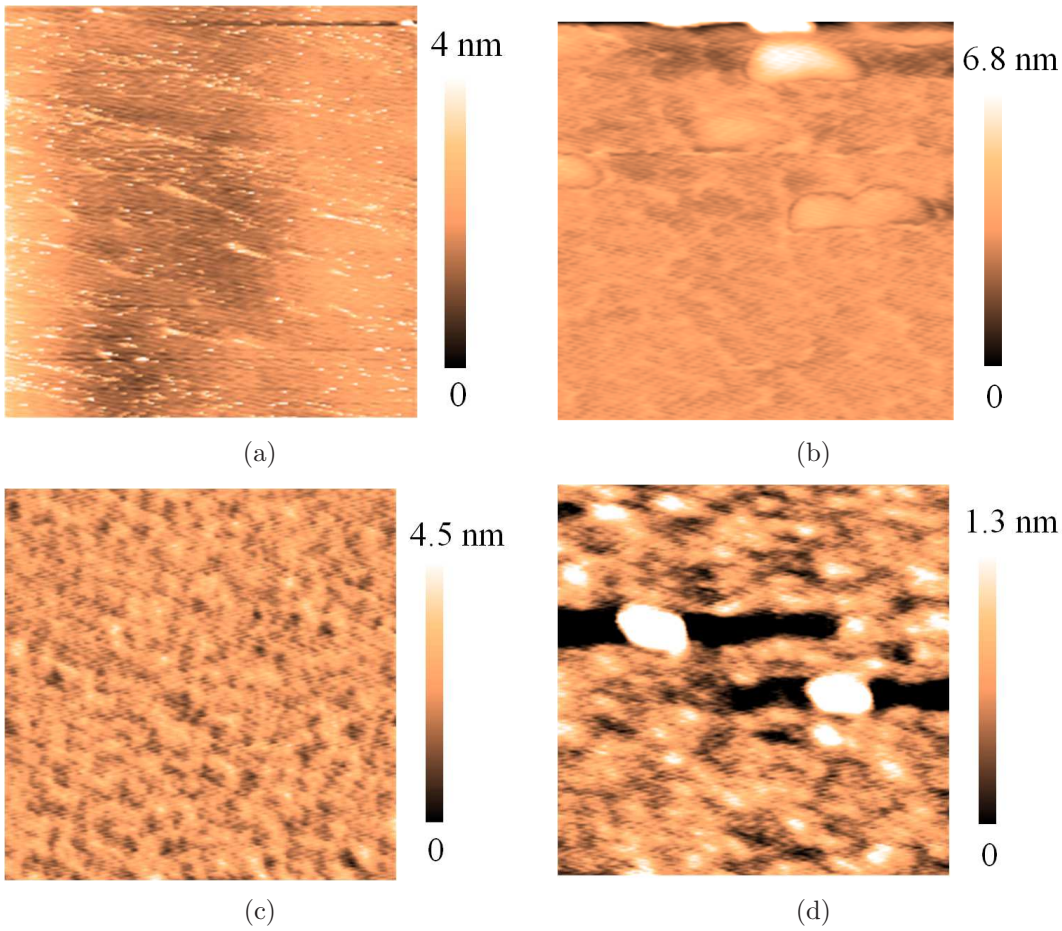

Figure 5.6: Tapping mode AFM images (a) a bare silicon surface, (b) a substrate subjected to silanization with APTES, (c) a thin film terminated with glutaraldehyde, and (d) the immobilized antibody (Anti-Human IgG (Rabbit monoclonal to Human IgG)). The size of scanning area is 1 $\mu m \times 1\ \mu m$.

5.6(d)). The RMS surface roughness increased to 0.63 nm which was less compared to the RMS roughness of the silanized surface. The reduction in the surface roughness could be attributed to the fact that the glutaraldehyde and the antibody treatment might have filled up the existing clefts and may have smoothened the surface. These values suggest that for all practical purposes, the layers can be considered smooth and the AFM image does indicate a homogeneous surface. It is observed that a uniform, homogenous and highly dense layer of biomolecules are immobilized with optimized silane layer on silicon substrate.

5.5.4 Detection of biomolecules

Apart from using anti-human IgG antibody (rabbit monoclonal to human IgG) for all the previous characterization results, we have also used other biomolecules of interest such as *Listeria monocytogenes* [45], myoglobin and dengue [27] to detect using the biomolecule immobilization protocol developed in the present work. Also, the developed method is successfully implemented by our research group on different configurations of silicon surfaces such as microchannels, microspots, microwells and micropillars [27, 28, 45].

The capture antibodies of human IgG (rabbit monoclonal to Human IgG), *Listeria monocytogenes*, myoglobin and dengue were successfully immobilized with optimized silane layer and glutaraldehyde linker. Further, standard sandwich immunoassay (antibody-antigen-antibody) is employed on respective capture antibody coated silicon substrates. Fluorescence microscopy is used to detect the respective FITC tagged detection antibodies bound to the surface after immunoassay. Figure 5.7 shows the fluorescent image of FITC tagged detection antibodies after immunoassay for different biomolecules. Note that green color indicates the fluorescence emitted by individual FITC tagged antibodies. Figures 5.7(a), 5.7(b) and 5.7(c) depicts the fluorescence image of FITC tagged molecules after employing immunoassay on flat silicon substrate whereas Fig. 5.7(d) depicts the pillared surface. Uniform fluorescence intensity is observed throughout the silicon surface. Some high intensity spots observed in Fig. 5.7(a) indicates the agglomeration of antibodies during immobilizing the FITC tagged antibodies for binding with antigen molecules. Figure 5.7 also demonstrates that the layer of silane on a silicon surface is appropriate for immobilization of antibodies for immunoassay.

5.6 Summary

The existing method of silane formation using (3-aminopropyl)triethoxysilane (APTES) on silicon substrates is modified to produce a thin, stable layer of silane for uniform immobilization of biomolecules. The effect of concentration of APTES solution and silanization time on formation of silane layer are investigated. Optimized silane layer is used to immobilize the biomolecules of interest with the help of glutaraldehyde linker. It is observed that optimized silane layer helped to form a uniform,

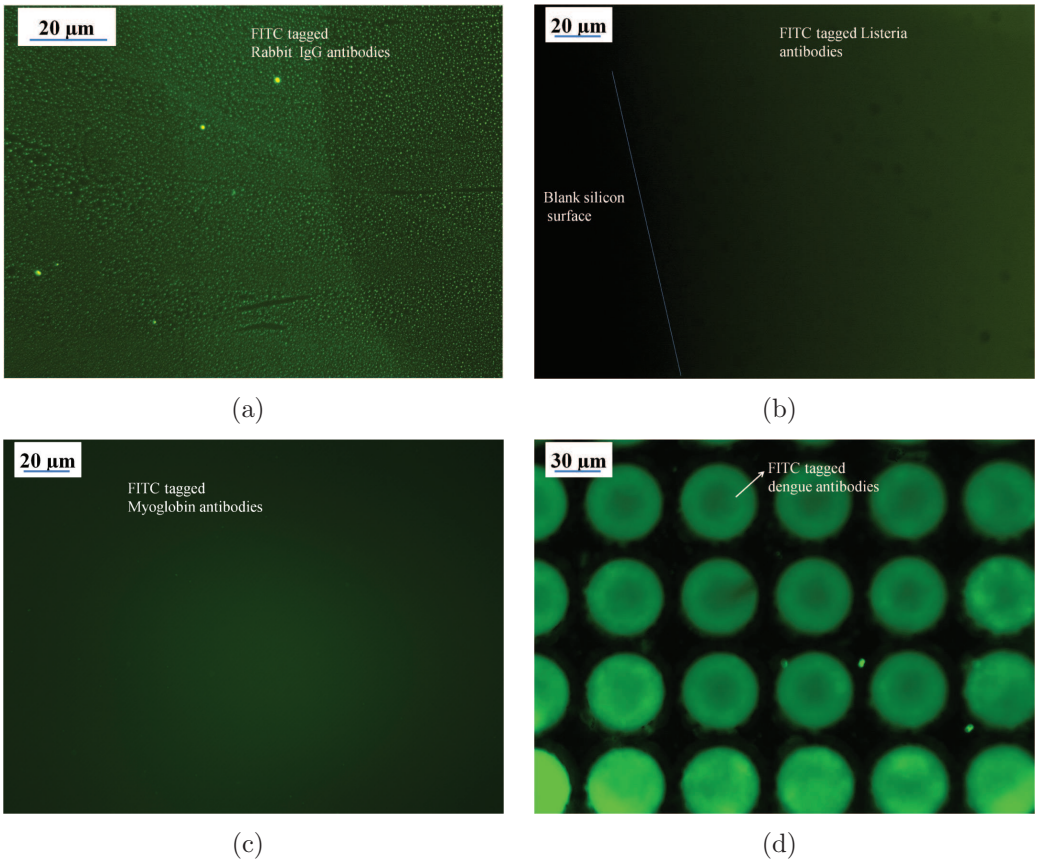

Figure 5.7: Fluorescent images of FITC tagged detection antibodies bound on the silicon surface after immunoassay: (a) anti-Human IgG detection (rabbit polyclonal to Human IgG) antibodies; (b) *Listeria monocytogenes* detection antibodies; (c) myoglobin detection antibodies; and (d) dengue detection antibodies on pillars (top view image of pillars). Note that green color indicates the fluorescence emitted by respective FITC tagged antibodies.

homogeneous and highly dense layer of biomolecules on the surface. The samples were characterized after every step of surface modification and biomolecule immobilization using Fourier Transform Infrared Spectroscopy (FTIR), spectroscopic ellipsometry, contact angle measurement system, atomic force microscopy, and fluorescence microscopy. The developed method of biomolecule immobilization using a thin stable silane layer is employed on different silicon substrates (flat and pillar). Also, immunoassay for detecting different biomolecules such as human IgG, *Listeria monocytogenes*, myoglobin and dengue on silicon substrate is employed using this method. It is observed that optimized silane layer helped to increase the densities of biomolecules on the surface, which will further help to increase the sensitivity of immunoassay.

Bibliography

[1] P. Jonkheijm, D. Weinrich, H. Schröder, C. Niemeyer, and H. Waldmann. Chemical strategies for generating protein biochips. *Angewandte Chemie International Edition*, 47(50):9618–9647, 2008.

[2] F. Rusmini, Z. Zhong, and J. Feijen. Protein immobilization strategies for protein biochips. *Biomacromolecules*, 8(6):1775–1789, 2007.

[3] F. Tao and S. Bernasek. *Functionalization of semiconductor surfaces*. John Wiley & Sons, 2012.

[4] N. Glass, R. Tjeung, P. Chan, L. Yeo, and J. Friend. Organosilane deposition for microfluidic applications. *Biomicrofluidics*, 5(3):1–7, 2012.

[5] J. Diao, D. Ren, J. Engstrom, and K. Lee. A surface modification strategy on silicon nitride for developing biosensors. *Analytical biochemistry*, 343(2):322–328, 2005.

[6] J. Yakovleva, R. Davidsson, A. Lobanova, M. Bengtsson, S. Eremin, T. Laurell, and J. Emnéus. Microfluidic enzyme immunoassay using silicon microchip with immobilized antibodies and chemiluminescence detection. *Analytical chemistry*, 74(13):2994–3004, 2002.

[7] M. Joshi, M. Goyal, R. Pinto, and S. Mukherji. Characterization of anhydrous silanization and antibody immobilization on silicon dioxide surface. *Computer Architectures for Machine Perception, 2003 IEEE International Workshop on*, pages 7–11, 2003.

[8] R. Pasternack, S. Rivillon Amy, and Y. Chabal. Attachment of 3-(aminopropyl) triethoxysilane on silicon oxide surfaces: dependence on solution temperature. *Langmuir*, 24(22):12963–12971, 2008.

[9] Z.-H. Wang and G. Jin. Silicon surface modification with a mixed silanes layer to immobilize proteins for biosensor with imaging ellipsometry. *Colloids and Surfaces B: Biointerfaces*, 34(3):173–177, 2004.

[10] N. Chaki and K. Vijayamohanan. Self-assembled monolayers as a tunable platform for biosensor applications. *Biosensors and Bioelectronics*, 17(1-2):1–12, 2002.

[11] B. Arkles and P. Dispersants. Hydrophobicity, hydrophilicity and silanes. *Paint and Coatings Industry magazine*, pages 1–10, 2006.

[12] N. Aissaoui, L. Bergaoui, J. Landoulsi, J. Lambert, and S. Boujday. Silanes layers on silicon surfaces: Mechanism of interaction, stability and influence on protein adsorption. *Langmuir*, 28(1):656–665, 2012.

[13] A. Krasnoslobodtsev and S. Smirnov. Effect of water on silanization of silica by trimethoxysilanes. *Langmuir*, 18(8):3181–3184, 2002.

[14] N. Lapin and Y. Chabal. Infrared characterization of biotinylated silicon oxide surfaces, surface stability, and specific attachment of streptavidin. *The Journal of Physical Chemistry B*, 113(25):8776–8783, 2009.

[15] O. Seitz, P. G. Fernandes, R. Tian, N. Karnik, H.-C. Wen, H. Stiegler, R. A. Chapman, E. M. Vogel, and Y. J. Chabal. Control and stability of self-assembled monolayers under biosensing conditions. *Journal of Materials Chemistry*, 21(12):4384–4392, 2011.

[16] G. T. Hermanson. *Bioconjugate techniques*. Academic press, 1996.

[17] Q. Weiping, X. Bin, W. Lei, W. Chunxiao, S. Zengdong, Y. Danfeng, L. Zuhong, and W. Yu. Orientation of antibodies on a 3-aminopropyltriethoxylsilane-modified silicon wafer surface. *Journal of Inclusion Phenomena*, 35(1-2):419–429, 1999.

[18] J. Kim, P. Seidler, C. Fill, and L. S. Wan. Investigations of the effect of curing conditions on the structure and stability of amino-functionalized organic films on silicon substrates by fourier transform infrared spectroscopy, ellipsometry, and fluorescence microscopy. *Surface Science*, 602(21):3323 – 3330, 2008.

[19] S.-H. Choi and B. min Zhang Newby. Suppress polystyrene thin film dewetting by modifying substrate surface with aminopropyltriethoxysilane. *Surface Science*, 600(6):1391 – 1404, 2006.

[20] A. Maria Chong and X. Zhao. Functionalization of sba-15 with aptes and characterization of functionalized materials. *The Journal of Physical Chemistry B*, 107(46):12650–12657, 2003.

[21] Q. Weiping, X. Bin, W. Lei, W. Chunxiao, Y. Danfeng, Y. Fang, Y. Chunwei, and W. Yu. Controlled site-directed assembly of antibodies by their oligosaccharide moieties onto APTES derivatized surfaces. *Journal of colloid and interface science*, 214(1):16–19, 1999.

[22] J. Landoulsi, M. J. Genet, K. El Kirat, C. Richard, S. Pulvin, and P. G. Rouxhet. Silanization with APTES for controlling the interactions between stainless steel and biocomponents: reality vs expectation. *Biomaterials–physics and chemistry*, 5:978–953, 2011.

[23] C.-M. Pradier and Y. J. Chabal. *Biointerface characterization by advanced IR spectroscopy*. Elsevier, 2011.

[24] C. Dixit, S. Vashist, B. MacCraith, and R. O'Kennedy. Multisubstrate-compatible ELISA procedures for rapid and high-sensitivity immunoassays. *Nature Protocols*, 6(4):439–445, 2011.

[25] Z. Wang and G. Jin. Covalent immobilization of proteins for the biosensor based on imaging ellipsometry. *Journal of immunological methods*, 285(2):237–243, 2004.

[26] A. Ahluwalia, D. De Rossi, C. Ristori, A. Schirone, and G. Serra. A comparative study of protein immobilization techniques for optical immunosensors. *Biosensors and Bioelectronics*, 7(3):207–214, 1992.

[27] N. S. K. Gunda, M. Singh, Y. Purwar, S. L. Shah, K. Kaur, and S. K. Mitra. Micro-spot with integrated pillars (MSIP) for detection of dengue virus NS1. *Biomedical microdevices*, 15(6):959–971, 2013.

[28] N. S. K. Gunda, M. Singh, Y. Purwar, S. L. Shah, K. Kaur, and S. K. Mitra. Microspot with integrated pillars (msip) for the detection of dengue ns1 virus. *223rd ECS Meeting Abstracts, May 12 - 16, 2013, Toronto, Canada*, (44):1475–1475, 2013.

[29] N. S. K. Gunda, B. Bera, N. K. Karadimitriou, S. K. Mitra, and S. M. Hassanizadeh. Reservoir-on-a-Chip (ROC): A new paradigm in reservoir engineering. *Lab Chip*, 11(22):3785–3792, 2011.

[30] N. S. K. Gunda, J. Joseph, A. Tamayol, M. Akbari, and S. K. Mitra. Measurement of pressure drop and flow resistance in microchannels with integrated micropillars. *Microfluidics and Nanofluidics*, 14(3-4):711–721, 2013.

[31] J. Joseph, N. S. K. Gunda, and S. K. Mitra. On-chip porous media: Porosity and permeability measurements. *Chemical Engineering Science*, 99:274–283, 2013.

[32] N. S. K. Gunda, S. Naicker, M. S. Ghoraishi, S. Bhattacharjee, T. G. Thundat, and S. K. Mitra. Microspot with integrated wells (MSIW) for the detection of e. coli. *ASME 2013 11th International Conference on Nanochannels, Microchannels, and Minichannels*, pages V001T10A001–V001T10A001, 2013.

[33] N. S. K. Gunda, S. Naicker, M. Ghoraishi, subir Bhattacharjee, T. Thundat, and S. K. Mitra. Rapid detection of total coliform and e. coli in contaminated water using chemically modified microwells. *224th ECS Meeting, October 27 - November 1, 2013, San Francisco, CA, USA*, (50):2788–2788, 2013.

[34] B. Nehilla, K. Popat, T. Vu, S. Chowdhury, R. Standaert, D. Pepperberg, and T. Desai. Neurotransmitter analog tethered to a silicon platform for neurobiomems applications. *Biotechnology and bioengineering*, 87(5):669–674, 2004.

[35] P. E. Pullen, J. J. Pesek, M. T. Matyska, and J. Frommer. Characterization by atomic force microscopy of fused-silica capillaries chemically modified for capillary electrokinetic chromatography. *Analytical chemistry*, 72(13):2751–2757, 2000.

[36] S.-W. Choi, W.-B. Choi, Y.-H. Lee, B.-K. Ju, and B.-H. Kim. Effect of oxygen plasma treatment on anodic bonding. *Journal of the Korean Physical Society*, 38(3):207–209, 2001.

[37] S.-W. Choi, W.-B. Choi, Y.-H. Lee, B.-K. Ju, M.-Y. Sung, and B.-H. Kim. The analysis of oxygen plasma pretreatment for improving anodic bonding. *Journal of The Electrochemical Society*, 149(1):G8–G11, 2002.

[38] J. Coburn and H. F. Winters. Plasma etchingA discussion of mechanisms. *Journal of vacuum Science and Technology*, 16(2):391–403, 1979.

[39] G. Higashi, Y. Chabal, G. Trucks, and K. Raghavachari. Ideal hydrogen termination of the Si (111) surface. *Applied physics letters*, 56:656, 1990.

[40] B. Anthony, L. Breaux, T. Hsu, S. Banerjee, and A. Tasch. In situ cleaning of silicon substrate surfaces by remote plasma-excited hydrogen. *Journal of Vacuum Science & Technology B: Microelectronics and Nanometer Structures*, 7(4):621–626, 1989.

[41] G. S. Oehrlein, G. J. Scilla, and S.-J. Jeng. Efficiency of oxygen plasma cleaning of reactive ion damaged silicon surfaces. *Applied physics letters*, 52(11):907–909, 1988.

[42] R. Tian, O. Seitz, M. Li, W. Hu, Y. J. Chabal, and J. Gao. Infrared characterization of interfacial Si-O bond formation on silanized flat SiO_2/Si surfaces. *Langmuir*, 26(7):4563–4566, 2010.

[43] G. Socrates and G. Socrates. *Infrared and Raman characteristic group frequencies: tables and charts*, volume 3. Wiley Chichester, UK, 2001.

[44] G. Rong and S. M. Weiss. Influence of biomolecule size on performance of nanostructured sensing devices. *International Society for Optics and Photonics, Optics East 2007*, pages 676909–676909, 2007.

[45] D. Sarkar, N. S. K. Gunda, I. Jamal, and S. K. Mitra. Optical biosensors with an integrated mach-zehnder interferometer for detection of listeria monocytogenes. *Biomedical microdevices, Accepted*, 2014.

Chapter 6

Microfluidic Immunoassay for Cardiac Markers Detection [1]

6.1 Overview

In Chapter 5, a reliable technique for immobilization of myoglobin on silicon surface is investigated. The technique described in Chapter 5 can be used to immobilize other biomolecules such as troponin T. However, the technique is useful for silicon based biosensors or LOC devices. In the present chapter, we explored and optimized the immobilization of biomolecules (such as troponin T) on gold surfaces. Troponin T (cTnT) releases in to the blood serum within 4-6 h after minor heart attack and remains elevated for up to 2 weeks, which will help in diagnosing the heart condition. In this work, a microfluidic channel with an array of gold strips is considered for detecting and quantifying the troponin T in an aqueous solution. Troponin T primary (capture) antibody is immobilized on gold strip using self assembled monolayer (SAM) consisting of a homogeneous mixture of oligo (ethylene glycol) (OEG)-terminated alkanethiolate and mercaptohexadecanoic acid (MHDA). Then, an aqueous solution containing troponin T antigen is injected into the microchannel to facilitate antibody-antigen reaction to take place in less time. Later, FITC tagged troponin T secondary (detection) antibody is dispensed in to the channel for quantification of troponin T antigen. Using confocal fluorescent reader, the variation of fluorescent intensity across the microchannel is measured and quantified the concentration of troponin T antigen with calibrated

[1] A version of this chapter has been published. N. S. K. Gunda and S. K. Mitra, Paper # FEDSM2013-16270, Proceedings of ASME 2013 Fluids Engineering Summer Meeting, Incline Village, Nevada, USA, July 7-11, 2013.

samples. Contact angle measurement system, Fourier Transform Infrared Spectroscopy and Ellipsometer are used to characterize the surface properties at each stage of biomolecule immobilization. We developed microfluidic based biosensor using optimized protocol for detecting troponin T in a sample.

6.2 Introduction

Myocardial Infarction (MI) is one of the major cardiovascular disease leading to human deaths in both developing and developed countries [1]. Existing methods of diagnosis for MI rely heavily on classical methods which are based on tests conducted in central laboratories that may take several hours or even days from when tests are ordered to when results are received [2]. The diagnosis of MI has been based on the World Health Organization (WHO) criteria, whereby patients must have at least two of three conditions: characteristic chest pain, diagnostic electrocardiogram (ECG) changes, and elevation of the biochemical markers in their blood samples [2]. Although, ECG is an important diagnostic tool, but it's performance is poor and half of the MI patients who present to the emergency department showed normal or no diagnostic electrocardiogram, which makes early diagnosis of MI more difficult [3, 4]. Therefore, identification of cardiac markers is critical in assisting the diagnosis of MI. A more sensitive and rapid technology platform is therefore needed to fulfill the rapid diagnosis requirements in MI detection. The early and fast detection of MI is very important not only for patient survival, but also reduces time and cost in successful prognosis of disease. The development of biosensors is probably one of the most promising technologies for fast, sensitive, specific and cost effective diagnosis of biochemical markers in blood. [5]. Biosensors can help in rapid diagnosis, providing better health care and reducing the waiting time for results dissemination which is highly stressful to the patients. Recently, lab-on-a-chip and microfluidics based biosensor technology is being focused for the detection of cardiac markers [6].

A biosensor is a device designed to detect and quantify target molecules that is widely used as a powerful analytical tool in medical diagnosis [6]. It includes proteins detection, nucleic acids or monitoring antigen - antibody interaction. In principle, it is generally fabricated by immobilizing a biological receptor material,

antibody on the surface of a suitable transducer that converts the biochemical signal into quantifiable electronic signals [7]. The specificity, selectivity and sensitivity of respective biomarkers detection using microfluidic based biosensors increases. Recently, Quereshi et al. [8] and Mohammad and Desmulliez [6] reviewed different types of microfluidic/lab on a chip based biosensors for the detection of cardiac markers using different techniques. Hence we are not providing extensive literature on the microfluidic based biosensor technology in this chapter.

Due to several advantages of microfluidic based biosensors such as less time for detection, low sample and reagent volume requirement, high sensitivity and selectivity, we proposed to develop a new microfluidic based biosensor for the rapid detection of one of the cardiac markers, troponin T. Antibody and antigen bindings are the most promising methodology for determining trace quantities of a specified biomarker because an antibody has high affinity and selectivity for their antigen or their targeted molecular surface [9]. Most of the existing antibody-antigen based biosensors for cardiac markers are developed on a flat gold surface under non-flow conditions [6, 8]. In the present work, a microfluidic channel with an array of gold strips is considered for detecting and quantifying the troponin T in an aqueous solution. Gold strips in the channel acts as reacting zones. This system allows to flow different reagents/samples in controlled manner for proper/uniform immbolization of antibodies on gold strips for antigen reaction, which is new compared to conventional methods of detection on flat surface. The present system allows us to study the effect of flow on antibody-antigen interaction along the length of the channel. Troponin T primary (capture) antibody is immobilized on gold strip using self assembled monolayer (SAM) consisting of a homogeneous mixture of oligo (ethylene glycol) (OEG)-terminated alkanethiolate and mercaptohexadecanoic acid (MHDA). Then, an aqueous solution containing troponin T antigen is injected into the microchannel to facilitate antibody-antigen reaction to take place in less time. Later, FITC tagged troponin T secondary (detection) antibody is dispensed in to the channel for quantification of troponin T antigen. Using confocal fluorescent reader, the variation of fluorescent intensity across the microchannel is measured and quantified the concentration of troponin T antigen with calibrated samples. Effect of troponin T antigen concentration and flow rates on the performance of the microfluidic based biosensor is studied. Contact angle measurement

system, Fourier Transform Infrared Spectroscopy and Ellipsometer are used to characterize the surface properties at each stage of biomolecule immobilization.

6.3 Materials and methods

6.3.1 Materials

Cardiac troponin T capture and detection antibodies (38 kDa), troponin T antigen, 16- mercaptohexdecanoic acid (MHDA), (1-Mercaptoundec-11-yl)tetra(ethylene glycol) (OEG), 1-Ethyl-3-(3-dimethylaminopropyl)-carbodiimide hydrochloride (EDC), N-hydroxysulfosuccinimide (NHS), MES buffer saline (0.1 M of 2-[morpholino]-ethanesulfonic acid, 0.9 % NaCl, pH 4.7) were obtained from Sigma Aldrich (USA). Other reagents and solvents were purchased commercially and used without further purification.

6.3.2 Fabrication of microfluidic channel integrated with an array of gold strips

The device (microfluidic channel integrated with an array of gold strips) was fabricated with two substrates, where a microchannel with inlet and outlet fluidic ports in top substrate and an array of rectangular gold strips in bottom substrate.

A PDMS based microchannel with inlet and outlet fluidic ports was fabricated using standard softlithography process as described elsewhere [24]. An array of gold strips on glass substrate was fabricated using standard photolithography process [11, 12]. Using oxygen plasma treatment, both gold strip surface and PDMS microchannel were bonded to make complete microfluidic device (microchannel integrated with an array of gold strips).

6.3.3 Immobilization of troponin T capture antibody on gold surface of device

A self assembled monolayer consisting (SAM) of a homogeneous mixture of oligo (ethylene glycol) (OEG)-terminated alkanethiolate and mercapto-hexadecanoic acid (MHDA) on gold is employed for immobilizing troponin T antibody. The SAM of OEG with high hydrophilicity, hydrogen bond accepter, and the zero net charge is suitable for creating the anti-fouling surface [13] The MHDA has COOH

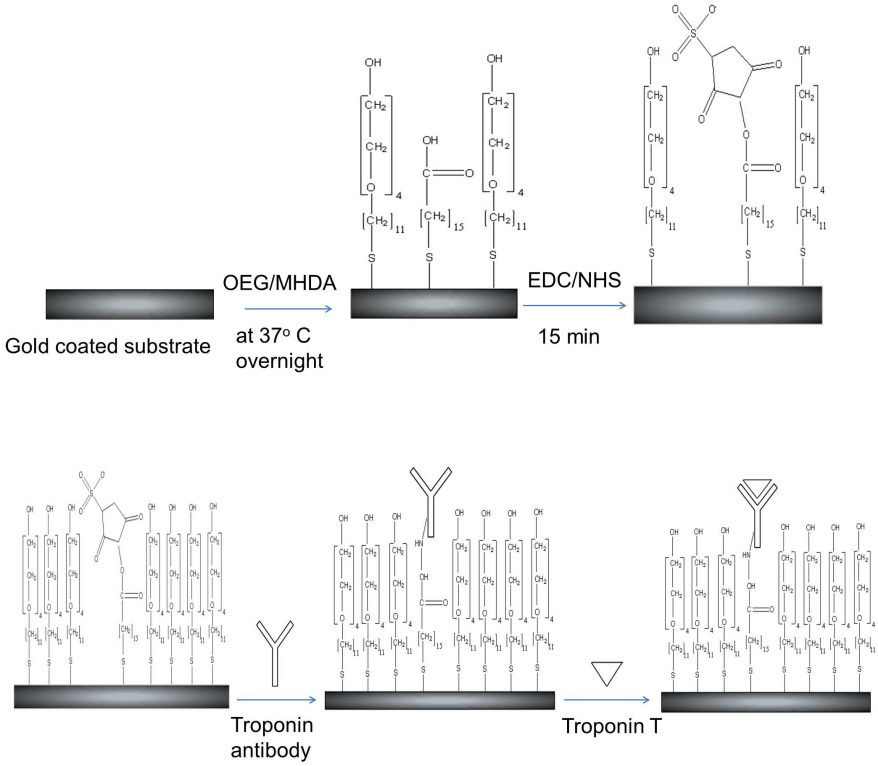

Figure 6.1: Schematic diagram of surface modification for the mixed SAM of OEG and MHDA and immobilization method of antibody binding carboxyl groups of MHDA on gold surface

groups which can be used to react with NH2 groups on the antibody. Cardiac troponin T antibody was immobilized on the carboxyl group of MHDA through the EDC/NHS activated carboxyl groups.

The protocol follows like this: Mixed OEG/MHDA SAM functionalization is done by filling the channel with the mixture of 1mM OEG and 0.3 mM MHDA and putting for overnight at 37^{o}C. We have to keep it in closed container for avoiding evaporation of SAM solution. Then channels were cleaned with absolute ethanol to remove unbounded OEG/MHDA and dried the channel by flowing nitrogen gas. EDC/NHS procedure is applied to activate the carboxyl groups of MHDA for binding with troponin T antibody. troponin T antibody solution (10 $\mu g/ml$) is filled inside the channel and kept for 10 min at room temperature. By flowing the Phosphate buffered saline (PBS) in the channel, unreacted antibodies were removed. The antibody immobilized chips are stored in Dulbecco's Phosphate Buffered Saline (D-PBS) under 4^{o}C until use. In all experiments, we are flowing the reagents/samples at 50 $\mu l/min$. Figure 6.1 show the schematic of the step by

step procedure of immobilization of troponin T on gold surface.

6.3.4 Binding of troponin T antigen

An aqueous solution of troponin T antigen is injected in to the troponin T capture antibody immobilized microfluidic channels (above prepared device). Later the binding of antigen is confirmed by injecting the FITC tagged detection antibodies of troponin T. Based on the measurement of fluorescence emitted by FITC molecules, concentration of the antigen is quantified using the fluorescent reader (ESElog, Qiagen, Germany). A parametric study is conducted at different concentration of troponin T antigen and at different flow rates conditions to understand the effects of low rates on the performance of biosensor and how the binding performance of antigens to antibodies varies along the microchannel.

6.4 Results and discussions

Protocol for immobolization of troponin T on gold surface has been studied before applying on the microfluidic based biosensor. Several characterization methods have been used for this study. Firstly, contact angle measurement was taken to determine the hydrophobicity and hydrophilicity of the flat surface. Secondly, ellipsometer was used to calculate the thickness of each layer on the surface. Thirdly, Fourier Transform Infrared Spectroscopy (FTIR) was used to verify the active molecules on the surface after each step of immobilization.

After every step of surface immobilization, contact angle measurement was done using Kruss DSA 100 (Kruss GmbH, Hamburg, Germany) to observe the change in the surface on the gold surface. Several readings were taken by putting 5 μl of water drops on sample surface. The gold surface exhibited a value of $\sim 52.1^o$. The OEG/MHDA SAM on gold surface showed a contact angle of $\sim 39.6^o$, which is slightly lower than the contact angle reported on similar SAM [9]. The contact angle is increased to $\sim 49^o$ after activating carboxyl group on MHDA using EDC/NHS procedure. The contact angle measurement after troponin T antibody immobilization is $\sim 46.4^o$ and contact angle decreased to $\sim 41.2^o$ after troponin T antigen binding to antibody.

The surface thickness of each layer after every immobilization step was mea-

sured using Spectroscopic Ellipsometry (Sopra GES 5). The data is further analyzed using Winelli Software taking bare gold surface as the reference to calculate thickness of layers formed on gold surface. All measurements were taken at an incidence angle of 45^o and with the wavelength range of 200 to 800 nm. The refractive index of 1.4 was used. The ellipsometry measurements were taken after each and every step of antibody immobilization to find the thickness of each layer formed. The results showed that each step is formed in a uniform layer on the surface of gold. The thickness of OEG/MHDA SAM on gold is $\sim$2.2 nm and the thickness of troponin T antibody layer on SAM is $\sim$6 nm.

Chemical analysis of the layers formed on the gold surface are analyzed using Thermo Nicolet Nexus (670 FTIR). 1000 scans are made on the surface to get infrared spectrum of absorption on the gold surface. The data was analyzed further based on the absorption spectrum of different chemical bonds in a wide range of about 1000 to 3500 cm^{-1}. Figure 6.2 depicts the FTIR absorption curves on bare gold surface, after OEG/MHDA SAM formation, after EDC/NHS activation, after troponin T immobilization and after troponin T antigen binding. From theoretical data, primary alcohols give spectral band in the wavenumber range of 1060-1025 cm^{-1} and the -OH in carboxylic acid gives band in the range of 1200-1015 cm^{-1} [9, 14]. The C=O in carboxylic group gives a strong band in the range of 700-590 cm^{-1} [9]. The -CH2- group in aliphatic compounds gives medium strong band in the spectral range of 2990-2850 cm^{-1} [14]. The FTIR absorption curve after OEG/MHDA SAM formation indicates the presence of -CH2 groups, alcohol and carboxylic group on gold surface showing the formation of OEG and MHDA SAM layers on gold. The sulphonic acid group gives a very strong band in the range of 1250-1150 cm^{-1} from theoretical data [14]. The absorption curve for "after EDC/NHS activation" shows the activation of carboxylic groups of MHDA. The peak in figure at around 1200 cm^{-1} shows the activation of carboxylic group by NHS addition. From theoretical data, it is known that the peptide bond in proteins give a very strong band in the spectral range of 1670-1630 cm^{-1} (-C=O-) and 1565-1475 cm^{-1} (-NH-) [14]. The absorption curves (after troponin T antibody immobilization and antigen binding) show the peaks at 1670-1630 cm^{-1} and 1565-1475 cm^{-1}, indicating the protein immobilization on the surface [9, 14].

A protocol for detecting the troponin T antigen on the gold surface is optimized

and verified with well-known characterization facility. This optimized protocol was implemented on the fabricated microfluidic device (microchannel integrated with an array of gold strips) to study the variation of antigen binding with respect to the channel length. FITC tagged detection antibodies of troponin T are added to the channel for quantifying the concentration of antigen. Using confocal fluorescent reader, the variation of fluorescent intensity emitted by FITC tagged detection antibodies across the microchannel is measured. Figure 6.3 shows the variation of fluorescent intensity with respect to length of the channel. It is observed that fluorescence intensity emitted by troponin T antibodies along the length of the channel is reduced due to decrease in antigen binding along the channel length.

6.5 Summary

In the present study, we developed a microfluidic based biosensor for detecting troponin T. A microfluidic channel integrated with an array of gold strips is considered for detecting and quantifying the troponin T in an aqueous solution. A thiol based immobilization/biofunctionalization protocol for detecting troponin T on gold surface is developed to employ on the microfluidic based biosensor. Ellipsometer, Fourier Transform Infrared Spectroscopy and Contact angle measurement system are used to characterize the surface properties at each stage of immobilization to confirm the accuracy of process. Change in fluorescence intensity along the length of the microchannel is measured and observed that binding of antigens along the length of the channel is reduced. Effect of troponin T antigen concentration and flow rates on the performance of the microfluidic based biosensor will be the scope of future work of this study.

Bibliography

[1] K. Reddy and S. Yusuf. Emerging epidemic of cardiovascular disease in developing countries. *Circulation*, 97(6):596–601, 1998.

[2] Z. Yang and D. Min Zhou. Cardiac markers and their point-of-care testing for diagnosis of acute myocardial infarction. *Clinical Biochemistry*, 39(8):771–780, 2006.

[3] S. Yusuf, M. Pearson, H. Sterry, S. Parish, D. Ramsdale, P. Rossi, and P. Sleight. The entry ecg in the early diagnosis and prognostic stratification of patients with suspected acute myocardial infarction. *European Heart Journal*, 5(9):690–696, 1984.

[4] S. Foy, I. Kennedy, H. Ikram, C. Low, T. Shirlaw, and I. Crozier. The early diagnosis of acute myocardial infarction. *Australian and New Zealand Journal of Medicine*, 21(3):335–337, 1991.

[5] M. Mascini and S. Tombelli. Biosensors for biomarkers in medical diagnostics. *Biomarkers*, 13(7-8):637–657, 2008.

[6] M. Mohammed and M. Desmulliez. Lab-on-a-chip based immunosensor principles and technologies for the detection of cardiac biomarkers: a review. *Lab Chip*, 11(4):569–595, 2010.

[7] P. Anderson, A. Greig, T. Mark, N. Malouf, A. Oakeley, R. Ungerleider, P. Allen, and B. Kay. Molecular basis of human cardiac troponin t isoforms expressed in the developing, adult, and failing heart. *Circulation Research*, 76(4):681–686, 1995.

[8] A. Qureshi, Y. Gurbuz, and J. H. Niazi. Biosensors for cardiac biomarkers detection: a review. *Sensors and Actuators B: Chemical*, 171:62–76, 2012.

[9] J. Liu, C. Chen, T. Ikoma, T. Yoshioka, J. Cross, S. Chang, J. Tsai, and J. Tanaka. Surface plasmon resonance biosensor with high anti-fouling ability for the detection of cardiac marker troponin T. *Analytica Chimica Acta*, 703(1):80–86, 2011.

[10] N. S. K. Gunda, S. K. Mitra, and V. R. Rao. Fabrication of dielectrophoretic microfluidic device. *ASME Conference Proceedings*, pages 113–119, 2009.

[11] N. S. K. Gunda and S. K. Mitra. Experimental investigation of dielectrophoretic behavior of myoglobin and silica particles on a microelectrode chip. *ASME 2010 8th International Conference on Nanochannels, Microchannels, and Minichannels Collocated with 3rd Joint US-European Fluids Engineering Summer Meeting, ICNMM2010*, (PARTS A AND B):1427–1433, 2010.

[12] N. S. K. Gunda and S. K. Mitra. Microfluidics for detection of myoglobin in blood samples. volume 35, pages 57–64, 2011.

[13] R. Wang, H. Kreuzer, and M. Grunze. Molecular conformation and solvation of oligo (ethylene glycol)-terminated self-assembled monolayers and their resistance to protein adsorption. *The Journal of Physical Chemistry B*, 101(47):9767–9773, 1997.

[14] J. A. Dean. Lange chemistry handbook. *McGraw-Hill, Inc*, 4, 1999.

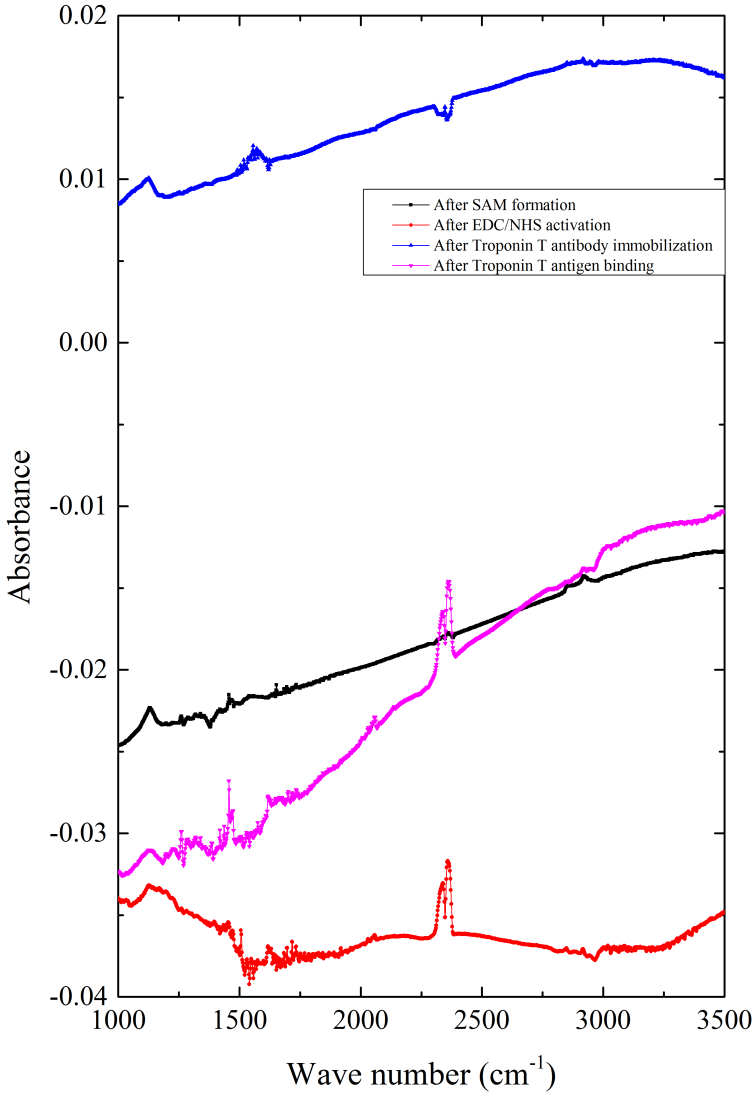

Figure 6.2: Representative FTIR spectra of different layers of immobilization process

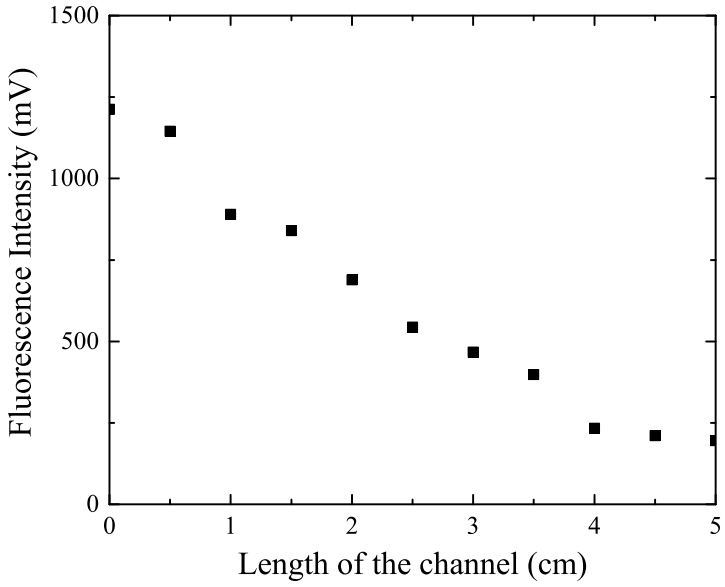

Figure 6.3: Variation of fluorescence intensity of FITC tagged detection antibodies of troponin T along the length of the channel

Chapter 7

Capillary Based Biofunctionalization of Microcantilever Arrays [1]

7.1 Overview

In Chapter 6, we developed and optimized immobilization protocol for detecting troponin T on gold surface. We detected the signal with fluorescence reader or microscopy. However, one can use other type of detection system such as cantilever platform. Cantilever systems are very useful for high sensitive measurements as well as for multi-analyte detection. Hence, in the present work, we focused on biofunctionalization of cantilever surfaces for multi-analyte detection. The present study demonstrate the challenges and opportunities available for functionalization of microcantilever arrays and address the challenges by proposing an innovative capillary action based functionalization using on-chip V-grooves connected to flexible capillaries. Cantilever array chip comprising 8 cantilevers spaced at 250 μm distance is simultaneously functionalized with different biomolecules by inserting into dimensional matched V-groove arrays. We demonstrated that a simple on-chip V-groove capillary functionalization is an easy, effective and highly repeatable by performing a standard sandwich immunoassay for detecting various cardiac markers such as myoglobin and troponin T.

[1] A version of this chapter has been published. N. S. K. Gunda and S. K. Mitra, Journal of Electrochemical Society, 161(2):B3167, 2014.

7.2 Introduction

Microcantilever based sensing system is one of the promising technologies available in micro/nanotechnology for ultra-high sensitive, real-time and label-free detection [1–12]. The sensing principle in such systems is based on bending or change in resonance frequency of cantilever due to change in surface stress because of adsorption of molecules. There are some challenges while using these microcantilevers for sensing biomolecules in liquid samples. Problems like effect of variations in pH, ionic and temperature of liquid samples and effect of hydrodynamic forces on cantilevers making them vibrate or dampen, which in turn provide some unwanted sensing signals [1, 2, 8, 13, 14]. Also, the method of sensing layer formation on the cantilever surface affects the sensing signals obtained from cantilever measurements [1, 2, 8, 13, 14]. By taking differential detection signals between reference and sensor cantilevers, one can eliminate such problems [13]. Array of cantilevers are used for such measurements. Such an array of cantilevers can also be used for multi-analyte detection for simultaneous detection of different biomolecules. However, simultaneous detection and differential measurements in solutions using cantilevers within an array is still not yet explored fully due to difficulties in specific parallel biofunctionalization [1–12]. The present work discusses the challenges and opportunities available for parallel biofunctionalization of cantilevers within an array.

Various biofunctionalization methods are available for producing a sensing layer on a cantilever surface, for example, physical adsorption, covalent, and bioaffinity immobilizations [15–17]. Among these methods, the covalent immobilization method using self-assembled monolayer (SAM) of organosilane on silicon surface and SAM of thiol on a gold surface have a great potential and advantages compared to others. The immobilization of the antibody is a critical step in the development of highly sensitive measurements [1, 2, 8, 15]. To develop a high quality sensing layer on a cantilever surface, it is important that the biomolecules are immobilized with a high density while maintaining a sufficient distance between each biomolecule. The biomolecule needs to be immobilized in such a manner that the structural integrity and the organization of the biomolecule at the interface are maintained while ensuring that the non-specific adsorption of the biomolecules

is minimal in order to improve detection performance. The method of covalent immobilization provides a uniform, homogenous, highly dense, properly oriented biomolecules on a given surface, which will enhance the sensitivity of the cantilevers. However, performing such immobilization methods on an array of microcantilevers for parallel biofunctionalization is a challenging task.

Cantilevers are operated in static and dynamic modes based on type of measurement. Static mode is used for measuring cantilever bending and dynamic mode is used for measuring change in resonance frequency. Based on the mode, the cantilevers are required to be functionalized on one side or both sides of the cantilever surface. The process of specific functionalization on one side/both sides of the cantilever surface with different sensing layers on an array of cantilevers is complex and challenging.

Pre-coating of cantilever surfaces with gold or polymer layers for biofunctionalization can be done with conventional micro/nano fabrication deposition methods such as spin coating, thermal evaporation, electron-beam-assisted evaporation, electrospray, vacuum deposition, air-brush spraying and shadow mask [1, 2, 8, 18–22]. All these methods have several limitations such as time consuming and require skillful handling [1, 2]. Moreover these methods are not useful for parallel functionalization of cantilevers and not possible for direct deposition of biomolecules.

Advanced techniques like inkjet spotting/printing is available for dispensing the drops of functionalized solutions on the cantilever surface [1, 2, 13, 23–25]. These advanced techniques are ideal for coating a large number of cantilever arrays. In addition, they are rapid, reliable and very efficient compared to the other methods. One of the main drawbacks of these sophisticated techniques is that they are expensive [1, 2]. Also it requires precise drop deposition, which is often difficult and requires micromanipulator for adjusting the cantilever chip or dispenser. The other main disadvantage with inkjet spotter is rapid evaporation of droplets dispensed on the cantilever surface, which leads to non-uniform coating of the cantilevers. These types of systems are useful for physioadsorption type immobilization methods and may not give repeatable results. A stable, uniform, compact, homogenous layer of biomolecules needs to be immobilizing on the surface for ultra-high sensitive measurements. To achieve such ultra-sensitive and repeatable measurements, biomolecules need to immobilize covalently to the surface of the cantilever where

the individual cantilever needs to expose to thiol/silane solutions (based on the surface) for at least one hour [15–17, 26]. It is not possible to achieve such covalent immobilization with inkjet spotting techniques due to rapid evaporation.

Capillary based microchannels can be used to eliminate some problems with existing techniques. Several researchers [13, 14, 27, 28] used arrays of circular glass capillaries for parallel biofunctionalization of individual cantilevers. These glass capillaries allow the solution in fluid reservoirs to flow on to the cantilever surface through the capillary action. The cantilevers can be incubated for certain period of time for covalent immobilization. The main drawbacks of such systems are requirement of proper sharp cutting of the glass capillaries and aligning them in an array to match the individual cantilevers within the cantilever array. However, the key advantage of any such capillary based system is that it requires no external pumps or energy to deposit/transport biomolecules, thereby reducing the overall power requirements of such sensors and enabling easy integration of the entire sensor platform on a chip.

The present work proposes a similar method of using capillary forces to achieve biofunctionalization of cantilever arrays with V-groove chips integrated with flexible fused silica capillaries. There are several challenges for parallel functionalization with the proposed technique, which are discussed in details here. This in turn provides tremendous opportunity to overcome these challenges and realize a reliable biofunctionalization technique for cantilever array. As an example of overcoming the challenges related to simultaneous functionalization of two different cantilever surfaces in a given array, here we have demonstrated the parallel functionalization of cantilevers within the cantilever array chip for simultaneous detection of two different cardiac markers (Myoglobin and Troponin T).

7.3 Materials and methods

7.3.1 Materials and chemicals

Microcantilever array (8 cantilevers per chip) chips were obtained from Micromotive GmbH, Mainz, Germany. Cantilevers are made of silicon material with $\sim 1 \pm 0.05\ \mu m$ thick, $\sim 90 \pm 2\ \mu m$ width and $\sim 500 \pm 4\ \mu m$ length. The pitch between two adjacent cantilevers in the array is 250 μm. The top surface of the

cantilevers was coated with 2 nm chromium layer, followed by a 20 nm gold layer. The gold layer was used to immobilize the biomolecules with thiol chemistry. Silicon V-groove (8channel array to match the number of cantilevers in the array) chips with a pitch of 250 μm between adjacent grooves and the Pyrex lids for the V-groove were acquired from OZ Optics Ltd., Ottawa, ON, Canada. Flexible fused silica capillary tubing of $\sim 100 \pm 4$ μm inner diameter and $\sim 238 \pm 8$ μm outer diameter was purchased from Polymicro Technologies, Molex Incorporated, Lisle, IL USA. Microcentrifuge tubes of 1.5 ml size were purchased from Fisher Scientific, Canada.

Human myoglobin antigens, myoglobin capture antibodies and myoglobin detection antibodies were obtained from Biospacific, Inc., Emeryville, CA, USA. Cardiac troponin T antigens, troponin T capture antibodies and troponin T detection antibodies were purchased from Sigma Aldrich, St. Louis, MO, USA. Fluorescein isothiocyanate (FITC) kits for coating detection antibodies of myoglobin and troponin T were procured from Innova Biosciences, Babraham, Cambridge, United Kingdom. 11-mercapto-1-undecanoic acid (MUA), 11-mercaptoundecanoal (MU), 1-Ethyl-3-[3-dimethylaminopropyl] carbodiimide hydrochloride (EDC) and N-hydroxysulfosuccinimide (NHS) were purchased from Sigma Aldrich. Other consumable reagents such as ethanol, phosphate buffer saline (PBS, pH 7.4) were obtained from Sigma Aldrich and were used without any purification.

7.3.2 Experimental set-up

Figure 7.1 shows the experimental set-up required for functionalizing the cantilever arrays. The set-up allows simultaneous functionalization of 8 cantilevers within an array with different biomolecules. The cantilevers are inserted into V-groove chips (with or without lid) using precise adjustable stage (3-Axis NanoMax Stage, Differential Drives, Closed-Loop Piezos with 20 nm positional resolution, Thorlabs Inc., Newton, NJ, USA). Using fused silica capillaries, the functionalization solutions, kept in fluid reservoirs (microcentrifuge tubes), are dispensed into V-grooves through capillary action to functionalize the cantilevers. Custom made microscope (0.5X-50X magnification, 9M pixel CMOS image sensor, adjustable stand, optical light source with fiber optics waveguide) is used to monitor the insertion of cantilever into V-groove chips as well as flow of functionalization solu-

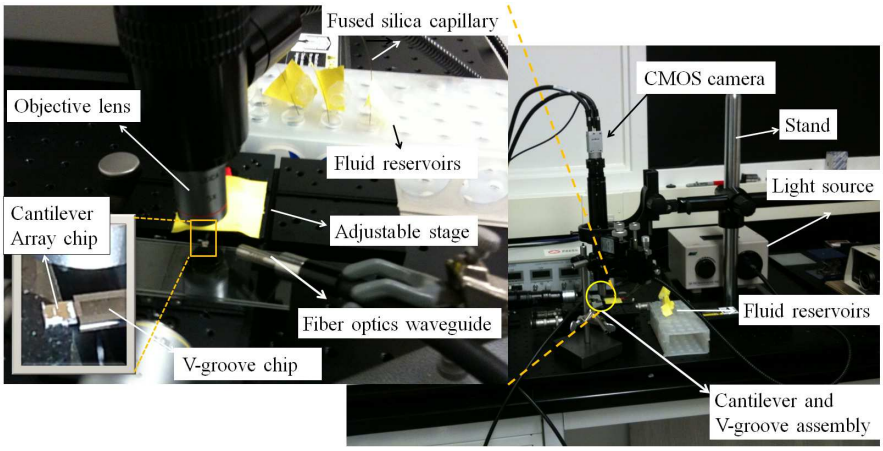

Figure 7.1: Experimental set-up for biofunctionalization of cantilevers with V-groove array chip.

tions on cantilevers. Figure 7.2 presents the scanning electron microscopic (SEM ZEISS, Germany) images of the cantilever arrays and V-groove array chips used in this work.

7.3.3 Biofunctionalization of cantilevers

The entire array containing individual cantilevers is chemically treated with mixture of 4mM of MUA and 1mM of MU solutions and activated with EDC/NHS procedure for immobilizing the biomolecules of interest. The detailed procedure for SAM coating and EDC/NHS activation on gold coated surfaces can be found in Gunda et al. [29, 30]. Figure 7.3 depicts the schematic illustration of cantilever biofunctionalization for detecting cardiac markers. The method involves: (a) cleaning of gold coated silicon cantilevers with UV/Ozone treatment; (b) treating cantilevers with SAM and activating with EDC/NHS procedure; (c) immobilization of capture antibodies (e) addition of antigen biomolecules; and (f) detection of antigens using FITC-tagged detection antibodies. Steps (b) to (f) are carried out by transporting the required analytes using capillary forces with the V-groove array chip.

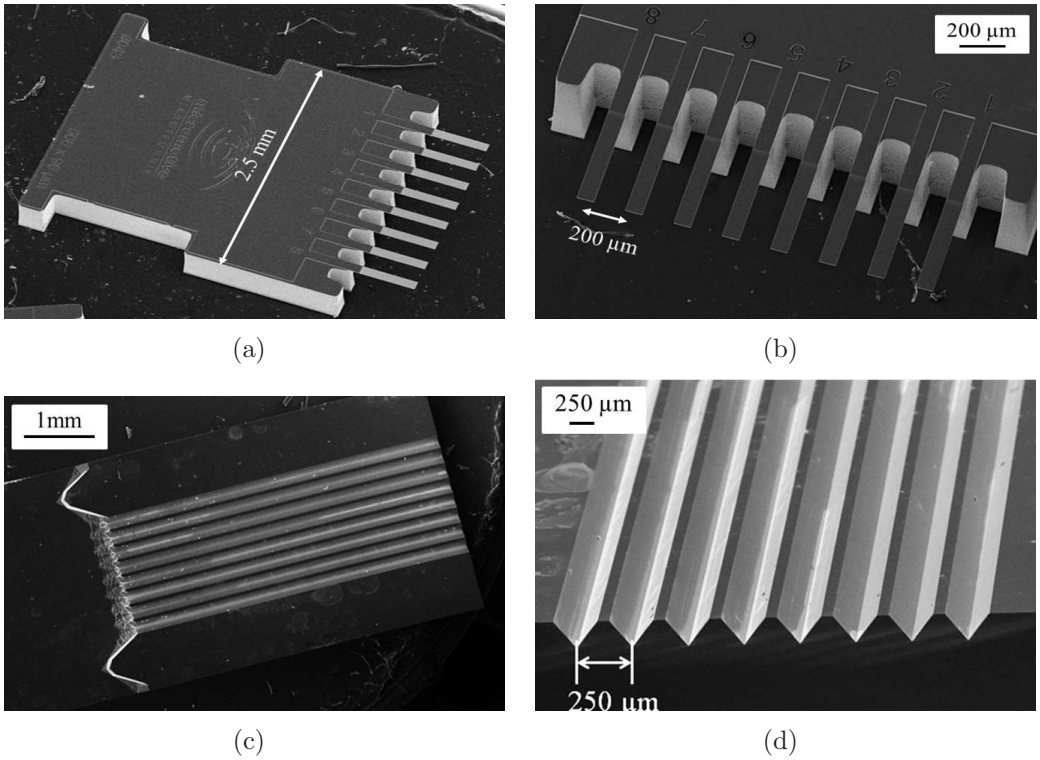

Figure 7.2: SEM images of (a) entire cantilever array chip, (b) exploded view of cantilevers arrays, (c) top view of V-groove array chip, and (d) side view of V-groove array chip.

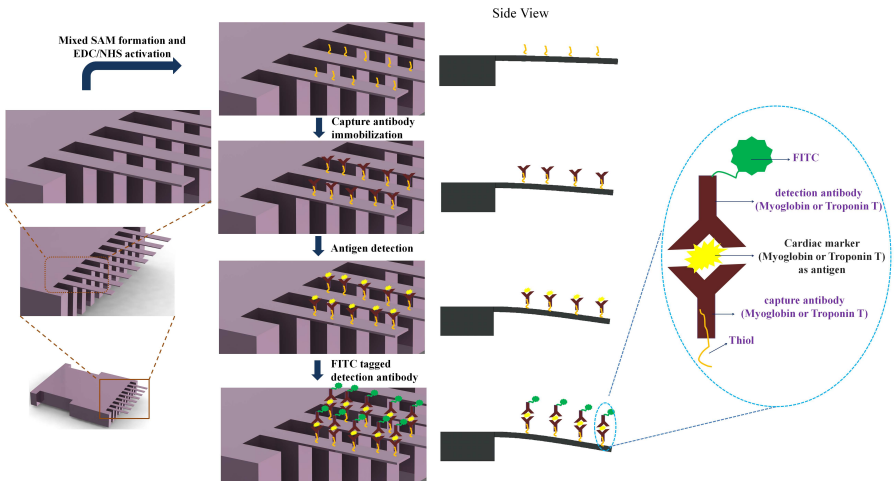

Figure 7.3: Schematic illustration of cantilever biofunctionalization for detecting cardiac markers. The method involves: (a) cleaning of gold coated silicon cantilevers with UV/Ozone treatment; (b) treating cantilevers with SAM and activating with EDC/NHS procedure; (c) immobilization of capture antibodies (e) addition of antigen biomolecules; and (f) detection of antigens using FITC-tagged detection antibodies.

7.4 Challenges with cantilever biofunctionalization

In this work, capillary-based functionalization through V-groove chip is developed for immobilizing the respective antibodies of cardiac markers on the gold-coated top surface of the cantilever. Further cardiac markers (antigens) are flowed on the cantilevers by capillary forces to react with respective antibodies available on the cantilever array. By using FITC tagged antibodies, respective cardiac markers are detected.

Several problems were faced in the biofunctionalization of cantilevers. Here we highlight some of the key issues related to this process. It is found that the individual cantilever in the array bends along the principal axis while inserting them into the V-grooves. Figure 7.4 shows such bending event of the cantilevers while inserting into the V-grooves without lid. This may break the cantilevers and may result in the non-uniform immobilization of biomolecules. Proper lid is required to close the V-groove chip to eliminate such bending of the cantilever.

It is observed that sometimes solution overflows on the cantilevers. Figure 7.5 shows the overflow of solution on individual cantilever as well as on entire cantilevers. Because of this overflow, solutions will mix and there will be a possibility of cross contamination of cantilevers. It is not possible to use it for simultaneous detection of different biomolecules. Figure 7.6 shows the fluorescent images of improper binding of FITC tagged myoglobin antibodies on the cantilevers after immunoassay in V-groove array chip with Pyrex lid assembly. Figure 7.6(a) shows the improper binding of FITC tagged myoglobin antibodies due to solution overflow on individual cantilever. It is observed that more number of antibodies bound to the cantilever surface at the location of solution overflow. Figure 7.6(b) shows the improper binding of FITC due to solution overflow on entire cantilever. It is observed that more number of antibodies get attached to the tips of a given cantilever surface and to its neighbors.

7.5 Solutions to overcome the challenges

One of the easiest method to resolve the challenges described earlier is to provide an appropriate cover for the V-groove chip, which will allow the enhancement of

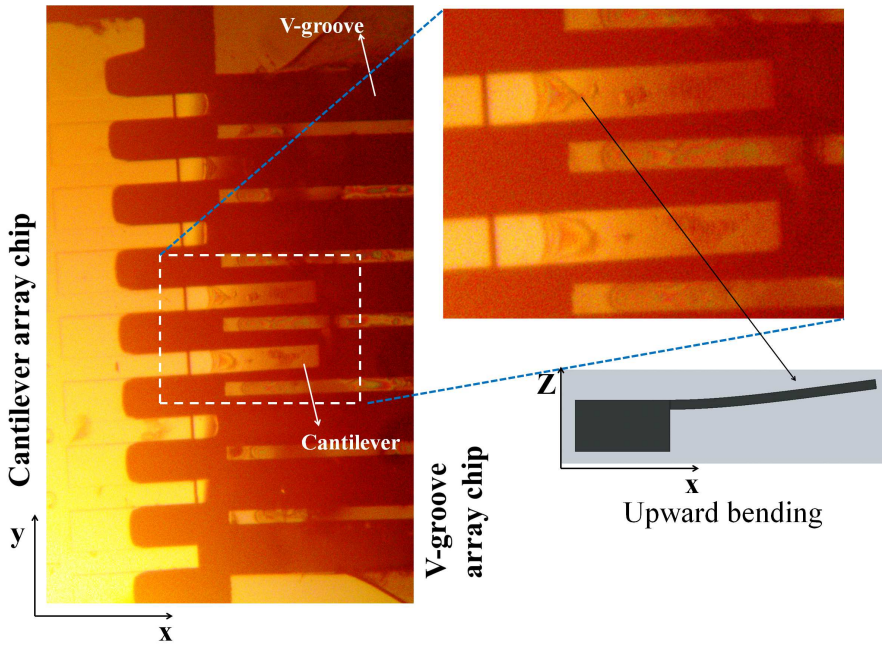

(a)

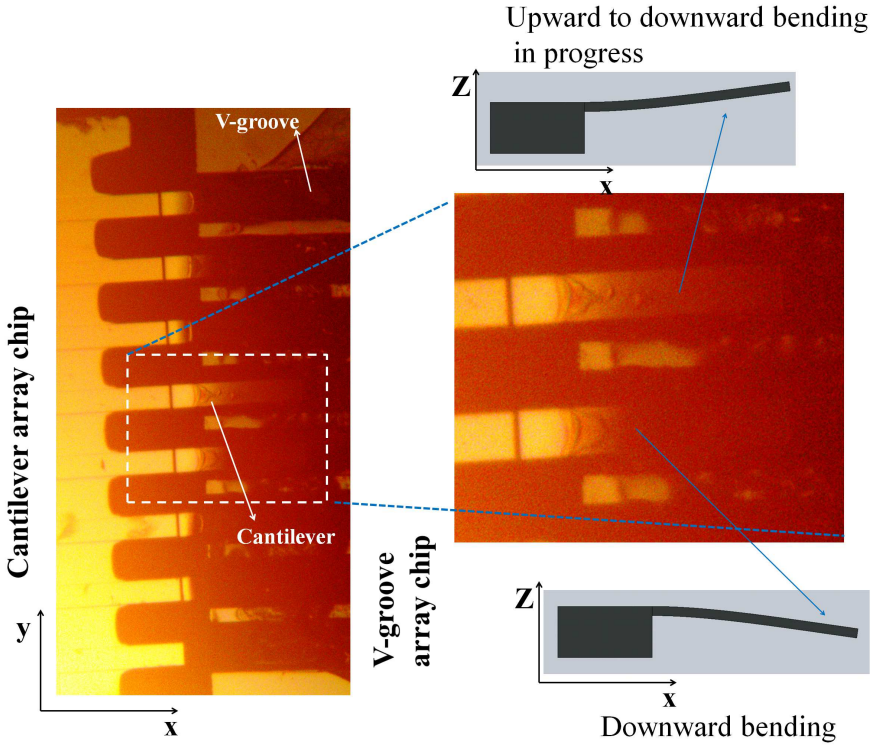

(b)

Figure 7.4: Bending of cantilevers after inserting the cantilevers into V-groove chip without lid: (a) upward bending of cantilevers, and (b) upward to downward bending in progress.

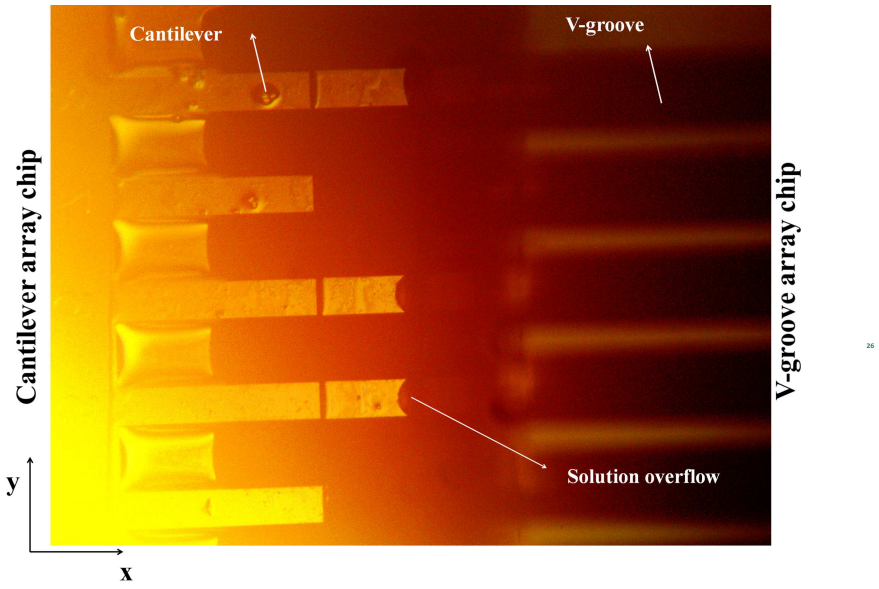

(a)

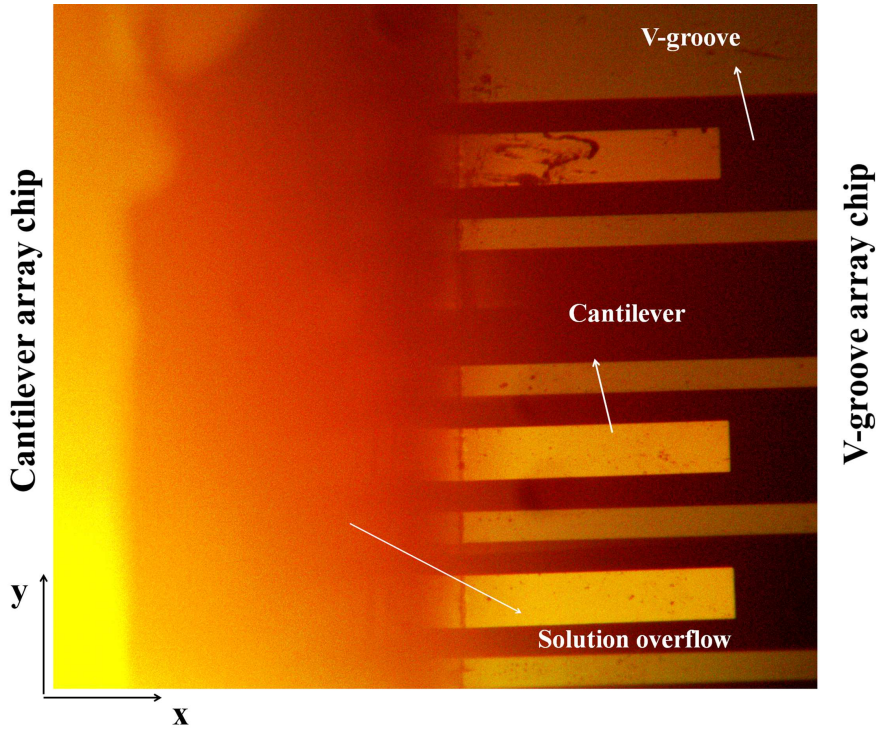

(b)

Figure 7.5: Solution overflow on cantilevers after inserting into V-groove chip with lid: (a) solution overflow on individual cantilever and (b) solution overflow on entire cantilever.

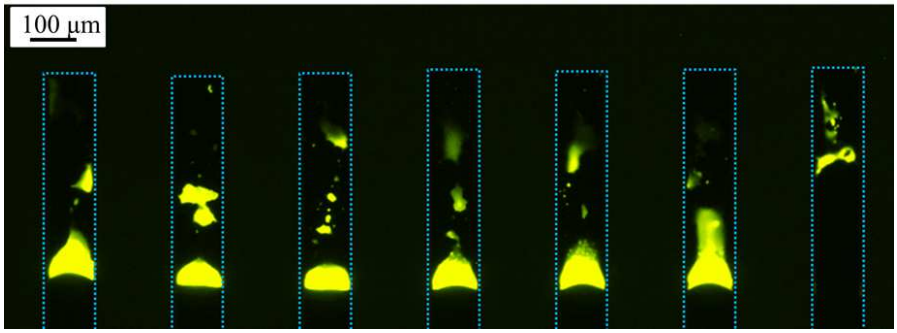

(a)

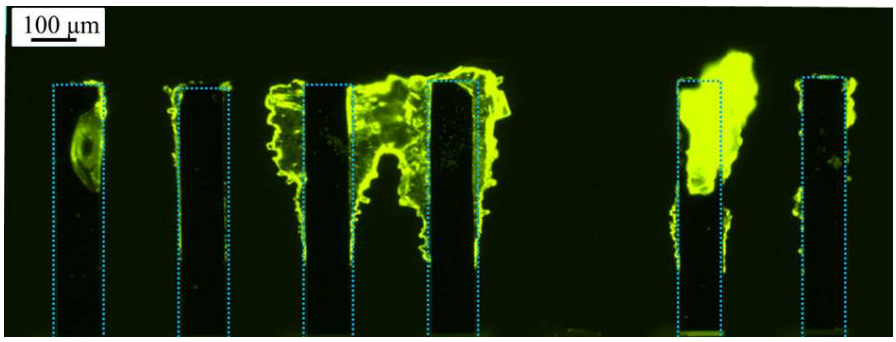

(b)

Figure 7.6: Fluorescent images of improper binding of FITC tagged myoglobin antibodies on the cantilevers after immunoassay in V-groove array chip with Pyrex lid assembly: (a) due to solution overflow on individual cantilever and (b) due to solution overflow on entire cantilever.

the capillary forces. Inside the V-groove, the following forces acts on the liquid column inside the groove, kept on a horizontal plan [31, 32]:

$$\frac{d(MV)}{dt} = F_c + F_v \tag{7.1}$$

where $M = \rho\pi R^2 L$ is the mass of the liquid inside the V-groove, $F_c = 2\pi R\Delta\gamma$ is total capillary force and $F_v = \eta(\partial V/\partial y)LR$ is viscous friction force at the wall. Here R is the effective radius of the V-groove, ρ is the density of solution, η is the viscosity of solution, L is the distance between meniscus to capillary entrance, V is velocity of meniscus, t is capillary filling time and y is the transverse coordinate or the coordinate perpendicular to the capillary walls.

As evident from Eq. 7.1, in order to assist the capillary action, the surface tension force needs to be enhanced, which scales as γR. Hence, by covering the V-groove with an appropriate lid, will essentially increase the surface tension forces required to achieve the necessary capillary transport for this proposed platform.

Figure 7.7 shows the assembly of cantilever array into the V-groove array chip with a covering lid. The cantilever array needs to be inserted into the V-grooves by adjusting the position of the cantilever chip using precise adjustable stage in x, y and z directions. Proper care is required to align the cantilevers to insert into V-groove slots; otherwise there is a chance of breaking the cantilevers. Since the Pyrex lid used for closing the V-groove chip is not bonded permanently, sometimes it may dislocate while inserting the cantilevers into the V-groove chip. This misalignment of lid and V-groove chip may cause overflow of the functionalization solution on the cantilevers (individual cantilever or entire cantilever array). This may lead to the improper immobilization of biomolecules. This type of overflow of solution on cantilevers can be avoided by proper alignment of lid with V-groove chip as well as by slow capillary action, which has been successfully achieved in this work. Figure 7.8 shows the fluorescent images of properly bound FITC tagged myoglobin antibodies on the cantilevers after immunoassay in V-groove array chip with Pyrex lid assembly.

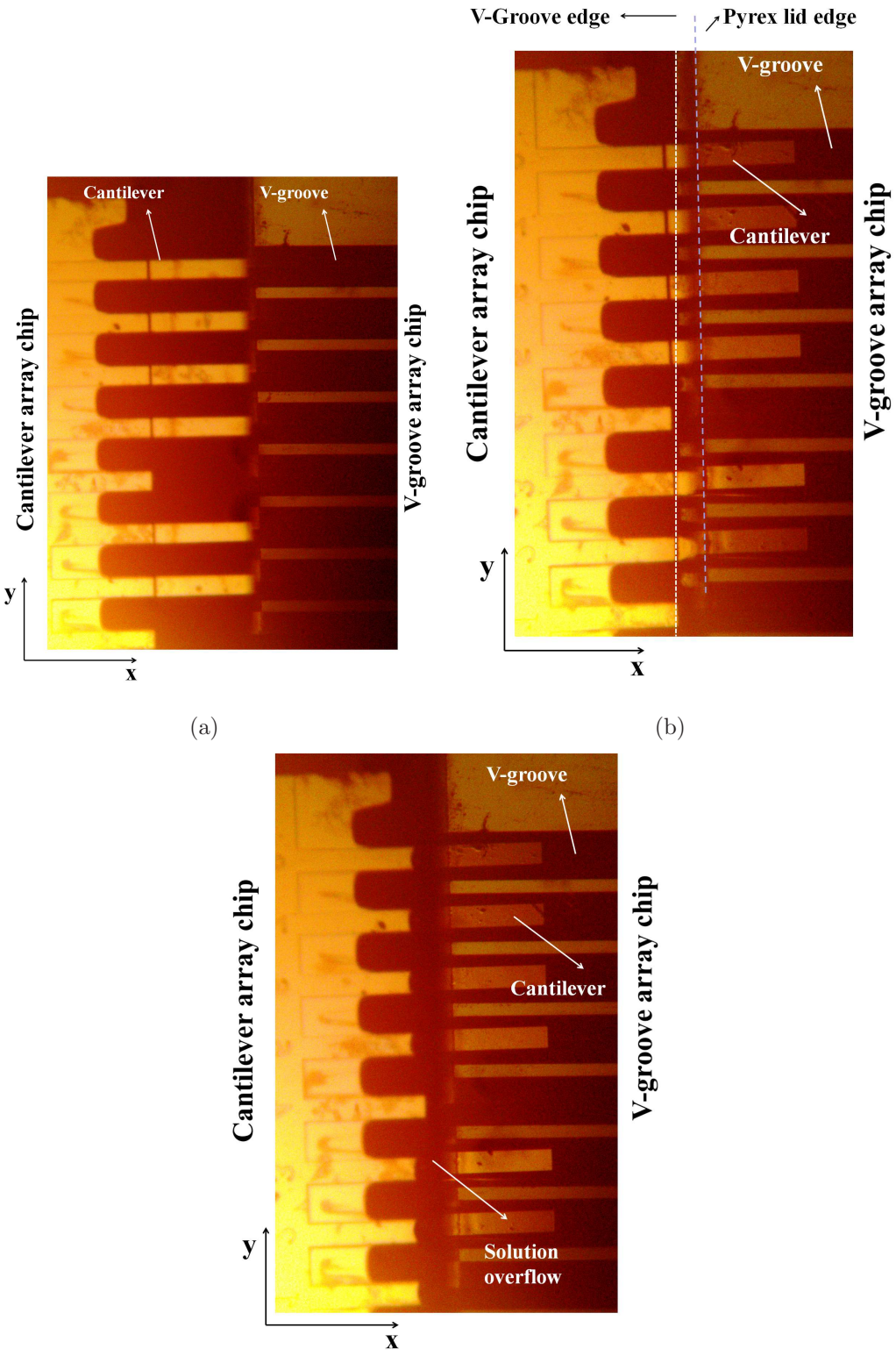

Figure 7.7: Assembly of cantilevers into V-groove chip with Pyrex lid: (a) partial insertion of cantilever array into V-groove array chip, (b) complete insertion of cantilever array into V-groove chip and misalignment of V-groove chip edge and Pyrex lid, and (c) solution overflow on individual cantilevers.

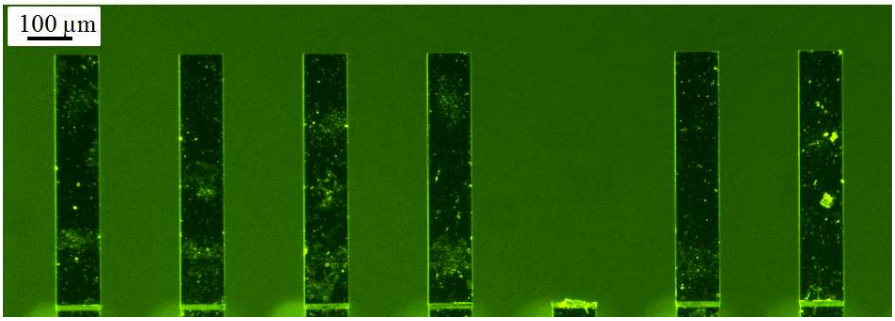

Figure 7.8: Fluorescent images of properly bound FITC tagged myoglobin antibodies on the cantilevers after immunoassay in V-groove array chip with Pyrex lid assembly.

7.6 Future directions

The future work will be to use the developed capillary based functionalization to build reliable multi-analyte detection systems using cantilever platforms. Here, as a proof of concept, we are presenting the simultaneous detection of myoglobin and troponin T using cantilever and V-groove chip with lid assembly. Figure 7.9 shows the fluorescent images of FITC tagged myoglobin detection antibodies and troponin T antibodies on the cantilevers after immunoassay in V-groove array chip with Pyrex lid assembly. Figure 7.9(a) shows the fluorescent images of the cantilevers before washing the cantilever chips with PBS after FITC tagged antibodies bound to respective antigens on the cantilever. Figure 7.9(b) shows the fluorescent images of the cantilevers after washing the cantilever chips with PBS after FITC tagged antibodies bound to respective antigens on the cantilever. Hence, by judicious use of capillary forces coupled with proper alignment of the V-groove and the cantilever array, one can achieve reliable biofunctionalization of individual cantilevers in a given array. The developed method could be exploted as an orthogonal sensing platform to detect multiple analytes simultaneously through selective biofunctionalization, as shown in Fig. 7.9 for two different cardiac markers.

7.7 Summary

In this work, we demonstrated the parallel biofunctionalization of cantilever arrays with V-groove array chips. We pointed to the challenges faced in functionalization and explored the possible mechanisms to uniformly functionalize the cantilevers.

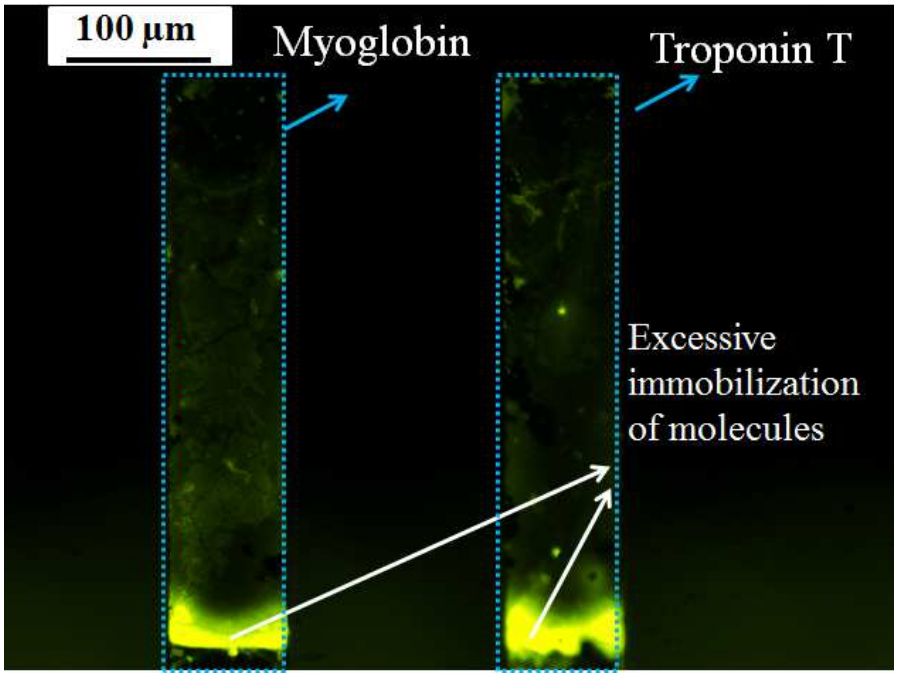

(a)

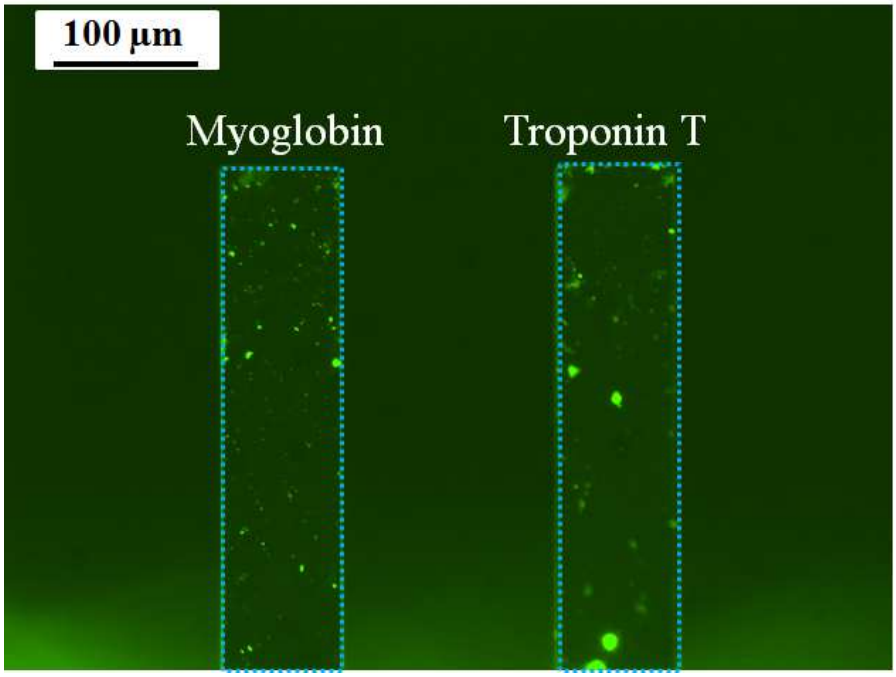

(b)

Figure 7.9: Fluorescent images of FITC tagged myoglobin antibodies and troponin T antibodies on the cantilevers after immunoassay in V-groove array chip with Pyrex lid assembly. (a) Before washing the cantilever chips with PBS after FITC tagged antibodies bound to respective antigens on the cantilever, and (b) after washing the cantilever chips with PBS after FITC tagged antibodies bound to respective antigens on the cantilever.

Challenges like cantilever upward bending, analyte over flow on individual cantilevers and even over flow on entire cantilever array are observed. Such problems are eliminated by proper assembly of V-groove chip with lid that can provide proper capillary action to flow the functionalized solution on cantilever surface for proper functionalization. We performed a standard sandwich immunoassay using the developed method for simultaneous detection myoglobin and troponin T cardiac markers.

Bibliography

[1] H. Lang, M. Hegner, and C. Gerber. Nanomechanical cantilever array sensors. *Springer Handbook of Nanotechnology*, pages 443–460, 2007.

[2] H. P. Lang, M. Hegner, and C. Gerber. Cantilever array sensors for bioanalysis and diagnostics. *Nanobiotechnology II: More Concepts and Applications*, pages 175–195, 2007.

[3] K. S. Hwang, S.-M. Lee, S. K. Kim, J. H. Lee, and T. S. Kim. Micro-and nanocantilever devices and systems for biomolecule detection. *Annual Review of Analytical Chemistry*, 2:77–98, 2009.

[4] A. Boisen and T. Thundat. Design & fabrication of cantilever array biosensors. *Materials Today*, 12(9):32–38, 2009.

[5] J. Fritz. Cantilever biosensors. *Analyst*, 133(7):855–863, 2008.

[6] R. Raiteri, M. Grattarola, H.-J. Butt, and P. Skládal. Micromechanical cantilever-based biosensors. *Sensors and Actuators B: Chemical*, 79(2):115–126, 2001.

[7] K. M. Goeders, J. S. Colton, and L. A. Bottomley. Microcantilevers: sensing chemical interactions via mechanical motion. *Chemical Reviews*, 108(2):522–542, 2008.

[8] M. Alvarez and L. M. Lechuga. Microcantilever-based platforms as biosensing tools. *Analyst*, 135(5):827–836, 2010.

[9] J. Thaysen, M. H. Jacobsen, and L. K. Nielsen. Nanomechanical sensor platform based on piezo-resistive cantilevers. *2005 NSTI Nanotechnology Conference and Trade Show*, pages 262–5, 2005.

[10] S. Xu and R. Mutharasan. Cantilever biosensors in drug discovery. *Expert Opinion on Drug Discovery*, 4(12):1237–1251, 2009.

[11] C. Ziegler. Cantilever-based biosensors. *Analytical and Bioanalytical Chemistry*, 379(7-8):946–959, 2004.

[12] L. G. Carrascosa, M. Moreno, M. Álvarez, and L. M. Lechuga. Nanomechanical biosensors: a new sensing tool. *TrAC Trends in Analytical Chemistry*, 25(3):196–206, 2006.

[13] A. Bietsch, J. Zhang, M. Hegner, H. P. Lang, and C. Gerber. Rapid functionalization of cantilever array sensors by inkjet printing. *Nanotechnology*, 15(8):873, 2004.

[14] Y. Arntz, J. Seelig, H. Lang, J. Zhang, P. Hunziker, J. Ramseyer, E. Meyer, M. Hegner, and C. Gerber. Label-free protein assay based on a nanomechanical cantilever array. *Nanotechnology*, 14(1):86, 2003.

[15] P. Jonkheijm, D. Weinrich, H. Schröder, C. Niemeyer, and H. Waldmann. Chemical strategies for generating protein biochips. *Angewandte Chemie International Edition*, 47(50):9618–9647, 2008.

[16] F. Rusmini, Z. Zhong, and J. Feijen. Protein immobilization strategies for protein biochips. *Biomacromolecules*, 8(6):1775–1789, 2007.

[17] F. Tao and S. Bernasek. *Functionalization of semiconductor surfaces*. John Wiley & Sons, 2012.

[18] R. Berger, C. Gerber, J. Gimzewski, E. Meyer, and H. Güntherodt. Thermal analysis using a micromechanical calorimeter. *Applied Physics Letters*, 69(1):40–42, 1996.

[19] L. Scandella, G. Binder, T. Mezzacasa, J. Gobrecht, R. Berger, H. Lang, C. Gerber, J. Gimzewski, J. Koegler, and J. Jansen. Combination of single crystal zeolites and microfabrication: Two applications towards zeolite nanodevices. *Microporous and Mesoporous Materials*, 21(4):403–409, 1998.

[20] R. Berger, C. Gerber, H. Lang, and J. Gimzewski. Micromechanics: A toolbox for femtoscale science:towards a laboratory on a tip. *Microelectronic Engineering*, 35(1):373–379, 1997.

[21] H. Lang, R. Berger, F. Battiston, J.-P. Ramseyer, E. Meyer, C. Andreoli, J. Brugger, P. Vettiger, M. Despont, T. Mezzacasa, et al. A chemical sensor based on a micromechanical cantilever array for the identification of gases

and vapors. *Applied Physics A: Materials Science & Processing*, 66:S61–S64, 1998.

[22] M. Baller, H. Lang, J. Fritz, C. Gerber, J. Gimzewski, U. Drechsler, H. Rothuizen, M. Despont, P. Vettiger, F. Battiston, et al. A cantilever array-based artificial nose. *Ultramicroscopy*, 82(1):1–9, 2000.

[23] A. Bietsch, M. Hegner, H. P. Lang, and C. Gerber. Inkjet deposition of alkanethiolate monolayers and dna oligonucleotides on gold: evaluation of spot uniformity by wet etching. *Langmuir*, 20(12):5119–5122, 2004.

[24] D. Lange, C. Hagleitner, A. Hierlemann, O. Brand, and H. Baltes. Complementary metal oxide semiconductor cantilever arrays on a single chip: mass-sensitive detection of volatile organic compounds. *Analytical Chemistry*, 74(13):3084–3095, 2002.

[25] C. Savran, T. Burg, J. Fritz, and S. Manalis. Microfabricated mechanical biosensor with inherently differential readout. *Applied Physics Letters*, 83(8):1659–1661, 2003.

[26] N. S. Kale, M. Joshi, P. Nageswara Rao, S. Mukherji, and V. Ramgopal Rao. Bio-functionalization of silicon nitride-based piezo-resistive microcantilevers. *Sadhana (Academy Proceedings in Engineering Sciences)*, 34(4):591–597, 2009.

[27] J. Fritz, M. Baller, H. Lang, T. Strunz, E. Meyer, H.-J. Güntherodt, E. Delamarche, C. Gerber, and J. Gimzewski. Stress at the solid-liquid interface of self-assembled monolayers on gold investigated with a nanomechanical sensor. *Langmuir*, 16(25):9694–9696, 2000.

[28] R. McKendry, J. Zhang, Y. Arntz, T. Strunz, M. Hegner, H. P. Lang, M. K. Baller, U. Certa, E. Meyer, H.-J. Güntherodt, et al. Multiple label-free biodetection and quantitative dna-binding assays on a nanomechanical cantilever array. *Proceedings of the National Academy of Sciences*, 99(15):9783–9788, 2002.

[29] N. S. K. Gunda and S. K. Mitra. Microfluidics for detection of myoglobin in blood samples. *ECS Transactions*, 35(7):57–64, 2011.

[30] N. S. K. Gunda, S. S. Roy, S. K. Mitra, and M. Singh. 2.2. 6 developing electrochemical impedance immunosensor for the detection of myoglobin. *Tagungsband*, pages 181–184, 2012.

[31] L. Joly. Capillary filling with giant liquid/solid slip: dynamics of water uptake by carbon nanotubes. *The Journal of Chemical Physics*, 135(21):214705, 2011.

[32] S. Das, P. R. Waghmare, and S. K. Mitra. Early regimes of capillary filling. *Physical Review E*, 86(6):067301, 2012.

Chapter 8

Development of Enhanced Rapid Detection of Total Coliform and *E.coli* [1]

8.1 Overview

In this chapter, we demonstrate an efficient, rapid technique for simultaneous detection of total coliform and *E.coli* in contaminated water samples using specifically formulated dual enzyme substrate chemical reagents. These formulated chemical reagents contain color producing Red-Gal susbtrate (6-Chloro-3-indolyl-β-D-galactoside), fluorescence producing MUG substrate (4-Methylumbelliferyl-β-D-glucuronide, trihydrate), color enhancing oxidizing agent $FeCl_3$ (Ferric chloride) and bacterial enzyme (protein) extracting reagent (B-PER). The proposed method uses microcentrifuge tube to test the preconcentrated water samples with developed chemical reagents which makes the method simple, easy to use and field deployable. The effect of each component of formulated chemical reagents on the rapid detection process is studied in detail. The developed method was also tested with actual water samples collected from different water sources and have shown promising results to be actually implemented as a field deployable solution for limited resource settings.

[1] A version of this chapter has been submitted for publication. N. S. K. Gunda, S. Naciker, M. S. Ghoraishi, S. Bhattacharjee, T. Thundat and S. K. Mitra, Water Research, Under Review, 2014.

8.2 Introduction

Water is one of the key elements required for the sustenance of human life. The most common sources of water are rivers, lakes, ponds, ground water and wells. Often these sources are contaminated by sewage sludge, agricultural wastes, fertilizers, chemicals, organic, inorganic materials, and dead animals. This leads to the growth of many water-borne pathogens including bacteria (e.g. Salmonella, Campylobacter, Shigella, Listeria monocytogenes, Enterobacter and various strains of *Escherichia Coli (E.coli)*), viruses (e.g. poliovirus, coronaviruses, rotavirus, norwalk virus and hepatitis), protozoa (e.g. Cryptosporidium), and other intestinal parasites (e.g. Helminths) that have huge implications on public health [18–20]. According to a recent World Health Organization (WHO) statistics, water-borne diseases (e.g. diarrhea, cholera, dysentery, typhoid) constitute roughly 4.1% of total Disability adjusted-life-year (DALY) global burden of diseases, and accounts for roughly 3.4 million deaths annually [2–8]. In United States, as per Center for Disease Control and Prevention (CDC), approximately 73,000 cases of *E.coli* infection are reported each year and approximately 0.08% of these cases results in deaths due to illnesses from these infections [2, 2, 3]. As incidences of repeated outbreaks of contamination of these pathogens (especially total coliform, faecal coliform and some strains of *E.coli*) in various parts of the world have grown to the level of epidemics, there is a pressing need for a rapid, reliable, simple, cost effective field deployable method for the detection of total coliform and *E.coli*, particularly in the developing world and in communities with minimal resources. These tests should be carried out both at the point of source and at the point of use in remote communities. Development of water quality testing methods for all pathogens is complex, expensive, and time-consuming. It is rather simple and cost effective to detect coliform bacteria. Coliform bacteria are organisms that are present in the environment and in the faeces of all warm-blooded animals and humans. There are three different groups of coliform bacteria: (a) total coliform, (b) faecal coliform and (c) *E.coli*, which are all indicators of drinking water quality and have different level of risk. Total coliform group is a large collection of different kinds of bacteria. Faecal coliforms are types of total coliform that exists mostly in faeces. *E.coli* is a sub-group of faecal coliform [18–20]. The presence of

coliform bacteria in water samples is an indicator of the presence of water-borne pathogens and precautionary measures are to be taken in these cases to avoid any outbreaks. The current techniques for detecting coliform in water samples require 24 to 48 hours (often requiring transportation of water samples to a microbiology laboratory), which is time-consuming and require trained professionals to perform the test in a laboratory [7, 55]. There is a necessity for a rapid method to detect total coliform and *E.coli* in water samples at the water source itself (on-site detection) and within minutes to provide early indicator of water quality to the public. Therefore, the main focus of the present work is to develop a simple, easy to use and rapid method for detecting pathogens such as total coliform and *E.coli* in contaminated water samples.

The conventional methods for the detection and enumeration of total coliform and *E.coli* involve filtering the water samples through a membrane filter, followed by counting number of *E.coli* colonies of the filtrate sample using plate counting method [23–26]. The counted colonies can be related to the number of cells based on which the quality of water is determined [23–26]. Even though these types of methods have been the gold standard for more than several decades, they require the use of well-equipped laboratory, often labor-intensive, carried out by qualified individual, and most importantly require more than 24 *hr* and long incubation processes to generate results. Rapid methods of detecting pathogens in water are becoming popular due to the recent surge in micro/nanotechnology. Typically, these methods can produce reliable results within 6 *hr*. With the better understanding of cellular structures combined with significant development in advanced technologies such as nanotechnology, microfluidics [36], and molecular biology [37], several rapid methods were shown to be very effective with promising results. These methods are quantum dots [38], flow cytometry [39], polymerase chain reaction (PCR) [17, 40, 41], DNA microarrays [43–46], surface plasmon resonance (SPR) [47, 48], enzyme linked immunosorbent assay (ELISA) [49], optofluidics [50], electrical impedance [51–53], microcantilevers, nanowires or resonators [35–41] and Fluorescent In-Situ Hybridization (FISH) [54]. The advantages and disadvantages of these novel methods are reviewed in details elsewhere [27–35]. These methods have significant challenges in terms of field deployment, even though they have demonstrated significant reduction in detection time for coliform and *E.coli* with

increased sensitivity and specificity. Of all these methods mentioned here, the best sensitivity is reported to be 1 CFU/100ml detected in 8 hr [52].

The ability to identify biological molecules or pathogens associated with certain enzymatic activity is considered as a possibility to develop a rapid method to detect total coliform and *E.coli* in water samples. *E.coli* is known to secret β-galactosidase and β-glucuronidase enzymes and therefore these enzymes can be used as the markers/indicators for total coliform and *E.coli* pathogens, respectively [53–55]. The detection of enzymes using defined substrate technology is well-known, robust and cost effective. The two most common substrates used for detection of enzymatic activities of *E.coli* are 4-Methylumbelliferyl-β-D-glucuronide, trihydrate (MUG - a fluorogenic substrate) and 6-Chloro-3-indolyl-β-D-galactoside (Red-Gal - a chromogenic substrate) [55, 57, 58]. The MUG molecule contains two key components: 4-Methylumbelliferyl (4-MU) and β-D-glucuronide. The presence of β-glucuronidase enzyme in *E.coli* cleaves this complex MUG molecule and releases fluorogenic compound 4-MU [55, 57, 58]. On the other hand, Red-Gal contains two key components: 6-Chloro-3-indolyl and β-D-galactoside. The presence of β-galactosidase enzyme in total coliform cleaves this complex Red-Gal molecule and releases red color producing 6-Chloro-3-indolyl compound [55, 57, 58]. Though these enzyme based techniques require more than 6 hr, they can be adapted for rapid testing to fit the purpose of deploying these techniques for field tests in remote communities.

Several methods were developed making use of the above mentioned enzymes (β-galactosidase and β-glucuronidase) on their ability of enzymatic reactions with a chromogenic or fluorogenic defined synthetic substrates to indicate presence/absence of water contaminants [54, 57, 57]. Certain methods provide quantitative information of bacteria count as most probable numbers (MPN) [54, 57]. Over the past decade, enzyme based methodologies are accepted as the standard method of analysis for water contaminants [56]. Out of these techniques, some of them claim to be a rapid detection method, achieved by using enhancing or inducing reagents [55, 57, 58]. In the last ten years, United States Environmental Protection Agency (USEPA) has approved ten such methods and they are Colilert (WP200, IDEXX, Westbrook, ME, USA), Colilert-18 (WP200-18, IDEXX, Westbrook, ME, USA), Colisure (WCLS200, IDEXX, Westbrook, ME, USA), m-Coli

Blue 24 (MOOPMCB2, Hach/Millipore Billerica, MA, USA), Readycult Coliforms 100 (EMD Chemicals Inc., Gibbstown, NJ, USA), Chromocult (EMD/Merck Laboratories, Gibbstown, NJ, USA), Coliscan (250MF, Micrology Laboratories, LLC Goshen, IN, USA), E-Colite (ECO-100, Charm Sciences Inc., Lawrence, MA, USA), MI Agar (B14985, S&S Biosciences, Fisher), and Colitag (4600-0012, CPI International, Santa Rosa, CA, USA) [7, 55, 56]. For all these methods, orthonitrophenyl-β-D galactopyranoside (ONPG), p-nitrophenyl-β-D-galactopyranoside (PNPG), 6-bromo-2-naphtyl-β-D-galactopyranoside, chlorophenol red β-galactopyranoside (CPRG), 5-bromo-4-chloro-3-indolyl-β-D-glucuronide (X-Gluc or BCIG) [59], 5-bromo-4-chloro-3-indolyl-β-D- galactopyranoside (X-Gal), SalmonGal, Indoxyl-β-D-galactopyranoside (IBDG) [57], phenolphthalein-mono-β-D- glucuronide complex and 2, 3, 5 triphenyltetrazolium chloride (TTC) have been commonly used as the color producing chromogenic defined enzyme substrates. The 4-methyllumbelliferyl-β-D- galactopyranoside (MUG-Gal) and 4-methyllumbelliferyl- β-D-glucuronide (MUG) [60] have been used as the fluorescence producing fluorogenic defined enzyme substrates [7, 55, 57, 58]. Paper based microfluidic approach has also been reported in the literature where chromogenic substrates are used to detect presence/absence of pathogens [20]. In such methods, antibody coated immunomagnetic beads are used to concentrate the pathogens, thereby reducing the time for analysis [20]. It was reported that 5-20 CFU/ml could be detected within 30 min using paper based system [20].

Recently, the feasibility of detecting *E.coli* in water using MUG substrate and quantifying the fluorescence produced due to reaction between MUG and β- glucuronidase enzyme in *E.coli*, as described earlier, using hand-held fluorescence detector has been demonstrated as a rapid approach [25]. A rapid method with detection time less than one hour can be realized using certain inducers and promoters [20]. By rapid extraction of enzymes from the cell, the detection time can be reduced significantly. This can be achieved by lysing the cells using thermal, electrical, mechanical, acoustic and chemical methods [63]. On the other hand, in the proposed method presented in this chapter, the lysis protocol adopted here is non destructive, which can be achieved quite readily by using reagents such as commercially available bacteria protein extraction reagent (B-PER). Triton X-100, chloroform or sodium dodecyl sulfate (SDS) [63–68] can also be used instead but

SDS often denatures the intracellular proteins.

Table 8.1: Existing combined enzymatic substrates for simultaneous detection of coliform and *E.coli*. The commerical products are denoted by "*".

Product/Reference	**Substrate**	**Time**	**Temperature**	**Concentration**
Kaspar et al.[69]	MUG and MUGal	30-60 min (24 hr incubated before test)	35-37^oC	presence/absence format
Iritani and Inzana [70]	ONPG and MUG	30-60 min (16-24 hr incubated before test)	37^oC	presence/absence format
Edberg et al.[71–73] and Covert et al. [74]	ONPG and MUG	24-48 hr	35^oC	1.2-7.5 $\times$ 10^7 CFU/ml
Grant [23] and Hamilton et al. [56]	m-ColiBlue24 and MUG	20-28 hr	35^oC	1-4 CFU
Tryland and Fiksdal [75]	MUG and MUGal	25 min	44.5^oC	10^5-10^6 CFU/ml
Geissler et al. [76]	CC and LMX	24-48 hr	37^oC	1.4-800 CFU/ml
Nelis and Van Poucke [52]	X-Gal and X-Gluc	8 hr	37^oC / 41.5^oC	1 $CFU/100ml$
Colilert* [7, 55]	ONPG and MUG	24-48 hr	35^oC	presence/absence format
Colilert-18* [7]	ONPG and MUG	18 hr	35^oC	presence/absence format
Colisure* [7, 55]	CPRG and MUG	24-48 hr	35^oC	presence/absence format
m-Coli Blue 24* [7]	TTC and BCIG	24 hr	35^oC	presence/absence format
Readycult Coliforms 100* [7, 55]	X-Gal and MUG	24 hr	35^oC	presence/absence format
Chromocult* [7]	Salmon-Gal and X-Gluc	24 hr	35^oC	presence/absence format
Coliscan* [7]	Red-Gal and X-Gluc	24 hr	35^oC	presence/absence format
E-Colite* [7]	X-Gal and MUG	48 hr	35^oC	presence/absence format
MI Agar* [7]	MUGal and IBDG	24 hr	35^oC	presence/absence format
Colitag* [7]	ONPG and MUG	22-26 hr	35^oC	presence/absence format
Hossain et al. [20]	XG and CPRG	30 min	20^oC	5-20 CFU/ml
Present Work	**Red-Gal, MUG, $FeCl_3$ and B-PER**	1-60 min	37^oC	4.0-4 $\times$ 10^7 CFU/ml

In the proposed rapid detection method presented here, we report a method wherein simultaneous detection of both total coliform and *E.coli* is performed within $1 - 60$ min. The present method uses specially prepared mixture of Red-Gal, MUG, Ferric Chloride ($FeCl_3$) and Bacterial Protein Extraction Reagents (B-PER). Red-Gal is used as the substrate to produce red color on reaction with β-galactosidase enzyme, MUG as the non-fluorogenic substrate to target the β-glucuronidase enzyme producing fluorogenic compound 4-MU, oxidizing agent (Ferric Chloride ($FeCl_3$)) to accelerate the chromogen formation, and the non destructive lysing agent (B-PER) to secret the enzymes [77]. The combination of chromogen and fluorogen compounds for simultaneous detection of total coliform and *E.coli* have already been used in commercial products. Table 8.1 provides a list of such existing commercial systems and other relevant research work in the context of detection of total coliform and *E.coli* in water samples. It was found that these existing methods were not able to detect the total coliform and *E.coli* within minutes. Also, there is a difficulty in using these methods in field due to the requirement of incubators and long wait times to obtain any meaningful test results that can be disseminated to the public. The present method proposed here allows the user to identify the total coliform and *E.coli* by visualizing the change in color or fluorescence within minutes of testing contaminated water. In addition, the ease of the testing method makes it field deployable.

8.3 Materials and methods

8.3.1 Materials

E.coli Castellani and Chalmers (ATCC 11229) was obtained from Stream Technologies, Inc., (Edmonton, Canada) and cultured overnight in Lauryl Tryptose Broth (LTB) at 37^oC. The cell count was then enumerated by the agar plate method and stored at 4^oC for future use. Serial dilutions were formulated in LTB to produce final cell densities in the range of 4.0 - 4×10^7 CFU/ml. The LTB medium (Fisher Scientific, Canada) contained the following reagents (in g/l): Pancreatic Digest of Casein (12.0); Proteose peptone (8.0); Lactose (5.0); Dipotassium phosphate (2.75); Monopotassium phosphate (2.75); sodium chloride (5.0); and Sodium lauryl sulfate (0.1). The LTB medium with MUG (Fisher Scientific, Canada)

contained the following reagents (in g/l): Tryptose (20.0); Lactose (5.0); Potassium phosphate dibasic (2.75); Potassium phosphate monobasic (2.75); Sodium chloride (5.0); Sodium lauryl sulfate (0.1); and MUG (0.05). The LTB (without MUG) was used to culture the bacteria and the LTB with MUG was used for the rapid detection test. The Red-Gal (6-Chloro-3-indolyl-β-D-galactoside) substrate was purchased from Research Organics, Cleveland, OH, USA and the MUG (4-Methylumbelliferyl-β-D-glucuronide, trihydrate) substrate was purchased from Bioworld, Dublin, OH, USA. B-PER was procured from Fisher Scientific, Canada. N,N-Dimethylformamide (DMF) and anhydrous Ferric Chloride ($FeCl_3$) were procured from Sigma-Aldrich, USA. Microcentrifuge tubes and 1.5 ml plastic cuvettes were purchased from Fisher Scientific, Canada. Materials were sterilized whenever necessary.

8.3.2 Equipment

UV-Vis spectrophotometer (Varian Carey 50, Agilent Technologies Canada Inc., Mississauga, ON, Canada) and spectrofluorometer (Varian Carey Eclipse, Agilent Technologies Canada Inc., Mississauga, ON, Canada) were used for measuring intensity of blue fluorescence produced by 4-MU. Plastic cuvettes were used for conducting optical measurements.

8.3.3 Procedure for total coliform and *E.coli* detection in water samples

The combination of chemicals required for the detection of total coliform and *E.coli* consists of four key ingredients, henceforth referred to, as reagents A, B, C and D. Chemical reagent A was prepared by dissolving a mixture of LTB with MUG and Red-Gal in DI Water. Chemical reagent B was B-PER. Chemical reagent C was prepared by dissolving $FeCl_3$ in DI water. Chemical reagent D was prepared by dissolving Red-Gal in a mixture of DMF and DI water. For a single test, we require approximately 100 μl of reagent A and approximately 200 μl of other reagents B, C and D [60, 61]. All the chemical reagents were maintained at pH 7. For more details on preparation of chemical reagents can be found in invention disclosure filed at the University of Alberta [60, 61].

The first step of the test method involves concentrating the pathogen sam-

ples in small volumes, by filtering 100 ml contaminated water samples with a syringe filter, steri-cup filter or any electrical based techniques. A few microliters of reagents A, B, C and D were then added sequentially to 100 μl of the pre-concentrated water sample in a 1.5 ml microcentrifuge tube and mixed in a vortex mixer. The microcentrifuge tube was then incubated for a certain period at 37^oC. A set of mixtures that would serve as negative controls, were also prepared with the reagents and DI water instead of bacteria contaminated water samples and incubated at 37^oC. These mixtures were monitored every 5 min for a period of 2 hours, followed by every one hour for a period of 12 hrs to observe any changes in the color of the solution. The appearance of red color in the tube was immediately observed, indicating the presence of total coliform. However, the presence of *E.coli* could only be indicated with the emission of blue fluorescence, which can be detected with a spectrofluorometer or a fluorescence microscope. It is important to note that such color indicators are for quick qualitative measurements only. The quantitative measurements would require well calibrated look-up tables [7, 55].

Another set of similar solutions were prepared and stored at room temperature to study the effects of temperature on the detection process. To study the effect of concentration of total coliform and *E.coli* bacteria, substrates and ingredients on the rapid detection process, *E.coli* (ATCC 11229) was used as the standard for testing. *E.coli* (ATCC 11229) acts as an indicator for both total coliform as well as *E.coli*, since it has both β-galactosidase and β-glucuronidase enzymes. For validation purposes, known concentrations of *E.coli* (ATCC 11229) were mixed with DI water and used in the present study.

8.4 Results and discussions

The initial experiments were conducted using Red-Gal substrate alone without using any other ingredients to enhance the enzymatic activity. The effect of temperature on the color change due to the enzymatic activity of β-galactosidase with Red-Gal substrate (in absence of any external inducing and promoting reagents) is studied here. Figure 8.1 shows the development of red color in *E.coli* samples (ATCC 11229) with Red-Gal substrates, which are incubated for 12 hr at two specific temperatures, 23^oC and 37^oC, respectively. It was observed that the in-

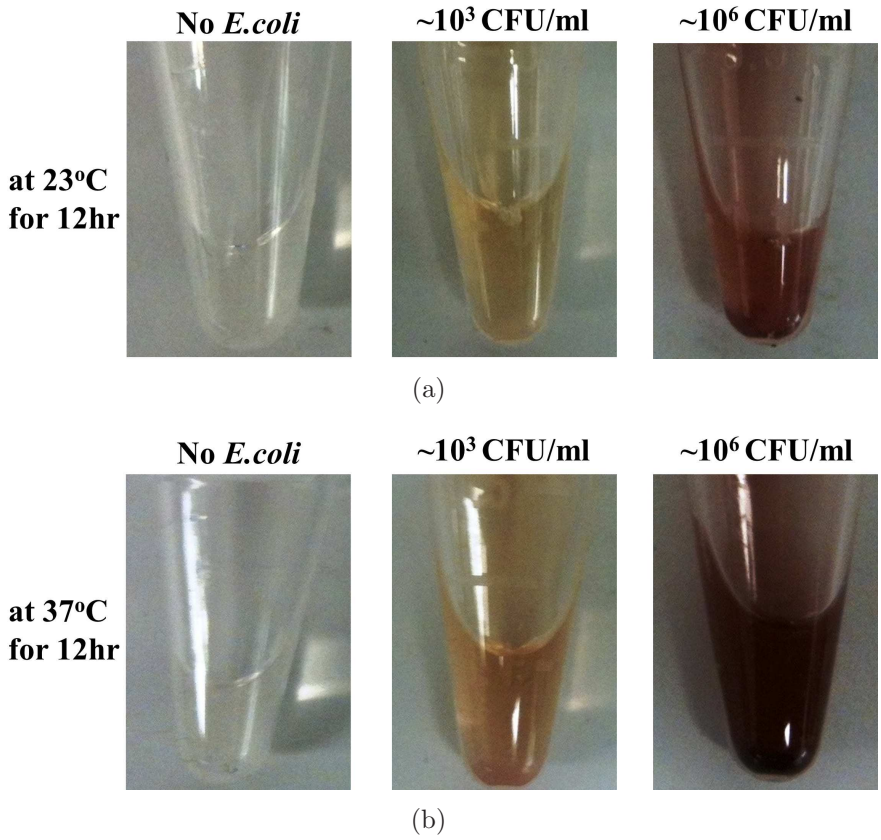

Figure 8.1: Observation of color change in microcentrifuge tube for the enzymatic reaction of *E.coli* with Red-Gal after incubating the samples for 12 *hr* at two specific temperatures: (a) at 23^oC and (b) at 37^oC. Note that the intensity of color change depends on the *E.coli* concentration in the samples.

tensity of the developed color is more for the samples, which were incubated at 37^oC compared to the samples, which were at room temperature (23^oC). The intensity of the color also depends on the concentration of the *E.coli* samples. These initial experiments without inducer and promoter reagents suggest that for rapid detection, an elevated temperature (eg., 37^oC as shown in Fig. 8.1(b)) is required for detection of *E.coli*. However, one needs to be aware that excessive temperature excursions beyond 37^oC can lead to death of the host cells [80, 81].

For the purpose of simultaneous detection of total coliform and *E.coli* from a single water sample, we selected a combination of Red-Gal and MUG. Red-Gal is used as the red color producing enzyme substrate to target the β-galactosidase enzyme in total coliform and MUG is used as the substrate to target β-glucuronidase enzyme in *E.coli* to produce fluorescence by the formation of 4-MU. A review of existing methods [7, 55, 57, 58] suggests that this combination has not been prop-

erly explored earlier. In addition, we used cell lysis detergents to extract the enzymes associated with the *E.coli*. This lysing method can take place within seconds and can induce the enzyme activity immediately to release the colored or fluorescent chemicals for visualization and measurement. As we were using a mixture of reagents (A, B, C, and D), it was worthwhile to investigate the effect of individual reagent on the overall detection process and will provide us with better insight on the choice of such "cocktail" for rapid detection of total coliform and *E.coli* in water samples.

As mentioned earlier, we have added $FeCl_3$ as an oxidizing agent to accelerate the dimerization of 4-Chloro-Indoxyl (which is released after cleaving the Red-Gal by β-galactosidase enzyme) to 4,4'-diChloro-Indigo. Hence, we have added $FeCl_3$ of given concentration to the Red-Gal substrate (described in Fig. 8.1) to understand the effect of such chemicals on the development of color. Figure 8.2 shows the effect of $FeCl_3$ as a color developing agent. It was observed that addition of $FeCl_3$ enhances the color development, which indicates that the $FeCl_3$ may be a good candidate for promoting the color development.

B-PER can also be used to induce the release of the enzymes and thus can reduce the time required for color development. Figure 8.3 shows the development of color due to the presence of mixture of Red-Gal, $FeCl_3$, MUG and B-PER in the microcentrifuge tube for *E.coli* concentration of $\sim 10^3\ CFU/ml$. It was observed that the time required for detection of *E.coli* was drastically decreased by adding all these ingredients.

The appearance of red color in Fig. 8.3 indicates the presence of total coliform (which also includes *E.coli*) and to confirm the specific presence of *E.coli*, one needs to observe the blue fluorescence in the microcentrifuge tubes. The simultaneous detection of both total coliform and *E.coli* was observed within 1 min of incubation at 37^oC for large concentration of *E.coli* such as $4 \times 10^7\ CFU/ml$, whereas for concentration of 4.0 CFU/ml to 40 CFU/ml, the detection time is around 60 mins. It was found that the intensity of red color increases with respect to time up to 10 hr (Fig. 8.3) and then remains constant. It is to be noted that the incubation process is not required for warm climatic regions, where the outside temperature is often around 35^oC. Hence, this technique becomes a rapid field deployable technology for tropical countries, as evident through a recent successful field trial

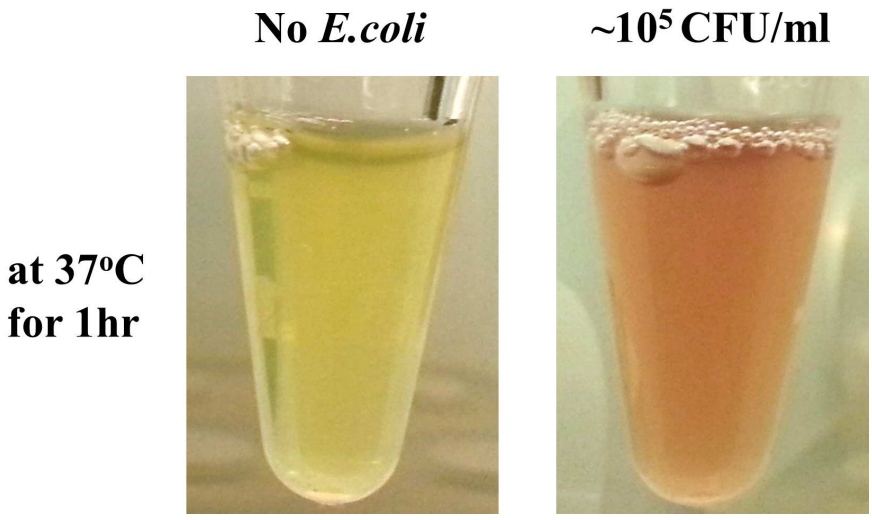

(a)

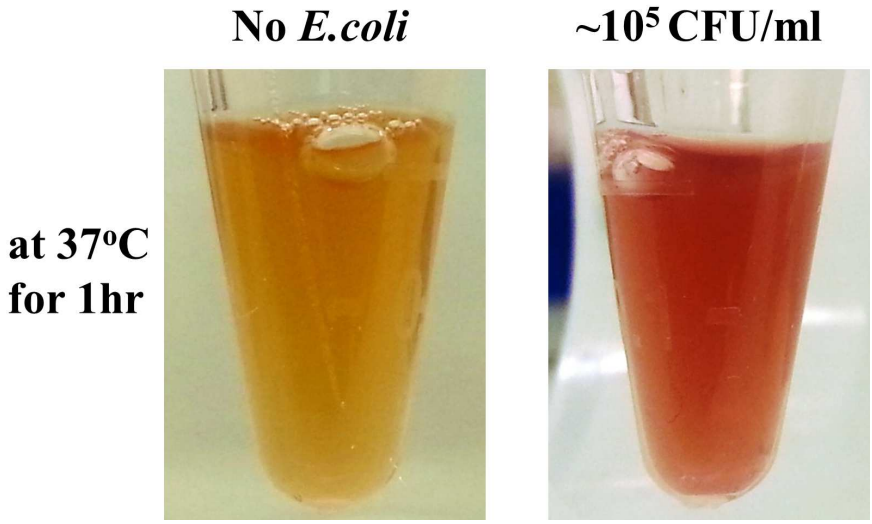

(b)

Figure 8.2: Observation of color change due to the enzymatic reaction of *E.coli* with Red-Gal after incubating the samples for 1 *hr* at 37^oC (a) with 100 μl of $FeCl_3$ and (b) with 200 μl of $FeCl_3$. Note that the color present in sample without any *E.coli* cells represents the baseline color produced by the compound ($FeCl_3$) itself.

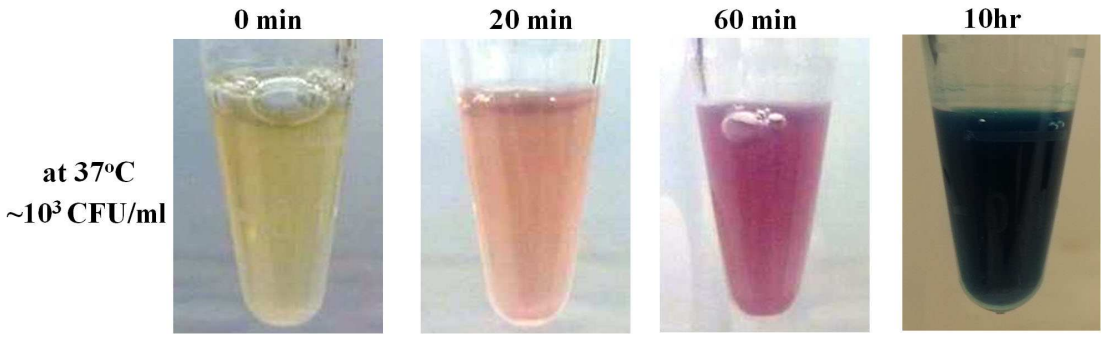

Figure 8.3: Observation of color change due to the enzymatic reaction of *E.coli* of concentration around 10^3 CFU/ml with combination of Red-Gal, MUG, $FeCl_3$ and B-PER which are incubated at 37^oC (a) 0 min; (b) 20 min; (c) 60 min; and (d) 10 hr. Note that the intensity of color change depends on the incubation time.

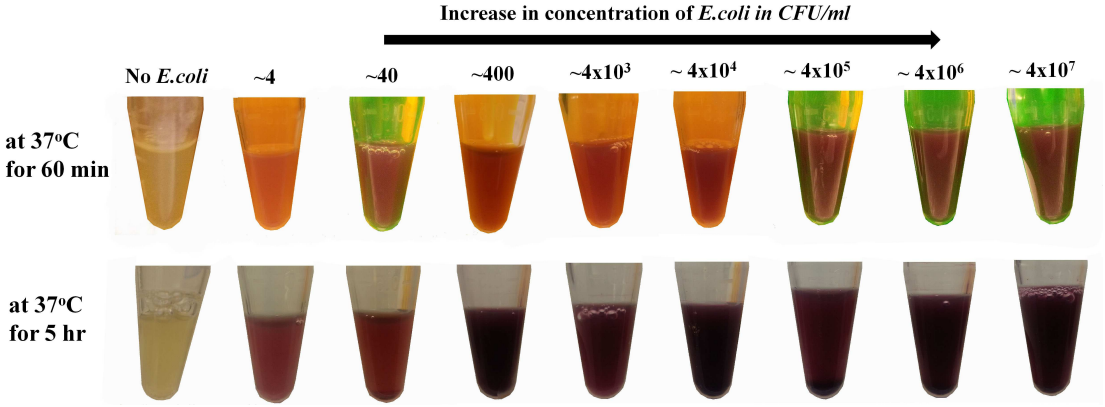

Figure 8.4: Appearance of red color in the microcentrifuge tubes for different known concentration of *E.coli* samples with optimized chemical reagents, which are incubated at 37^oC for 1 hr and 5 hr, respectively. Note that the intensity of color change depends on the incubation time and the concentration of *E.coli*.

conducted by the researchers in India [82].

Figure 8.4 shows the appearance of red color in the microcentrifuge tubes for different known concentration of *E.coli* samples with optimized chemical reagents, which were incubated at 37^oC for 1 hr and 5 hr, respectively. Note that the intensity of color change depends on the incubation time as well as concentration of *E.coli*. It was observed that the appearance of the red color for samples (4×10^7 CFU/ml and 4×10^6 CFU/ml) happens within 1 to 2 min, which shows that the developed method is indeed one of the rapid detection technique for total coliform.

To confirm the presence of *E.coli* in tested sample, the samples are excited at around 350 to 360 nm with ultra-violet (UV) in spectrofluorometer. The β-

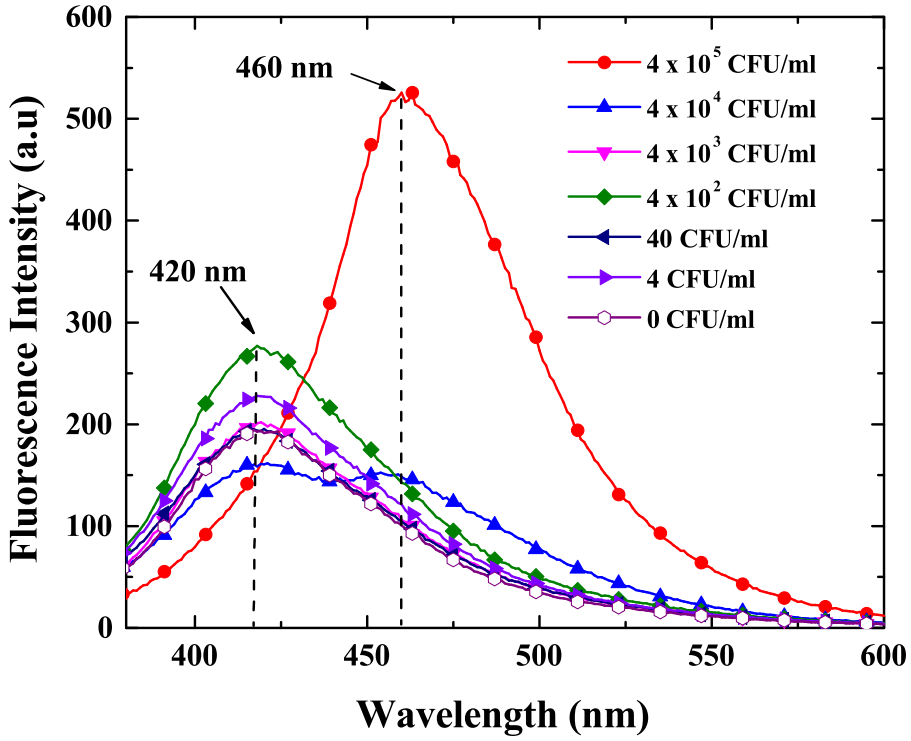

Figure 8.5: Spectrum of fluorescent intensity emitted by *E.coli* samples when excited at 350 *nm* in the presence of Red-Gal, MUG, B-PER, and $FeCl_3$ after 5 min of incubation. Note that 420 *nm* indicates the peak for unreacted MUG and around 460 *nm* indicates the peak for released product 4-MU after MUG and β-glucuronidase reaction.

glucuronidase enzyme of *E.coli* cleaves the MUG substrate and produces fluorogenic compound 4-MU which will emit as blue fluorescence at around 460 nm. Figure 8.5 depicts the spectrum of fluorescent intensity emitted by *E.coli* samples when excited at 350 *nm* in the presence of Red-Gal, MUG, B-PER, and $FeCl_3$ after 5 min of incubation. The presence of the peak at 420 nm in Fig. 8.5 indicates the presence of unreacted MUG. Also, the presence of the peak at 460 nm in Fig. 8.5 indicates the released product 4-MU. It is found that for *E.coli* concentration of 4×10^4 CFU/ml and 4×10^5 CFU/ml, the appearance of fluorescence peak for 4-MU within 5 *min*.

The red color intensity produced by the cleavage of Red-Gal substrate depends on the number of *E.coli* cells in the tested samples. To determine the relationship between color intensity and the *E.coli* concentration, the former is quantified

by color absorbance measurements with UV-Vis spectrophotometer at 525 nm wavelength after one hour of incubation. Figure 8.6(a) illustrates that the color intensity due to the cleavage of Red-Gal increased linearly with the increase in *E.coli* concentration. Further, the linear correlation between the color intensity and *E.coli* concentration was confirmed using the purified β-galactosidase enzyme assay (data not shown here). The color intensity was proportional to the amount of β-galactosidase enzyme added to the mixture of pure deionized water samples with LTB, Red-Gal, MUG, B-PER and $FeCl_3$.

The blue fluorescence intensity produced by the cleavage of MUG i.e., 4-MU compound is determined by measuring the fluorescence intensity of tested samples with spectrofluorometer. The samples were incubated for one hour before taking the measurements. The samples were excited at 350 nm and measured the fluorescence intensity emitted at 460 nm wavelength. Figure 8.6(b) shows the variation of fluorescence intensity of 4-MU compound with respect to *E.coli* concentration. It was observed that there was a linear correlation between fluorescence emitted by the cleavage of MUG and the *E.coli* concentration. In general, Fig. 8.6 can be used to determine the unknown concentration of total coliform or *E.coli* in water samples.

The optimized chemical reagents and developed protocol were employed to detect the total coliform and *E.coli* in 14 different water samples collected from different source conditions (rivers, wells, lakes, ponds, etc.) in India and Canada. Sample # 2 to 8 are from different wells, river, and hand pump from undisclosed location in Mumbai, India and Sample # 9 to 15 are from nearby pond and river creek in an undisclosed location in Edmonton, Canada. Sample # 1 is a control sample which is DI water with zero *E.coli* cells. It was found that the developed method was simple and easy to use for testing contaminated water samples in the field. Figure 8.7 shows the appearance of color in these microcentrifuge tubes which were incubated for one hour at 37^oC. Note that the intensity of color change depends on the concentration of *E.coli*. Most of the water samples (Sample # 2-6) confirmed the presence of total coliform and *E.coli* within 1 to 5 minutes and other samples produced less intensity of red color (Sample # 8 to 14) within one hour. Sample # 7 and Sample # 15 do not show any color development even after one hour of incubation. As expected, the control sample # 1 does not show

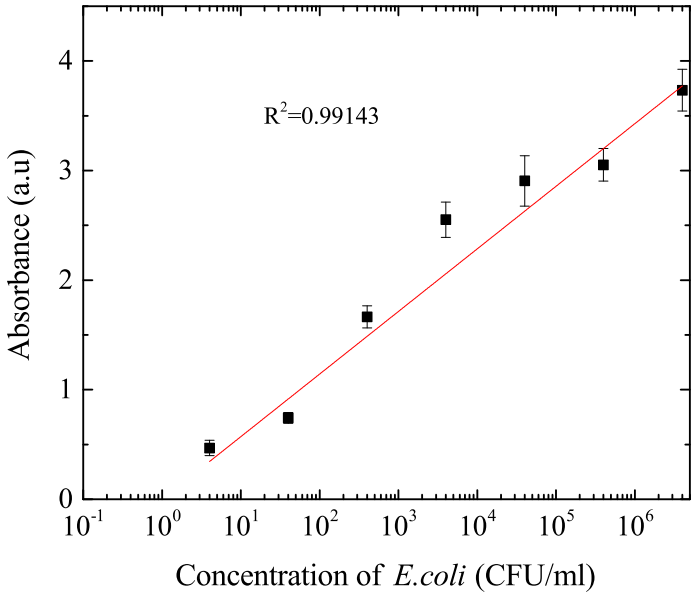

(a)

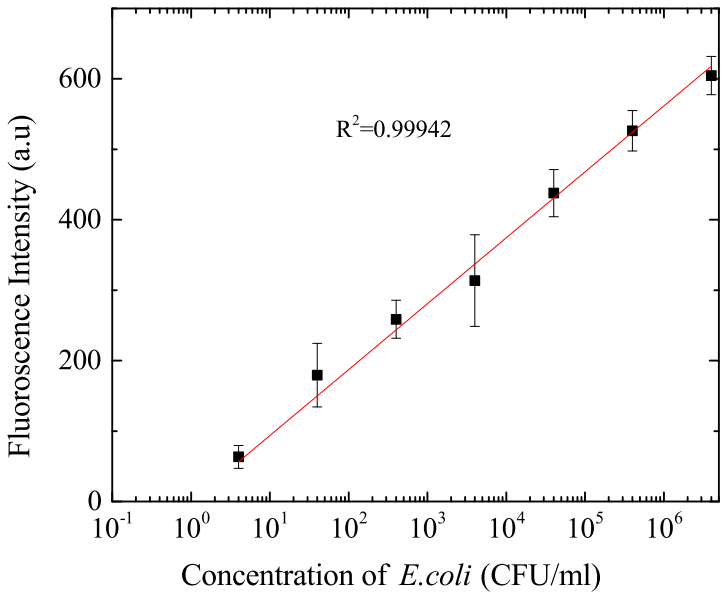

(b)

Figure 8.6: (a) Variation of color intensity due to the enzymatic reaction of *E.coli* with Red-Gal after incubating the *E.coli* samples of different concentration for 1 *hr*. (b) Variation of fluorescence intensity due to enzymatic reaction of *E.coli* with MUG after incubating the *E.coli* samples of different concentrations for 1 *hr*.

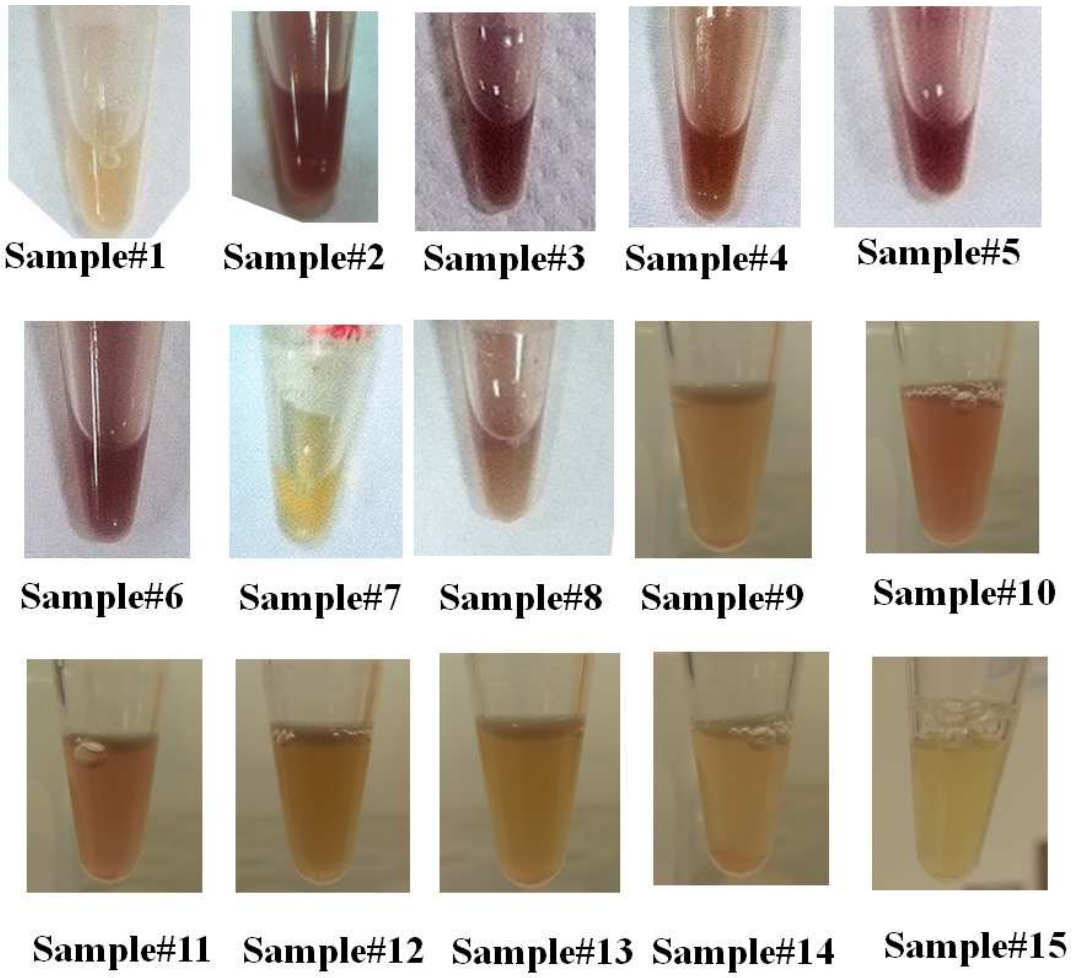

Figure 8.7: Appearance of red color in the microcentrifuge tubes for 14 different water samples and one negative control (Sample#15) sample, which are incubated for one hour at 37^oC. Note that the intensity of color change depends on concentration of *E.coli*.

any color development, which indicates that the certain degree of reliability of our proposed rapid testing method. Through this preliminary testing of water samples, we demonstrate that the proposed technique is simple, rapid, easy to use and is field deployable, particularly in limited resource setting communities.

8.5 Summary

In this work, we provide a simple approach towards the development of a rapid method for simultaneous detection of total coliform and *E.coli* in contaminated water samples. A specifically formulated dual enzyme substrate chemical reagents, consisting of a mixture of Red-Gal substrate, MUG substrate, $FeCl_3$, and B-PER

is used for the rapid detection purpose. The effect of Red-Gal, MUG, $FeCl_3$ and B-PER on rapid detection process were studied in detail. It was observed that oxidizing agent ($FeCl_3$) and lysing agent (B-PER) are essential for enhancing the rapid detection process. The present method was able to detect *E.coli* within 1 - 60 min at 37^oC. The rapid detection time and ease of use, particularly with field samples as demonstrated here, make it a very promising technique for "early warning" water monitoring system in limited resource setting communities.

Bibliography

[1] I. Déportes, J.-L. Benoit-Guyod, and D. Zmirou. Hazard to man and the environment posed by the use of urban waste compost: a review. *Science of the Total Environment*, 172(2):197–222, 1995.

[2] R. Girones. Tracking viruses that contaminate environments. *Microbe-American Society for Microbiology*, 1(1):19, 2006.

[3] M. Steele and J. Odumeru. Irrigation water as source of foodborne pathogens on fruit and vegetables. *Journal of Food Protection®*, 67(12):2839–2849, 2004.

[4] M. D. Sobsey, C. E. Stauber, L. M. Casanova, J. M. Brown, and M. A. Elliott. Point of use household drinking water filtration: a practical, effective solution for providing sustained access to safe drinking water in the developing world. *Environmental science & technology*, 42(12):4261–4267, 2008.

[5] J. Bartram and S. Cairncross. Hygiene, sanitation, and water: forgotten foundations of health. *PLoS medicine*, 7(11):e1000367, 2010.

[6] A. Prüss-Üstün, R. Bos, F. Gore, J. Bartram, et al. *Safer water, better health: costs, benefits and sustainability of interventions to protect and promote health.* World Health Organization, 2008.

[7] L. Fewtrell and J. Bartram. *Water quality: Guidelines, standards, and health: Assessment of risk and risk management for water-related infectious disease.* IWA Publishing, 2001.

[8] K. Onda, J. LoBuglio, and J. Bartram. Global access to safe water: accounting for water quality and the resulting impact on MDG progress. *International Journal of Environmental Research and Public Health*, 9(3):880–894, 2012.

[9] J. Olstadt, J. Schauer, J. Standridge, and S. Kluender. A comparison of ten USEPA approved total coliform E.*coli* tests. *Journal of Water and Health*, 5(2):267–282, 2007.

[10] E. Machdar, N. van der Steen, L. Raschid-Sally, and P. Lens. Application of quantitative microbial risk assessment to analyze the public health risk from

poor drinking water quality in a low income area in accra, ghana. *Science of the Total Environment*, 449:134–142, 2013.

[11] P. Griffin, S. Ostroff, R. Tauxe, K. Greene, J. Wells, J. Lewis, and P. Blake. Illness associated with *escherichia coli* 0157:H7 infections. A broad clinical spectrum. *Annals of Internal Medicine*, 109(9):705–712, 1988.

[12] M. Manafi. New developments in chromogenic and fluorogenic culture media. *International Journal of Food Microbiology*, 60(2):205–218, 2000.

[13] M. Grant. A new membrane filtration medium for simultaneous detection and enumeration of Escherichia coli and total coliforms. *Applied and Environmental Microbiology*, 63(9):3526–3530, 1997.

[14] R. Lifshitz and R. Joshi. Comparison of a novel coliplate kit and the standard membrane filter technique for enumerating total coliforms and Escherichia coli bacteria in water. *Environmental Toxicology and Water Quality*, 13(2):157–164, 1998.

[15] R. T. Noble, S. B. Weisberg, M. K. Leecaster, C. D. McGee, K. Ritter, K. O. Walker, and P. M. Vainik. Comparison of beach bacterial water quality indicator measurement methods. *Environmental Monitoring and Assessment*, 81(1-3):301–312, 2003.

[16] R. T. Noble, M. K. Leecaster, C. D. McGee, S. B. Weisberg, and K. Ritter. Comparison of bacterial indicator analysis methods in stormwater-affected coastal waters. *Water Research*, 38(5):1183–1188, 2004.

[17] R. Kwapiszewski, M. Skolimowski, K. Ziółkowska, E. Jedrych, M. Chudy, A. Dybko, and Z. Brzózka. A microfluidic device with fluorimetric detection for intracellular components analysis. *Biomedical Microdevices*, 13(3):431–440, 2011.

[18] A. J. Baeumner, R. N. Cohen, V. Miksic, and J. Min. RNA biosensor for the rapid detection of viable Escherichia coli in drinking water. *Biosensors and Bioelectronics*, 18(4):405–413, 2003.

[19] H. Zhu, U. Sikora, and A. Ozcan. Quantum dot enabled detection of Escherichia coli using a cell-phone. *Analyst*, 137(11):2541–2544, 2012.

[20] J. Comas-Riu and N. Rius. Flow cytometry applications in the food industry. *Journal of Industrial Microbiology & Biotechnology*, 36(8):999–1011, 2009.

[21] R. Kong, S. Lee, T. Law, S. Law, and R. Wu. Rapid detection of six types of bacterial pathogens in marine waters by multiplex PCR. *Water Research*, 36(11):2802–2812, 2002.

[22] N. Wéry, C. Lhoutellier, F. Ducray, J.-P. Delgenès, and J.-J. Godon. Behaviour of pathogenic and indicator bacteria during urban wastewater treatment and sludge composting, as revealed by quantitative pcr. *Water Research*, 42(1):53–62, 2008.

[23] L. Heijnen and G. Medema. Method for rapid detection of viable escherichia coli in water using real-time nasba. *water Research*, 43(12):3124–3132, 2009.

[24] J. E. Afset, G. Bruant, R. Brousseau, J. Harel, E. Anderssen, L. Bevanger, and K. Bergh. Identification of virulence genes linked with diarrhea due to atypical enteropathogenic Escherichia coli by DNA microarray analysis and PCR. *Journal of Clinical Microbiology*, 44(10):3703–3711, 2006.

[25] S. Bekal, R. Brousseau, L. Masson, G. Prefontaine, J. Fairbrother, and J. Harel. Rapid identification of Escherichia coli pathotypes by virulence gene detection with DNA microarrays. *Journal of Clinical Microbiology*, 41(5):2113–2125, 2003.

[26] G. Bruant, C. Maynard, S. Bekal, I. Gaucher, L. Masson, R. Brousseau, and J. Harel. Development and validation of an oligonucleotide microarray for detection of multiple virulence and antimicrobial resistance genes in Escherichia coli. *Applied and Environmental Microbiology*, 72(5):3780–3784, 2006.

[27] S. Chen, S. Zhao, P. F. McDermott, C. M. Schroeder, D. G. White, and J. Meng. A DNA microarray for identification of virulence and antimicrobial resistance genes in Salmonella serovars and Escherichia coli. *Molecular and Cellular Probes*, 19(3):195–201, 2005.

[28] J. Waswa, J. Irudayaraj, and C. DebRoy. Direct detection of E.*coli* o157: H7 in selected food systems by a surface plasmon resonance biosensor. *LWT-Food Science and Technology*, 40(2):187–192, 2007.

[29] C.-J. Huang, J. Dostalek, A. Sessitsch, and W. Knoll. Long-range surface plasmon-enhanced fluorescence spectroscopy biosensor for ultrasensitive detection of E.*coli* o157: H7. *Analytical Chemistry*, 83(3):674–677, 2011.

[30] V. Jasson, L. Jacxsens, P. Luning, A. Rajkovic, and M. Uyttendaele. Alternative microbial methods: an overview and selection criteria. *Food Microbiology*, 27(6):710–730, 2010.

[31] P. Kiesel, J. Martini, M. Huck, M. Bern, and N. Johnson. Opto-fluidic detection platform for pathogen detection in water. *Optical Society of America, CLEO: Science and Innovations*, page CWL1, 2011.

[32] L. Yang. Electrical impedance spectroscopy for detection of bacterial cells in suspensions using interdigitated microelectrodes. *Talanta*, 74(5):1621–1629, 2008.

[33] L. Yang and R. Bashir. Electrical/electrochemical impedance for rapid detection of foodborne pathogenic bacteria. *Biotechnology Advances*, 26(2):135–150, 2008.

[34] X. Guo, A. Kulkarni, A. Doepke, H. B. Halsall, S. Iyer, and W. R. Heineman. Carbohydrate-based label-free detection of Escherichia coli ORN 178 using electrochemical impedance spectroscopy. *Analytical Chemistry*, 84(1):241–246, 2011.

[35] L. Fu, K. Zhang, S. Li, Y. Wang, T.-S. Huang, A. Zhang, and Z.-Y. Cheng. In situ real-time detection of *e.coli* in water using antibody-coated magnetostrictive microcantilever. *Sensors and Actuators, B: Chemical*, 150(1):220–225, 2010.

[36] J. Yi, W. Shih, and W.-H. Shih. Effect of length, width, and mode on the mass detection sensitivity of piezoelectric unimorph cantilevers. *Journal of Applied Physics*, 91(3):1680–1686, 2002.

[37] S. Li, L. Fu, J. Barbaree, and Z.-Y. Cheng. Resonance behavior of magnetostrictive micro/milli-cantilever and its application as a biosensor. *Sensors and Actuators, B: Chemical*, 137(2):692–699, 2009.

[38] L. Fu, S. Li, K. Zhang, I.-H. Chen, V. Petrenko, and Z. Cheng. Magnetostrictive microcantilever as an advanced transducer for biosensors. *Sensors*, 7(11):2929–2941, 2007.

[39] S. Li, L. Orona, Z. Li, and Z.-Y. Cheng. Biosensor based on magnetostrictive microcantilever. *Applied Physics Letters*, 88(7):073507–073507, 2006.

[40] B. Ilic, D. Czaplewski, M. Zalalutdinov, H. Craighead, P. Neuzil, C. Campagnolo, and C. Batt. Single cell detection with micromechanical oscillators. *Journal of Vacuum Science and Technology B: Microelectronics and Nanometer Structures*, 19(6):2825–2828, 2001.

[41] B. Dhayal, W. Henne, D. Doorneweerd, R. Reifenberger, and P. Low. Detection of Bacillus subtilis spores using peptide-functionalized cantilever arrays. *Journal of the American Chemical Society*, 128(11):3716–3721, 2006.

[42] B. Bottari, D. Ercolini, M. Gatti, and E. Neviani. Application of FISH technology for microbiological analysis: current state and prospects. *Applied Microbiology and Biotechnology*, 73(3):485–494, 2006.

[43] S. B. Shinde, C. B. Fernandes, and V. B. Patravale. Recent trends in *in-vitro* nanodiagnostics for detection of pathogens. *Journal of Controlled Release*, 159(2):164–180, 2012.

[44] G. López-Campos, J. V. Martínez-Suárez, M. Aguado-Urda, and V. López-Alonso. Detection, identification, and analysis of foodborne pathogens. In *Microarray Detection and Characterization of Bacterial Foodborne Pathogens*, pages 13–32. Springer, 2012.

[45] P. Arora, A. Sindhu, N. Dilbaghi, and A. Chaudhury. Biosensors as innovative tools for the detection of food borne pathogens. *Biosensors and Bioelectronics*, 28(1):1–12, 2011.

[46] A. K. Bhunia, V. Nanduri, E. Bae, and E. D. Hirleman. Biosensors, foodborne pathogen detection. *Encyclopedia of Industrial Biotechnology: Bioprocess, Bioseparation, and Cell Technology*, 2010.

[47] V. Velusamy, K. Arshak, O. Korostynska, K. Oliwa, and C. Adley. An overview of foodborne pathogen detection: in the perspective of biosensors. *Biotechnology Advances*, 28(2):232–254, 2010.

[48] A. K. Bhunia. Biosensors and bio-based methods for the separation and detection of foodborne pathogens. *Advances in Food and Nutrition Research*, 54:1–44, 2008.

[49] O. Tokarskyy and D. L. Marshall. Immunosensors for rapid detection of Escherichia coli o157: H7-perspectives for use in the meat processing industry. *Food Microbiology*, 25(1):1, 2008.

[50] O. Lazcka, F. Campo, and F. X. Munoz. Pathogen detection: a perspective of traditional methods and biosensors. *Biosensors and Bioelectronics*, 22(7):1205–1217, 2007.

[51] A. K. Deisingh and M. Thompson. Biosensors for the detection of bacteria. *Canadian Journal of Microbiology*, 50(2):69–77, 2004.

[52] H. Nelis and S. Van Poucke. Enzymatic detection of coliforms and Escherichia coli within 4 hours. *Water, Air, and Soil Pollution*, 123(1-4):43–52, 2000.

[53] S. Edberg, E. Rice, R. Karlin, and M. Allen. Escherichia coli: the best biological drinking water indicator for public health protection. *Journal of Applied Microbiology*, 88(S1):106S–116S, 2000.

[54] A. Rompré, P. Servais, J. Baudart, M.-R. de Roubin, and P. Laurent. Detection and enumeration of coliforms in drinking water: current methods and emerging approaches. *Journal of Microbiological Methods*, 49(1):31–54, 2002.

[55] M. Manafi, W. Kneifel, and S. Bascomb. Fluorogenic and chromogenic substrates used in bacterial diagnostics. *Microbiological Reviews*, 55(3):335–348, 1991.

[56] M. Manafi. Fluorogenic and chromogenic enzyme substrates in culture media and identification tests. *International Journal of Food Microbiology*, 31(1):45–58, 1996.

[57] K. P. Brenner, C. C. Rankin, Y. R. Roybal, G. N. Stelma, P. V. Scarpino, and A. P. Dufour. New medium for the simultaneous detection of total coliforms and Escherichia coli in water. *Applied and Environmental Microbiology*, 59(11):3534–3544, 1993.

[58] W. P. Hamilton, M. Kim, and E. L. Thackston. Comparison of commercially available Escherichia coli enumeration tests: Implications for attaining water quality standards. *Water Research*, 39(20):4869–4878, 2005.

[59] W. D. Watkins, S. R. Rippey, C. R. Clavet, D. J. Kelley-Reitz, W. Burkhardt, et al. Novel compound for identifying Escherichia coli. *Applied and Environmental Microbiology*, 54(7):1874–1875, 1988.

[60] G. Dahlén and A. Linde. Screening plate method for detection of bacterial β-glucuronidase. *Applied Microbiology*, 26(6):863–866, 1973.

[61] S. Z. Hossain, C. Ozimok, C. Sicard, S. D. Aguirre, M. M. Ali, Y. Li, and J. D. Brennan. Multiplexed paper test strip for quantitative bacterial detection. *Analytical and Bioanalytical Chemistry*, 403(6):1567–1576, 2012.

[62] D. Wildeboer, L. Amirat, R. Price, and R. Abuknesha. Rapid detection of Escherichia coli in water using a hand-held fluorescence detector. *Water Research*, 44(8):2621–2628, 2010.

[63] R. B. Brown and J. Audet. Current techniques for single-cell lysis. *Journal of The Royal Society Interface*, 5(Suppl 2):S131–S138, 2008.

[64] A. Aspedon and K. Nickerson. A two-part energy burden imposed by growth of Enterobacter cloacae and Escherichia coli in sodium dodecyl sulfate. *Canadian Journal of Microbiology*, 39(6):555–561, 1993.

[65] Y. Tanji, K. Asami, X.-H. Xing, and H. Unno. Controlled expression of lysis genes encoded in T4 phage for the gentle disruption of Escherichia coli cells. *Journal of Fermentation and Bioengineering*, 85(1):74–78, 1998.

[66] A. Abolmaaty, M. El-Shemy, M. Khallaf, and R. Levin. Effect of lysing methods and their variables on the yield of Escherichia coli 0157: H7 DNA and its PCR amplification. *Journal of Microbiological Methods*, 34(2):133–141, 1998.

[67] M. Trkov, I. Majerkov, B. Jerašek, A. Štefanovičová, N. Rijpens, and T. Kuchta. Detection of Salmonella in food over 30 h using enrichment and polymerase chain reaction. *Food microbiology*, 16(4):393–399, 1999.

[68] S. Chalabaev, C. Anderson, A. Onderdonk, and D. Kasper. Sensitivity of Francisella tularensis to ultrapure water and deoxycholate: Implications for bacterial intracellular growth assay in macrophages. *Journal of Microbiological Methods*, 85(3):230–232, 2011.

[69] C. W. Kaspar, P. A. Hartman, and A. K. Benson. Coagglutination and enzyme capture tests for detection of Escherichia coli β-galactosidase, β-glucuronidase, and glutamate decarboxylase. *Applied and Environmental Microbiology*, 53(5):1073–1077, 1987.

[70] B. Iritani and T. Inzana. Evaluation of a rapid tube assay for presumptive identification of Escherichia coli from veterinary specimens. *Journal of Clinical Microbiology*, 26(3):564–566, 1988.

[71] S. C. Edberg, M. J. Allen, and D. B. Smith. National field evaluation of a defined substrate method for the simultaneous enumeration of total coliforms and Escherichia coli from drinking water: comparison with the standard multiple tube fermentation method. *Applied and Environmental Microbiology*, 54(6):1595–1601, 1988.

[72] S. C. Edberg, M. J. Allen, and D. Smith. National field evaluation of a defined substrate method for the simultaneous detection of total coliforms and Escherichia coli from drinking water: comparison with presence-absence techniques. *Applied and Environmental Microbiology*, 55(4):1003–1008, 1989.

[73] S. C. Edberg, M. J. Allen, D. B. Smith, and N. J. Kriz. Enumeration of total coliforms and Escherichia coli from source water by the defined substrate technology. *Applied and Environmental Microbiology*, 56(2):366–369, 1990.

[74] T. Covert, L. Shadix, E. Rice, J. Haines, and R. Freyberg. Evaluation of the autoanalysis colilert test for detection and enumeration of total coliforms. *Applied and Environmental Microbiology*, 55(10):2443–2447, 1989.

[75] I. Tryland and L. Fiksdal. Enzyme characteristics of β-D-Galactosidase-and β-D-Glucuronidase-positive bacteria and their interference in rapid methods for detection of waterborne coliforms and Escherichia coli. *Applied and Environmental Microbiology*, 64(3):1018–1023, 1998.

[76] K. Geissler, M. Manafi, I. Amoros, and J. Alonso. Quantitative determination of total coliforms and Escherichia coli in marine waters with chromogenic and fluorogenic media. *Journal of Applied Microbiology*, 88(2):280–285, 2000.

[77] N. S. K. Gunda, S. Naicker, M. S. Ghoraishi, S. Bhattacharjee, T. G. Thundat, and S. K. Mitra. Microspot with Integrated Wells (MSIW) for the detection of e. coli. *ASME 2013 11th International Conference on Nanochannels, Microchannels, and Minichannels*, pages V001T10A001–V001T10A001, 2013.

[78] S. K. Mitra, N. S. K. Gunda, S. K. Naicker, M. S. Ghoraishi, S. Bhattacharjee, and T. Thundat. Enhanced rapid detection of e.coli, 2013. ROI No. 2013040, University of Alberta, TEC Edmonton, Alberta, Canada.

[79] S. K. Mitra, N. S. K. Gunda, S. K. Naicker, M. S. Ghoraishi, S. Bhattacharjee, and T. Thundat. Microspot with integrated wells (MSIW) for the detection of *e.coli*, 2013. ROI No. 2013041, University of Alberta, TEC Edmonton, Alberta, Canada.

[80] R. Blaustein, Y. Pachepsky, R. Hill, D. Shelton, and G. Whelan. Escherichia coli survival in waters: Temperature dependence. *Water Research*, 47(2):569–578, 2013.

[81] J. L. Alonso, A. Soriano, O. Carbajo, I. Amoros, and H. Garelick. Comparison and recovery of Escherichia coli and thermotolerant coliforms in water with a chromogenic medium incubated at 41 and 44.5$^o c$. *Applied and Environmental Microbiology*, 65(8):3746–3749, 1999.

[82] A. Salz. University of Alberta researchers in Edmonton create a device that can detect *e.coli* in minutes. *Edmonton Sun*, 2013. September

23, 2013, http://www.edmontonsun.com/2013/09/23/university-of-alberta-researchers-in-edmonton-create-a-device-that-can-detect-e-coli-in-minutes.

Chapter 9

Mobile Water Kit (MWK) for Rapid Detection of Total Coliform and *E.coli* [1]

9.1 Overview

In this work, we have developed and demonstrated a rapid and low-cost water monitoring sensor that can simultaneously detect both total coliform and *E.coli* bacteria in contaminated drinking water samples. The test method, called Mobile Water Kit (MWK), comprises of a set of custom chemical reagents that would serve as colorimetric or fluorometric chemosensors, syringe filter units and a smartphone platform that would serve as the detection/analysis system. The MWK provides information about the presence/absence of total coliform and *E.coli* in water samples. The MWK has preliminarily been tested for its selectivity, sensitivity and accuracy, with samples of known concentrations of bacteria. The MWK has also been tested with contaminated water samples collected during the two field trials conducted in Canada and India, and the obtained results were confirmed with conventional laboratory methods.

9.2 Introduction

There is a pressing need to access clean and safe potable water for developing world and in communities with minimal resource settings. According to World Health Organization (WHO) statistics, approximately 884 million people (which

[1] A version of this chapter has been submitted for publication. N. S. K. Gunda, S. Naciker, S. Shinde, S. Kimbahune, S. Shrivastava, and S. K. Mitra, Analyst, Under Review, 2014.

means 1 in 8 people worldwide) do not have access to clean and safe potable water [1]. In most of these cases, contaminated water is consumed without any prior treatment processes. Water-borne diseases (especially diarrhoeal diseases) account for roughly 4.1% of total global burden of diseases, and approximately 3.4 million deaths are reported annually owing to water, sanitation, and hygiene-related causes [2–8]. Almost 90% of those deaths, (mostly children under the age of 5) occur in the developing world and in communities with minimal resources [8–10]. One of the major causes for such public health concern is the lack of consistent and economical methods to provide safe and uncontaminated drinking water to communities. Among all available methods of water treatment, an effective chlorination process at the point of use is cost effective, which can eliminate certain pathogens in drinking water. However, chlorination results in an unpleasant taste in drinking water and is not always necessary [11–13]. Moreover, there are certain health risks associated with excessive chlorination [11–13]. Hence, it is important to assess the requirement for chlorination [11–13]. A natural corollary to the above challenges is to develop water monitoring systems capable of rapid and accurate determination of the pathogens or the presence or absence of a suitable indicator (such as *E.coli*) in water. Therefore, there is a need for simple, rapid, and low-cost water monitoring system for evaluating the bacteriological quality of drinking water at the point of use. It will also provide answer to a critical question whether chlorination is required or not? Such water monitoring system can also act as an early warning for the community by providing information on the quality and safety of the water source. The main challenge for such water monitoring system (or sensor) would be to detect low concentrations of target contaminants in a prescribed volume of water sample ($\sim$100 ml) within a reasonable time ($\sim$ 1 hr). According to Health Canada and United States Environmental Protection Agency (USEPA) standards, the target concentration value for *E.coli* is zero Colony-Forming Units (CFU) per 100 ml for potable water and 126 CFU/100ml for recreational water [7, 14–17].

Coliforms are a group of bacteria present in the environment and in the intestines of all warm-blooded animals and humans [18–20]. According to source and characteristics of bacteria, coliform bacteria are grouped as either total coliform or faecal coliform. Total coliform comprises of faecal coliform bacteria such as *E.coli* and other coliform bacteria that are present in the environment. Faecal

coliform bacteria are found in bodily waste, animal droppings, and in soil [18–20]. Often total coliform and *E.coli* count are a good indicator of water contamination, as their presence indicate the likelihood of other deadly bacteria (viz Salmonella spp, Vibrio cholerae), viruses (like Hepatitis and Rotavirus), etc., in drinking water [21, 22].

Usually, the conventional methods take around 24 to 48 hours to detect coliform bacteria in contaminated water samples [23–35]. These conventional methods require transporting of water samples to a designated microbiology laboratory, which can be a challenge for remote locations. These methods are also time-consuming and require trained professionals to test water samples in the laboratory. Recently, numerous advanced methods based on interfacing micro and nanotechnology with molecular (immunological or genetic detection) and enzymatic methods have been developed for coliform detection [17, 36–41, 43–54]. However, these advanced techniques have significant challenges in terms of field deployment, even though they are rapid and highly sensitive [17, 36–41, 43–54]. The challenges and potential of these novel methods are reviewed in detail elsewhere [27–35]. Most of the detection principles are based on instant culturing of bacteria, enzymatic reactions, and molecular (immunological or genetic) methods of detection. Presently, different alternative assays are commercially available to detect total coliform and *E.coli*. USEPA has approved ten such methods that include Colilert® (WP200, IDEXX, Westbrook, ME, USA), Colilert-18® (WP200-18, IDEXX, Westbrook, ME, USA), Coliscan® (250MF, Micrology Laboratories, LLC Goshen, IN, USA), Colisure® (WCLS200, IDEXX, Westbrook, ME, USA), MI Agar (B14985, S&S Biosciences, Fisher), Readycult® Coliforms 100 (EMD Chemicals Inc., Gibbstown, NJ, USA), Chromocult® (EMD/Merck Laboratories, Gibbstown, NJ, USA), E-Colite® (ECO-100, Charm Sciences Inc., Lawrence, MA, USA), m-Coli Blue 24® (MOOPMCB2, Hach/Millipore Billerica, MA, USA), and Colitag® (4600-0012, CPI International, Santa Rosa, CA, USA) [7, 55, 56]. Like conventional methods, most of these tests too require certain equipment and dedicated laboratories to test the water samples for accurate and reliable results, and may be cost-intensive as well. Though, these laboratory tests are highly sensitive, they are time consuming and are not applicable in the field for point of use testing of water quality. The main reason for the prolonged durations to perform these tests, is the low

concentration of target bacteria in drinking water samples. Therefore, there is a necessity for a simple, easy to use, rapid and low-cost test method for on-field detection of bacteria from 100 ml of drinking water samples. These methods can be used frequently to test the water quality with minimum expenses and also provide early warning signals about water quality. Moreover, the public in general, will be more interested in qualitative results than quantitative results. Hence, "positive/negative" type of detection tests at the point of use are more desirable for limited resource communities compared to expensive analytical tests with readouts for actual CFU/100ml of water.

In the present work, we have developed a rapid and low-cost field test that can simultaneously detect total coliform and *E.coli* in contaminated water samples. The test method comprises of a low-cost water monitoring system, called Mobile Water Kit (MWK), coupled with a smartphone platform, for quantitative analysis. The MWK is simple, rapid, easy to use and is based on rapid enzymatic activity of specific enzymes produced by total coliform and *E.coli* bacteria, with specifically formulated chemical reagents. Dual enzyme substrates, the chromogen 6-Chloro-3-indolyl-β-D-galactopyranoside (Red-Gal) and the fluorogen 4-Methylumbelliferyl-β-D-glucuronide (MUG), are combined with other key ingredients to induce the production of the enzymes galactosidase and glucuronidase, respectively. These enzymes in turn cleave the specific substrates (Red-Gal and MUG) to release colored or fluorescent molecules, resulting in a change in the color of the solution. Several review articles are available on methods for detecting total coliform and *E.coli* by enzymatic methods[7, 55, 57, 58]. Recently, Gunda et al.[59] explored this combination for simultaneous detection of total coliform and *E.coli* of contaminated water samples in a microcentrifuge tube. The MWK has been developed based on this discovery of rapid detection of pathogens in contaminated water. This system consists of 100ml/60ml leur lock syringe, 0.45 μm pore size syringe filter unit, specifically formulated chemical reagents, and a smartphone with mHealth *E.coli* application (App). The test method involves collecting 100 ml of contaminated water sample in a syringe and filtering it through a 0.45 μm pore size syringe filter unit. After the filtration, the formulated chemical reagents are added, in a sequential manner, onto the syringe filter unit. The appearance of the red color on the syringe filter surface indicates the presence of total col-

iform and *E.coli*. The change in color can be captured using a smartphone and the images can be analyzed using the custom built mHealth *E.coli* App to provide quantitative results. The mHealth App facilitates communication with the end users via Short Message Service (SMS). The mHealth App can also access the in-built global positioning system (GPS) of the smartphone and thereby can provide unique location identifier for the contaminated water sources. This water monitoring platform is not only capable of providing real-time data for contaminated water source locations, but can also provide an "early warning" system to detect any outbreak of water-borne diseases in the community.

In remote communities, be it in developing countries like India or in First Nation communities in Canada's North, as an individual user of water from different sources, one will be interested to know if there is *E.coli* present or absent in the potable water, rather than having a quantified data in terms of CFU/100ml. Such quantified data is of interest to regulators, municipality water board, etc., but has little significance to millions of people living in impoverishment. MWK provides an answer to this bottom billion people, who now can be empowered to make their choice of drinking water by this simple "yes/no" test. The present method focuses on the presence or absence of the total coliform/*E.coli* in potable water samples; hence visual observation of tested filter surfaces is good enough for general public to understand whether the water is contaminated or not. In future, our plan is to integrate LED light source of a given excitation wavelength and a receiver to provide quantification capability for the MWK.

9.3 Materials and Methods

9.3.1 Materials

Enzymatic chromogen substrate, Red-Gal (6-Chloro-3-indolyl-β-D-galactoside), was obtained from Research Organics, Cleveland, OH, USA and fluorogen substrate, 4-methyllumbelliferyl-β-D-glucuronide (MUG), was purchased from Bioworld, Dublin, OH, USA. Bacteria protein extraction reagent (B-PER), Lauryl Tryptose Broth (LTB) nutrient broth medium and the LTB medium with MUG were obtained from Fisher Scientific, Canada. N,N-Dimethylformamide (DMF) and anhydrous Ferric Chloride ($FeCl_3$) were obtianed from Sigma-Aldrich, USA.

Figure 9.1: Mobile water kit (MWK) used in the field trials for simultaneous detection of total coliform and *E.coli*.

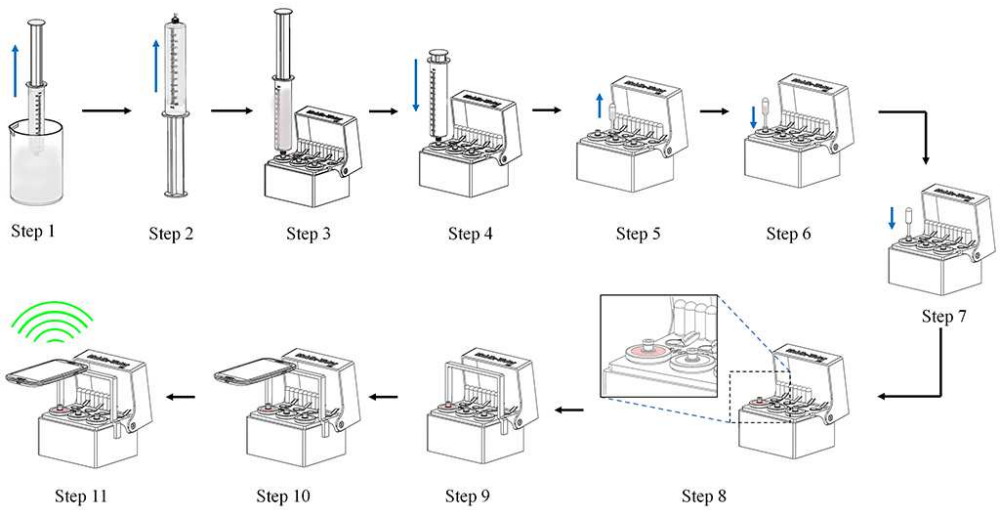

Figure 9.2: Step by step procedure to use MWK for water monitoring: (Step 1) Collect water in a syringe; (Step 2) Remove any air bubble in the syringe; (Step 3) Fix syringe to the syringe filter; (Step 4) Push syringe plunger to filter water; (Step 5) Take chemical reagent A using pipette; (Step 6) Add to syringe filter unit; (Step 7) Repeat steps 5 and 6 to add other chemical reagents B, C and D; (Step 8) Observe the appearance of red color; (Step 9) Put support for controlling smartphone location; (Step 10) Take picture of tested filter surface with smartphone camera after 1 hr; and (Step 11) Transmit the picture to server and initiate other App operations (details provided in Fig. 3) using cellular network.

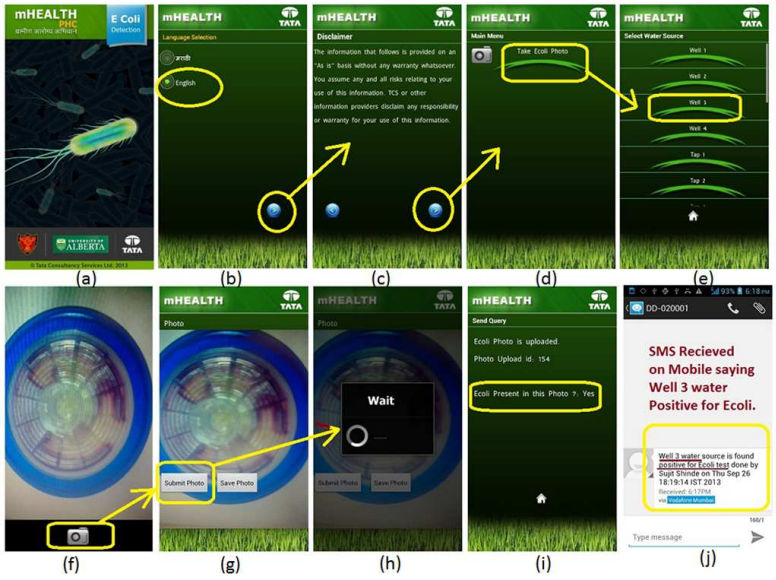

Figure 9.3: Step by step procedure to capture the image of tested syringe filter unit using mHealth *E.coli* App. (a) Select the mHealth *E.coli* App in smartphone; (b) Select language English; (c) Accept Disclaimer statement; (d) Click Take *E.coli* Photo; (e) Select the water source type (well, tap, river, etc.); (f) Take the picture of tested filter; (g) Click the submit button; (h) Wait to upload the picture and receive the result; (i) View the result (if result is Yes: *E.coli* is present or if result is No: *E.coli* is absent); and (j) Received text message on subscribed users' mobile regarding the quality of water.

E.coli Castellani and Chalmers (American Type Culture Collection (ATCC) 11229), *E.coli* O157 (National Collection of Type Cultures (NCTC) 12900 and NCTC 13125) were obtained from Stream Technologies, Inc., (Edmonton, Canada). The cultured *E.coli* Castellani and Chalmers (ATCC 8739) and *Enterobacter spp* were obtained from Bhavan's Research Center (BRC), Mumbai, India. *E.coli* DH5α (ATCC 67878) strain was acquired from Biological and Medicinal Chemistry Laboratory (BMCL), University of Alberta, Edmonton, Canada. *Listeria Monocytogenes* (ATCC 43251) and *Pseudomonas fluorescens* were purchased from Cedarlane, Burlington, ON, Canada. All these bacteria samples were cultured in nutrient broth medium overnight at 37^oC in microbiological incubator (Model IMC18 120V, Heratherm, Thermo Scientific, Canada). Unless otherwise stated, serial dilution was made in LTB to produce bacteria concentrations in the range of 2 - 2×10^8 CFU/ml. Here, in order to generate contaminated water samples for laboratory testing purpose, we have further diluted above prepared concentrated samples (1 ml) with DI Water (99 ml) to generate 100 ml of laboratory test water sample with final bacteria concentrations in the range of 2 - 2×10^8 CFU/100ml. These known bacteria concentration water samples were used to check the performance of MWK in the laboratory. The LTB (without MUG) is used to culture the bacteria and the LTB with MUG is used for formulating chemical reagents.

Sterile Millex®Syringe filter units with mixed cellulose esters, 33 mm diameter, 0.45 μm pore size, 150 μm thick, were obtained from EMD Millipore Corporation, Billerica, MA, USA. 100 ml / 60 ml capacity plastic syringes (sterile, leur lock, disposable) were obtained from BD (Becton, Dickinson and Company), Canada. Microcentrifuge tubes of 1.5 ml, sterile, snap-fit, plastic were purchased from Fisherbrand premium, Fisher Scientific, Canada. Pipette (10 μl to 100 μl) and the respective pipette tips were obtained from Eppendorf Canada, Mississauga, ON, Canada. Deionized (DI) water was used to prepare most of the solutions. Materials were sterilized whenever needed in an autoclave (Tuttnauer 3850M Autoclave, Heidolph North America, Elk Grove Village, IL, USA).

9.3.2 Formulation of chemical reagents

Four chemical reagents (A, B, C and D) were specifically formulated using the procured chemicals and stored in separate sterile microcentrifuge tubes. Reagent

A was prepared by dissolving a mixture of LTB with MUG (35.7 mg) and Red-Gal (0.30 mg) in deionized (DI) water (1 ml). Reagent B was B-PER (1 ml). Reagent C was prepared by dissolving $FeCl_3$ (20 mg) in DI water (1 ml). Reagent D was prepared by dissolving Red-Gal (30 mg) in a mixture of DMF (0.5 ml) and DI water (0.5 ml). For a single test, we require approximately 100 μl of reagent A and approximately 20 μl of each other reagents B, C and D [59–62]. All the chemical reagents were maintained at pH 7. The combination of Red-Gal and MUG is used to detect *E.coli* pathogens that secrete β-galactosidase and β-glucuronidase enzymes. In the present study, we focused our efforts only to observe the red color due to enzymatic reaction of β-galactosidase enzyme with Red-Gal and in future studies, we will incorporate a system to observe the blue fluorescence generated by the enzymatic reaction of β-glucuronidase with MUG. The inclusion of B-PER in MWK is to accelerate the extraction of β-galactosidase and β-glucuronidase enzymes by lysing the bacteria cells without denaturing the bacteria. $FeCl_3$ solution is used to accelerate the dimerization of the released indoxyls to indigo, the color producing molecule on the syringe filter surface, which is visible by naked eye. The combination of these chemical reagents enhances the rapid detection process, which was not explored previously in any commercially available test kits.

9.3.3 Components of MWK

The MWK can be used for simultaneous detection of total coliform and *E.coli*. It allows users to simultaneously test three contaminated water samples. The MWK consists of a box with three components: The main unit allows placement of three syringe filter units, four specifically formulated chemical reagents (A, B, C and D), 12 pipette tips/droppers to dispense the chemical reagents on the filter unit. The bottom reservoir is used to store the filtered water, which can be periodically drained as required. The top lid is used for covering the box to avoid exposure to dust and other environmental contaminations. In addition, the kit contains three sterile 100 ml / 60 ml leur lock syringes, sterile container to collect water samples and a smartphone operating on android (which is equipped with a custom built mobile application called mHealth *E.coli* App). Figure 9.1 shows the main components of a field deployable MWK.

Figure 9.4: Comparison of the filter surface between an unused (clean) and an used syringe filter unit. It is to be noted that the appearance of color on the used filter indicates the presence of total coliform and *E.coli*.

9.3.4 Water monitoring using MWK

The contaminated water sample was collected in a sterile container, followed by transferring the sample to a 100 ml / 60 ml sterile syringe (as per USEPA standard). The syringe was attached to one of the three syringe filter units. Any air bubbles in the syringe should be removed before attaching it to the syringe filter unit. After attachment, the syringe plunger rod is pushed to filter the water sample until no water residue is present in the syringe (complete filtration of water sample). Any bacterium present in the water sample is retained or concentrated on to the surface of the syringe filter unit. The syringe was removed from the syringe filter unit after filtration. A few microliters of specifically formulated chemical reagents A, B, C and D were then added into the syringe filter unit in a sequential manner. The syringe filter unit was incubated for a certain period at 37^oC. The filters were then monitored for over a period of one hour, followed by every 15 min for a period of 2 hr to observe any changes in the color. The presence of total coliform bacteria in contaminated water sample was detected by the appearance of the red color on the surface of the syringe filter unit. The observation of color change is for rapid qualitative results only. The entire procedure to use MWK for water monitoring is schematically illustrated in Fig. 9.2.

The mHealth *E.coli* App operated through a smartphone can be used to analyze the image of the tested syringe filter unit. The color change of the filter surface is then processed using mHealth and then broadcasted over the mobile phone network. The step by step procedure for the use of mHealth *E.coli* App to capture the image of tested syringe filter unit, thereby providing an early warning system through short messaging service (SMS), is illustrated in Fig. 9.3.

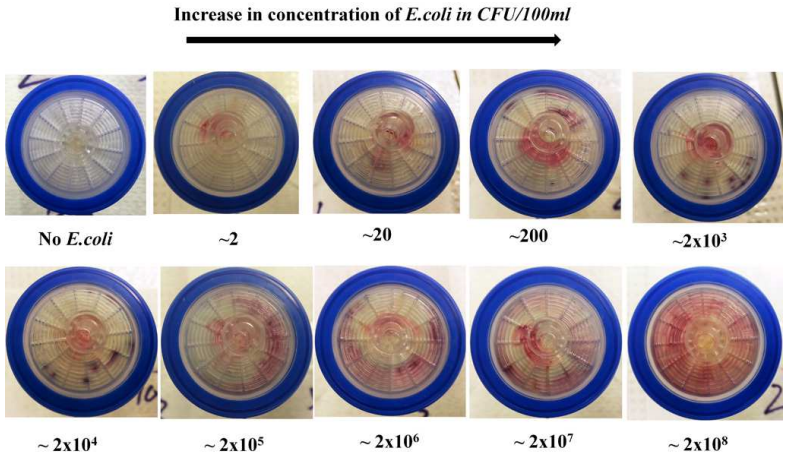

Figure 9.5: Appearance of red color on the syringe filter unit for different known concentrations of *E.coli* in laboratory water samples. Note that the color intensity depends on the incubation time and the concentration of *E.coli*.

In summary, the test method with MWK involves: (a) filtering of the contaminated water through syringe filter unit to concentrate the contaminants on the surface of the filter, (b) adding the specifically formulated chemical reagents on the filter surface to interact with contaminants, (c) allowing the chemical reagents to interact with contaminants for a certain period, (d) detecting the presence of total coliform and *E.coli* by the appearance of red color on the filter surface, (e) capturing the image of tested filter surface (refer Fig. 9.4) for further image processing and confirming the presence of total coliform and *E.coli* through custom made mHealth *E.coli* App in a smartphone, (e) determining the risk level for drinking water sources according to total coliform and *E.coli* levels, (f) creating an interactive, searchable map of water quality results through in-built GPS, and (g) transmitting water quality alerts to the community via SMS.

9.3.5 Confirmation of MWK with standard methods

Classical microbiological tests, including estimation of number of the coliform groups by the multiple tube dilution tests (Presumptive test, confirmed test, or completed test) (IS1622:1981) were performed on field water samples to cross-check the results, which were obtained by using MWK. The water samples for these confirmatory tests were collected directly from different sources, for which MWKs were deployed. For each test, three sterile polystyrene bottles (capacity 100 ml) were

used to collect three samples for the same water source. Well-established confirmatory laboratory methods (as per IS1622:1981) such as MacConkey's Broth [63, 64], brilliant green lactose bile (BGLB) broth [65, 66] and Indole test [67, 68] were used for identifying and enumerating total coliform, faecal coliform and *E.coli*, respectively. These standard water quality tests were conducted at the BRC, Mumbai, India. A detailed description of the confirmatory tests is provided in the Supplementary Information.

9.4 Results and Discussions

The MWK method was first tested with known concentration of bacteria before deploying in the field. *E.coli* Castellani and Chalmers (ATCC 11229) were used as standards for the validation of the kit. *E.coli* Castellani and Chalmers act as indicators for both total coliform and *E.coli* since it has both β-galactosidase and β-glucuronidase enzymes.

9.4.1 Sensitivity

The MWK has been repeatedly used for 10 to 12 times with different concentration of bacteria to determine the sensitivity and limit of detection. Figure 9.5 shows the appearance of red color on the syringe filter unit for different known concentrations of *E.coli* (ATCC 11229) mixed with DI water. It was observed that the intensity of color increases with the increase in the concentration of *E.coli*. Figure 9.6 depicts the variation in the response time of the system for different concentrations of *E.coli* samples. It was found that the appearance of the red color for samples (2×10^8 CFU/100ml and 2×10^7 CFU/100ml) occurs within 30 sec to 60 sec. The present method was able to detect up to 2 CFU/100ml (detection time between 30 min to 65 min) and this can be considered as the limit of detection. Water samples with more than 200 CFU/100ml of *E.coli* can be easily detected within 15 min to 20 min, which is very rapid compared to other existing methods [7, 55, 56].

9.4.2 Specificity

The reported method was verified for its specificity by using different positive and negative controls. *E.coli* Castellani and Chalmers (ATCC 11229 and ATCC 8739),

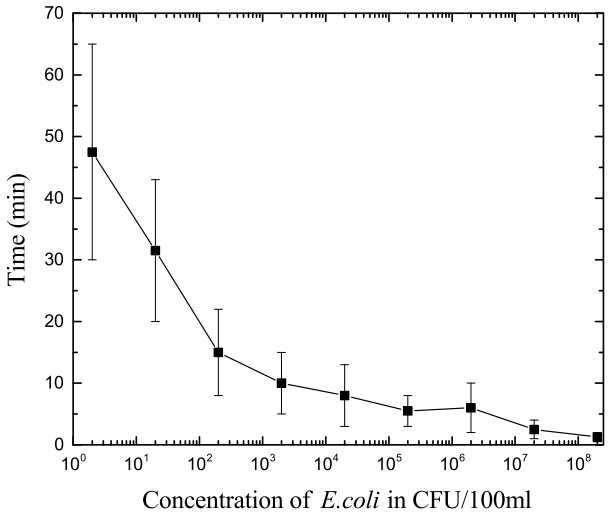

Figure 9.6: Variation in the response time of MWK with the appearance of red color on the syringe filter with different known concentrations of *E.coli* in laboratory water samples.

E.coli O157 (NCTC 12900 and NCTC 13125), *Enterobacter* and *E.coli* DH5α (ATCC 67878) were used as positive controls for both total coliform and *E.coli*. *Listeria Monocytogenes* (ATCC 43251), *Pseudomonas fluorescens* and deionized water without any *E.coli* were used as negative controls. Figure 9.7 shows the tested syringe filter unit with positive and negative controls. Figure 9.7(a) shows the appearance of red color on the surface of the syringe filter unit due to different positive controls. As expected, negative controls have not produced any color on the syringe filter unit (see Fig. 9.7(b)) indicating the specificity of the present method. These filters with controlled samples were kept for 2 hr.

9.4.3 Field trials in Canada and India

The first set of field trials were conducted by testing 21 different water samples collected from diverse sources such as rivers, wells, lakes, and ponds in two disparate geographical regions - India and Canada. Figure 9.8 depicts the test results for the collected water samples. Sample # 1 is a negative control that has DI water without any bacteria. Sample # 2 to 7 are from nearby ponds and river creeks in undisclosed locations in Edmonton, Canada. Sample # 8 to 21 are from different wells, river, and hand pump from undisclosed locations in Mumbai, India. Most

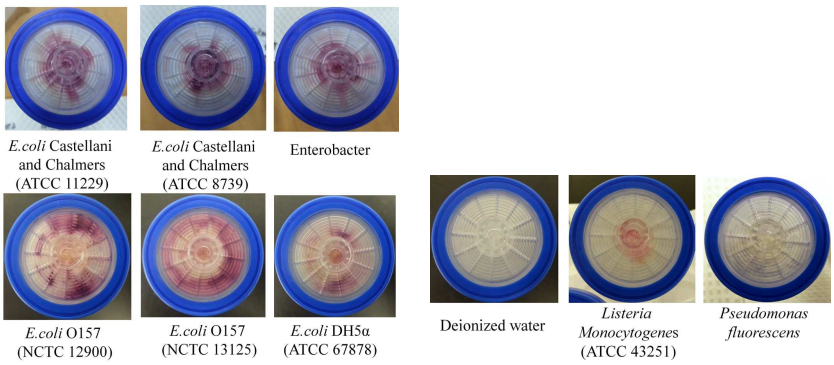

Figure 9.7: (a) Positive control tests using different strains (as labeled) of coliform bacteria including *E.coli*. (b) Negative control tests with DI water (no *E.coli* cells) and other pathogens (as labeled) which do not belong to the coliform bacteria strain.

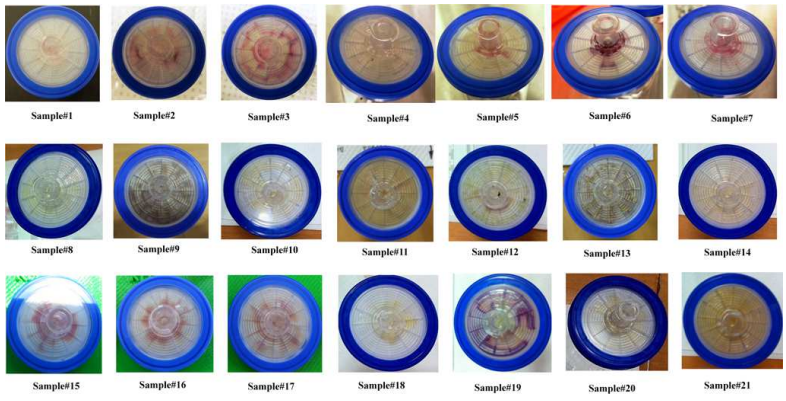

Figure 9.8: Appearance of red color on the syringe filter unit for 21 different water samples collected in first field trial (in Canada and India). Here Sample # 1 acts as a negative control. Note that the color intensity depends on the concentration of *E.coli*.

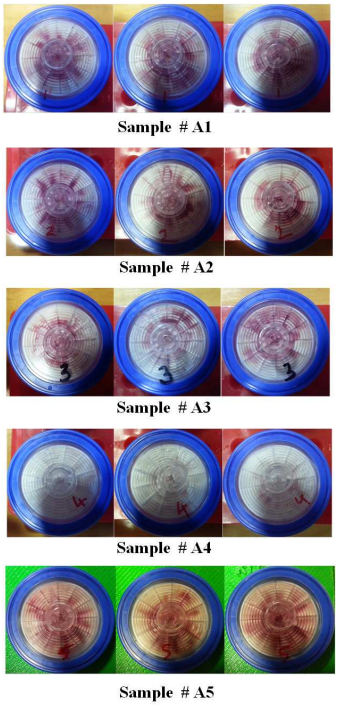

Figure 9.9: Appearance of red color on the syringe filter units for 5 different water samples in the second field trial in India.

of the water samples (Sample # 2, 3, 6, 9, 11, 13, 15, 16, 17, 19 and 21) confirmed the presence of total coliform and *E.coli* within 30 sec to 5 min. A few samples produced less intensity of the red color (Sample # 4, 5, 7, 12 and 20), the images of which were recorded within 8 min to 15 min after completing the sequential dispensing of reagents A, B, C and D. Sample # 1, 8, 10, 14 and 18 do not show any color development even after one hour. As predicted, the negative control sample # 1 does not produce any red color. Further, preliminary confirmatory tests were conducted by selecting two random water sources in Mumbai, India, and sending the water samples from those sources for conventional laboratory tests at BRC, Mumbai. The detail results (see Table S1) for such confirmatory tests are documented in the supplementary information. The confirmatory tests suggest that the first field trial was overall successful in detecting total coliform and *E.coli* in contaminated water sources.

During the second field trial, to demonstrate the reproducibility, we used three sterile syringes of 100 ml capacity and filled them with water from the same source and tested them individually in MWK. As shown in Fig. 9.9, these tests are re-

producible across the three filter surfaces, where similar color change (visible to naked eyes) is observed for the same source water. The sample # in Fig. 9.9 indicates different water sources, located at different geographical location within the community, that were tested with the kit and each time we have obtained reproducible results without performing any adjustments to MWK. All samples, except Sample # A4 (this sample was from a deep tube well where chances of any faecal contamination was minimal), indicate the presence of total coliform in the collected water samples. The obtained presence/absence test results were confirmed by testing the same water samples with conventional laboratory methods at BRC, Mumbai, the details (see Table S2) of which are provided in the Supplementary Information. Such confirmatory tests again demonstrated that the second field trial was equally successful in properly detecting the water-borne pathogens. So far MWK has been cross-checked with respect to model fluids containing known concentration of *E.coli* and a few actual field samples collected in Canada and India. Further, detailed validation exercise is required with different water source samples correspondingly tested with different known laboratory methods to make MWK a commercially viable product.

9.5 Future Outlook: Towards continuous mobile water monitoring system

Typical potable water sources for rural communities, particularly in countries like India, are wells, river, and hand-pumps. Often the water from these sources are polluted by sewage sludge, agricultural wastes, fertilizers, chemicals, organic, inorganic materials, dead animals and other contaminants leading to the growth of water-borne pathogens including bacteria (e.g. Salmonella, Campylobacter, Listeria and various strains of *E.coli*), viruses (e.g. Rota and Hepatitis), protozoa (e.g. Cryptosporidium, Giardia) and other intestinal parasites (e.g. Helminths). Therefore, the deployment of the Mobile Water Kit (MWK) has been focused for developing countries, like India, for continuous monitoring of water quality through the detection of total coliform and *E.coli* presence in water.

Figure 9.10 shows an integrated approach of deployment of MWK in limited resource communities, where not only one does the water quality monitoring, but

also provides water treatment solution to the compromised water sources through effective chlorination treatment. A typical community, as depicted in Fig. 9.10, would have a number of wells, water taps, and hand pumps, often distributed across a wide geographical location. The water quality testing using MWK can be carried out in such communities by the accredited social health activists (ASHAs) workers (community health female worker), who are typically employed through the primary health center (PHC) of the community. These ASHA workers, empowered with MWK and smartphones will upload the test results (image of the tested syringe filter unit) to the server through the mHealth *E.coli* App on their smartphones. The image of the filter surface is then processed using mHealth and then broadcasted over the mobile phone network via SMS. The software can also access the in-built GPS of the smartphone and thereby identify the test location and create a searchable water quality map for the community. The software also sends message to all the end users including villagers and the PHC doctors about the quality of the water sources. This "early warning" system will help the health official (at the PHC) to take appropriate measures for chlorine treatment of the infected wells. After effective chlorination, the wells will be tested again to assess the quality of treated water. The mHealth platform have uniquely tagged ID (unique identifiers through GPS location tracker in-built with the mobile phone) for all the wells in that region (including those which need chlorination). In parallel, ASHA workers can send the water samples to a conventional microbiology laboratory (like the Bhavan's Research Center (BRC), Mumbai, India) for confirmatory testing of results obtained by MWK.

The idea of using MWK is to empower individual community households in limited resource setting with their choice of clean water. Typically, each household sends a member of the family (often women) to fetch water from wells and other sources in early morning hours. It is envisaged, that each ASHA worker will be provided with MWK with necessary supplies and a smartphone, who will be responsible for 3-4 wells in a given community. As explained earlier, these ASHA workers will perform the water quality test by the procedure outlined in Fig. 9.2. At the end of sequential operation of dispensing all the chemicals (A, B, C, and D), the person has to wait for 1 hr before capturing the filter surface image by the smartphone camera (Step 10 in Fig. 9.2). Even though the person can observe the

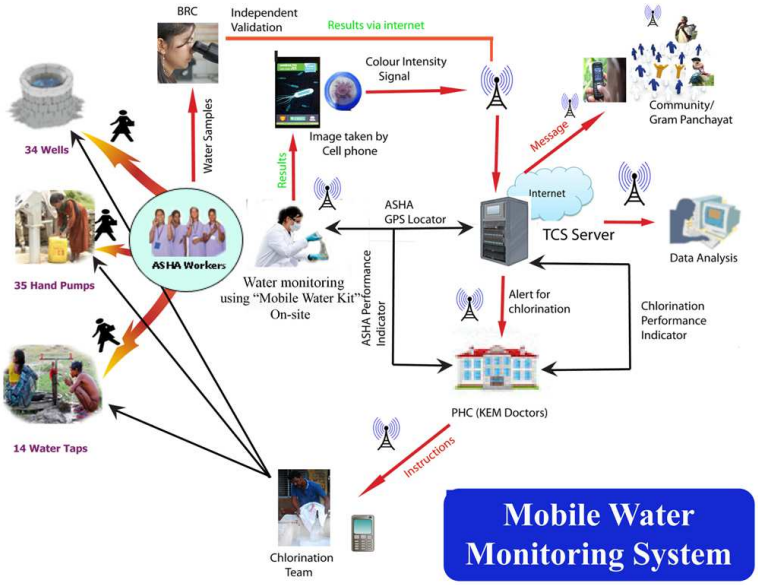

Figure 9.10: Schematic showing an integrated plan for the deployment of mobile water monitoring system in India.

presence of red color on the filter surface much earlier than 1 hr and can report it via the App system, shown in Fig. 9.3, it is important to provide a standardized protocol to ASHA worker. It may so happen that the contamination level in the wells can be very low ($\sim$ 3 - 5 CFU/100ml) and our controlled laboratory experiments, as shown in Fig. 9.6, suggest that under such low concentration, the color appearance only happens after around 50 min. Hence, to avoid any possibility of misinterpretation of the MWK result, we felt that a standard protocol of taking image after 1 hr would be a good practice for the ASHA workers. It is to be noted that while performing field trials in the designated community in Mumbai, the level of contamination in these wells were so significant, that we always found the color change to occur within 10 min.

It is to be noted that the present version of MWK does not have the capability of capturing blue fluorescence emitted by the syringe filter surface in presence of *E.coli* in water. The current MWK only provides qualitative indication of presence of *E.coli*/total coliform through the visual observation of red color on the syringe filter surface. There could be two mechanisms by which one can quantify the number of *E.coli* cells in contaminated water through the use of MWK (to be incorporated in its future version). Firstly, one can correlate the intensity of the red color on the filter surface, captured by the cell phone camera, with the

concentration of *E.coli* cells through controlled laboratory experiments and then create a look-up table, which can be integrated with the App. Hence, in the field, once an image of the filtered surface is captured by the cell phone camera, the end-user can immediately know the possible range of *E.coli* concentration in 100 ml of actual field samples. Secondly, one can observe the appearance of blue fluorescence under exposure to long wavelength ultraviolet light (350-360 nm). The blue fluorescence results confirm the presence of *E.coli* due to the enzymatic reaction of β-glucuronidase with MUG. One can use battery operated handheld fluorescence reader to quantify the blue fluorescence signal emitted on syringe filter surface. However, as mentioned earlier, such quantification may be of interest to regulators, but have very less relevance to public at large. The chemicals used in MWK allow us to adopt both the methods for quantification purpose, which will be taken up in near future as one of the goals for product development.

In this work, MWK is deployed and tested for drinking water only. We are not using the present kit for any industrial waste water or processed industrial water. Therefore, chances of any background interference on the color producing reagents are minimal, which was substantiated by successful field trials where different sources of potable water were tested and matched with independent laboratory tests for the same water sample. Future scope of the present work will be to study the effect of other environmental parameters such as turbidity, salinity, etc.

9.6 Conclusions

We have demonstrated a simple, easy to use, inexpensive, rapid and field deployable test method, called Mobile Water Kit (MWK), for detecting total coliform and *E.coli* in contaminated water samples. The MWK comprises of a low-cost water monitoring sensor coupled with a smartphone platform. The test method is based on rapid enzymatic process to detect the specific enzymes related to total coliform and *E.coli*. The test method concentrates the contaminants in water sample on the syringe filter unit and then allows the contaminants to interact with specifically formulated chemical reagents. The presence of total coliform and *E.coli* is identified through the appearance of red color. This method has been successfully tested with known concentrations of bacteria as well as with contaminated water

samples in the field. Its performance has also been tested with conventional laboratory methods. It was found that the results from the two field trials, conducted in Canada and India, corroborate well with the laboratory test results for total coliform. The mHealth *E.coli* App facilitates the transfer of the test results to the communities and water managers, thereby creating an early warning system for monitoring the water quality. The MWK is a promising test method for water quality monitoring in limited resource setting communities. It needs to be further validated for its functionality and applicability towards broader implementation in communities around the world.

Bibliography

[1] E. Kallman, J. A. Smith, and V. Oyanedel-Craver. Field evaluation of locally produced silver-impregnated ceramic filters for point-of-use water purification in san mateo ixtatan, guatemala. *Proceedings of the Water Environment Federation*, 2009(1):19–30, 2009.

[2] M. D. Sobsey, C. E. Stauber, L. M. Casanova, J. M. Brown, and M. A. Elliott. Point of use household drinking water filtration: a practical, effective solution for providing sustained access to safe drinking water in the developing world. *Environmental science & technology*, 42(12):4261–4267, 2008.

[3] J. Bartram and S. Cairncross. Hygiene, sanitation, and water: forgotten foundations of health. *PLoS medicine*, 7(11):e1000367, 2010.

[4] A. Prüss-Üstün, R. Bos, F. Gore, J. Bartram, et al. *Safer water, better health: costs, benefits and sustainability of interventions to protect and promote health.* World Health Organization, 2008.

[5] L. Fewtrell and J. Bartram. *Water quality: Guidelines, standards, and health: Assessment of risk and risk management for water-related infectious disease.* IWA Publishing, 2001.

[6] K. Onda, J. LoBuglio, and J. Bartram. Global access to safe water: accounting for water quality and the resulting impact on MDG progress. *International Journal of Environmental Research and Public Health*, 9(3):880–894, 2012.

[7] J. Olstadt, J. Schauer, J. Standridge, and S. Kluender. A comparison of ten USEPA approved total coliform E.*coli* tests. *Journal of Water and Health*, 5(2):267–282, 2007.

[8] E. Machdar, N. van der Steen, L. Raschid-Sally, and P. Lens. Application of quantitative microbial risk assessment to analyze the public health risk from poor drinking water quality in a low income area in accra, ghana. *Science of the Total Environment*, 449:134–142, 2013.

[9] M. Du Preez, K. G. McGuigan, and R. M. Conroy. Solar disinfection of drinking water in the prevention of dysentery in south african children aged

under 5 years: the role of participant motivation. *Environmental science & technology*, 44(22):8744–8749, 2010.

[10] C. Boschi-Pinto, C. F. Lanata, and R. E. Black. The global burden of childhood diarrhea. In *Maternal and Child Health*, pages 225–243. Springer, 2009.

[11] U. Von Gunten. Ozonation of drinking water: Part ii. disinfection and byproduct formation in presence of bromide, iodide or chlorine. *Water Research*, 37(7):1469–1487, 2003.

[12] M. I. Cedergren, A. J. Selbing, O. Löfman, and B. A. Källen. Chlorination byproducts and nitrate in drinking water and risk for congenital cardiac defects. *Environmental research*, 89(2):124–130, 2002.

[13] A. Adin, J. Katzhendler, D. Alkaslassy, and C. Rav-Acha. Trihalomethane formation in chlorinated drinking water: a kinetic model. *Water Research*, 25(7):797–805, 1991.

[14] M. H. Cassin, A. M. Lammerding, E. C. Todd, W. Ross, and R. S. McColl. Quantitative risk assessment for Escherichia coli o157: H7 in ground beef hamburgers. *International Journal of Food Microbiology*, 41(1):21–44, 1998.

[15] K. Dhriti, G. Mathur, R. Prem, M. Singh, V. Rawat, G. Seshadri, A. Manjeet, and R. Khandal. Water quality issues needing technological interventions: Sustainable availability for all. In *Water and Health*, pages 305–353. Springer, 2014.

[16] P. Payment, J. Siemiatycki, L. Richardson, G. Renaud, E. Franco, and M. Prevost. A prospective epidemiological study of gastrointestinal health effects due to the consumption of drinking water. *International Journal of Environmental Health Research*, 7(1):5–31, 1997.

[17] J. Bartram. *Heterotrophic plate counts and drinking-water safety: the significance of HPCs for water quality and human health.* IWA Publishing, 2003.

[18] I. Déportes, J.-L. Benoit-Guyod, and D. Zmirou. Hazard to man and the environment posed by the use of urban waste compost: a review. *Science of the Total Environment*, 172(2):197–222, 1995.

[19] R. Girones. Tracking viruses that contaminate environments. *Microbe-American Society for Microbiology*, 1(1):19, 2006.

[20] M. Steele and J. Odumeru. Irrigation water as source of foodborne pathogens on fruit and vegetables. *Journal of Food Protection®*, 67(12):2839–2849, 2004.

[21] E. M. Smith and C. P. Gerba. Development of a method for detection of human rotavirus in water and sewage. *Applied and environmental microbiology*, 43(6):1440–1450, 1982.

[22] V. Richardson, J. Hernandez-Pichardo, M. Quintanar-Solares, M. Esparza-Aguilar, B. Johnson, C. M. Gomez-Altamirano, U. Parashar, and M. Patel. Effect of rotavirus vaccination on death from childhood diarrhea in mexico. *New England Journal of Medicine*, 362(4):299–305, 2010.

[23] M. Grant. A new membrane filtration medium for simultaneous detection and enumeration of Escherichia coli and total coliforms. *Applied and Environmental Microbiology*, 63(9):3526–3530, 1997.

[24] R. Lifshitz and R. Joshi. Comparison of a novel coliplate kit and the standard membrane filter technique for enumerating total coliforms and Escherichia coli bacteria in water. *Environmental Toxicology and Water Quality*, 13(2):157–164, 1998.

[25] R. T. Noble, S. B. Weisberg, M. K. Leecaster, C. D. McGee, K. Ritter, K. O. Walker, and P. M. Vainik. Comparison of beach bacterial water quality indicator measurement methods. *Environmental Monitoring and Assessment*, 81(1-3):301–312, 2003.

[26] R. T. Noble, M. K. Leecaster, C. D. McGee, S. B. Weisberg, and K. Ritter. Comparison of bacterial indicator analysis methods in stormwater-affected coastal waters. *Water Research*, 38(5):1183–1188, 2004.

[27] S. B. Shinde, C. B. Fernandes, and V. B. Patravale. Recent trends in *in-vitro* nanodiagnostics for detection of pathogens. *Journal of Controlled Release*, 159(2):164–180, 2012.

[28] G. López-Campos, J. V. Martínez-Suárez, M. Aguado-Urda, and V. López-Alonso. Detection, identification, and analysis of foodborne pathogens. In *Microarray Detection and Characterization of Bacterial Foodborne Pathogens*, pages 13–32. Springer, 2012.

[29] P. Arora, A. Sindhu, N. Dilbaghi, and A. Chaudhury. Biosensors as innovative tools for the detection of food borne pathogens. *Biosensors and Bioelectronics*, 28(1):1–12, 2011.

[30] A. K. Bhunia, V. Nanduri, E. Bae, and E. D. Hirleman. Biosensors, foodborne pathogen detection. *Encyclopedia of Industrial Biotechnology: Bioprocess, Bioseparation, and Cell Technology*, 2010.

[31] V. Velusamy, K. Arshak, O. Korostynska, K. Oliwa, and C. Adley. An overview of foodborne pathogen detection: in the perspective of biosensors. *Biotechnology Advances*, 28(2):232–254, 2010.

[32] A. K. Bhunia. Biosensors and bio-based methods for the separation and detection of foodborne pathogens. *Advances in Food and Nutrition Research*, 54:1–44, 2008.

[33] O. Tokarskyy and D. L. Marshall. Immunosensors for rapid detection of Escherichia coli o157: H7-perspectives for use in the meat processing industry. *Food Microbiology*, 25(1):1, 2008.

[34] O. Lazcka, F. Campo, and F. X. Munoz. Pathogen detection: a perspective of traditional methods and biosensors. *Biosensors and Bioelectronics*, 22(7):1205–1217, 2007.

[35] A. K. Deisingh and M. Thompson. Biosensors for the detection of bacteria. *Canadian Journal of Microbiology*, 50(2):69–77, 2004.

[36] R. Kwapiszewski, M. Skolimowski, K. Ziółkowska, E. Jedrych, M. Chudy, A. Dybko, and Z. Brzózka. A microfluidic device with fluorimetric detection for intracellular components analysis. *Biomedical Microdevices*, 13(3):431–440, 2011.

[37] A. J. Baeumner, R. N. Cohen, V. Miksic, and J. Min. RNA biosensor for the rapid detection of viable Escherichia coli in drinking water. *Biosensors and Bioelectronics*, 18(4):405–413, 2003.

[38] H. Zhu, U. Sikora, and A. Ozcan. Quantum dot enabled detection of Escherichia coli using a cell-phone. *Analyst*, 137(11):2541–2544, 2012.

[39] J. Comas-Riu and N. Rius. Flow cytometry applications in the food industry. *Journal of Industrial Microbiology & Biotechnology*, 36(8):999–1011, 2009.

[40] R. Kong, S. Lee, T. Law, S. Law, and R. Wu. Rapid detection of six types of bacterial pathogens in marine waters by multiplex PCR. *Water Research*, 36(11):2802–2812, 2002.

[41] N. Wéry, C. Lhoutellier, F. Ducray, J.-P. Delgenès, and J.-J. Godon. Behaviour of pathogenic and indicator bacteria during urban wastewater treatment and sludge composting, as revealed by quantitative pcr. *Water Research*, 42(1):53–62, 2008.

[42] L. Heijnen and G. Medema. Method for rapid detection of viable escherichia coli in water using real-time nasba. *water Research*, 43(12):3124–3132, 2009.

[43] J. E. Afset, G. Bruant, R. Brousseau, J. Harel, E. Anderssen, L. Bevanger, and K. Bergh. Identification of virulence genes linked with diarrhea due to atypical enteropathogenic Escherichia coli by DNA microarray analysis and PCR. *Journal of Clinical Microbiology*, 44(10):3703–3711, 2006.

[44] S. Bekal, R. Brousseau, L. Masson, G. Prefontaine, J. Fairbrother, and J. Harel. Rapid identification of Escherichia coli pathotypes by virulence gene detection with DNA microarrays. *Journal of Clinical Microbiology*, 41(5):2113–2125, 2003.

[45] G. Bruant, C. Maynard, S. Bekal, I. Gaucher, L. Masson, R. Brousseau, and J. Harel. Development and validation of an oligonucleotide microarray for detection of multiple virulence and antimicrobial resistance genes in Escherichia coli. *Applied and Environmental Microbiology*, 72(5):3780–3784, 2006.

[46] S. Chen, S. Zhao, P. F. McDermott, C. M. Schroeder, D. G. White, and J. Meng. A DNA microarray for identification of virulence and antimicrobial resistance genes in Salmonella serovars and Escherichia coli. *Molecular and Cellular Probes*, 19(3):195–201, 2005.

[47] J. Waswa, J. Irudayaraj, and C. DebRoy. Direct detection of E.*coli* o157: H7 in selected food systems by a surface plasmon resonance biosensor. *LWT-Food Science and Technology*, 40(2):187–192, 2007.

[48] C.-J. Huang, J. Dostalek, A. Sessitsch, and W. Knoll. Long-range surface plasmon-enhanced fluorescence spectroscopy biosensor for ultrasensitive detection of E.*coli* o157: H7. *Analytical Chemistry*, 83(3):674–677, 2011.

[49] V. Jasson, L. Jacxsens, P. Luning, A. Rajkovic, and M. Uyttendaele. Alternative microbial methods: an overview and selection criteria. *Food Microbiology*, 27(6):710–730, 2010.

[50] P. Kiesel, J. Martini, M. Huck, M. Bern, and N. Johnson. Opto-fluidic detection platform for pathogen detection in water. *Optical Society of America, CLEO: Science and Innovations*, page CWL1, 2011.

[51] L. Yang. Electrical impedance spectroscopy for detection of bacterial cells in suspensions using interdigitated microelectrodes. *Talanta*, 74(5):1621–1629, 2008.

[52] L. Yang and R. Bashir. Electrical/electrochemical impedance for rapid detection of foodborne pathogenic bacteria. *Biotechnology Advances*, 26(2):135–150, 2008.

[53] X. Guo, A. Kulkarni, A. Doepke, H. B. Halsall, S. Iyer, and W. R. Heineman. Carbohydrate-based label-free detection of Escherichia coli ORN 178 using electrochemical impedance spectroscopy. *Analytical Chemistry*, 84(1):241–246, 2011.

[54] B. Bottari, D. Ercolini, M. Gatti, and E. Neviani. Application of FISH technology for microbiological analysis: current state and prospects. *Applied Microbiology and Biotechnology*, 73(3):485–494, 2006.

[55] M. Manafi. New developments in chromogenic and fluorogenic culture media. *International Journal of Food Microbiology*, 60(2):205–218, 2000.

[56] W. P. Hamilton, M. Kim, and E. L. Thackston. Comparison of commercially available Escherichia coli enumeration tests: Implications for attaining water quality standards. *Water Research*, 39(20):4869–4878, 2005.

[57] M. Manafi, W. Kneifel, and S. Bascomb. Fluorogenic and chromogenic substrates used in bacterial diagnostics. *Microbiological Reviews*, 55(3):335–348, 1991.

[58] M. Manafi. Fluorogenic and chromogenic enzyme substrates in culture media and identification tests. *International Journal of Food Microbiology*, 31(1):45–58, 1996.

[59] N. S. K. Gunda, M. S. Ghoraishi, S. K. Naicker, S. Bhattacharjee, T. Thundat, and S. K. Mitra. Enhanced rapid detection of total coliform and *e.coli* in contaminated water samples using specifically formulated dual enzyme substrate chemical reagents. *Water Research, Under Review*, 2014.

[60] S. K. Mitra, N. S. K. Gunda, S. K. Naicker, M. S. Ghoraishi, S. Bhattacharjee, and T. Thundat. Enhanced rapid detection of E.coli, 2013. ROI No. 2013040, University of Alberta, TEC Edmonton, Alberta, Canada.

[61] S. K. Mitra, N. S. K. Gunda, S. K. Naicker, M. S. Ghoraishi, S. Bhattacharjee, and T. Thundat. Microspot with integrated wells (MSIW) for the detection of E.coli, 2013. ROI No. 2013041, University of Alberta, TEC Edmonton, Alberta, Canada.

[62] S. K. Mitra, N. S. K. Gunda, and S. K. Naicker. Mobile Water Kit (MWK): A smartphone compatible low-cost water monitoring system for rapid detection of total coliform and E.coli, 2014. ROI No. 2013084, University of Alberta, TEC Edmonton, Alberta, Canada.

[63] W. Cuthbert, J. Panes, and E. Hill. Survival of bacterium coli type i and streptococcus faecalis in soil. *Journal of Applied Microbiology*, 18(3):408–414, 1955.

[64] B. Eddy and A. Kitchell. Cold-tolerant fermentative gram-negative organisms from meat and other sources. *Journal of Applied Microbiology*, 22(1):57–63, 1959.

[65] J. E. Sworobuk, C. B. Law, and G. K. Bissonnette. Assessment of the bacteriological quality of rural groundwater supplies in northern west virginia. *Water, Air, and Soil Pollution*, 36(1-2):163–170, 1987.

[66] K. Venkateswaran, A. Murakoshi, and M. Satake. Comparison of commercially available kits with standard methods for the detection of coliforms and Escherichia coli in foods. *Applied and Environmental Microbiology*, 62(7):2236–2243, 1996.

[67] S. C. Edberg and C. M. Kontnick. Comparison of beta-glucuronidase-based substrate systems for identification of Escherichia coli. *Journal of Clinical Microbiology*, 24(3):368–371, 1986.

[68] R. M. Niemi, J. Mentu, A. Siitonen, and S. Niemelä. Confirmation of Escherichia coli and its distinction from Klebsiella species by gas and indole formation at 44 and 44.5^{o}C. *Journal of Applied Microbiology*, 95(6):1242–1249, 2003.

Chapter 10

Chemically Modified Microwells for Rapid Detection of Total Coliform and *E.coli* [1]

10.1 Overview

The present work developed a new method for detecting *E.coli* in contaminated water using microspot with integrated wells (MSIW). The method involves the fabrication of MSIW, coating the MSIW with enzyme substrates such as 4-MUG substrate (4-Methylumbelliferyl-β-D-glucuronide, trihydrate) and Red-Gal substrate(6-Chloro-3-indolyl-β-D-galactoside) in proper medium and dispensing the contaminated water into MSIW. GlucuronidaseA (gusA) gene in *E.coli* encodes the *beta*-D-Glucuronidase (GUS) to hydrolyze the substrate 4-MUG enzymatically which leads to the generation of the fluorigenic compound 4-MU. β-galactosidase enzyme in *E.coli* produces red color when it reacts with Red-Gal substrate. Using portable optical readers, average color/fluorescence intensity emitting by MSIW is measured and quantified. Comparing obtained intensity values with calibrated intensity values, the level of contamination can be predicted for early warnings.

10.2 Introduction

Escherichia coli (*E.coli*) is a bacterium that is commonly found in the lower intestine of warm-blooded organisms [1, 2]. *E.coli* can be found in food products and

[1] A version of this chapter has been published. N. S. K. Gunda, S. Naicker, M. S. Ghoraishi, S. Bhattacharjee, T. G. Thundat and S. K. Mitra, Paper # ICNMM2013-73037, Proceedings of ASME 2013 11th International Conference on Nanochannels, Microchannels, and Minichannels, Sapporo, Japan, June 16-19, 2013.

contaminated drinkable water. Most *E.coli* are harmless, but some can cause serious food poisoning in humans, and are occasionally responsible for product recalls due to food contamination [3]. The CDC (Center for Disease Control and Prevention) estimates about 73,000 cases of *E.coli* infection occur each year in United States [3]. About 61 people die from the illness [2]. Greatest threat to drinkable water resources is contamination by microbial pathogens, so water quality is routinely assessed by testing for the presence of *E.coli* using pathogenic activity.

Three main groups of detections methods for *E.coli*: 1) Molecular whole-cell and surface recognition methods [4, 5]; 2) Enzyme/substrate methods [6–8]; and 3) Nucleic acid detection methods [9]. Antibody-antigen binding [4, 5] and receptor-ligand binding based techniques comes under molecular whole-cell and surface recognition methods. Capture antibodies needs to be coated on the surface of the chips for capturing the *E.coli* samples in water. The production of specific antibodies is time consuming and expensive process. Enzyme/substrate based methods are proven to be one of the best methods for improved specificity of bacteria detection. Fluorophore or color dye-tagged growth substrate in specific broth is used in such techniques [6–8]. Upon growth specific enzymes of bacteria cleave the fluorophore or color compound from the substrate, causing the fluorescence or color increase. These type of detection takes 7 hr to 24 hr for detection. Buehler et al. [10] identified specific enzymes for *E.coli*. *E.coli* can produce either β-glucuronidase [7, 10] or β-galactosidase, [11] based on the type of *E.coli* strains. Hence, these enzymes have therefore been considered to be a suitable indicator for E. coli especially for the detection of fecal contamination of food and water. Nucleic acid methods, such as PCR (polymerase chain reaction) [9, 12–15], microarrays [16], and NASBA (Nucleic acid sequence based amplification) [17], are highly specific and sensitive techniques for detecting bacteria. Based upon known sequence complementarity, different specific strains of bacteria can be identified. There are several other lab based conventional techniques (for example: membrane filtration, multiple tube fermentation, etc.) to detect *E.coli* in the contaminated water. All the above discussed methods are expensive, time consuming and not portable. Water samples need to bring to the labs for testing contaminants.

Currently, there is a need to develop a hand-held, inexpensive and easy to use diagnostic system for fast and accurate results. Several groups implemented

microfluidic based biosensors [18–21] for rapid detection of *E.coli*. However, they are not able to detect low concentration of *E.coli* samples. Additionally some instruments such as impedance analyzer, microscopes etc. required for quantification. In the present work, we developed a new method for detecting *E.coli* in contaminated water using microspot with integrated wells (MSIW). Improved and modified enzyme/substrate detection method is employed on the MSIW to enhance the sensitivity, specificity and selectivity. In addition, amount of reagents and time required for the test has been reduced. MSIWs can detect low concentration of samples since there are no fluid movement within the MSIW. Methodology starts with fabrication of MSIW and then applying the specifically formulated enzymatic method on micro-wells. Further measurements are conducted to quantify the color or fluorescence emitted by the wells.

10.3 Materials and Methods

10.3.1 Materials

E.coli samples of different strains (0157, Castellani and Chalmers (ATCC 11229), Dh5α) were obtained from University of Alberta, Edmonton, Canada. 4-MUG substrate (4-Methylumbelliferyl-β-D-glucuronide, trihydrate) was purchased from Bioworld, Dublin, OH, USA. Red-gal (6-Chloro-3-indolyl-β-D-galactoside) was purchased from Research Organics, Cleveland, OH, USA. Lauryl Tryptose Broth (LTB) and Bacteria protein extraction reagent (B-PER) were obtained from Fisher Scientific, Canada. N,N-Dimethylformamide (DMF), Anhydrous Ferric Chloride ($FeCl_3$)were bought from Sigma-Aldrich, USA. 100-mm-diameter silicon (Si) substrate was purchased from Silicon Valley Microelectronics Inc., Santa Clara, CA, USA. Polydimethylsiloxane (PDMS) was obtained from Dow Corning Corporation, Midland, MI, USA.

10.3.2 Methods

Fabrication of MSIP:

We used silicon and PDMS based MSIWs in this work. The silicon MSIW were fabricated using the standard photolithography process. MSIW fabrication is similar to the fabrication of micropillars reported elsewhere [22, 23] but briefly de-

scribed here. A 100-mm-diameter Si substrate was taken and cleaned with Piranha solution. Further, a $\sim$ 0.52-micron thick oxide layer was thermally grown on top of it followed by patterning of MSIWs on silicon/silicon-dioxide substrate with standard photolithography using HPR504 (Fuji-film Electronic Materials Inc., Mesa, Arizona) positive photoresist (PPR). Subsequently oxide and silicon layers are anisotropically etched in plasma-reactive ion etchers (dry etching technique, DRIE). After etching the silicon for about $\sim$ 70 μm, the PPR on the substrate was stripped off using acetone and the substrate was thoroughly cleaned in Branson PPR stripper. Then oxide layer was removed using plasma-reactive ion etchers. PDMS based MSIWs were fabricated using standard softlithography process as described elsewhere [24]. A micro-spot of 2 mm diameter with square/staggered configuration of wells is considered in this work. A schematic of MSIW and SEM image of the wells inside the silicon MSIW and PDMS MSIW is shown in Fig. 10.1.

Coating of MSIW:

Fabricated MSIW were coated with specifically formulated enzyme substrate solution with a mixture of 4-MUG substrate, Red-Gal substrate, Ferric chloride in DMF and B-PER. Mixture of above prepared solution (5 μl) is dispensed into MISW, which is kept at room temperature for 1 hr for coating of the mixture to be effective. After coating, MSIW were cleaned with LTB.

Detection of *E.coli*:

Coated MSIWs were used for detecting *E.coli*. Different concentrations of *E.coli* samples of 1-5 μl volume is dispensed on the coated MSIW and kept at room temperature. GlucuronidaseA (gusA) gene in *E.coli* encodes the β-D-Glucuronidase (GUS) to hydrolyze the substrate 4-MUG (in the coating) enzymatically which leads to the generation of the fluorigenic compound 4-MU. The presence or absence of an active β-galactosidase in *E.coli* is detected by Red-Gal (substrate), which produces a characteristic red color when cleaved by β-galactosidase enzyme, thereby providing an easy means of distinguishing the presence or absence of *E.coli* in water. Using portable optical color/fluorescent readers (Lateral flow reader and ESElog, Qiagen, Germany) [25], the average color/fluorescent intensity emitted

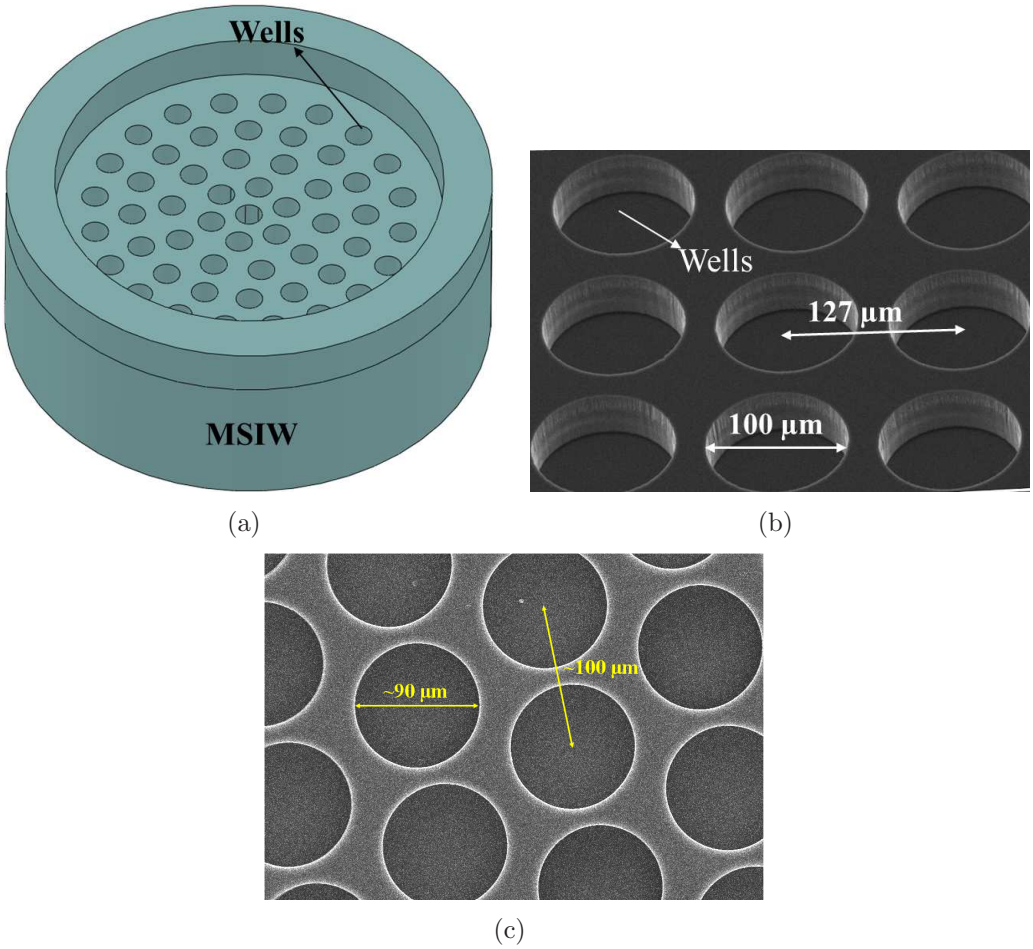

Figure 10.1: (a) Schematic of MSIW and (b) SEM image of the wells inside the silicon based MSIW (c)SEM image of the wells inside the PDMS based MSIW

by the MSIWs is measured. Based on intensity, the level of contamination can be predicted for early warnings.

10.4 Results and Discussions

Before the protocol for detection of *E.coli* is conducted for MSIW, the chemistry is first tested on micro-centrifuge tubes of 1.5 ml size(purchased from Fisher scientific, Canada). The color or fluorescence producing conditions with different concentrations of chemical reagents, substrates and *E.coli* samples are optimized. We tried with different *E.coli* samples in LTB medium (0157, Castellani and Chalmers (ATCC 11229), Dh5α) with Red-gal and 4-MUG substrates. In all experiments, E.coli ATCC 11229 (Castellani and Chalmers) has been used for convenience and testing. Testing of other E.coli samples are in progress and will be reported elsewhere. Specifically formulated enzyme substrate solution is prepared with a mixture of 4-MUG substrate, Red-Gal substrate, Ferric chloride in DMF and B-PER. Then *E.coli* sample of known concentration is added and incubated at room temperature (or at 37^{o}C) for development of color or fluorescence. The presence of *E.coli* as red color with Red-gal substrate is observed within 70 min of incubation. This shows that some strains of *E.coli* has β-galactosidase enzyme which cleaves the Red-gal compound to produce red color. With time, the intensity of the red color increased up to 12 hr and then remained constant. The intensity of the red color produced by different concentrations of *E.coli* with Red-gal substrate solution is shown in Fig. 10.2.

The developed protocols were applied on to the MSIWs and measured the intensity of the developed color/fluorescence after enzymatic reaction. Color (red) identification in silicon based MSIWs is difficult compared to PDMS based MSIWs, since silicon material itself emits a color which interferes with red color produced in the reaction. Hence we used PDMS based MSIWs for the most of the present work. Figure 10.3 shows the optical image of the PDMS based MSIWs after treating *E.coli* with Red-Gal substrate. A light red-color is obtained at the time of enzymatic reaction within 5 to 10 min. It is observed that, the intensity of the color has been increased with respect to time. It is observed that MSIW reduces the reaction time compared to conventional centrifuge tube based method, probably

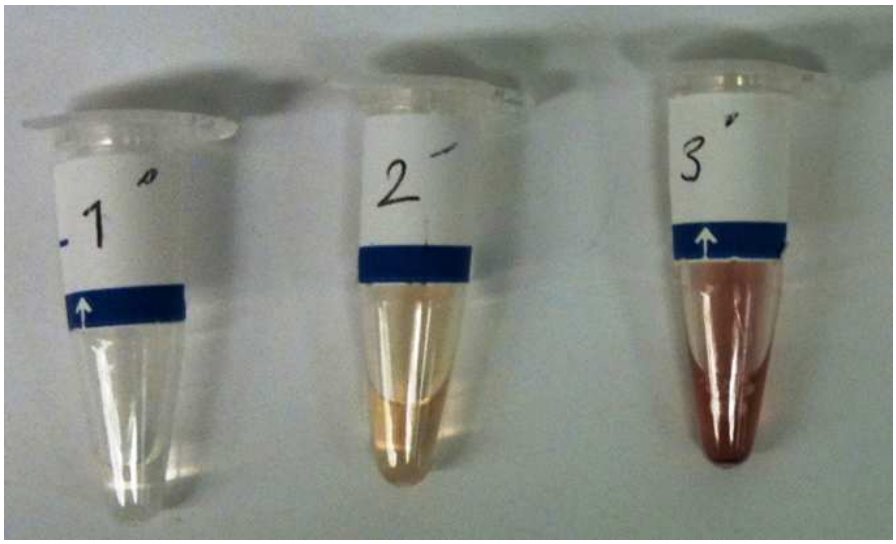

(a)

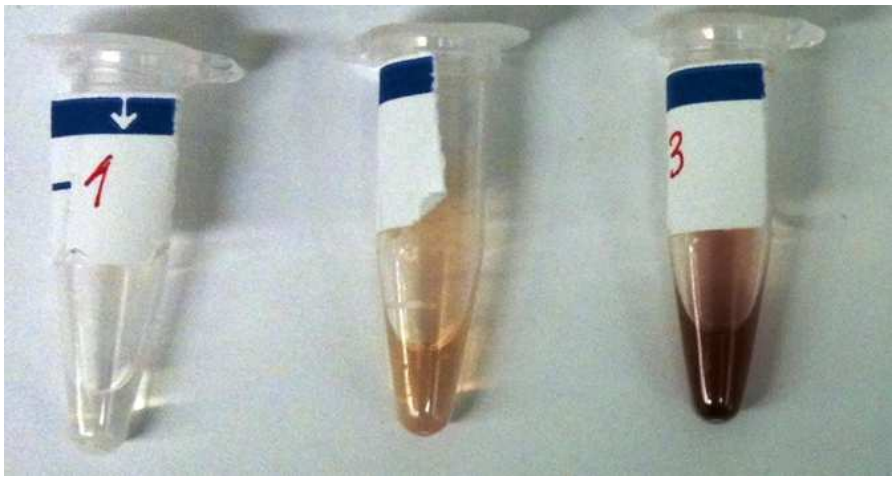

(b)

Figure 10.2: *E.coli* with Red-gal after incubating the samples for 12 hours (a) at room temperature and (b) at 37^{o}C; Label 1 and 1' on the tubes indicate the *E.coli* concentration of 10 CFU/ml, Label 2 and 2' belongs to *E.coli* concentration of 100 CFU/ml and label 3 and 3' related to *E.coli* concentration of 1000 CFU/ml

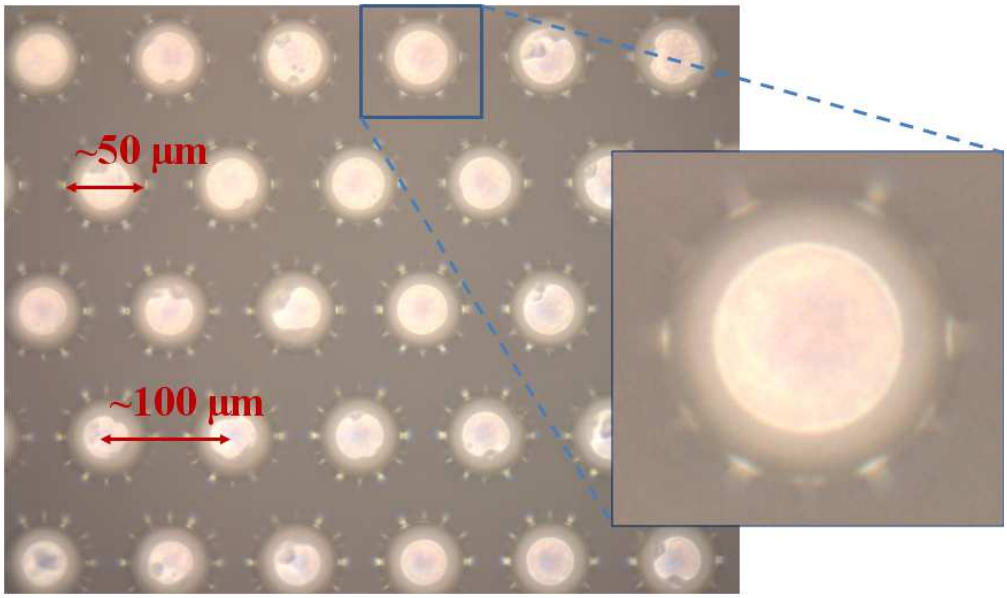

Figure 10.3: Optical image of the coated PDMS based MSIWs after reacting with *E.coli*

due to increase in reaction surface area and decrease in volume of the samples.

The average color or fluorescent intensity emitted by MSIW after enzymatically reacting with respective substrates is measured using portable optical reader. Figure 10.4 shows the increase in color or fluorescent intensity emitted by MSIWs with increase in incubation time. It is observed that intensity values increases linearly within first few mins and then slowly increases (non linearly) the intensity values up to a maximum value and then remain constant throughout the time period. This means that in first few min, *E.coli* is reacting with enzymatic substrate and the reaction is completed after 10 to 15 min.

As we are coating MSIWs with specifically formulated enzyme substrate solution, the density of the substrates (MUG or Red-gal) to react with E.coli increases and hence the time and concentration required for the reaction reduces. Due to high density of wells in MSIW, the reaction surface area is increased compared to other microfluidic approaches. This type of wells can enhance the signal intensity even with low concentration samples [26–28].

A scanning electron microscope is employed to observe the coating and reaction zones of MSIWs. Figure 10.5 shows a dried PDMS MSIWs (after complete reaction with *E.coli*). It is found that coating of microwells is not uniform. It is required to coat the MSIWs uniformly for accurate measurement of intensity values.

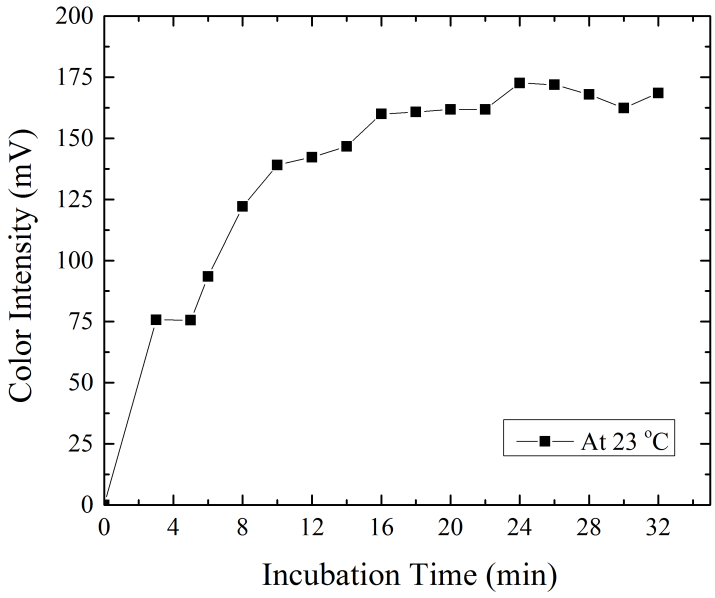

(a)

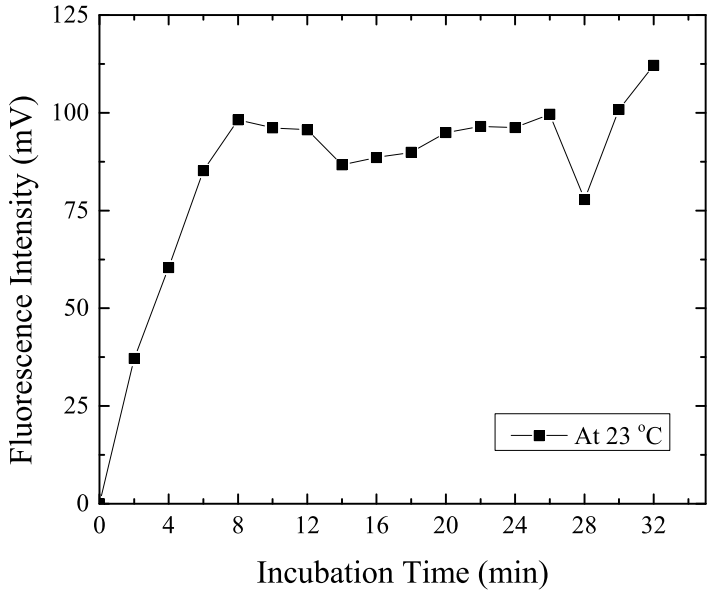

(b)

Figure 10.4: Variation of color/fluorescent intensities with respect to incubation time for reaction. (a) Color intensity produced by Red-gal substrate after enzymatically reacting with *E.coli* (b) Fluorescence intensity produced by MUG substrate after enzymatically reacting with *E.coli*

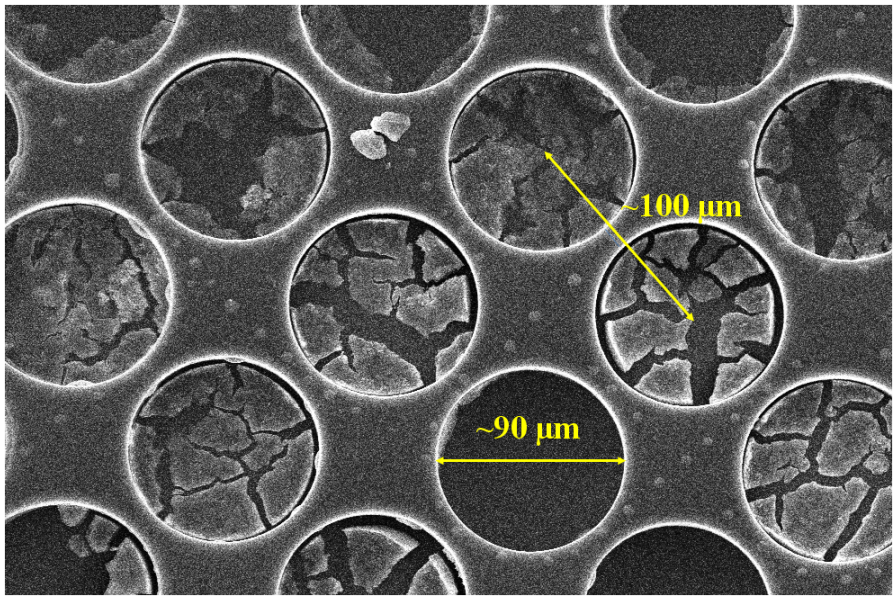

(a)

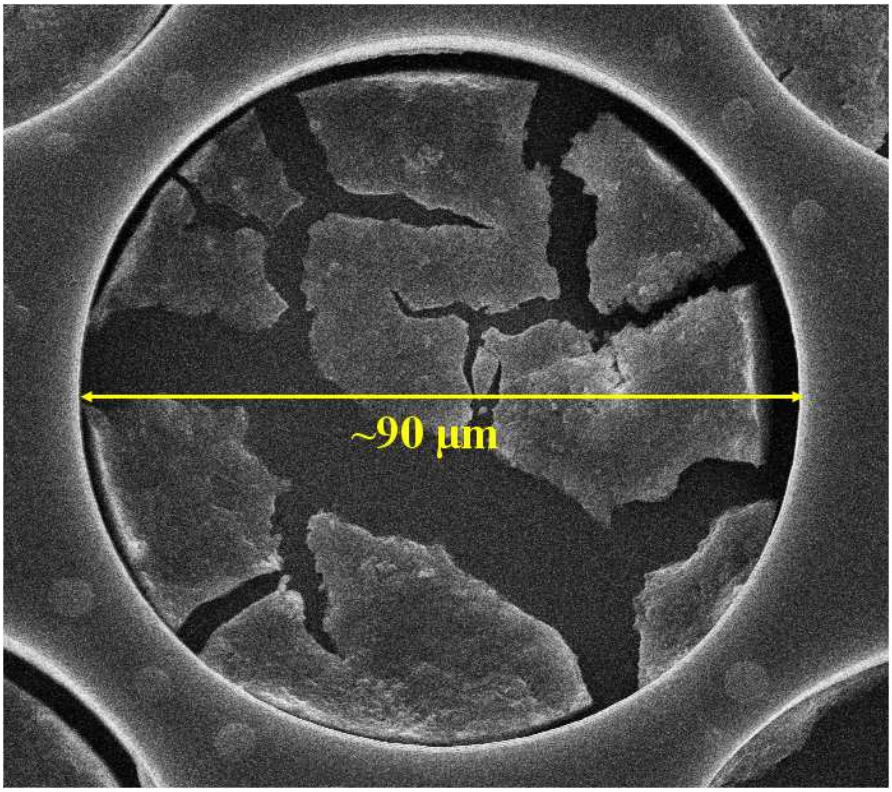

(b)

Figure 10.5: (a) SEM image of dried PDMS MSIWs after complete reaction of *E.coli* with Red-gal; (b) Exploded view of dried well of MSIW

10.5 Summary

We developed a rapid diagnostic device for detecting *E.coli* (ATCC 11229, Castellani and Chalmers) in water by employing the enzymatic method on microspot with integrated wells (MSIW). Initially the detection protocol is optimized in micro-centrifuge tubes and found that approx. 70 min required to detect *E.coli*. Then this optimized protocol is employed on MSIWs, which has taken 10 to 15 min to detect *E.coli*. It is observed that MSIW reduces the reaction time compared to conventional centrifuge tube based method, probably due to increase in reaction surface area and decrease in volume of the samples.

Bibliography

[1] S. Makrides. Strategies for achieving high-level expression of genes in Escherichia coli. *Microbiological Reviews*, 60(3):512–538, 1996.

[2] P. Griffin, S. Ostroff, R. Tauxe, K. Greene, J. Wells, J. Lewis, and P. Blake. Illness associated with *escherichia coli* 0157:H7 infections. A broad clinical spectrum. *Annals of Internal Medicine*, 109(9):705–712, 1988.

[3] http://www.cdc.gov/ecoli/, (Accessed January 10, 2013).

[4] D. Shelton and J. Karns. Quantitative detection of Escherichia coli O157 in surface waters by using immunomagnetic electrochemiluminescence. *Applied and Environmental Microbiology*, 67(7):2908–2915, 2001.

[5] M. Varshney and Y. Li. Interdigitated array microelectrode based impedance biosensor coupled with magnetic nanoparticle–antibody conjugates for detection of escherichia coli o157: H7 in food samples. *Biosensors and Bioelectronics*, 22(11):2408–2414, 2007.

[6] H. Sarhan and H. Foster. A rapid fluorogenic method for the detection of escherichia coli by the production of β-glucuronidase. *Journal of Applied Microbiology*, 70(5):394–400, 2008.

[7] G. Pettibone. The use of lauryl tryptose broth containing 4-methylumbelliferyl-β-d-glucuronide (MUG) to enumerate escherichia coli from freshwater sediment. *Letters in Applied Microbiology*, 15(5):190–192, 1992.

[8] I. Gaudet, L. Florence, and R. Coleman. Evaluation of test media for routine monitoring of Escherichia coli in nonpotable waters. *Applied and Environmental Microbiology*, 62(11):4032–4035, 1996.

[9] T. Bellin, M. Pulz, A. Matussek, H. Hempen, and F. Gunzer. Rapid detection of enterohemorrhagic escherichia coliby real-time pcr with fluorescent hybridization probes. *Journal of Clinical Microbiology*, 39(1):370–374, 2001.

[10] H. Buehler, P. Katzman, and E. Doisy. Studies on β-glucuronidase from E. coli. *Proceedings of the Society for Experimental Biology and Medicine. Society for Experimental Biology and Medicine (New York, NY)*, 76(4):672–676, 1951.

[11] S. Edberg and M. Edberg. A defined substrate technology for the enumeration of microbial indicators of environmental pollution. *The Yale Journal of Biology and Medicine*, 61(5):389, 1988.

[12] A. Ibekwe, P. Watt, C. Grieve, V. Sharma, and S. Lyons. Multiplex fluorogenic real-time PCR for detection and quantification of Escherichia coli O157: H7 in dairy wastewater wetlands. *Applied and Environmental Microbiology*, 68(10):4853–4862, 2002.

[13] N. Jothikumar and M. Griffiths. Rapid detection of Escherichia coli O157: H7 with multiplex real-time PCR assays. *Applied and Environmental Microbiology*, 68(6):3169–3171, 2002.

[14] A. Bhagwat. Simultaneous detection of Escherichia coli O157: H7, Listeria monocytogenes and Salmonella strains by real-time PCR. *International Journal of Food Microbiology*, 84(2):217–224, 2003.

[15] A. Ibekwe and C. Grieve. Detection and quantification of Escherichia coli O157: H7 in environmental samples by real-time PCR. *Journal of Applied Microbiology*, 94(3):421–431, 2003.

[16] D. Chandler, J. Brown, D. Call, S. Wunschel, J. Grate, D. Holman, L. Olson, M. Stottlemyre, and C. Bruckner-Lea. Automated immunomagnetic separation and microarray detection of E. coli O157: H7 from poultry carcass rinse. *International Journal of Food Microbiology*, 70(1):143–154, 2001.

[17] L. Heijnen and G. Medema. Method for rapid detection of viable escherichia coli in water using real-time NASBA. *Water Research*, 43(12):3124–3132, 2009.

[18] M. Varshney, Y. Li, B. Srinivasan, and S. Tung. A label-free, microfluidics and interdigitated array microelectrode-based impedance biosensor in combination with nanoparticles immunoseparation for detection of escherichia coli

o157: H7 in food samples. *Sensors and Actuators B: Chemical*, 128(1):99–107, 2007.

[19] J. Yoon, J. Han, C. Choi, M. Bui, R. Sinclair, et al. Real-time detection of escherichia coli in water pipe using a microfluidic device with one-step latex immunoagglutination assay. *Transactions of the ASABE*, 52(3):1031–1039, 2009.

[20] S. Z. Hossain, C. Ozimok, C. Sicard, S. D. Aguirre, M. M. Ali, Y. Li, and J. D. Brennan. Multiplexed paper test strip for quantitative bacterial detection. *Analytical and Bioanalytical Chemistry*, 403(6):1567–1576, 2012.

[21] X. Fan, I. White, S. Shopova, H. Zhu, J. Suter, and Y. Sun. Sensitive optical biosensors for unlabeled targets: A review. *Analytica Chimica Acta*, 620(1-2):8–26, 2008.

[22] N. S. K. Gunda, J. Joseph, A. Tamayol, M. Akbari, and S. K. Mitra. Measurement of pressure drop and flow resistance in microchannels with integrated micropillars. *Microfluidics and nanofluidics*, 14(3-4):711–721, 2013.

[23] N. S. K. Gunda, B. Bera, N. Karadimitriou, S. K. Mitra, and S. Hassanizadeh. Reservoir-on-a-Chip (ROC): A new paradigm in reservoir engineering. *Lab on a Chip - Miniaturisation for Chemistry and Biology*, 11(22):3785–3792, 2011.

[24] N. S. K. Gunda, S. K. Mitra, and V. R. Rao. Fabrication of dielectrophoretic microfluidic device. *ASME Conference Proceedings*, pages 113–119, 2009.

[25] D. Wildeboer, L. Amirat, R. Price, and R. Abuknesha. Rapid detection of Escherichia coli in water using a hand-held fluorescence detector. *Water Research*, 44(8):2621–2628, 2010.

[26] S. R. Rasmussen, M. R. Larsen, and S. E. Rasmussen. Covalent immobilization of dna onto polystyrene microwells: the molecules are only bound at the 5' end. *Analytical Biochemistry*, 198(1):138–142, 1991.

[27] E. Ostuni, C. S. Chen, D. E. Ingber, and G. M. Whitesides. Selective deposition of proteins and cells in arrays of microwells. *Langmuir*, 17(9):2828–2834, 2001.

[28] M. Steinitz. Quantitation of the blocking effect of tween 20 and bovine serum albumin in elisa microwells. *Analytical Biochemistry*, 282(2):232–238, 2000.

Chapter 11

Conclusion

Different aspects for the development of rapid techniques for healthcare and environmental monitoring are explored.

The first objective of this research was to develop a portable and inexpensive lab-on-a-chip device for the early prediction of potential heart attacks.

In order to achieve this objective, an investigation and implementation of separating myoglobin molecules from blood sample using DEP in a microfluidic device was attempted. A mathematical model and numerical simulation of dielectrophoretic behavior of a myoglobin molecule in a microchannel with parallel array of electrodes at the bottom wall of the microchannel were investigated. A dielectric myoglobin model was developed by approximating the shape of the myoglobin molecule as sphere, oblate, and prolate spheroids. A generalized dielectrophoretic force acting on respective shapes of the molecule was derived. Both the non-dimensional electric field and square electric field gradients were calculated with Green's theorem method and finite element method. The results were also compared with Fourier series method [65], closed form solutions by Morgan et al. [65] and Chang et al. [66]. The excellent agreement between Greens theorem based analytical solution and numerical solutions were observed. The crossover frequency of 40 MHz was obtained for given properties of the myoglobin molecules. It was observed that the crossover frequency for myoglobin increased with increase in conductivity of the medium. The hydration layer reduced the crossover frequency of myoglobin molecules to 28 MHz. Both positive and negative DEP effects on the myoglobin molecules were observed at 50 MHz and 1 kHz applied frequency, respectively. The effect of different shapes of myoglobin on the DEP force was studied and it was observed that there is no significant effect on DEP force. The

concentration of molecules was maximum at $y^* = 1.25$ height at 1 KHz frequency and 10 V applied voltage. These findings showcase the potential of DEP force for manipulating nano-scale biomolecules.

As the next step, the mixing of two different colloidal suspensions under the influence of DEP force was theoretically investigated. A mathematical model was developed based on Laplace, heat conduction, Stokes, and convection-diffusion-migration equations to calculate electric field, temperature, velocity, and concentration distributions, respectively. The effects of SWDEP, TWDEP, SWET and TWET on the performance of micromixers and microconcentrators were studied numerically. Analytical and numerical solutions of DEP and ET forces along the length and height of the channel were compared. The effects of electrode size and placement on micromixing and microconcentrating performance were studied and the velocity and concentration distributions have been compared. The results indicate that SWDEP forces can be used to collect the particles at different locations. SWET and TWET forces can be used to manipulate the fluid along with the particles. Based on position and size of the electrodes, the size and location of the concentration regions changes by both DEP and ET forces. The movement of particles from the lower half of the channel to the upper half of the channel was observed using TWDEP forces. The shape and configuration of electrodes for efficient mixing in the microchannel was obtained from this study. Alternatively, the influence of electrothermal (ET) fluid flow for mixing application was also studied. Further, the effect of different types of DEP and ET were studied. The results obtained in this study provided sufficient information to design the mixing and separation components for lab-on-a-chip device.

A set of proof-of-concept experiments were then carried out using myoglobin and silica particles. Silica particles were used to mimic the myoglobin. Different DEP phenomena under different operating conditions were studied. Silica particles were found to exhibit both positive and negative DEP effects. Positive DEP is observed at 0 to 1 KHz frequency range and $5-10$ V applied voltage, and negative DEP is observed at 10 KHz to 40 KHz frequency range and 10 V applied voltage. Myoglobin responds to positive DEP effects at 5 kHz frequency and 5 V.

Further, experimental investigation of on-chip immunoassay was carried out. Different protocols were developed to immobilize the biomolecules on commonly

available microfluidic substrates such as silicon, glass and gold surfaces. Surface analytical techniques were used to characterize each step of immobilization. In this work, the existing method of silane formation using (3-aminopropyl)triethoxysilane (APTES) on silicon substrates was modified to produce a thin, stable layer of silane for uniform immobilization of biomolecules. The effect of concentration of APTES solution and silanization time on formation of silane layer were investigated. Optimized silane layer was used to immobilize the biomolecules of interest with the help of glutaraldehyde linker. It was observed that optimized silane layer helped to form a uniform, homogeneous and highly dense layer of biomolecules on the surface. The samples were characterized after every step of surface modification and biomolecule immobilization using Fourier Transform Infrared Spectroscopy (FTIR), spectroscopic ellipsometry, contact angle measurement system, atomic force microscopy, and fluorescence microscopy. The developed method of biomolecule immobilization using a thin stable silane layer was employed on different silicon substrates (flat and pillar). Also, immunoassay for detecting different biomolecules such as human IgG, *Listeria monocytogenes*, myoglobin and dengue on silicon substrate was employed using this method. It was observed that the optimized silane layer helped to increase the densities of biomolecules on the surface, which will further help to increase the sensitivity of immunoassay.

Later, a thiol based immobilization/biofunctionalization protocol for detecting Troponin T on gold surface was developed. Ellipsometer, Fourier Transform Infrared Spectroscopy and Contact angle measurement system were used to characterize the surface properties at each stage of immobilization to confirm the accuracy of process. We employed the optimized protocol to develop a microfluidic based biosensor for detecting Troponin T. Here, we considered a microfluidic channel integrated with an array of gold strips for detecting and quantifying the Troponin T in an aqueous solution. Change in fluorescence intensity along the length of the microchannel was measured and the observations indicate that binding of antigens along the length of the channel was reduced.

In addition to the development of optimized protocols for immobilizing the biomolecules on silicon and gold surfaces, we demonstrated the parallel biofunctionalization of cantilever arrays with V-groove array chips. We pointed the challenges faced in functionalization and explored the possible mechanisms to uni-

formly functionalize the cantilevers. Challenges like cantilever upward bending, analyte over flow on individual cantilevers and even over flow on entire cantilever array were observed. Such problems were eliminated by proper assembly of V-groove chip with lid that can provide proper capillary action to flow the functionalized solution on cantilever surface for proper functionalization. We performed a standard sandwich immunoassay using the developed method for simultaneous detection myoglobin and troponin T cardiac markers.

Possible implications: The development of such tools for cardiac marker detection take us one step closer to building simpler systems for early diagnosis of heart attacks and also pave the way for such products to be introduced to address several other health related problems pertaining to systems such as endocrine system.

The second objective of this research was to develop a rapid and low-cost field deployable test kit for detecting total coliform and *E.coli* in contaminated water samples.

We have demonstrated a simple approach for rapid simultaneous detection of total coliform and *E.coli* in contaminated water samples. A specifically formulated dual enzyme substrate chemical reagents, consisting of a mixture of Red-Gal substrate, MUG substrate, $FeCl_3$, and B-PER were used for the rapid detection purpose. The effect of Red-Gal, MUG, $FeCl_3$ and B-PER on rapid detection process were studied in detail. It was observed that oxidizing agent ($FeCl_3$) and lysing agent (B-PER) are essential for enhancing the rapid detection process. The present method was able to detect *E.coli* within 1 - 60 min at 37^oC. In this method, we need to provide pre-concentrated water samples for the test kit. Hence, to deploy this technique in the field (on-site), we have demonstrated a simple, easy to use, inexpensive, rapid and field deployable test method, called Mobile Water Kit (MWK), for detecting total coliform and *E.coli* in contaminated water samples. The MWK comprises of a low-cost water monitoring sensor coupled with a smartphone platform. The test method was based on rapid enzymatic process to detect the specific enzymes related to total coliform and *E.coli*. The test method concentrates the contaminants in water sample on the syringe filter unit and then allows the contaminants to interact with specifically formulated chemical reagents. The presence of total coliform and *E.coli* is identified through the appearance of

red color and blue fluorescence, respectively. This method has been successfully tested with known concentrations of bacteria as well as with contaminated water samples in the field. Its performance has also been validated with conventional laboratory methods. It was found that the results from the two field trials, conducted in Canada and India, corroborate well with the laboratory test results for total coliform. The mHealth *E.coli* App facilitates the transfer of the test results to the communities and water managers, thereby creating an early warning system for monitoring the water quality. The MWK is a promising test method for water quality monitoring in limited resource setting communities. It needs to be further validated for its functionality and applicability towards broader implementation in communities.

Further, the detection protocols optimized in micro-centrifuge tubes were used to develop a rapid and ultrasensitive diagnostic device for detecting *E.coli* in water by employing the enzymatic method on microspots with integrated wells (MSIW). This new method of chemically modified microwells were able to detect *E.coli* concentration of 40 CFU/ml within 10 to 15 min. It was observed that MSIW reduces the reaction time compared to conventional centrifuge tube based method or syringe filter based method, probably due to the increase in reaction surface area and decrease in volume of the samples.

Possible implications: The development of chemicals and methods for rapid detection of total coliform and *E.coli* can lead us to build simpler and easy to use rapid detection kits for other bacterial, viral, protozoal, parasitic and toxin detections.

11.1 Thesis significant contributions

Here are the list of contributions of this thesis work.

- Mathematical model for understanding the dielectrophoretic behavior of myoglobin molecules is developed. The effects of different parameters such as conductivity of medium, applied voltage, frequency and hydration layer on dielectrophoretic behavior of myoglobin molecules are studied. The results obtained for DEP behavior of myoglobin molecules from the developed model are compared with other models.

- Dielectrophoretic and electrothermal force based micromixers and microconcentrators are developed. The effect of different parameters such as electrode configuration, applied voltage, phase change and frequency on mixing and concentration performance are studied. The experimental behavior of myoglobin and silica particles under DEP was investigated.

- Optimized protocols for immobilization of biomolecules on silicon and gold surfaces are developed. Surface analytical techniques such as Fourier Transform Infrared Spectroscopy (FTIR), Spectroscopic Ellipsometery, Contact angle measurement, Atomic Force Microscopy (AFM) and Fluorescence Microscopy, were employed to characterize modified silicon and gold surfaces

- Successfully immobilized different biomolecules on different silicon and gold surfaces using organosilane and alkane thiols, respectively. Novel capillary based method for simultaneous functionalization of different microcantilever surfaces was developed.

- A simple and rapid method for simultaneous detection of coliform and *E.coli* was developed. Formulated dual enzyme substrate chemical reagents to enhance rapid enzymatic reaction. The effect of each component of formulated chemical reagent was studied on rapid detection performance.

- A rapid and low-cost field deployable water monitoring sensor, called Mobile Water Kit (MWK), was developed to detect coliform and *E.coli* bacteria. MWK was tested with actual field water samples collected from different water sources in India and Canada

- An ultra sensitive and rapid detection of *E.coli* was developed by chemically modifying the microwells using formulated chemical reagents.

11.2 Future work and recommendations

Implementation of DEP assisted on-chip microbead based immunoassay

An experimental method to implement the DEP assisted on-chip microbead based immunoassay to detect myoglobin from blood samples can be developed. The separation of myoglobin from blood sample can be carried out initially and then

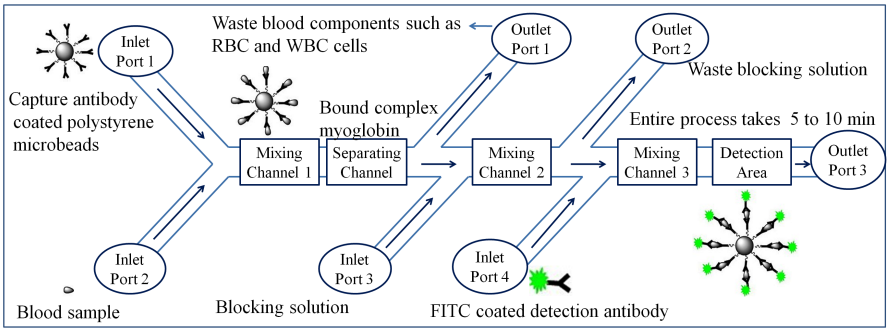

Figure 11.1: Schematic of DEP assisted on-chip micro-bead based immunoassay for detecting myoglobin

myoglobin can be detected using FITC labeled detection antibodies. Finally concentration of myoglobin can be measured from the blood sample. A proposed schematic of the lab-on-a-chip device can used for the detection of myoglobin molecules with DEP assisted on-chip microbead based immunoassay process is depicted in Fig. 11.1. It begins with the mixing of myoglobin antigens available in blood sample with capture-antibody coated microbeads. This mixing of complimentary biomolecules results in the formation of bound-complex myoglobin. The bound-complex myoglobin is separated from the other components of blood in the separating channel and mixed with blocking solution to deactivate the other bonding sites on the microbeads. The blocked bound-complex myoglobin is then mixed with Fluorescein isothiocyanate (FITC) labeled detection-antibodies to form a three-layered bound-complex myoglobin. Subsequently, fluorescent microscopy is employed, followed by the post-processing of obtained images, upon which the quantification of myoglobin molecules can be achieved. The mixing and separation tasks in this device can be carried out by using the DEP phenomena.

Future work for water monitoring work has been provided in section 9.5. Further work may need to incorporate the quantification of total coliform and *E.coli* using handheld reader for both red color and blue fluorescence measurements. Additional modifications to MWK may be needed to enhance the appearance of color/fluorescence.

List of Publications

Book chapters

1. **N. S. K. Gunda** and S. K. Mitra, Dielectrophoresis for manipulation of biomolecules, *Biomedical Engineering/Book 4*, ISBN 978-953-307-557-0, 2011.

Journal Papers Published

1. D. Sarkar, **N. S. K. Gunda**, I. Jamal, and S. K. Mitra, Optical biosensors with an integrated Mach-Zehnder Interferometer for detection of Listeria monocytogenes, *Biomedical Microdevices*, DOI:10.1007/s10544-014-9853-5, 2014.

2. **N. S. K. Gunda** and S. K. Mitra, Challenges and Opportunities for Capillary Based Biofunctionalization of Microcantilever Arrays, *Journal of Electrochemical Society*, 161(2):B3167, 2014.

3. **N. S. K. Gunda**, M. Singh, Y. Purwar, S. L. Shah, K. Kaur, and S. K. Mitra, Micro-spot with integrated pillars (MSIP) for detection of dengue, *Biomedical Microdevices*, 15:959, 2013.

4. J. Joseph, **N. S. K. Gunda**, and S. K. Mitra, On-chip Porous Media: Porosity and permeability measurements, *Chemical Engineering Science*, 99:274, 2013.

5. **N. S. K. Gunda**, J. Joseph, A. Tamayol, M. Akbari, and S. K. Mitra, Measurement of pressure drop and flow resistance in microchannels with integrated micropillars, *Microfluidics and Nanofluidics*, 14(3-4):711-721, 2013.

6. **N. S. K. Gunda**, S. Bhattacharjee, and S. K. Mitra, Study on the use of dielectrophoresis and electrothermal forces to produce on-chip micromixers and microconcentrators, *Biomicrofluidics*, 6:034118, 2012.

7. S. Das, P. Waghmare, M. Fan, **N. S. K. Gunda**, S. Roy, and S. K. Mitra, Dynamics of liquid droplets in an evaporating drop: Liquid droplet Coffee Stain effect, *RSC Advances*, 2:8390-8401, 2012.

8. **N. S. K. Gunda**, and S. K. Mitra, Direct Simulation of Transport Properties from Three-Dimensional (3D) Reconstructed Solid-Oxide Fuel-Cell (SOFC) Electrode Microstructures, *Journal of Physics: Conference Series (JPCS)*, 362:012001, 2012.

9. B. Bera, **N. S. K. Gunda**, S. K. Mitra, and D. Vick, Characterization of nanometer-scale porosity in reservoir carbonate rock by focused ion beam-scanning electron microscopy, *Microscopy and Microanalysis*, 18(1):171-178, 2012.

10. **N. S. K. Gunda**, B. Bera, N. K. Karadimitriou, S. K. Mitra, and S. M. Hassanizadeh, Reservoir-on-a-Chip (ROC): A new paradigm in reservoir engineering, *Lab on a Chip*, 11(22):3785-3792, 2011.

11. **N. S. K. Gunda**, H. Choi, A. Berson, B. Kenney, K. Karan, J. G. Pharaoh and S. K. Mitra, Focused Ion Beam Scanning Electron Microscopy on Solid-Oxide Fuel-Cell Electrode: Image analysis and computing effective transport properties, *Journal of Power Sources*, 196:3592-3603, 2011.

12. **N. S. K. Gunda** and S. K. Mitra, Modeling of Dielectrophoretic Transport of Myoglobin Molecules in Microchannels, *Biomicrofluidics*, 4:014105, 2010.

Journal Papers Under Review

1. **N. S. K. Gunda**, M. Singh, L. Norman, K. Kaur and S. K. Mitra, Optimization and characterization of biomolecule immobilization on silicon substrates using (3-aminopropyl)triethoxy silane (APTES) and glutaraldehyde linker, *Applied Surface Science*, Under Review, 2014.

2. **N. S. K. Gunda**, S. Naciker, M. S. Ghoraishi, S. Bhattacharjee, T. Thundat and S. K. Mitra, Enhanced rapid detection of total coliform and *E.coli* in contaminated water samples using specifically formulated dual enzyme substrate chemical reagents, *Water Research*, Under Review, 2014.

3. **N. S. K. Gunda**, S. Naciker, S. Shinde, S. Kimbahune, S. Shrivastava, and S. K. Mitra, Mobile Water Kit (MWK): A Smartphone Compatible Low-Cost Water Monitoring System for Rapid Detection of Total Coliform and *E.coli*, *Analyst*, Under Review, 2014.

Report of Inventions

1. S. K. Mitra, **N. S. K. Gunda**, S. K. Naicker, M. S. Ghoraishi, S. Bhattacharjee, and T. Thundat, Enhanced rapid detection of *E.coli*, ROI No. 2013040, University of Alberta, TEC Edmonton, Alberta, Canada, 2013.

2. S. K. Mitra, **N. S. K. Gunda**, S. K. Naicker, M. S. Ghoraishi, S. Bhattacharjee, and T. Thundat, Microspot with integrated wells (MSIW) for the detection of *E.coli*, ROI No. 2013041, University of Alberta, TEC Edmonton, Alberta, Canada, 2013.

3. S. K. Mitra, S. K. Naicker, R. Chavali, and **N. S. K. Gunda**, Low-cost Rapid Fluoride Detector for Water, ROI No. 2013063, University of Alberta, TEC Edmonton, Alberta, Canada, 2014.

4. S. K. Mitra, S. K. Naicker, R. Chavali, and **N. S. K. Gunda**, Glucometer Compatible Low-cost Rapid Fluoride Detector for Water, University of Alberta, TEC Edmonton, Alberta, Canada, 2014.

5. S. K. Mitra, **N. S. K. Gunda**, S. K. Naicker, and R. Chavali, Glucometer Compatible Low-cost Rapid *E.coli* Detector for Water, University of Alberta, TEC Edmonton, Alberta, Canada, 2014.

6. S. K. Mitra, S. K. Naicker, R. Chavali, and **N. S. K. Gunda**, Glucometer Compatible Low-cost Rapid Arsenic Detector for Water, University of Alberta, TEC Edmonton, Alberta, Canada, 2014.

7. S. K. Mitra, **N. S. K. Gunda**, and S. K. Naicker. Mobile Water Kit (MWK): A smartphone compatible low-cost water monitoring system for rapid detection of total coliform and *E.coli*, University of Alberta, TEC Edmonton, Alberta, Canada, 2014.

Conference Proceedings

1. B. S. Gill, **N. S. K. Gunda** and S. K. Mitra, Impact of Injection Rate on Oil Recovery Using a Novel Reservoir on-Chip (ROC)- Waterflood on a CHIP, SPE 169492-MS, Western North America and Rocky Mountain Joint Conference and Exhibition, Denver, Co, USA, April 15-18, 2014.

2. **N. S. K. Gunda**, S. Naicker, M. S. Ghoraishi, S. Bhattacharjee, T. G. Thundat, and S. K. Mitra, Rapid Detection of Total Coliform and E.Coli in Contaminated Water Using Chemically Modified Microwells, Paper # J4-2788, Proceedings of 224th ECS Meeting, San Francisco, USA, October 27 to November 1, 2013.

3. **N. S. K. Gunda** and S. K. Mitra, Distinguished Invited Speaker–Capillary-Based Assay for Cardiac Markers With Cantilever Platform, Paper # J4-2792, Proceedings of 224th ECS Meeting, San Francisco, USA, October 27 to November 1, 2013.

4. **N. S. K. Gunda** and S. K. Mitra, Microfluidic Based Biosensor for Detection of Cardiac Markers, Paper # FEDSM2013-16270, Proceedings of ASME 2013 Fluids Engineering Summer Meeting, Incline Village, Nevada, USA, July 7-11, 2013.

5. **N. S. K. Gunda**, S. Naicker, M. S. Ghoraishi, S. Bhattacharjee, T. G. Thundat and S. K. Mitra, Microspot with Integrated Wells (MSIW) for the detection of E.coli, Paper # ICNMM2013-73037, Proceedings of ASME 2013 11th International Conference on Nanochannels, Microchannels, and Minichannels, Sapporo, Japan, June 16-19, 2013.

6. **N. S. K. Gunda**, S. Naicker, and S. K. Mitra, Electrochemical detection of cardiac myoglobin using microchannel with interdigitated electrodes (MCIE), Paper # J2-1473, Proceedings of 223rd ECS Meeting, Toronto, Canada, May 12-17, 2013.

7. **N. S. K. Gunda**, M. Singh, Y. Purwar, S.Shah, K. Kaur, and S. K. Mitra, Microspot with integrated pillars (MSIP) for the detection of Dengue NS1 virus, Paper # J2-1475, Proceedings of 223rd ECS Meeting, Toronto, Canada, May 12-17, 2013.

8. **N. S. K. Gunda**, A. Tamayol, M. Akbari, S. K. Mitra, and M. Bahrami, Creeping Flow Through Microchannels with Integrated Micro-pillars, Paper # ICNMM2012-73199, Proceedings of ASME 2012 10th International Conference on Nanochannels, Microchannels and Minichannels, Rio Grande, Puerto Rico, USA, July 8 - 12, 2012.

9. J. Joseph, **N. S. K. Gunda**, and S. K. Mitra, Monte Carlo Simulations to Determine Effective Gas Diffusivity of an Actual Porous Medium Image Obtained from Focused Ion Beam Scanning Electron Microscopy, Paper # ICNMM2012-73169. Proceeding of ASME 2012 10th International Conference on Nanochannels, Microchannels and Minichannels, Rio Grande, Puerto Rico, USA, July 8 - 12, 2012.

10. **N. S. K. Gunda**, and S. K. Mitra, Direct Simulation of Transport Properties from Three-Dimensional (3D) Reconstructed Solid-Oxide Fuel-Cell (SOFC) Electrode Microstructures, 1st European Conference on Gas Micro Flows, Skiathos Island, Greece, June 6 - 8, 2012.

11. **N. S. K. Gunda**, M. Singh, S. S. Roy, and S. K. Mitra, Developing Electrochemical Impedance Immunosensor for the Detection of Myoglobin in Blood Serum, IMCS 2012 - The 14th International Meeting on Chemical Sensors, Nrnberg/Nuremberg, Germany, May 20 - 23, 2012. C11. M. Singh, **N. S. K. Gunda**, S. K. Mitra and K. Kaur, Site Specific and Oriented Protein Immobilization on Silicon for Bioassays, Abstract submitted, IMCS 2012-The 14th International Meeting on Chemical Sensors, Nuremberg, Germany, May 20 - 23, 2012.

12. S.S. Roy, **N. S. K. Gunda**, P. R. waghmare and S. K. Mitra (2012), Exploring the bead-based immunofluorescence assay for vitamin D detection, Abstract submitted, IMCS 2012-The 14th International Meeting on Chemical Sensors, Nuremberg, Germany, May 20 - 23, 2012.

13. **N. S. K. Gunda** and S. K. Mitra, Quantification of Solid Oxide Fuel Cells from Three-dimensional Physically Realistic Network Structures, Paper # ESFuelCell2011-54929, Proceedings of ASME 2011 5th International Conference on Energy Sustainability & 9th Fuel Cell Science, engineering and Technology Conference, ESFuelCell2011, Washington, DC, USA, August 7-10, 2011.

14. **N. S. K. Gunda** and S. K. Mitra, Microfluidics for Detection of Myoglobin in Blood Sample, Paper # E2-1167R, Proceedings of 219th ECS Meeting, Montreal, Canada, May 1-6, 2011.

15. K. K. Mohan, **N. S. K. Gunda**, A. Srividya, A. K. Verma, The Analytical Network Process (ANP) Model for Improvement of QoS at prototype level, International Conference on Reliability, Quality and Information Technology, ICRQIT-2011, Kathmandu, Nepal, December 7-9, 2011.

16. B. Bera, **N. S. K. Gunda**, N. Karadimitriou, S.K. Mitra and S. M. Hassanizadeh, Investigation of Two-Phase Flow in a Pore Network Fabricated on a Glass Micro-model, Paper # AJK2011-36002, Proceedings of ASME Fluids Engineering Division Summer Meeting 2011, Hamamatsu, Japan, July 24-29, 2011,.

17. **N. S. K. Gunda**, S. Chakraborty and S. K. Mitra, The Study of Combined Electroosmotic and Pressure Driven Flow in Wavy Nanochannels, Paper # IMECE2010-39255, Proceedings of the ASME 2010 International Mechanical Engineering Congress and Exposition, IMECE2010, Vancouver, British Columbia, Canada, November 12-18, 2010.

18. **N. S. K. Gunda** and S. K. Mitra, Experimental Investigation of Dielectrophoretic Behavior of Myoglobin and Silica Particles on a Microelectrode Chip, Paper # FEDSM-ICNMM2010-30306, Proceedings of ASME 2010 3rd Joint US-European Fluids Engineering Summer Meeting and 8th International Conference on Nanochannels, Microchannels, and Minichannels, FEDSM2010-ICNMM2010, Montreal, Canada, August 2-4, 2010.

19. **N. S. K. Gunda** and S. K. Mitra, Modeling of Dielectrophoresis for Myoglobin Molecules in a Microchannel with Parallel Electrodes, Paper # IMECE2009-10765, Proceedings of the ASME 2009 International Mechanical Engineering Congress and Exposition, IMECE09, Lake Buena Vista, Florida, USA, November 13-19, 2009.

20. **N. S. K. Gunda**, S. K. Mitra and S. Bhattacharjee, Dielectrophoretic Mixing with Novel Electrode Geometry, Paper # FEDSM2009-78260, Proceedings of the ASME 2009 Fluids Engineering Division Summer Meeting, FEDSM09, Vail, Colorado, August 2-6, 2009.

21. **N. S. K. Gunda**, S. K. Mitra and V. R. Rao, Fabrication of Dielectrophoretic Microfluidic Device, Paper # ICNMM2009-82170, Proceedings of

the Seventh International ASME Conference on Nanochannels, Microchannels and Minichannels, ICNMM09, Pohang, South Korea, June 22-24, 2009.

Oral Presentations

1. **N. S. K. Gunda**, S. Naicker, M. S. Ghoraishi, S. Bhattacharjee, T. G. Thundat, and S. K. Mitra, Rapid Detection of Total Coliform and E.Coli in Contaminated Water Using Chemically Modified Microwells, Paper # J4-2788, Proceedings of 224th ECS Meeting, San Francisco, USA, October 27 to November 1, 2013.

2. **N. S. K. Gunda** and S. K. Mitra, Microfluidic Based Biosensor for Detection of Cardiac Markers, Paper # FEDSM2013-16270, Proceedings of ASME 2013 Fluids Engineering Summer Meeting, Incline Village, Nevada, USA, July 7-11, 2013.

3. **N. S. K. Gunda**, S. Naicker, and S. K. Mitra, Electrochemical detection of cardiac myoglobin using microchannel with interdigitated electrodes (MCIE), Paper # J2-1473, Proceedings of 223rd ECS Meeting, Toronto, Canada, May 12-17, 2013.

4. **N. S. K. Gunda**, M. Singh, Y. Purwar, S.Shah, K. Kaur, and S. K. Mitra, Microspot with integrated pillars (MSIP) for the detection of Dengue NS1 virus, Paper # J2-1475, Proceedings of 223rd ECS Meeting, Toronto, Canada, May 12-17, 2013.

5. **N. S. K. Gunda** and S. K. Mitra, Experimental Investigation of Dielectrophoretic Behavior of Myoglobin and Silica Particles on a Microelectrode Chip, Paper # FEDSM-ICNMM2010-30306, Proceedings of ASME 2010 3rd Joint US-European Fluids Engineering Summer Meeting and 8th International Conference on Nanochannels, Microchannels, and Minichannels, FEDSM2010-ICNMM2010, Montreal, Canada, August 2-4, 2010.

6. **N. S. K. Gunda**, S. K. Mitra and S. Bhattacharjee, Dielectrophoretic Mixing with Novel Electrode Geometry, Paper # FEDSM2009-78260, Proceedings of the ASME 2009 Fluids Engineering Division Summer Meeting, FEDSM09, Vail, Colorado, August 2-6, 2009.

Poster Presentations

1. **N. S. K. Gunda**, M. Singh, D. Sarkar, P. R. Waghmare, S. S. Roy, K. Kaur and S. K. Mitra, Integrated microfluidic based immunosensor platforms for rapid detection of biomolecules, Colloids and Nanomedicine 2012, Amsterdam, The Netherlands, July 15 - 17, 2012.

2. **N. S. K. Gunda**, B. Bera, D. Vick, N. Karadimitriou, S. K. Mitra and S. M. Hassanizadeh, Reservoir-on-a-Chip (ROC): A new paradigm for flow in porous media, Gordon Research Conference, Les Diablerets, Switzerland, June 23-24 2012.

3. B. Mounika, **N. S. K. Gunda** and S. K. Mitra, Detection of cardiac markers using microfluidic cantilever, Research Poster Symposium, University of Alberta, Edmonton, Canada, June 20 (2012).

4. M. Singh, **N. S. K. Gunda**, K. Kaur, and S. K. Mitra, Bioconjugation: Covalent Immobilization on silane monolayer for Microfluidics Applications, 95th Canadian chemistry conference and exhibition, Calgary, Alberta, Canada, May 26 - 30, 2012.

5. B. Bera, **N. S. K. Gunda**, N. K. Karadimitriou, S. K. Mitra and S. M. Hassanizadeh, Fabrication of Quartz-etched Micro-model for Two-phase Flow Studies, Proceedings of 3rd International Conference on Porous media & Annual meeting of the International Society for Porous Media, INTERPORE2011, Bordeaux, France, March 29-31, 2011.

6. P. R. Waghmare, **N. S. K. Gunda** and S. K. Mitra, Transportation and Separation of Specific Biomolecule of Interest in Microfluidic Device, Proceedings of the ASME 2009 International Mechanical Engineering Congress and Exposition, IMECE09, Lake Buena Vista, Florida, USA, November 13-19, 2009.

7. **N. S. K. Gunda**, P. R. Waghmare and S. K. Mitra, Microfluidic Device for Separation of Biomolecules, Poster # BN08POS-067, Proceedings of the 2nd Bangalore Nano Conference, Bangalore, India, December 11-13, 2008.

Appendix A

Detailed expressions

A1. Detailed expressions for E_x, E_y, $\partial E_x/\partial x$, $\partial E_y/\partial y$, $\partial E_x/\partial y$ and $\partial E_y/\partial x$

The detailed expressions for E_x, E_y, $\partial E_x/\partial x$, $\partial E_y/\partial y$, $\partial E_x/\partial y$ and $\partial E_y/\partial x$ are given in this section. These components are derived by differentiating the potential distribution function given in Eq. 2.22. The expressions derived in this paper for potential, electric field in x and y directions are similar to the Wang et al.,[52] Clague at al.[53] and Molla et al.[36, 37] with different notation. Here the simplified and modified expressions are provided. The following expressions can be used to calculate the DEP forces by substituting into Eq. 2.1

$$\begin{aligned} E_x =& \frac{1}{\pi}\sum_{i=-\infty}^{\infty}\left\{\phi_e(x)y\left(\frac{1}{y^2+(x-q_i)^2}-\frac{1}{y^2+(x-p_i)^2}\right)\right\} \\ &+\frac{1}{\pi}\sum_{i=-\infty}^{\infty}\left\{-\phi_g(x)y\left(\frac{1}{y^2+(x-q_i)^2}-\frac{1}{y^2+(x-p_{i+1})^2}\right)\right. \\ &+Sy\left(\frac{x-q_i}{y^2+(x-q_i)^2}-\frac{x-p_{i+1}}{y^2+(x-p_{i+1})^2}\right) \\ &\left.-S\left(tan^{-1}\left[\frac{x-q_i}{y}\right]-tan^{-1}\left[\frac{x-p_{i+1}}{y}\right]\right)\right\} \end{aligned} \tag{A.1}$$

$$\begin{aligned} E_y =& \frac{1}{\pi}\sum_{i=-\infty}^{\infty}\left\{-\phi_e(x)\left(\frac{x-q_i}{y^2+(x-q_i)^2}-\frac{x-p_i}{y^2+(x-p_i)^2}\right)\right\} \\ &+\frac{1}{\pi}\sum_{i=-\infty}^{\infty}\left\{+\phi_g(x)\left(\frac{x-q_i}{y^2+(x-q_i)^2}-\frac{x-p_{i+1}}{y^2+(x-p_{i+1})^2}\right)\right. \\ &+Sy^2\left(\frac{1}{y^2+(x-q_i)^2}-\frac{1}{y^2+(x-p_{i+1})^2}\right) \\ &\left.+\frac{S}{2}\left(ln\left[(x-q_i)^2+y^2\right]-ln\left[(x-p_{i+1})^2+y^2\right]\right)\right\} \end{aligned} \tag{A.2}$$

$$
\begin{aligned}
\frac{\partial E_x}{\partial x} =& -\frac{\partial E_y}{\partial y} \\
&= \frac{1}{\pi}\sum_{i=-\infty}^{\infty}\left\{-2\phi_e(x)y\left(\frac{x-q_i}{[y^2+(x-q_i)^2]^2}-\frac{x-p_i}{[y^2+(x-p_i)^2]^2}\right)\right\} \\
&+\frac{1}{\pi}\sum_{i=-\infty}^{\infty}\left\{+2\phi_g(x)y\left(\frac{x-q_i}{[y^2+(x-q_i)^2]^2}-\frac{x-p_{i+1}}{[y^2+(x-p_{i+1})^2]^2}\right)\right. \\
&+Sy\left(\frac{y^2-(x-q_i)^2}{[y^2+(x-q_i)^2]^2}-\frac{y^2-(x-p_{i+1})^2}{[y^2+(x-p_{i+1})^2]^2}\right) \\
&\left.-2Sy\left(\frac{1}{y^2+(x-q_i)^2}-\frac{1}{y^2+(x-p_{i+1})^2}\right)\right\}
\end{aligned}
\tag{A.3}
$$

$$
\begin{aligned}
\frac{\partial E_x}{\partial y} =& \frac{\partial E_y}{\partial x} \\
&= \frac{1}{\pi}\sum_{i=-\infty}^{\infty}\left\{-\phi_e(x)\left(\frac{y^2-(x-q_i)^2}{[y^2+(x-q_i)^2]^2}-\frac{y^2-(x-p_i)^2}{[y^2+(x-p_i)^2]^2}\right)\right\} \\
&+\frac{1}{\pi}\sum_{i=-\infty}^{\infty}\left\{+\phi_g(x)\left(\frac{y^2-(x-q_i)^2}{[y^2+(x-q_i)^2]^2}-\frac{y^2-(x-p_{i+1})^2}{[y^2+(x-p_{i+1})^2]^2}\right)\right. \\
&-2Sy^2\left(\frac{x-q_i}{[y^2+(x-q_i)^2]^2}-\frac{x-p_{i+1}}{[y^2+(x-p_{i+1})^2]^2}\right) \\
&\left.+2S\left(\frac{x-q_i}{y^2+(x-q_i)^2}-\frac{x-p_{i+1}}{y^2+(x-p_{i+1})^2}\right)\right\}
\end{aligned}
\tag{A.4}
$$

Appendix B

AFM Data

B1. AFM Data after oxygen plasma treatment

Figure B.1 shows the AFM images obtained after the oxygen plasma treatment (80 sccm, 150 mT, 225 W RF) on silicon surface (1 μm $\times$ 1 μm) after 10 min duration. Surface roughness for this surface is approximately 0.51 nm.

B2. AFM Data for APTES treated silicon surface

Figure B.2 shows the packing of APTES on silicon surface (1 μm $\times$ 1 μm) after one hour incubation time whereas Fig. B.3 depicts the APTES layer on silicon surface for 5 μm $\times$ 5 μm. This demonstrates that packing of monolayer is uniform.

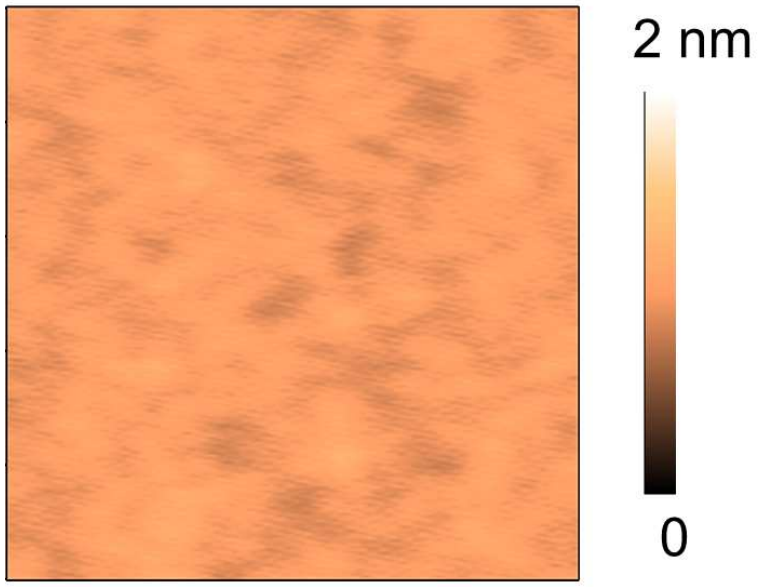

Figure B.1: Tapping mode AFM images for a silicon substrate after oxygen plasma treatment for 10 min duration. The size of scanning area is 1 μm $\times$ 1 μm. The side bar indicates the height scale.

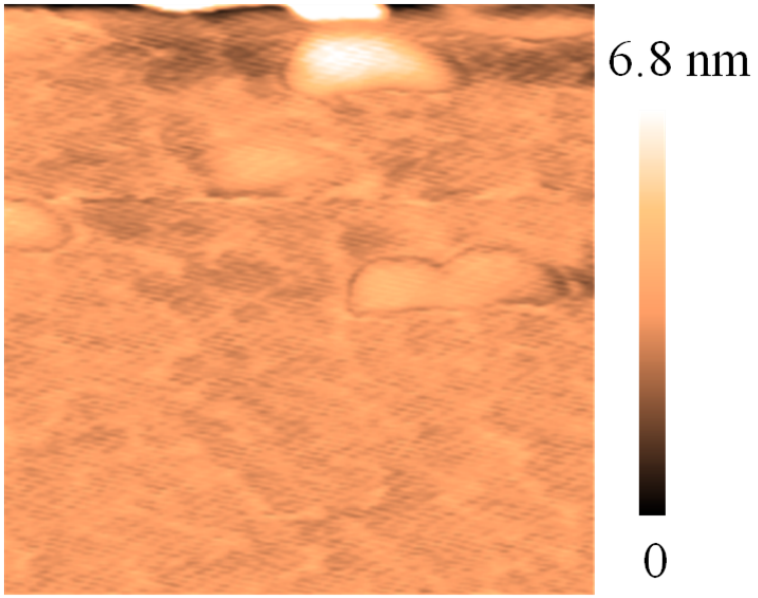

Figure B.2: Tapping mode AFM images for a substrate subjected to silanization with APTES. The size of scanning area is 1 μm $\times$ 1 μm. The side bar indicates the height scale.

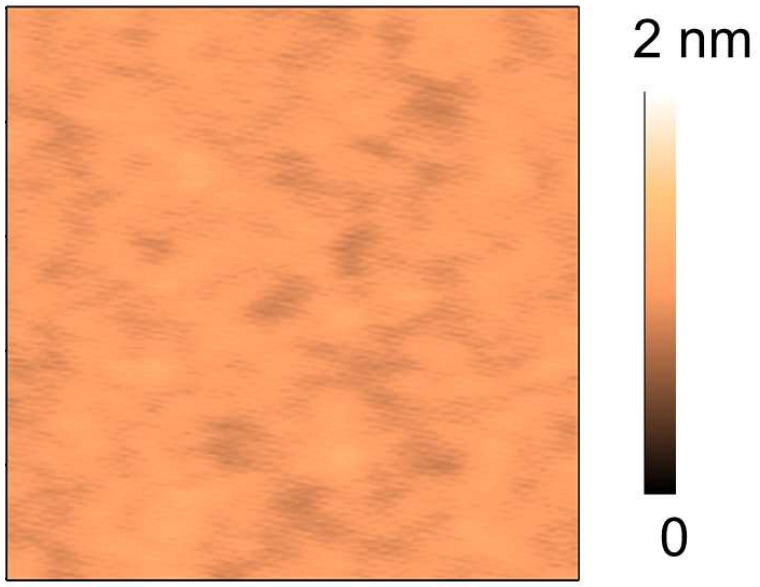

Figure B.3: Tapping mode AFM images for a substrate subjected to silanization with APTES. The size of scanning area is 5 μm $\times$ 5 μm. The side bar indicates the height scale.

Appendix C

Standard Confirmatory Tests

C1. Standard confirmatory tests

Classical microbiological tests, including estimation of number of the coliform groups by the multiple tube dilution tests (presumptive test, confirmed test, or completed test) (IS1622:1981) were performed on field water samples to cross-check the results obtained by MWK.

C1.1.Test for coliform

The coliform group includes aerobic and facultative anaerobic gram negative, non-spore forming rod shaped bacteria which ferments lactose with gas formation within 48 hr at 37^{o}C. The standard test for the estimation of number of the coliform groups may be carried out either by multiple tube dilution tests (presumptive test, confirmed test, or completed test) or by the membrane filter technique. The presumptive, confirmed and completed tests with Most Probable Number (MPN) or multiple tube dilution tests are presented as total independent procedures. Standard practice in water analysis is to plant five tubes for each dilution and a minimum three different dilutions are employed.

MacConkey broth was used as a presumptive medium for the enumeration of coliform bacteria in water samples. Ten tubes of 10 ml volume for single strength and five tubes of 10 ml volume for the double strength MacConkey broth were prepared and sterilized at 15 psi for 15 min. Ten milliliters of water sample was then added to each of the five tubes for the double strength medium. For the single strength medium, 1 ml of water sample was added to the first five tubes and 0.1 ml of water sample was added to rest of the five tubes. All above said tubes were incubated at 37^{o}C for 18-24 hr. The presence of coliform bacteria was identified by the yellow coloration (indicating the growth with acid) and gas production with inverted Durham tube. The results were recorded using MPN Table. All positive

cultures were retained for further confirmatory tests.

C1.2. Test for Faecal coliform

This procedure is used to differentiate coliforms of faecal origin from those of non faecal origin. Faecal coliforms are those coliform which can ferment lactose at 44.5^{o}C within 24±2 hr with the production of gas. Brilliant green bile lactose (BGBL) broth medium is used for this test. All presumptive positive tubes of the coliform test were subcultured in BGBL medium and incubated at 44.5^{o}C for 24 hr in a water bath. Gas formation within 24 hr was an indicator of the presence of faecal coliform.

BGBL broth medium was used as a confirmatory test for fecal coliforms. Four milliliters of the medium was dispensed into dilution tubes and sterilized at 15 psi for 15 min. The samples that tested positive for the presence of total coliform in section 1.1 were inoculated into the dilution tubes containing the BGBL broth medium and incubated at 44.5^{o}C for 18-24 hr. The presence of faecal coliform was confirmed by the production of gas in inverted Durham tube.

C1.3.Test for *E.coli*

E.coli is one of the members of faecal coliform which ferments lactose with the production of gas at 44.5^{o}C within 24 hr as well as produces indole from tryptophone at 44.5^{o}C within 24 hr. All the positive tubes of BGBL broth at 44.5^{o}C (faecal coliforms) were subcultured in tubes of peptone water and incubated at 44.5^{o}C for 24±2 hr. A few drops of Kovacs reagent were then added to each of these tubes. The presence of *E.coli* was identified by the appearance of pink color while the absence of *E.coli* was indicated by the appearance of yellow color.

C2. Confirmatory Results

The results obtained by the MWK were initially confirmed with conventional laboratory test results using most probable number (MPN) by randomly selecting two water sources. Table S1 provides the confirmatory test results for Sample # 9 and Sample # 11. The column 1 of Table C.1 and C.2 represents sample numbers. The columns 2, 3 and 4 represent the total coliform count (MPN/100ml), faecal coliform count (MPN/100ml) and *E.coli* count (MPN/100ml) in the water samples, respectively. It was found that for all these tests, Sample # 9 showed significant amount of coliform, which is corroborated by higher color intensity for Sample # 9 in Fig. 9.8. Similarly, for Sample # 11, one observes less amount

Sample Number	Total coliform count $MPN/100ml$ (Presumptive coliform count)	Faecal coliform count $MPN/100ml$ (Confirmed coliform count)	*E.coli* count $MPN/100ml$
Sample # 9	>1600	>1600	1600
Sample # 11	>1600	1600	170

Table C.1: Laboratory test results by different established methods for water samples (Sample # 9 and Sample # 11) tested during the first field trial.

Sample Number	Total coliform count $MPN/100ml$ (Presumptive coliform count)	Faecal coliform count $MPN/100ml$ (Confirmed coliform count)	*E.coli* count $MPN/100ml$
Sample # A1	900	348	175
Sample # A2	$\geq$1600	130	109
Sample # A3	300	<2	<2
Sample # A4	2	<2	<2
Sample # A5	$\geq$1600	240	40

Table C.2: Laboratory test results by different established methods for water samples tested during the second field trial.

of coliform, as compared to Sample # 9, which is again corroborated with lower color intensity in Fig. 9.8 for this sample.

The quantification of total coliform, faecal coliform and *E.coli* for the second field trial were conducted at the BRC, Mumbai, India, using well-established methods. It was observed that for all these tests, Sample # A2 and A5 had substantial amount of coliform, which is indicated by significant color intensity for these samples (refer Fig. 9.9). Likewise, for Sample # A1 and A3, less amount of coliform is identified, as compared to Sample # A2 and A5, which is again corroborated with much lower color intensity for these samples in Fig. 9.9.